Universidade Vigo

UNIVERSITY OF VIGO
DEPARTMENT OF ELECTRONICS TECHNOLOGY

DISSERTATION SUBMITTED FOR THE DEGREE OF
DOCTOR OF PHILOSOPHY AT THE UNIVERSITY OF VIGO

"INTERNATIONAL DOCTOR MENTION"

TRANSIENT RESPONSE ANALYSIS AND DESIGN OF CURRENT-CONTROLLED GRID-TIED CONVERTERS

Author: Ana Vidal González

Supervisors: Jesús Doval Gandoy
Francisco D. Freijedo Fernández

Vigo, 15th May 2015

PH.D. COMMITTEE MEMBERS:

Josep M. Guerrero

Alejandro G. Yepes

Eva González-Romera

Jörg Dannehl

Li Ran

María Isabel Milanés-Montero

15th May 2015

University of Vigo

Vigo, Spain

Vita

Ana Vidal González was born in Vilagarcía de Arousa, Spain, in 1985. She received the B.Sc. degree in Industrial Electronic Engineering and the M.Sc. degree in Automation and Industrial Electronic Engineering from the University of Vigo, Spain, in 2007 and 2010, respectively, both with Distinction.

From November 2009, she works in the Applied Power Electronics Technology Research Group (APET) of the University of Vigo. She is currently working toward the Ph.D. degree in such group, being funded by the Spanish Government (FPU grant holder). From March 2013 to June 2013, she joined the Electrical Power Research Group of the University of Warwick in the United Kingdom for a research stay. Her research interests include digital control of power electronics converters, with special focus on grid-connected applications, such as those based on renewable energy.

She has coauthored 30 published technical papers in the field of power electronics [1–30]. Fourteen of them are published in JCR-indexed journals [1–11, 14, 27, 28]. She is a member of the Institute of Electrical and Electronic Engineers (IEEE), the IEEE Industrial Electronics Society, the IEEE Industry Applications Society and the IEEE Power Electronics Society.

Transient Response Analysis and Design of Current-Controlled Grid-Tied Converters

Ana Vidal González

(ABSTRACT)

In the current scenario of the electric grid, high penetration of renewable energy sources, distributed power generation systems and power electronic converters coexist. In order to prevent destabilization, the system operators have defined international grid codes (GCs), which, in case of a fault, ask generation units to remain connected and support the grid during a certain time, by means of reactive current injection. Aside from the compliance of these and other ancillary services, installations must fulfill the specific demands of the end-customers.

Regardless of the generation unit nature, voltage source converters (VSCs) are the most common option as interface for grid connection in most of these applications. In order to guarantee the proper behavior of the system, together with the satisfaction of all the restrictions, a rigorous analysis and design of the control loops of such converters becomes crucial. This challenge should start from the innermost loops, which are usually current ones, since they establish the performance of the overall system, specially in terms of transient response. Therefore, the main objective of this dissertation is to provide a thorough study of the current control closed loop, oriented to an accurate tuning of the regulators.

In order to achieve such goal, a precise model of the current loop is needed. Linear low-order time-averaged plant models are usually selected, since their use allows to apply the well-known linear analysis and design methods. Additionally, the plant model parameters should be accurately identified in each specific working conditions. Linked to this aspect are some of the contributions of this thesis. Firstly, a method to estimate the VSC equivalent loss resistance is developed. This parameter permits to reflect on the plant model the effects associated to the converter losses, which have a great impact on the current loop behavior, particularly when the design constraints are established in terms of transient response, as it is demonstrated. Even though the role of the converter equivalent loss resistance is commonly accepted, just a few works aimed at current loop analysis and design consider it and, at this point, the available information on how to obtain its value is scarce.

Aside from the variations caused by the working conditions in the resistance, the plant inductance may also present important uncertainties with respect to the value of the VSC L/LCL interface filter measured at rated conditions (e.g., owing to core saturation and current magnitude, to temperature, to minor internal faults or changes...). Besides, extra impedance may be present in the electric circuit due to the existence of additional elements, such as the coupling transformer, the grid impedance or long wires. Therefore, a method to identify both parameters in the previously referred plant model, namely the equivalent inductance and resistance, is presented. Such estimation technique is an improvement of the above-mentioned one presented in this thesis (aimed only at the resistance identification). Both proposals have their basis on model

reference adaptive systems. Unlike the available techniques, these are specifically targeted at transient response optimization of grid-tied converters. The variables to be identified are iteratively estimated so as to minimize the error between the actual and the expected closed-loop current step response. Consequently, the proposed identification methods are directly oriented to the fulfillment of time-domain specifications. They can be applied either online or offline, during a precommissioning stage.

Once the plant parameters are identified, and after selecting the most suitable controller structure, the regulator has to be accurately designed. One common choice in grid-connected applications are resonant controllers, given their ability to regulate with zero steady-state error both sequences, while providing a good combination of simplicity and high performance. Regarding the integral gain of proportional-resonant (PR) controllers, although some qualitative guidelines are available for its tuning, they mostly do not consider the delay effect. Furthermore, they are not aimed at the optimization of the disturbance rejection transient response, which is crucial to fulfill the low-voltage ride-through requirement of GCs and, as proved in this work, more demanding than the reference tracking one. One of the contributions of this thesis is a methodology to assess and design both types of transient responses when PR current controllers are implemented. The developed methodology is based on the analysis of the error signal transfer function roots by means of root loci. The optimal gains are determined to attain fast and nonoscillating transient responses, i.e., to minimize the settling time. As demonstrated, such gains result from a tradeoff between optimizing the transients caused by reference changes and the transients due to alterations at the point of common coupling.

On the other hand, a study about the suitability of different resonant regulators in grid-tied applications in terms of settling time, overshoot and harmonic distortion is not available in the literature. In this dissertation, an in-depth comparison between vector proportional-integral (VPI) and PR controllers in these terms is provided. Since the VPI controller tuning oriented to those aims has not been approached yet either, firstly, a rigorous analysis and design is conducted by applying to this regulator the methodology described above, which was originally designed for the PR controller.

Contributions of this dissertation have been published in four JCR-indexed journal papers and presented at three international conferences.

Acknowledgments

First of all, I would like to express my most sincere gratitude to my supervisor Dr. Jesús Doval Gandoy for offering me this challenging opportunity and for his guidance, as well as for introducing to me the appealing world of power electronics. When I first talked to him, I could not imagine he was such a knowledgeable, honest and patient person.

Secondly, I wish to thank my other supervisor Dr. Francisco D. Freijedo, for his continuous support despite the distance, for his passion, for his ideas and for the endless lines of conversation we have shared along these years. Thank you, Fran.

In addition, my labmate Dr. Alejandro G. Yepes deserves a special mention. I would like to acknowledge him for his numerous constructive comments, which have undoubtedly made an impact on the quality of this work. This dissertation would have not been possible without the support of the three persons listed above.

I would also like to show my appreciation to Prof. Li Ran for allowing me to join to the Electrical Power research group of the University of Warwick for a research stay. He and all the marvelous people I met there made me feel like home, in particular Yuan Tang, Fan Li, Ortiz and my loved landlady Julie Kendall.

I wish to thank all my colleagues of the Applied Power Electronics Technology research group, for the good moments and jokes shared, as well as for their help, specially to Dr. Óscar López, Jano, Pablo, Fernando, Diego, Miguel, Jose Miguel, Ortiz (once again), Felipe, Javi, Alex, Guede and Toni.

I also appreciate the funding offered by the Spanish Government (code: FPU12/00117).

On the other hand, I must recognize the support of my friends, who had no doubts I could do this, and have helped me disconnect from work. To my former flatmates and classmates, to the people in La Florida halls of residence, to my hometown friends (specially to Rober, Rosa and Lucio), and to the wonderful and so dissimilar people I have recently met as part of the MQA Florida running club, many thanks.

And finally, I would really like to thank my little family. To my parents Paloma and Antonio (I wish you could be with us), and to my brother Óscar, for the education I've received and for all their support. To you Javi, for your love, for knowing me so well, and for letting me know you.

A mi familia:
Paloma, Antonio, Óscar y Javi.

Contents

List of Figures

List of Tables

List of Abbreviations and Acronyms

AM	adjustable model
DAC	digital-to-analog converter
DPGS	distributed power generation system
DSP	digital signal processor
GC	grid code
IET	Institution of Engineering and Technology
IEEE	Institute of Electrical and Electronic Engineers
IAE	integral absolute error
IE	integral error
IMC	internal model control
LVRT	low-voltage ride-through
PCC	point of common coupling
PI	proportional-integral
PICCD	PI controller with state-feedback cross-coupling decoupling
PLL	phase-locked loop
PR	proportional-resonant
p.u.	per-unity
PWM	pulse-width modulation
RM	reference model
SRF	synchronous reference frame
THD	total harmonic distortion
VPI	vector proportional-integral

MRAS	model reference adaptive system
VSC	voltage source converter
WIAE	weighted IAE
ZOH	zero-order hold
1DOF	one degree-of-freedom
2DOF	two degrees-of-freedom

Nomenclature

a	Variable which refers to the d and/or the q axes of an SRF.
A	Amplitude of the cosine term in Δi^* or in Δv_{PCC}.
A_{new}	New amplitude of the cosine term in Δi^* or in Δv_{PCC}.
A_{old}	Previous amplitude of the cosine term in Δi^* or in Δv_{PCC}.
B	Amplitude of the sine term in Δi^* or in Δv_{PCC}.
B_{new}	New amplitude of the sine term in Δi^* or in Δv_{PCC}.
B_{old}	Previous amplitude of the sine term in Δi^* or in Δv_{PCC}.
C	Dc-link capacitance of the VSC.
$\mathbf{C}$	Clarke transformation matrix.
C_{F}	Capacitance in an LCL filter.
ct	Center of the circumference described by the variation of the pole position with K.
e	$= i^* - i$. Current error.
E	Z transform of e.
$\widehat{e}$	Estimated e.
e_{PLL}	Phase error of the PLL.
e_α	α-axis current error.
$\hat{e}_\alpha$	Estimated α-axis current error.
$e_{\alpha\beta}$	$= e_\alpha + \mathrm{j}\, e_\beta$. Current error complex vector, expressed in the $\alpha\beta$ frame.
e_β	β-axis current error.
$e_{\Delta i^*}$	Current error caused by a transient in i^*.

$E_{\Delta i^*}$	Z transform of $e_{\Delta i^*}$.
$e_{\Delta v_{\mathrm{PCC}}}$	Current error caused by a transient in v_{PCC}.
$E_{\Delta v_{\mathrm{PCC}}}$	Z transform of $e_{\Delta v_{\mathrm{PCC}}}$.
$e_{\Delta \widehat{v}_{\mathrm{PCC}}}$	Current error caused by a transient in $\widehat{v}_{\mathrm{PCC}}$.
$E_{\Delta \widehat{v}_{\mathrm{PCC}}}$	Z transform of $e_{\Delta \widehat{v}_{\mathrm{PCC}}}$.
f	Frequency in hertz.
f_{res}	Resonant frequency in hertz.
f_{s}	Sampling frequency in hertz.
f_{sw}	Switching frequency in hertz.
G_{C}	Transfer function of a current controller.
$G_{\mathrm{C}_{\mathrm{dq}}}$	Transfer function of a current controller, expressed in SRF.
$G_{\mathrm{C}_{\alpha\beta}}$	Transfer function of a current controller, expressed in the $\alpha\beta$ frame.
G_{CL}	Closed-loop transfer function of the current loop.
$G_{\mathrm{CL}_{\alpha\beta}}$	Closed-loop transfer function of the current loop, expressed in the $\alpha\beta$ frame.
G_{d}	Transfer function of the remaining delay after applying delay compensation, expressed in SRF.
G_{DB}	Transfer function of the deadbeat controller.
G_{DR}	Transfer function of the disturbance rejection capability of the current loop.
$G_{\mathrm{DR}_{\alpha\beta}}$	Transfer function of the disturbance rejection capability of the current loop, expressed in the $\alpha\beta$ frame.
G_{L}	$= I(s)/V_{\mathrm{C}}(s)$. Transfer function of the current loop admittance.
$G_{\mathrm{L}}^{\mathrm{Tustin}}$	G_{L} discretized with the Tustin method.
$G_{\mathrm{L}}^{\mathrm{ZOH}}$	G_{L} discretized with the ZOH method.
$G_{\mathrm{L}_{\mathrm{dq}}}$	$= I_{\mathrm{dq}}(s)/V_{\mathrm{C}_{\mathrm{dq}}}(s)$. Transfer function of the current loop admittance, expressed in SRF.
$G_{\mathrm{L}_{\alpha\beta}}$	$= I_{\alpha\beta}(s)/V_{\mathrm{C}_{\alpha\beta}}(s)$. Transfer function of the current loop admittance, expressed in the $\alpha\beta$ frame.
$G_{\mathrm{L}_{\alpha\beta}}^{\mathrm{Tustin}}$	$G_{\mathrm{L}_{\alpha\beta}}$ discretized with the Tustin method.

$G_{\mathrm{L}_{\alpha\beta}}^{\mathrm{ZOH}}$	$G_{\mathrm{L}_{\alpha\beta}}$ discretized with the ZOH method.
G_{LCL}	$= I(s)/V_{\mathrm{C}}(s)$. Transfer function of the current loop admittance when an LCL filter is employed.
G_{OL}	Open-loop transfer function of the current loop.
G'_{OL}	Simplified open-loop transfer function of the current loop.
G''_{OL}	Non-simplified open-loop transfer function of the current loop.
G_{PI}	Transfer function of a PI controller tuned at $h = 1$.
G_{PI_h}	Transfer function of a PI controller tuned at the harmonic order h.
$G_{\mathrm{PI}_h}^{+}$	G_{PI_h} implemented in a positive SRF.
$G_{\mathrm{PI}_h}^{-}$	G_{PI_h} implemented in a negative SRF.
G_{cPI_h}	Transfer function of a complex vector PI controller tuned at the harmonic order h.
$G_{\mathrm{cPI}_h}^{+}$	G_{cPI_h} implemented in a positive SRF.
$G_{\mathrm{cPI}_h}^{-}$	G_{cPI_h} implemented in a negative SRF.
G_{PL}	Transfer function of the current loop plant admittance, together with the 1.5-sample delay.
$G_{\mathrm{PL}}^{\mathrm{d}}$	Transfer function of the current loop plant admittance, together with the 1.5-sample delay and delay compensation.
G_{PR}	Sum of the different G_{PR_h} implemented.
G_{PR_h}	Transfer function of a PR controller tuned at the harmonic order h.
$G_{\mathrm{PR}_h}^{\mathrm{d}}$	Transfer function of a PR controller with delay compensation tuned at the harmonic order h.
G_{VPI_h}	Transfer function of a VPI controller tuned at the harmonic order h.
$G_{\mathrm{VPI}_h}^{\mathrm{d}}$	Transfer function of a VPI controller with delay compensation tuned at the harmonic order h.
h	Harmonic order.
i	Converter current.
I	Laplace or Z transform of i.
i^*	Reference for i.
I^*	Laplace or Z transform of i^*.

i_a	i_d and/or i_q.
$i_a^{\widehat{\tau}=\tau}$	$i_\mathrm{d}^{\widehat{\tau}=\tau}$ and/or $i_\mathrm{q}^{\widehat{\tau}=\tau}$.
i_abc	Three-phase converter current.
I_AMP	Amplitude of the commanded step.
i_d	Projection of the converter current onto the d axis of an SRF.
i_d^*	Reference for i_d.
I_d^*	Z transform of i_d^*.
$i_\mathrm{d}^{\widehat{\tau}=\tau}$	i_d when τ is correctly identified.
i_dc	Direct current externally supplied to (or demanded from) the dc-link of the VSC.
i_dq	$= i_\mathrm{d} + \mathrm{j}\, i_\mathrm{q}$. Converter current complex vector, expressed in SRF.
I_dq	Laplace or Z transform of i_dq.
i_dq^*	Reference for i_dq.
I_dq^*	Z transform of i_dq^*.
$i_\mathrm{dq}^{\widehat{\tau}=\tau}$	i_dq when τ is correctly identified.
i_G	Grid current.
I_G	Laplace or Z transform of i_G.
$i_{\mathrm{G}_\mathrm{abc}}$	Three-phase grid current.
$i_{\mathrm{G}\,\alpha\beta}$	$= i_{\mathrm{G}\,\alpha} + \mathrm{j}\, i_{\mathrm{G}\,\beta}$. Grid current complex vector, expressed in the $\alpha\beta$ frame.
$I_{\mathrm{G}\,\alpha\beta}$	Laplace or Z transform of $i_{\mathrm{G}\,\alpha\beta}$.
i_n	n-phase converter current.
i_new^*	New i^*.
i_old^*	Previous i^*.
i_q	Projection of the converter current onto the q axis of an SRF.
i_q^*	Reference for i_q.
I_q^*	Z transform of i_q^*.
$i_\mathrm{q}^{\widehat{R}=R}$	i_q when R is correctly identified.

$i_{\mathrm{q}}^{\widehat{R}<R}$ — i_{q} when R is underestimated.

$i_{\mathrm{q}}^{\widehat{R}>R}$ — i_{q} when R is overestimated.

$i_{\mathrm{q}}^{\widehat{\tau}=\tau}$ — i_{q} when τ is correctly identified.

$i_{\alpha\beta}$ — $= i_\alpha + \mathrm{j}\, i_\beta$. Converter current complex vector, expressed in the $\alpha\beta$ frame.

$I_{\alpha\beta}$ — Laplace or Z transform of $i_{\alpha\beta}$.

$i_{\alpha\beta}^*$ — Reference for $i_{\alpha\beta}$.

$I_{\alpha\beta}^*$ — Laplace or Z transform of $i_{\alpha\beta}^*$.

IAE_a — $\mathrm{IAE_d}$ and/or $\mathrm{IAE_q}$.

$\mathrm{IAE_d}$ — Integral absolute error between the d-axis outputs of the simulated and the actual current loops.

$\mathrm{IAE_q}$ — Integral absolute error between the q-axis outputs of the simulated and the actual current loops.

IE_a — $\mathrm{IE_d}$ and/or $\mathrm{IE_q}$.

$\mathrm{IE_d}$ — Integral error between the d-axis outputs of the simulated and the actual current loops.

$\mathrm{IE_q}$ — Integral error between the q-axis outputs of the simulated and the actual current loops.

k — Iteration number.

K — $= K_{\mathrm{P}}/\widehat{L}$. Gain of a controller tuned at $h = 1$.

K_h — $= K_{\mathrm{P}_h}/\widehat{L}$. Gain of a controller tuned at the harmonic order h.

K_{I} — Integral gain of a controller.

K_{I_h} — Integral gain of a controller tuned at the harmonic order h.

$k_{\max}$ — Number of iterations needed.

K_{opt} — $= 0.039 \cdot 2\pi f_{\mathrm{s}}$. Gain aimed at optimized settling time and overshoot for synchronous proportional-integral (PI) controllers.

K_{P} — Proportional gain of a controller.

K_{P_h} — Proportional gain of a controller tuned at the harmonic order h.

$K_{\mathrm{P_T}}$ — Sum of the K_{P_h} gains included in G_{PR_h}.

$K_{\gamma 1,\gamma 2}$ — Limit values of K between which p_1^{cl} and p_2^{cl} are complex.

K^{met}	K employed during the estimation process.
L	Actual inductance of the current loop.
$\widehat{L}$	Estimate of the current-loop inductance.
L_{CS}	Converter-side inductance in an LCL filter.
L_{F}	Inductance of the filter in series with the VSC.
L_{GS}	Grid-side inductance in an LCL filter.
L_{LOW}	Underestimated value of L that corresponds to a precision better than υ_{d}.
L_{sim}	Inductance of the simulated current control loop.
L_{TH}	Thevenin equivalent inductance seen from the point of common coupling (PCC).
L_{UPP}	Overestimated value of L that corresponds to a precision better than υ_{d}.
L^{met}	L identified by the method. Average between L_{LOW} and L_{UPP}.
L_{F}_under	Auxiliary variable that indicates whether the inductance is underestimated or overestimated.
L_low_bound	Auxiliary boolean variable that indicates whether the lower bound in L estimation has been found.
L_upp_bound	Auxiliary boolean variable that indicates whether the upper bound in L estimation has been found.
m	PWM reference signal.
m_{abc}	Three-phase PWM reference signal.
m_{dq}	$= m_{\text{d}} + \text{j}\, m_{\text{q}}$. PWM reference signal complex vector, expressed in SRF.
n	$=$ a, b or c. Refers to the phase.
Q	Reactive power.
P	Active power.
$\mathbf{P}$	Park transformation matrix.
P_{dc}	Power demanded by a dc load.
p_l	lth pole of $E_{\Delta i^*}$, $E_{\Delta v_{\text{PCC}}}$ or G_{CL}.
p_l^{cl}	lth closed-loop pole of a transfer function.

p_l^{met}	lth pole of G_{CL} for $K = K^{\text{met}}$.
p_l^{ol}	lth open-loop pole of a transfer function.
p_l^{PR}	lth pole of $E_{\Delta i^*}$ or $E_{\Delta v_{\text{PCC}}}$ when a PR controller regulates the current.
p_l^{VPI}	lth pole of $E_{\Delta i^*}$ or $E_{\Delta v_{\text{PCC}}}$ when a VPI controller regulates the current.
P_{level}	Power level: power that the installation is actually managing.
P_{rated}	Rated power.
PWM_{dq}	Transfer function of the PWM, expressed in SRF.
$\text{PWM}_{\alpha\beta}$	Transfer function of the PWM, expressed in the $\alpha\beta$ frame.
R	Actual resistance of the current loop.
$\widehat{R}$	Estimate of the current-loop resistance.
R_{C}	VSC equivalent loss resistance: resistance that models the effects associated to the losses in the current loop.
$R_{\text{C}}^{\text{met}}$	R_{C} identified by the method.
R_{CS}	Parasitic resistance of the converter-side inductor in an LCL filter.
R_{D}	Damping resistance in an LCL filter.
R_{F}	Parasitic resistance of the filter in series with the VSC.
R_{GS}	Parasitic resistance of the grid-side inductor in an LCL filter.
R_{L}	Dc load.
R_{LOW}	Underestimated value of R that corresponds to a precision better than υ_{q}.
R_{sim}	Resistance of the simulated current control loop.
R_{TH}	Thevenin equivalent resistance seen from the PCC.
R_{UPP}	Overestimated value of R that corresponds to a precision better than υ_{q}.
R^{a}	"Active resistance": fictitious resistance added to the control loop to enhance the disturbance rejection capability.
R^{met}	R identified by the method. Average between R_{LOW} and R_{UPP}.
rd	Radius of a circumference described by the variation of the position of the poles with K.

R_low_bound	Auxiliary boolean variable that indicates whether the lower bound in R estimation has been found.
t	Time.
T_d	$= 1.5T_\mathrm{s}$. Time delay.
T_s	Sampling period.
$T_\mathrm{s}^\mathrm{base}$	Base value of the sampling period.
t_sto	Storing time.
$t_{2\%}$	Settling time with a tolerance band of 2%.
$t_{5\%}$	Settling time with a tolerance band of 5%.
u	Voltage or current.
u_a	a-phase u.
u_b	b-phase u.
u_c	c-phase u.
u_d	Projection of u onto the d axis of an SRF.
u_dq	$= u_\mathrm{d} + \mathrm{j}\, u_\mathrm{q}$. u complex vector, expressed in SRF.
u_q	Projection of u onto the q axis of an SRF.
u_α	α-axis u.
$u_{\alpha\beta}$	$= u_\alpha + \mathrm{j}\, u_\beta$. u complex vector, expressed in the $\alpha\beta$ frame.
u_β	β-axis u.
v	Voltage.
v_C	Converter output voltage.
V_C	Laplace or Z transform of v_C.
$v_{\mathrm{C}_\mathrm{abc}}$	Three-phase converter output voltage.
$v_{\mathrm{C}_\mathrm{dq}}$	$= v_{\mathrm{C}_\mathrm{d}} + \mathrm{j}\, v_{\mathrm{C}_\mathrm{q}}$. Complex vector of the converter output voltage, expressed in SRF.
$V_{\mathrm{C}_\mathrm{dq}}$	Laplace or Z transform of $v_{\mathrm{C}_\mathrm{dq}}$.
v_{C_n}	n-phase converter output voltage.

$v_{\mathrm{C}\,\alpha\beta}$ $= v_{\mathrm{C}\,\alpha} + \mathrm{j}\, v_{\mathrm{C}\,\beta}$. Complex vector of the converter output voltage, expressed in the $\alpha\beta$ frame.

$V_{\mathrm{C}\,\alpha\beta}$ Laplace or Z transform of $v_{\mathrm{C}\,\alpha\beta}$.

v_{D} Voltage drop in the capacitor branch.

$v_{\mathrm{D}_{\mathrm{abc}}}$ Three-phase voltage drop in the capacitor branch.

v_{D_n} n-phase voltage drop in the capacitor branch.

$v_{\mathrm{D}\,\alpha\beta}$ $= v_{\mathrm{D}\,\alpha} + \mathrm{j}\, v_{\mathrm{D}\,\beta}$. Complex vector of the voltage drop in the capacitor branch, expressed in the $\alpha\beta$ frame.

$V_{\mathrm{D}\,\alpha\beta}$ Laplace or Z transform of $v_{\mathrm{D}\,\alpha\beta}$.

v_{dc} Dc-link voltage of the VSC.

v_{dc}^{*} Reference for v_{dc}.

v_{G} Grid voltage.

$v_{\mathrm{G}_{\mathrm{abc}}}$ Three-phase grid voltage.

v_{G_n} n-phase grid voltage.

$V_{\mathrm{LL}_{\mathrm{rated}}}$ Rated line-to-line voltage.

v_{PCC} Voltage at the PCC.

$\widehat{v}_{\mathrm{PCC}}$ Measured voltage at the PCC, which is fedforward.

V_{PCC} Laplace or Z transform of v_{PCC}.

$v_{\mathrm{PCC}_{\mathrm{abc}}}$ Three-phase PCC-voltage.

$v_{\mathrm{PCC}_{\mathrm{d}}}$ Projection of the PCC-voltage onto the d axis of an SRF.

$v_{\mathrm{PCC}_{\mathrm{dq}}}$ $= v_{\mathrm{PCC}_{\mathrm{d}}} + \mathrm{j}\, v_{\mathrm{PCC}_{\mathrm{q}}}$. PCC-voltage complex vector, expressed in SRF.

$\widehat{v}_{\mathrm{PCC}_{\mathrm{dq}}}$ Measured PCC-voltage complex vector, expressed in SRF, which is fedforward.

v_{PCC_n} n-phase PCC-voltage.

$v_{\mathrm{PCC}_{\mathrm{q}}}$ Projection of the PCC-voltage onto the q axis of an SRF.

$v_{\mathrm{PCC}_{\mathrm{rms}}}$ Root mean square value of v_{PCC}.

$v_{\mathrm{PCC}\,\alpha\beta}$ $= v_{\mathrm{PCC}\,\alpha} + \mathrm{j}\, v_{\mathrm{PCC}\,\beta}$. PCC-voltage complex vector, expressed in the $\alpha\beta$ frame.

$V_{\mathrm{PCC}\,\alpha\beta}$ Laplace or Z transform of $v_{\mathrm{PCC}\,\alpha\beta}$.

$\widehat{v}_{\mathrm{PCC}\,\alpha\beta}$	Measured PCC-voltage complex vector, expressed in the $\alpha\beta$ frame, which is fedforward.
$v'_{\mathrm{PCC}\,\alpha\beta}$	Resulting disturbance after the feed-forward compensation.
$V'_{\mathrm{PCC}\,\alpha\beta}$	Laplace or Z transform of $v'_{\mathrm{PCC}\,\alpha\beta}$.
WIAE_a	$\mathrm{WIAE_d}$ and/or $\mathrm{WIAE_q}$.
$\mathrm{WIAE_d}$	Weighted $\mathrm{IAE_d}$.
$\mathrm{WIAE_q}$	Weighted $\mathrm{IAE_q}$.
Y	Admittance.
Y_{CS}	Converter-side admittance in an LCL filter.
$Y_{\mathrm{CS_{dq}}}$	Converter-side admittance in an LCL filter, expressed in SRF.
$Y_{\mathrm{CS}_{\alpha\beta}}$	Converter-side admittance in an LCL filter, expressed in the $\alpha\beta$ frame.
Y_{GS}	Grid-side admittance in an LCL filter.
$Y_{\mathrm{GS_{dq}}}$	Grid-side admittance in an LCL filter, expressed in SRF.
$Y_{\mathrm{GS}_{\alpha\beta}}$	Grid-side admittance in an LCL filter, expressed in the $\alpha\beta$ frame.
$\mathcal{Z}$	Z transform.
Z	Impedance.
Z_{D}	Impedance offered by the capacitor branch in an LCL filter.
$Z_{\mathrm{D_{dq}}}$	Impedance offered by the capacitor branch in an LCL filter, expressed in SRF.
$Z_{\mathrm{D}_{\alpha\beta}}$	Impedance offered by the capacitor branch in an LCL filter, expressed in the $\alpha\beta$ frame.
z_l	lth zero.
Z_{TH}	Thevenin equivalent impedance seen from the PCC.
$\mathcal{Z}^{-1}$	Inverse Z transform.
Δ_{d}	Correction percentage of a L estimate.
Δ_{q}	Correction percentage of an R estimate.
Δi^*	Transient in i^*.
ΔL_{F}	Uncertainties in the inductance with respect to L_{F}.

Δv_{PCC}	Transient in v_{PCC}.
$\Delta v_{\mathrm{PCC}_{\mathrm{abc}}}$	Three-phase transient in v_{PCC}.
$\Delta v_{\mathrm{PCC}_{\alpha\beta 0}}$	Transient in v_{PCC}, expressed in the $\alpha\beta$ frame, including the homopolar component.
$\Delta \widehat{v}_{\mathrm{PCC}}$	Transient in $\widehat{v}_{\mathrm{PCC}}$.
ε_a	ε_{d} and/or ε_{q}.
ε_{d}	Error between the d-axis outputs of the simulated and the actual current loops.
$\varepsilon_{\mathrm{dq}}$	Complex error between the outputs of the simulated and the actual current loops.
ε_{q}	Error between the q-axis outputs of the simulated and the actual current loops.
ϕ'_h	Phase lead for the controller tuned at the harmonic order h.
φ	Arbitrary initial angle.
λ	Generic natural value.
θ_1	$= \omega_1 t + \varphi$. Instantaneous phase angle of v_{PCC} fundamental component.
ρ	$= \mathrm{e}^{RT_{\mathrm{s}}/L}$.
τ	$= L/R$. Plant time constant.
υ_a	υ_{d} and/or υ_{q}.
υ_{d}	$\mathrm{WIAE}_{\mathrm{d}}$ threshold.
υ_{q}	$\mathrm{WIAE}_{\mathrm{q}}$ threshold.
ω	Frequency in radians per second.
ω_1	Fundamental frequency in radians per second.

Specific nomenclature of the Appendix B

b_j	$= r_j + r_j^*$. Second-order coefficient of p_j-p_j^* residues.
c_j	$= -(r_j + r_j^*)\,\mathfrak{Re}(p_j) + (r_j - r_j^*)\,\mathfrak{Im}(p_j)$. First-order coefficient of p_j-p_j^* residues.
d'_j	$= r_j + r_j^*$. Residue of the cosine term.
f'_j	$= r_j - r_j^*$. Residue of the sine term.

i	$= 1, 2, ...\kappa$. Refers to a specific real pole.
j	$= 1, 2, ...\chi$. Refers to a specific pair of conjugate poles.
l	$= 1, 2, ...\iota$. Refers to a specific pole (real or complex).
p_i	ith real pole.
p'_i	p_i equivalent in the z-domain.
p_j	jth complex pole.
p^*_j	Conjugate of p_j.
p'_j	p_j equivalent in the z-domain.
r	Residue.
r_i	Residue of p_i.
r_j	Residue of p_j.
r_l	Residue of p_l.
r^*_j	Residue of p^*_j.
χ	Number of complex conjugate pole pairs.
ι	Number of real and complex poles.
κ	Number of real poles.
σ'_j	Real term of p'_i or p'_j.
ω'_{d_j}	Imaginary term of p'_i or p'_j.

Chapter 1

Introduction

1.1 Motivation and Objectives

In the current scenario of the electric grid, high penetration of renewable energy sources, distributed power generation systems (DPGSs) and power electronic converters coexist. In order to prevent destabilization, the system operators have defined international grid codes (GCs), which, in case of a fault, ask generation units to remain connected and support the grid during a certain time, by means of reactive current injection. Aside from the compliance of these and other ancillary services, installations must fulfill the specific demands of the end-customers.

Regardless of the generation unit nature, voltage source converters (VSCs) are the most common option as interface for grid connection in most of these applications. In order to guarantee the proper behavior of the system, together with the satisfaction of all the restrictions, a rigorous analysis and design of the control loops of such converters becomes crucial. This challenge should start from the innermost loops, which are usually current ones, since they establish the performance of the overall system, specially in terms of transient response. The main objective of this dissertation is to provide a thorough study on the current control closed loop, oriented to an accurate tuning of the regulators. This general goal can be divided into another two, which are in turn linked to the main two tasks (shown below) developed in this thesis.

- Firstly, it is necessary to have a precise estimate of the parameters (inductance and resistance) in the generally-accepted plant model of the current loop, for all the specific working conditions. Thus, parameter identification techniques particularly oriented to transient response optimization are needed.

- Secondly, once the plant parameters are identified, and after selecting the most suitable controller structure, the regulator has to be accurately designed. Hence, tuning methods aimed at settling time minimization in the presence of sags at the point of common coupling (PCC) and of current reference changes should be developed. Some other constraints such as total harmonic distortion (THD) reduction have to be considered. The suitability of the different available controllers should be evaluated.

1.2 Background and Review of Previous Research

1.2.1 Framework

The worldwide energy consumption is expected to have grown dramatically by 2040, especially owing to the increasing wealth in emerging economies, such as those of China and India [31]. In order to meet such demand, it is necessary to reduce the overall world's dependence on fossil fuels, given their limited character and their negative environmental impact, keeping in mind that a sudden complete avoidance would be impractical. In this gradual transition, renewable energies are playing a key role [32]. As an example, wind power had at the end of 2013 a total installed capacity above 318 GW, which involves an eightfold increase over the past decade [32].

Most of these renewable energy based systems are connected to the grid and distributed along the power system [33–36]. Thus, the traditional unidirectional centralized organization of the power flow is evolving towards a more flexible and bidirectional scenario, where loads and sources coexist at the same level. Despite the clear advantages of this new model, such as loss reduction or facilitating rural electrification, some problems have arisen in cases of large penetration to guarantee the stability and reliability of the power system, mainly due to the stochastic behavior of their input power. Consequently, the transmission/distribution system operators of the different areas have defined stricter interconnection requirements for these generation units, which are compiled in the new grid codes (GCs) [37–41], and more regulations are expected in the upcoming years.

Power electronic converters are generally used as the interface between the different players (generation units, controllable loads, storage systems...) and the grid [33, 42]. Their appropriate control permits a flexible interconnection between both ends, matching their dissimilar characteristics in terms of frequency, voltage, harmonic content, active and reactive power, etc. [43, 44]. Not only should advanced control techniques be able to fulfill the restrictive ancillary services imposed by the system operators, but also the specific demands of the end-customers [44].

Regarding generation units, depending on the nature of the input power and the selected topology, more than one power electronic converter may be needed. In wind turbine systems, the full-scale back-to-back topology is gaining popularity, since, at the expense of larger converters, it enables these renewable energy sources to act as conventional power plants, thanks to the full control of the active and reactive power [44–49]. Such solution is composed of two current-controlled VSCs, usually known as generator-side and grid-side converters, decoupled by a dc link, which allow bidirectional power flow [33, 44, 45, 47–49]. On the other hand, among the large variety of topologies for photovoltaic systems, many of the options are characterized by including a boost dc-dc stage together with ac-dc grid-side converter [33, 42, 50].

1.2.2 Grid-Tied VSCs

Fig. 1.1 illustrates the most common configuration of a three-phase grid-tied VSC, which may correspond with the previously mentioned grid-side converter. Owing to its bidirectionality, this converter can work either as a rectifier, demanding power from the grid and delivering it to a dc load, or as an inverter, supplying power to the grid (or to an ac load) from the dc power source, which represents a wide variety of DPGSs.

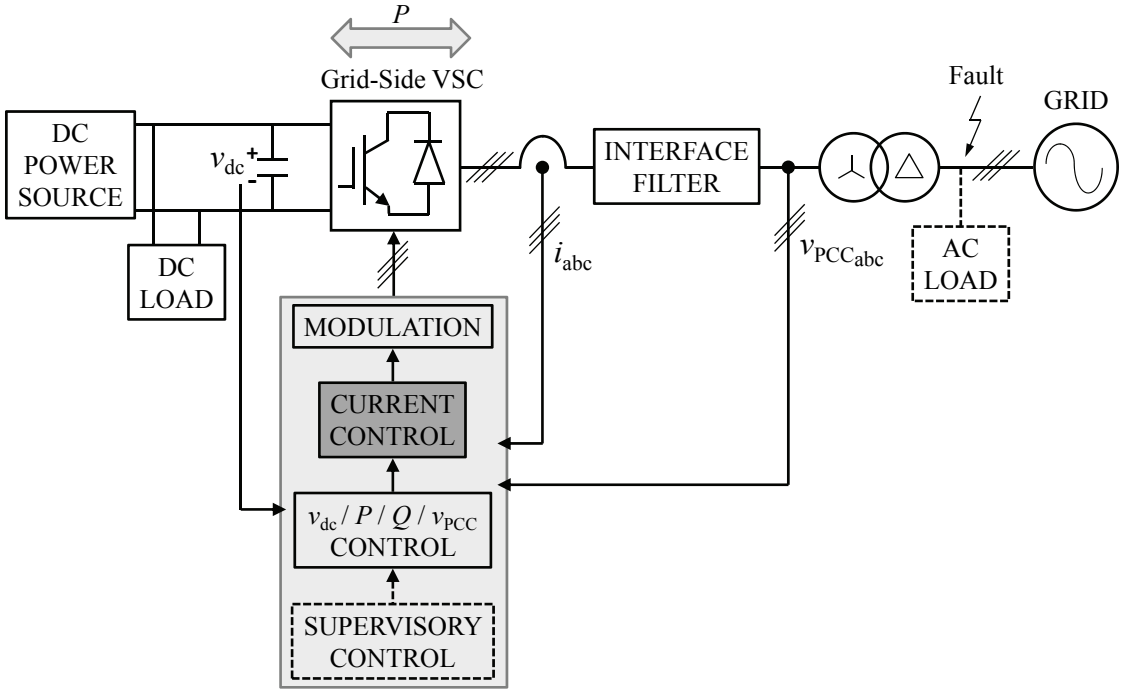

Figure 1.1: Scheme of a grid-tied VSC and its control.

The main tasks of this converter are the interaction with the grid and maintaining the dc-link voltage v_{dc} constant. Hence, regardless of the control strategy, the ac power and the dc-link voltage have to be regulated, either directly or indirectly [42]. Two main solutions are distinguished. Firstly, multiple cascaded loops of linear controllers followed by a modulation stage can be adopted (cf. Fig. 1.1) [42, 51]. Another possibility is to employ direct power control, which selects the voltage vector to be applied by the converter directly, from the output of nonlinear hysteresis controllers that regulate the power [42, 52]. This kind of controller features a faster dynamics, but leads to higher ripples in the power signals and currents, as well as to a variable switching frequency [42, 52, 53]. Additional blocks, such as a virtual flux estimator, an elaborate switching lookup table or a conventional modulation stage, may be added to overcome these drawbacks, at the cost of complicating the algorithm to a certain extent [42, 52, 53].

This thesis is focused on the first solution, i.e., implementing control and modulation in different stages. Hence, the control algorithms treated throughout this text are valid independently from the number of levels of the VSC. Only the modulation, which is out of scope of the proposal, would need to be adapted [42, 52]. Concerning the control, the most common strategy consists in implementing outer loops that regulate the dc-link voltage and the reactive power Q, which set the references for inner current loops [34, 42, 48, 51, 54, 55]. Alternatively, an active power P controller may replace the dc-link voltage one [56]. On the other hand, in case of weak grids, e.g., microgrids, outer ac voltage regulators are necessary to ensure the voltage at the PCC v_{PCC} [57, 58]. Moreover, microgrids would also need a supervisory level of control, known as frequency and voltage droop, to avoid circulating power flow when more than one generation unit is connected in parallel [57, 58].

1.2.3 Current Control of Grid-Connected Converters

In all these grid-tied applications, inner current regulators are generally implemented. Outer loops should be designed to be substantially slower than inner loops to preserve stability. In this manner, the dynamics of both loops is decoupled and they can be studied separately [42, 59]. Hence, in this work, the investigation is limited to the current loop, which should be designed to offer a suitable harmonic rejection and the appropriate power factor, as well as to be robust against disturbances in the utility network. Moreover, the loop should also attain a fast transient response when the reference is modified and also in the presence of grid faults. During these events, modern GCs demand renewable energy based generation units to remain connected during certain time, which is known as low-voltage ride-through (LVRT) capability [37, 39–41, 48, 60–64]. Furthermore, some of them also require generators to support the grid by supplying a specific amount of reactive current, which depends on the voltage drop, within a certain response time [37, 39–41, 64]. From the point of view of the current loop, in order to fulfill these tight specifications, when a fault is detected, references for the current loop have to be recalculated, which often implies to disconnect the outer power controllers with slow dynamics [48]. Additionally, an accurate tuning of the selected controller structure is needed.

Numerous strategies have been published related to current reference generation for LVRT [35, 47, 65–71]. In general, to avoid tripping, the maximum current must be limited [47, 54, 68, 70]. Besides, power oscillations in the active and reactive power (and in the dc bus), which are a consequence of the interaction between voltages and currents of different sequences, may be reduced at the cost of injecting unbalanced currents into the grid [47, 66–69, 71, 72]. Limitations of the techniques that directly rely on extreme situations of the latter premise are analyzed in [73]. With the objective of achieving a more flexible active and reactive power control, able to fulfill the current and foreseeable GC requirements, different reference generation methods have been recently proposed, most of them based on raising the PCC voltage, while trying to equalize the three phases (which prevents the system from tripping) [35, 54, 70, 72, 74]. In any case, the definition of the current references is disregarded in this study.

In this thesis, a thorough analysis and design of the current control closed loop is developed, with the aim of fulfilling all the different constraints mentioned above. Two main tasks are crucial.

- Firstly, a precise model of the current loop is needed. Linear plant models are selected in this study, since their use allows to apply the well-known linear analysis and design methods [34, 75–78]. Thus, the widely-employed low-order time-averaged plant admittance models in this kind of applications are also adopted here [10, 77, 79–81]. In addition, their parameters should be accurately identified in each specific working condition. This includes both the equivalent inductance and resistance in the plant model of current-controlled grid-tied VSCs.

- Secondly, once the plant parameters are identified, keeping in mind the constraints and objectives of the specific application (THD, power factor, settling time, overshoot...), the most appropriate controller structure should be selected, and its regulators have to be precisely tuned.

1.2.4 Stationary and Synchronous Reference Frames

Given a three-phase sinusoidal system u_a, u_b and u_c of frequency ω_1, where u denotes either voltage v or current i, the Clarke transformation $\mathbf{C}$ permits to obtain an equivalent stationary system (also known as $\alpha\beta$ frame) of two orthogonal components u_α and u_β as follows [82]:

$$\begin{pmatrix} u_\alpha \\ u_\beta \end{pmatrix} = \underbrace{\frac{2}{3}\begin{pmatrix} 1 & -\frac{1}{2} & -\frac{1}{2} \\ 0 & \frac{\sqrt{3}}{2} & -\frac{\sqrt{3}}{2} \end{pmatrix}}_{\mathbf{C}} \cdot \begin{pmatrix} u_a \\ u_b \\ u_c \end{pmatrix} \tag{1.1}$$

provided that the homopolar component is zero (i.e., $u_a + u_b + u_c = 0$). The two variables are related as $u_{\alpha\beta} = u_\alpha + \mathrm{j}\, u_\beta$, and both contain information about positive and negative sequences of u and none about its zero sequence. Hence, in this condition, the three-phase system may be regulated with only two controllers, one in each of the $\alpha\beta$ axes.

With the aim of transforming the three-phase sinusoidal system into a continuous one, and thus, simplifying its analysis and control, it is possible to define a synchronous reference frame (SRF) rotating with the frequency of the former, i.e., ω_1. Such equivalent frame is also known as dq frame, and can be obtained by means of the Park transformation $\mathbf{P}$ [83]

$$\begin{pmatrix} u_d \\ u_q \end{pmatrix} = \underbrace{\frac{2}{3}\begin{pmatrix} \cos(\theta_1) & \cos(\theta_1 - \frac{2\pi}{3}) & \cos(\theta_1 + \frac{2\pi}{3}) \\ -\sin(\theta_1) & -\sin(\theta_1 - \frac{2\pi}{3}) & -\sin(\theta_1 + \frac{2\pi}{3}) \end{pmatrix}}_{\mathbf{P}} \cdot \begin{pmatrix} u_a \\ u_b \\ u_c \end{pmatrix} \tag{1.2}$$

where $\theta_1 = \omega_1 t + \varphi$ is the instantaneous phase angle at instant t, with φ being an arbitrary initial angle, while u_d and u_q denote the projections of the direct d and quadrature q rotating axes, with $u_{dq} = u_d + \mathrm{j}\, u_q$.

The transformations defined in (1.1) and (1.2) are both magnitude invariant, i.e., the amplitude of the signals in the different frames is maintained. In order to obtain power invariant transformations, the factor $2/3$ that multiplies both matrices $\mathbf{C}$ and $\mathbf{P}$ must be substituted by $\sqrt{2/3}$.

From Fig. 1.2, rotations of an angle $\theta_1 = \omega_1 t + \varphi$ allow to obtain equivalences between the stationary and synchronous reference frames:

$$u_{\alpha\beta} = u_{dq}\, e^{\mathrm{j}\omega_1 t} = u_{dq}\, [\cos(\omega_1 t) + \mathrm{j}\, \sin(\omega_1 t)] \tag{1.3}$$

$$u_{dq} = u_{\alpha\beta}\, e^{-\mathrm{j}\omega_1 t} = u_{\alpha\beta}\, [\cos(\omega_1 t) - \mathrm{j}\, \sin(\omega_1 t)]\,. \tag{1.4}$$

1.2.5 Plant Model for Current-Controlled Grid-Tied VSCs

Passive filters are employed as the interface between the VSCs and the grid. They mitigate the switching harmonics that result from the modulation, and hence, reduce the losses and help meeting the connection requirements [42, 84]. In addition, their inductive character allows for proper operation of the grid-tied VSC, since the amplitude and phase imposed by the control at its output is able to regulate the active and reactive power flow [42]. Interface filters can be mainly classified into first-order, second-order and third-order ones, i.e., L, LC and LCL filters, respectively [85]. In this section, LC filters are considered as a particular case of LCL ones, so they are not analyzed separately [85].

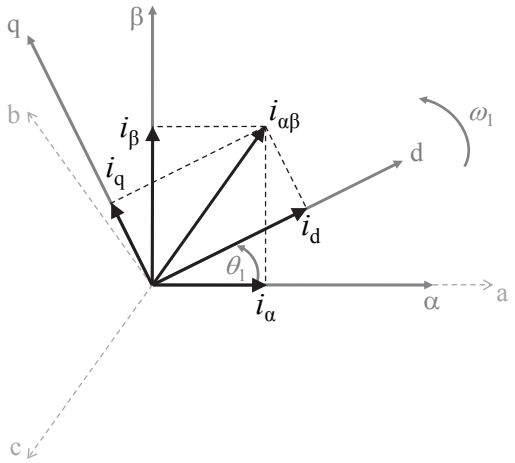

Figure 1.2: Equivalence between the stationary and synchronous reference frames. The SRF rotates with $\theta_1 = \omega_1 t + \varphi$.

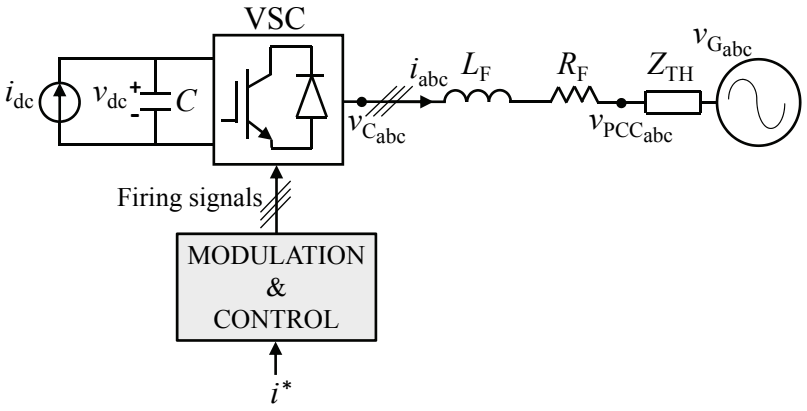

(a) L filter.

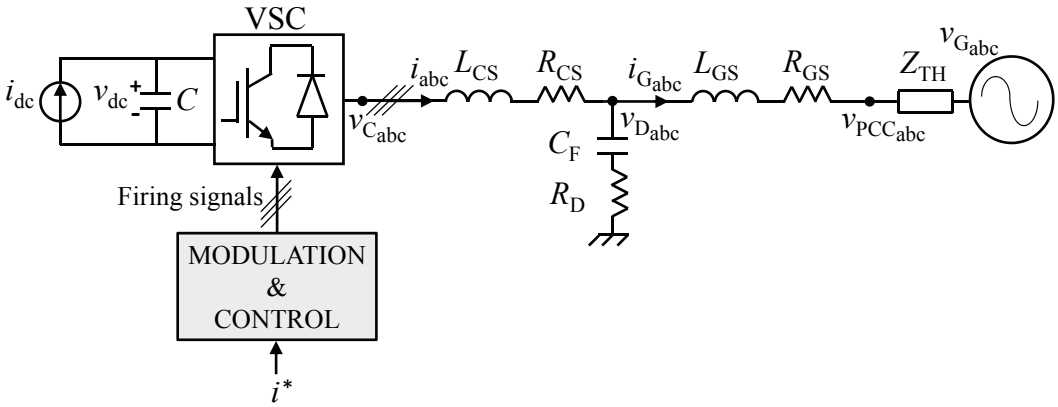

(b) LCL filter.

Figure 1.3: Current-controlled VSC connected to the grid (supplying power to it) through a low-pass filter. Other control inputs are omitted for clarity.

1.2.5.1 L Filters

Fig. 1.3a illustrates a three-phase VSC connected to the grid through an L filter. The variables i_{dc}, v_{dc} and C stand for the direct current delivered to (or demanded from) the dc-link, its voltage and its capacitance, respectively. The n-phase voltage at the converter output, at the PCC, current and grid voltage are denoted by v_{C_n}, v_{PCC_n}, i_n and v_{G_n}, respectively. The filter inductance and its parasitic resistance are represented by L_{F} and R_{F}, respectively. The complex variable Z_{TH} symbolizes the Thevenin equivalent impedance seen from the PCC, which is a combination of passive elements. Such impedance can be mainly attributed to the coupling transformer and to the grid, and, as done in other works, it is assumed to be principally inductive and resistive and (almost) balanced [58, 86–91]. Note that, even though the analysis developed in this work is oriented to grid connection, the scheme in Fig. 1.3a is also valid for variable speed drives supplying non-salient synchronous machines, as well as asynchronous ones; in the latter case, provided that the back electromotive force is perfectly decoupled [10, 85, 92].

The plant admittance can be modeled in the stationary reference frame as

$$G_{\mathrm{L}_{\alpha\beta}}(s) = \frac{I_{\alpha\beta}(s)}{V_{\mathrm{C}_{\alpha\beta}}(s)} = \frac{1}{sL+R}. \tag{1.5}$$

L represents the equivalent inductance in the plant model of the current loop, which is defined as $L = L_{\mathrm{F}} + L_{\mathrm{TH}}$, with $L_{\mathrm{TH}} = \mathfrak{Im}\{Z_{\mathrm{TH}}\}/\omega$. In addition to R_{F}, the equivalent resistance of the loop $R = R_{\mathrm{F}} + R_{\mathrm{TH}} + R_{\mathrm{C}}$ also includes $R_{\mathrm{TH}} = \mathfrak{Re}\{Z_{\mathrm{TH}}\}$ and the equivalent loss resistance of the converter R_{C} [76, 93–95]. The plant admittance of (1.5) may be expressed in the SRF, leading to $G_{\mathrm{L}_{\mathrm{dq}}}(s)$, by applying (1.4) to the former:

$$G_{\mathrm{L}_{\mathrm{dq}}}(s) = \frac{I_{\mathrm{dq}}(s)}{V_{\mathrm{C}_{\mathrm{dq}}}(s)} = \frac{1}{sL+R+\mathrm{j}\omega_1 L} \tag{1.6}$$

where ω_1 is the fundamental frequency of the signal to be controlled, i.e., of i.

1.2.5.2 LCL Filters

Given the higher attenuation of switching harmonics, which permits to reduce the size (and the cost) of the passive elements, LCL filters have become really popular in grid-tied applications [36, 84, 96–101]. Especially, in those with a really high power rate, in which a low switching frequency is mandatory to limit the losses [42, 96, 97, 102]. Additionally, LCL filters can mitigate the electromagnetic interference [42, 103]. However, selection of their parameters implies a much more complicated process compared to the case of L filters, as apart from the output current ripple, many other factors have to be considered altogether [96, 102, 104]. Furthermore, the inherent resonance of LCL filters, due to the interaction between inductive and capacitive components, requires the adoption of damping techniques to avoid the possible system instability [99]. There are two main options, namely, passive damping, which consists in adding a physical resistor [96, 102, 104], and active damping, which modifies the control algorithms, either by considering an extra filter on the control signal, or by using the feedback of an additional variable, e.g., the capacitor current [84, 88, 97–99, 105–107].

Fig. 1.3b depicts a VSC connected to the grid through an LCL filter. L_{CS} and L_{GS} are the inductances of the converter- and grid-side inductors, respectively, while R_{CS} and R_{GS}, their parasitic resistances. C_{F} denotes the capacitance of the filter, while R_{D} symbolizes the addition

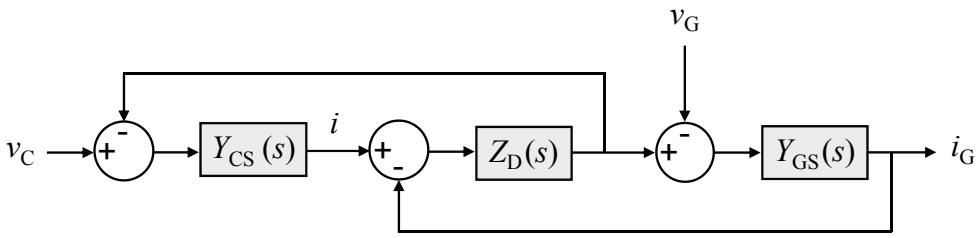

Figure 1.4: Block diagram of an LCL filter.

of the capacitor parasitic resistance and the previously mentioned optional resistor, in charge of the passive damping [96, 102, 104]. The voltage drop in the capacitor branch corresponding to the n-phase is represented by v_{D_n}.

Despite the fact that either the converter current i or the grid current i_G can be controlled, only the former possibility is evaluated in this study. In the power range of kW- MW, the current sensors are usually integrated in the converter, which allows for more effective protection, but the passive filter is outside [106, 108, 109]. Moreover, sensing the converter current might be the only possible option when the capacitor and grid-side inductance are distributed along the system [4, 7, 36].

From Fig. 1.3b, the following transfer functions can be defined in the stationary reference frame:

$$Y_{CS_{\alpha\beta}}(s) = \frac{I_{\alpha\beta}(s)}{V_{C_{\alpha\beta}}(s) - V_{D_{\alpha\beta}}(s)} = \frac{1}{sL_{CS} + (R_{CS} + R_C)} \tag{1.7}$$

$$Y_{GS_{\alpha\beta}}(s) = \frac{I_{G_{\alpha\beta}}(s)}{V_{D_{\alpha\beta}}(s) - V_{G_{\alpha\beta}}(s)} = \frac{1}{s(L_{GS} + L_{TH}) + (R_{GS} + R_{TH})} \tag{1.8}$$

$$Z_{D_{\alpha\beta}}(s) = \frac{V_{D_{\alpha\beta}}(s)}{I_{\alpha\beta}(s) - I_{G_{\alpha\beta}}(s)} = \frac{1}{sC_F} + R_D. \tag{1.9}$$

It is worth noticing that the effects associated to the converter losses, i.e., R_C, have been included in the converter-side plant admittance Y_{CS}, whereas Z_{TH} has been considered in the grid-side plant admittance Y_{GS}. The impedance offered by the capacitor branch is represented by Z_D. Alternatively, as in the case of L filters, these two admittances and the impedance may be expressed with respect to the SRF, by applying (1.4) to the three equations, leading respectively to $Y_{CS_{dq}}(s)$, $Y_{GS_{dq}}(s)$ and $Z_{D_{dq}}(s)$.

From these three expressions, the total plant admittance when an LCL filter is employed can be modeled by the block diagram of Fig. 1.4 [85], as well as by

$$G_{LCL}(s) = \frac{I(s)}{V_C(s)} = \frac{Y_{CS}(s)\,[1 + Y_{GS}(s)\,Z_D(s)]}{1 + Y_{CS}(s)\,Z_D(s) + Y_{GS}(s)\,Z_D(s)} \tag{1.10}$$

when the converter current is controlled. Note that neither $\alpha\beta$ nor dq subscripts are included in $G_{LCL}(s)$, since it is valid for both cases, but Y_{CS}, Y_{GS} and Z_D should be defined in the appropriate reference frame.

Fig. 1.5 shows the Bode diagrams of an L and an LCL filter, with equivalent parameters at low frequencies, i.e., $L_F = L_{GS} + L_{CS}$ and $R_F = R_{GS} + R_{CS}$ [55, 102, 106, 109, 110]. Both frequency responses are approximately equivalent for frequencies below the resonant one

$$f_{res} = \frac{1}{2\pi}\sqrt{\frac{L_{CS} + L_{GS}}{C_F L_{CS} L_{GS}}}. \tag{1.11}$$

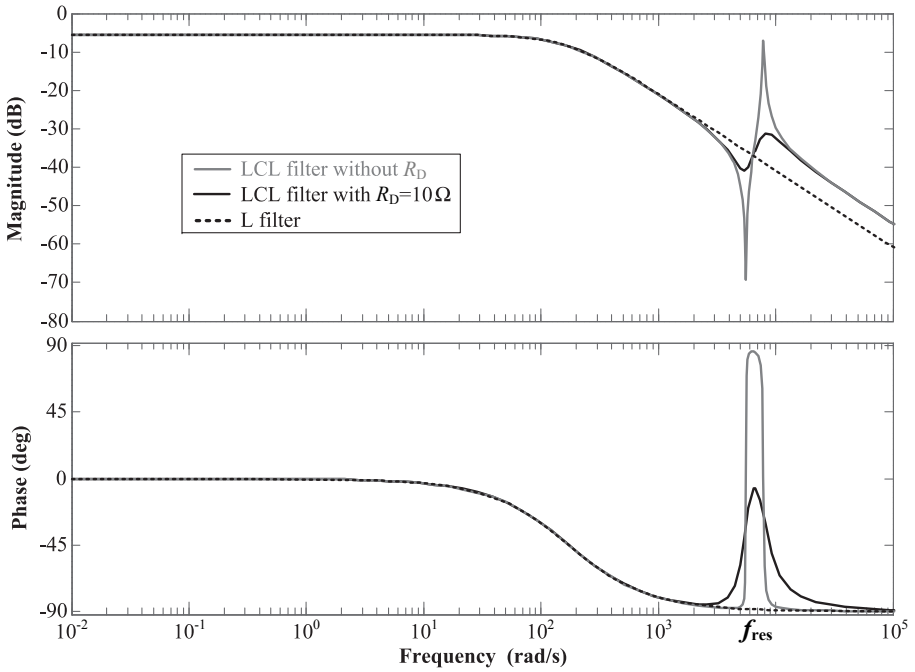

Figure 1.5: Bode diagrams of L and LCL filters, with equivalent parameters at low frequencies (i.e., $L_F = L_C + L_G$ and $R_F = R_C + R_G$). Parameters: $L = L_F = 10.9\,\text{mH}$, $R = 1.9\,\Omega$, $R_F = 0.45\,\Omega$, $L_{CS} = 5.9\,\text{mH}$, $L_{GS} = 5\,\text{mH}$, $R_{CS} = 0.4\,\Omega$, $R_{GS} = 0.05\,\Omega$, $C_F = 6\,\mu\text{F}$ and $R_D = 0$ or $R_D = 10\,\Omega$.

Moreover, adding passive damping ($R_D \neq 0$) does not affect the previous assertion, as it can be checked from the black curves in Fig. 1.5 [105]. Hence, the plant model of an LCL filter, i.e., (1.10) is usually simplified as that of an L filter with equivalent parameters at low frequencies, i.e., (1.5), to design the current controller [55, 102, 108–111].

It is worth mentioning that the frequency response of G_{LCL} does not exhibit a 60 dB decay rate for $f > f_{res}$ (cf. Fig. 1.5), since it corresponds with the ratio between $I(s)$ and $V_C(s)$, not between $I_G(s)$ and $V_C(s)$ [85].

1.2.5.3 Current Control Closed Loop

Fig. 1.6a shows the block diagram in the s-domain of the current control closed loop with respect to the stationary frame. The current reference, its actual value and the tracking error are respectively denoted by $i^*_{\alpha\beta}$, $i_{\alpha\beta}$ and $e_{\alpha\beta} = i^*_{\alpha\beta} - i_{\alpha\beta}$. $G_{C_{\alpha\beta}}(s)$ represents the current controller and $G_{L_{\alpha\beta}}(s)$ is defined as (1.5). The VSC introduces a gain equal to half the dc-link voltage v_{dc}, which is compensated by multiplying the output of the current controller by the inverse of such gain. Hence, from now on, this gain will be disregarded. The computational delay (i.e., a delay of one sample [76, 80]) is represented as e^{-sT_s}, with T_s being the sampling period. The regularly sampled pulse-width modulation (PWM) introduces half a sample delay when employing a triangular carrier, which can be modeled with good precision by a zero-order hold (ZOH) [76, 80, 112]:

$$\text{PWM}_{\alpha\beta}(s) = \frac{1 - e^{-sT_s}}{s}. \tag{1.12}$$

$G_{C_{\alpha\beta}}(s)$ should present an infinite open-loop gain at the frequency of the PCC voltage $v_{PCC_{\alpha\beta}}$, so that a perfect rejection of this disturbance is assured in steady state. In most cases, this

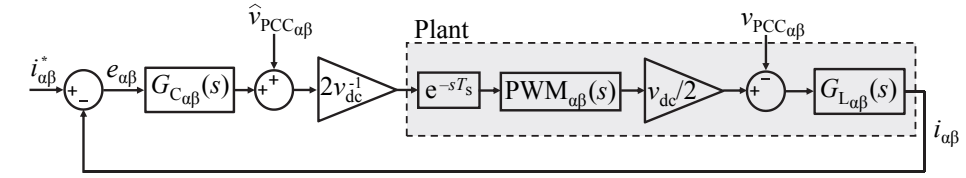

(a) In stationary frame.

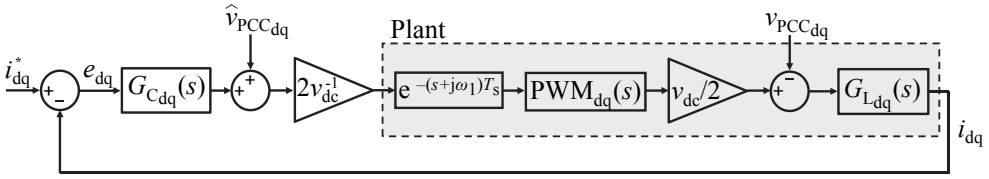

(b) In SRF.

Figure 1.6: Block diagram of current control closed loop in the s-domain.

voltage may be measured ($\widehat{v}_{\mathrm{PCC}_{\alpha\beta}}$) and fedforward at the output of the current controller to further improve the transient performance in the presence of grid faults [34, 65, 69, 113].

According to Fig. 1.6a, the overall transfer function of the current loop is defined as

$$I_{\alpha\beta}(s) = G_{\mathrm{CL}_{\alpha\beta}}(s) I^*_{\alpha\beta}(s) + G_{\mathrm{DR}_{\alpha\beta}}(s) V_{\mathrm{PCC}_{\alpha\beta}}(s) \tag{1.13}$$

where the closed-loop transfer functions of command tracking $G_{\mathrm{CL}_{\alpha\beta}}(s)$ and disturbance rejection $G_{\mathrm{DR}_{\alpha\beta}}(s)$ can be respectively expressed as follows:

$$G_{\mathrm{CL}_{\alpha\beta}}(s) = \frac{G_{\mathrm{C}_{\alpha\beta}}(s)\,\mathrm{e}^{-sT_\mathrm{s}}\,\mathrm{PWM}_{\alpha\beta}(s) G_{\mathrm{L}_{\alpha\beta}}(s)}{1 + G_{\mathrm{C}_{\alpha\beta}}(s)\,\mathrm{e}^{-sT_\mathrm{s}}\,\mathrm{PWM}_{\alpha\beta}(s) G_{\mathrm{L}_{\alpha\beta}}(s)} \tag{1.14}$$

and

$$G_{\mathrm{DR}_{\alpha\beta}}(s) = -\frac{G_{\mathrm{L}_{\alpha\beta}}(s)}{1 + G_{\mathrm{C}_{\alpha\beta}}(s)\,\mathrm{e}^{-sT_\mathrm{s}}\,\mathrm{PWM}_{\alpha\beta}(s) G_{\mathrm{L}_{\alpha\beta}}(s)}. \tag{1.15}$$

To consider the effect of the feedforward, $V_{\mathrm{PCC}_{\alpha\beta}}(s)$ should be replaced by $V'_{\mathrm{PCC}_{\alpha\beta}}(s) = V_{\mathrm{PCC}_{\alpha\beta}}(s) - \widehat{V}_{\mathrm{PCC}_{\alpha\beta}}\,\mathrm{e}^{-sT_\mathrm{s}}\,\mathrm{PWM}_{\alpha\beta}(s)$ in the former equations, as done in [10].

In order to obtain the equivalent transfer functions in the discrete-time domain, the computational delay is substituted by z^{-1}. Besides, the ZOH discretization method is applied to $G_{\mathrm{L}_{\alpha\beta}}(s)$ when preceded by $\mathrm{PWM}_{\alpha\beta}(s)$ leading to

$$G^{\mathrm{ZOH}}_{\mathrm{L}_{\alpha\beta}}(z) = \mathcal{Z}\left\{\mathcal{L}^{-1}\left[\mathrm{PWM}_{\alpha\beta}(s)\,G_{\mathrm{L}_{\alpha\beta}}(s)\right]\big|_{t=kT_\mathrm{s}}\right\} = \frac{z^{-1}}{R}\,\frac{1-\rho^{-1}}{1-z^{-1}\rho^{-1}} \tag{1.16}$$

with $\rho = e^{RT_\mathrm{s}/L}$, so that the effect of the modulation is also included in this transfer function [77, 79, 80, 112, 114]. The Tustin discretization method is employed when an accurate equivalence of just $G_{\mathrm{L}_{\alpha\beta}}(s)$ (without any delay) is sought [79]:

$$G^{\mathrm{Tustin}}_{\mathrm{L}_{\alpha\beta}}(z) = \frac{1}{(\frac{2}{T_\mathrm{s}}\frac{1-z^{-1}}{1+z^{-1}})L + R} = \frac{1+z^{-1}}{(R+\frac{2L}{T_\mathrm{s}}) + z^{-1}(R-\frac{2L}{T_\mathrm{s}})}. \tag{1.17}$$

Therefore, (1.14) and (1.15) can be defined in the discrete-time domain as

$$G_{\mathrm{CL}_{\alpha\beta}}(z) = \frac{G_{\mathrm{C}_{\alpha\beta}}(z) z^{-1} G^{\mathrm{ZOH}}_{\mathrm{L}_{\alpha\beta}}(z)}{1 + G_{\mathrm{C}_{\alpha\beta}}(z) z^{-1} G^{\mathrm{ZOH}}_{\mathrm{L}_{\alpha\beta}}(z)} \tag{1.18}$$

and

$$G_{\mathrm{DR}_{\alpha\beta}}(z) = -\frac{G^{\mathrm{Tustin}}_{\mathrm{L}_{\alpha\beta}}(z)}{1 + G_{\mathrm{C}_{\alpha\beta}}(z) z^{-1} G^{\mathrm{ZOH}}_{\mathrm{L}_{\alpha\beta}}(z)}. \tag{1.19}$$

Alternatively, the current control closed loop may be expressed with respect to the SRF frame by applying (1.4) to the different equations. Fig. 1.6b depicts the corresponding block diagram in the *s*-domain.

1.2.6 Parameter Identification

Precise knowledge of the equivalent inductance and resistance in the previously described plant model of the current loop is essential to guarantee its performance. Otherwise, it is not possible to assure that the design objectives will be fulfilled.

Information about the VSC interface filter parameters at nominal conditions is often not enough. Parameter uncertainties may arise owing to two main causes. Firstly, the existence of a non negligible impedance at the PCC, Z_{TH}, which, as explained in section §1.2.5, is part of the impedance of the current loop, and thus, should be considered in the plant model [see (1.5)] [88, 90, 91, 97, 100, 101, 111, 115]. This extra impedance can be attributed to other elements such as the grid, the coupling transformer, long wires...[86, 87, 91, 101, 103, 111]. Secondly, the variation with the working conditions in the value of the different components, even those connected before the PCC, i.e., those that form part of the VSC setup [55, 116]. Frequency, cable overload, core saturation and current magnitude, temperature, minor internal faults or changes, aging of components and other environmental conditions are some of the possible reasons [55, 86, 87, 89, 100, 103, 117]. Such variation is particularly significant in those parameters employed to model the losses [55], e.g., in R_{C}, the VSC equivalent loss resistance. Besides, errors in the original measurements also result in parameter mismatches.

From the point of view of the local system, stability and performance of the current control loop are affected by parameter uncertainties [91, 107, 115–118]. In addition, regardless of the interface filter order, particularly influenced are the specifications in terms of transient response (e.g., settling time and overshoot) [10, 80, 119–121]. In order to overcome these challenging issues, plant parameters should be accurately identified in the different working conditions and the controller gains adjusted accordingly [122].

Several solutions are possible, depending on the nature of the uncertainties. If the plant parameters are expected not to change or to do it in certain operating conditions (e.g., when the current magnitude is modified), an offline estimation can suffice [121]. In order to guarantee the precision of the estimates, the identification should be performed in the same circumstances at which the converter will be working during normal operation, but during a precommissioning stage [116]. Once estimated, the corresponding parameters should be employed to accurately tune the current controller [111, 116]. The resulting parameters could be stored in a table, linked to the working conditions and an open-loop adaptive control may be implemented to update the controller in real time (as a function of the working conditions). This kind of algorithm is usually known as “gain-scheduling” technique [116, 123–125].

In the case that plant parameters are expected to change in real time, online estimation together with an adaptive control should be implemented to maintain the performance [55, 86, 87, 100, 107, 115, 117, 126].

1.2.6.1 Overview of the Different Identification Methods

Different parameter estimation methods can be found in the literature. A large group of them calculates the impedance directly from the measurements, as the quotient between an ac voltage and current [115, 116, 118, 121, 126, 127]. Depending on the point at which such voltage is measured, the identified impedance would have a different definition. In the case that the ac voltage is estimated from the duty cycles and the dc-link voltage [126], it would correspond to the total equivalent impedance in the plant model of the current loop. Hence, it would include the effects associated to the converter losses (nonlinearities, voltage drops...), as well as the filter and the PCC impedances. If the voltage were measured at the converter output [127], the identified impedance would be the addition of that of the interface filter and Z_{TH}, excluding the converter effect. Measuring the voltage at the PCC, implies that only Z_{TH} would be estimated [115, 116, 118, 121]. These assertions are valid under the assumption that no parallel branches are connected, or if so, that they can be neglected at certain frequencies, e.g., the capacitor branch in LCL filters at low frequencies [55, 118].

Instead of direct calculations, adaptive observers are preferred for parameter estimation in many works [55, 86, 87, 89–91, 100, 103, 117, 128]. Most of these methods have their basis on model reference adaptive systems (MRASs) [123], which are briefly addressed in section §1.2.6.2. In this technique, the output of the estimator, which generally acts as adjustable model (AM), is compared to the actual output of the system, which takes the role of reference model (RM) [86, 87, 89, 100, 103, 117, 128]. The error between both is employed to update the observer, i.e., the AM. When using MRAS-based or other adaptive observers, several algorithms may be implemented to iteratively minimize the error, being the most popular ones the recursive least squares method [91, 100], the extended Kalman filter [90] and the gradient projection one [86, 87, 128], although custom-made options are also possible [55, 117]. Furthermore, neural networks [86, 87, 103] and sliding-mode surfaces [89] can also be defined to help stabilize the algorithms. In these methods, depending on how the observer is defined, the identified impedance would be only Z_{TH} [90, 91], the addition of the latter and that of the interface filter [55], or it would also include the effects associated to the converter losses [86, 87, 89, 100, 103, 128].

On the other hand, estimation methods may be classified into active or passive, depending on whether some kind of disturbance is needed or not for them to work [90, 118]. Passive methods are non intrusive and take advantage of the information already present in the system. Examples can be found in [55, 86, 87, 89, 90, 103, 126, 128]. Some active methods inject a known and periodical distortion into the grid, e.g., at a interharmonic frequency [118], by using a discrete-interval binary sequence [115] or by means of an impulse [116]. Some others need a change in the operating conditions [91, 100, 121, 127].

Nevertheless, none of these impedance estimation techniques is oriented to exactly the same objective as the one sought in this thesis: an accurate analysis and design of the transient response of the current loop in grid-tied VSCs. Some of them have completely different targets, e.g., islanding detection, in order to fulfill the stringent requirements for the grid connection of photovoltaic systems [90, 91, 118, 127], or active filtering [121]. Thus, the estimated

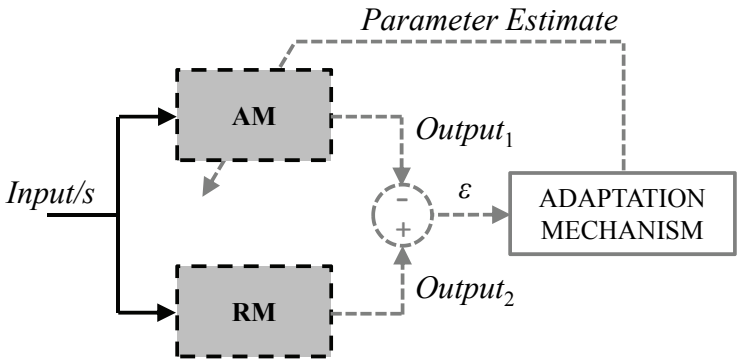

Figure 1.7: Block diagram of the basic MRAS technique.

impedance does not correspond with the equivalent one in the current loop plant model. Among all the techniques focused on improving the performance of the current loop, [100] is particularly intended for resonance damping and [117], for dc-link ripple minimization. The others have a more general purpose, but they are not aimed at transient response optimization either [55, 86, 87, 89, 103, 115, 116, 126, 128]. Although [126] could estimate the equivalent impedance of the current loop, as described at the beginning of this subsection, simplifications are made so as unity power factor is assumed and only the inductance is identified. Neither are the two parameters (equivalent inductance and resistance) estimated in [116] nor in [55]. Besides, while the former is only valid offline, the latter is specifically designed for predictive current controllers. At the cost of injecting a specific sequence and of computing a logarithmic averaging algorithm, the grid impedance estimation method in [115] may also include capacitors. Delay is disregarded when defining the different observers in [86, 87, 89, 103, 128], so identification might not be accurate at low ratios between the sampling and fundamental frequencies. In addition, despite including real time simulation results, these proposals have not been tested with an actual converter.

Therefore, an estimation method specifically designed according to the aim of this thesis, i.e., to the analysis and design of the current loop transient response, is presented in chapter §2 for the equivalent resistance in the current loop plant model, and in chapter §3, for both the equivalent inductance and resistance. The proposals have their basis on MRASs. The variables to be identified are iteratively estimated so as to minimize the error between the actual and the expected closed-loop current step response. Consequently, the proposed identification methods are directly oriented to the fulfillment of time-domain specifications.

1.2.6.2 General Outlook on MRASs

The first scheme of model reference adaptive control was proposed by Whitaker et al. in 1958 [129]. Since then, MRAS-based techniques have been widely employed either as simple estimators or as part of adaptive control solutions [123]. In other words, not only do they permit to improve the accuracy of the plant model, but also an online redesign of the controller.

Classical schemes are founded on the premise that one variable in the model that is related to the parameter to be estimated can be calculated in two different ways: by means of an RM, in which the value of the parameter to be estimated does not need to be introduced by the designer, and by means of an AM, in whose equations it does [123, 130] (cf. Fig. 1.7). The error between the output of both models is employed to drive an adaptation mechanism that updates

the AM and iteratively converges to zero as the estimated value of the parameter approaches the real one [123, 130–132]. In that moment, the output of the AM coincides with that of the RM, which defines the desired performance for the system [123]. As recursive closed-loop methods, MRAS-based solutions guarantee a greater accuracy in the estimates than the open-loop identification schemes, at the cost of a larger computational burden [123].

Apart from the grid-connection applications described in the previous section, the use of MRAS techniques to estimate the stator resistance in industrial drives has attracted much attention during the last years [130–136]. In these proposals, the basic scheme in Fig. 1.7 is adapted to each case and specifications: to the improvement of the behavior of the speed observer for sensorless control [130, 131, 133], to condition monitoring [132, 134], or to precise current loop design [135, 136]. Hence, some of these solutions permit the estimation of one or two extra parameters (besides the stator resistance) in the motor plant model, such as the rotor speed, the rotor flux magnitude or the rotor resistance [130, 131, 133, 136]. Therefore, as this extra dynamics is not reflected on the plant model described in section §1.2.5, these methods cannot be directly applied to solve the problem described in this thesis. A similar situation happens in [130], since the duality of stator and rotor equations is used to define the AM and the RM. Regarding the other works, the remaining delay after applying delay compensation is neglected in the AM of [134], whereas in that of [135], the modulation delay is ignored. These omissions may lead to important mismatches as the sampling frequency f_s decreases and are specially critical when the target of the estimation is to precisely design the closed-loop transient response. On the other hand, owing to the quantity selected to be compared in both models of [132], this proposal cannot be extended to estimate both the equivalent inductance and resistance in the plant model. Consequently, as reported in the previous section, particularly designed estimation methods are developed in this thesis, based on the general ideas collected from the bibliography.

1.2.7 Control Structures

Multiple structures can be implemented to regulate the ac current [42]. Among the linear alternatives that require a separate modulation algorithm, the most popular ones are probably deadbeat controllers [34, 42, 55, 80, 86, 89, 137], proportional-integral (PI) controllers [10, 42, 80, 92, 138–141] and resonant controllers [27, 34, 42, 77, 79, 80, 114, 142–148]. A brief overview of deadbeat controllers is included in the following, together with a more detailed presentation of PI and proportional-resonant (PR) regulators, which are object of analysis along this thesis.

1.2.7.1 Deadbeat Controllers

Deadbeat controllers belong to the family of predictive regulators [34, 42]. Hence, they can either directly generate the modulation pulses or be followed by a modulation stage [42]. The deadbeat controller is obtained by setting the closed-loop transfer function of the current loop, which is given in (1.18), so that the delay at all frequencies is as low as possible. Since 2 is the immediate integer above the actual number of delay samples, which is 1.5 (cf. section §1.2.5.3), $G_{\mathrm{CL}_{\alpha\beta}}(z) = z^{-2}$ [34, 42, 85, 137, 149]. Thus, from the latter and (1.18), the deadbeat controller

transfer function is

$$G_{\mathrm{DB}}(z) = \frac{1}{z^{-1} G^{\mathrm{ZOH}}_{\mathrm{L}_{\alpha\beta}}(z)} \frac{z^{-2}}{1-z^{-2}}. \tag{1.20}$$

Substituting $G^{\mathrm{ZOH}}_{\mathrm{L}_{\alpha\beta}}(z)$ in the latter equation by (1.16) yields to

$$G_{\mathrm{DB}}(z) = \frac{R}{1-\rho^{-1}} \frac{1-z^{-1}\rho^{-1}}{1-z^{-2}}. \tag{1.21}$$

It is worth mentioning that this definition of deadbeat controller, which was already presented in [85], is more accurate than those in many studies, which neglect either the computation or the modulation delays in the plant model, or the resistance or consider $G_{\mathrm{CL}_{\alpha\beta}}(z) = z^{-1}$ [34, 42, 80, 86, 87, 149–151]. When properly tuned, the deadbeat controller shows a superior performance in terms of transient response than the other digital alternatives [80, 85, 86, 137]. Nevertheless, different drawbacks have been reported. Firstly, owing to the fact that they are directly defined from the plant model, deadbeat controllers exhibit a significant sensitiveness to parameter mismatches, as well as to converter nonlinearities, such as dead times [42, 55, 85–87, 89, 137]. Related to these aspects, it is their poor disturbance rejection capability [80, 85, 137]. Another weak point is their inability to achieve zero steady-state error at frequencies different from 0 Hz, which is a problem when controlling alternate signals in stationary frame [85]. Besides, deadbeat controllers are particularly sensitive to noise on the measured variables [80, 137]. In order to overcome these problems, parameter estimators, dead time compensation algorithms, feedforward of the PCC voltage and delay compensation techniques may be implemented at the cost of a slower transient response [55, 80, 86, 87, 89, 103, 128, 137, 151].

1.2.7.2 PI Controllers

PI controllers are one of the most extended solutions to regulate constant references. However, when controlling alternate signals of frequency ω_1 in stationary frame, they are unable to provide zero steady-state error. To overcome this issue, they are implemented in a reference frame synchronous with the frequency to be controlled, i.e., with ω_1, so that alternate signals of that frequency are transformed into dc quantities, thanks to the Park transform (cf. section §1.2.4) [80, 138].

Mainly, two different structures of PI controllers in the SRF can be distinguished: the classical PI controller (with or without state-feedback cross-coupling decoupling) and the complex vector PI controller.

A) Classical PI Controller

A classical PI controller of the form

$$G_{\mathrm{PI}}(s) = K_{\mathrm{P}} + \frac{K_{\mathrm{I}}}{s} \tag{1.22}$$

should be implemented in each of the two axes of the SRF, where K_{P} and K_{I} denote the proportional and integral gains, respectively. An equivalent structure can be employed to regulate a harmonic component of order h

$$G_{\mathrm{PI}_h}(s) = K_{\mathrm{P}_h} + \frac{K_{\mathrm{I}_h}}{s}. \tag{1.23}$$

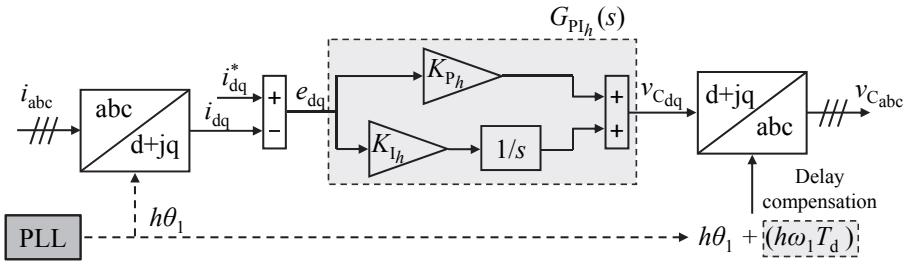

Figure 1.8: Classical PI controller implemented in SRF and Park transforms.

when implemented in an SRF rotating at $h\omega_1$, in case of positive-sequence harmonics, or at $-h\omega_1$, in case of negative-sequence ones. The proportional and integral gains are represented by K_{P_h} and K_{I_h}, respectively. Fig. 1.8 depicts the corresponding complex vector block diagram, where the angle needed for the Park transform $h\theta_1$ is provided by a phase-locked loop (PLL) [152]. A delay compensation term can be included by simply adding a phase lead to $h\theta_1$ before being input to the inverse transformation [10, 80, 139]. This leading angle is usually chosen to compensate the time delay of the plant $T_{\mathrm{d}} = 1.5T_{\mathrm{s}}$ (cf. section §1.2.5.3) at dc, which implies the addition of an angle $\omega_1 T_{\mathrm{d}}$ [10, 139, 153], as shown in Fig. 1.8.

Fig. 1.9a illustrates the complex vector block diagram of the current control closed loop in an SRF when a classical PI controller is implemented. The delay compensation term is modeled in this scheme as $\mathrm{e}^{\mathrm{j}\omega_1 T_{\mathrm{d}}}$ (see the block labeled accordingly in the center of the figure) [10]. Due to the cross coupling between the d and q axes in $G_{\mathrm{L_{dq}}}(s)$, the performance of the control loop degrades, especially as the synchronous frequency increases [10, 92, 140, 141]. This problem may be avoided by adding a current feedback with a gain $\mathrm{j}\omega_1\widehat{L}$ to the controller output, as depicted with dashed lines in Fig. 1.9a. This modification of the classical PI controller is very popular and often known as PI controller with state-feedback cross-coupling decoupling (PICCD) [10, 34, 58, 78, 140, 141, 154]. If the delay were neglected, it would be equivalent to moving the plant pole to the real axis, i.e., to replacing $G_{\mathrm{L_{dq}}}(s)$ by $G_{\mathrm{L}_{\alpha\beta}}(s)$ [85, 140]. Hence, in these conditions, the open-loop transfer function of the current control loop would be as follows:

$$G_{\mathrm{OL}}(s) = G_{\mathrm{PI}_h}(s)\, G_{\mathrm{L}_{\alpha\beta}}(s) = \frac{sK_{\mathrm{P}_h} + K_{\mathrm{I}_h}}{s}\frac{1}{sL+R}. \tag{1.24}$$

If the IMC principle is adopted, which is aimed at canceling the plant pole by the controller zero, the latter transfer function can be further simplified as $G_{\mathrm{OL}}(s) = K_h/s$, where K_h coincides with the controller bandwidth and is the only degree of freedom of the resulting regulator. This involves selecting the PI controller gains as $K_{\mathrm{P}_h}/K_{\mathrm{I}_h} = L/R$ and $K_{\mathrm{P}_h} = K_h L$, as well as having a correct estimation of the plant parameters L and R [10, 81, 92, 140, 141]. The corresponding scheme is depicted in Fig. 1.9b.

In order to obtain the equivalent transfer function of the classical PI controller in the discrete-time domain $G_{\mathrm{PI}_h}(z)$, the Tustin transform is applied to $G_{\mathrm{PI}_h}(s)$ following the indications in [79]:

$$G_{\mathrm{PI}_h}(z) = K_{\mathrm{P}_h} + \frac{K_{\mathrm{I}_h}}{\frac{2}{T_{\mathrm{s}}}\frac{1-z^{-1}}{1+z^{-1}}} = K_{\mathrm{P}_h} + K_{\mathrm{I}_h}\frac{T_{\mathrm{s}}}{2}\frac{1+z^{-1}}{1-z^{-1}} \tag{1.25}$$

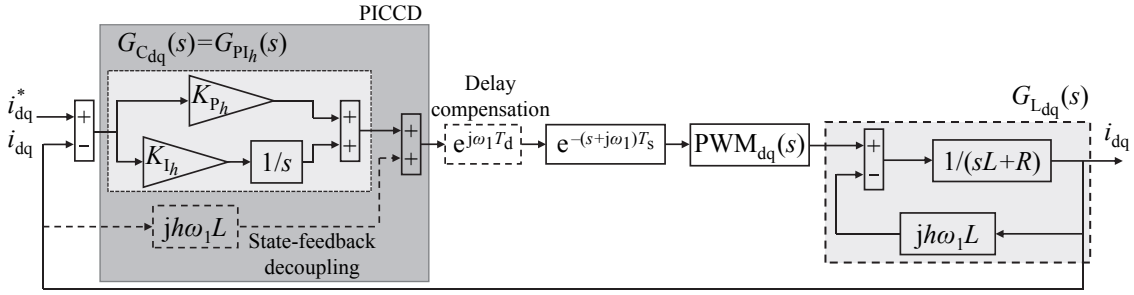

(a) Classical PI controller (with cross-coupling decoupling (PICCD)).

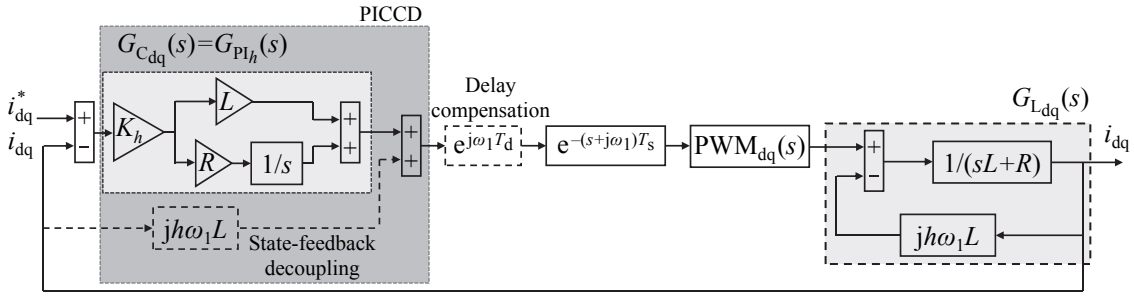

(b) Classical PI controller (with cross-coupling decoupling (PICCD)) tuned according to IMC principle.

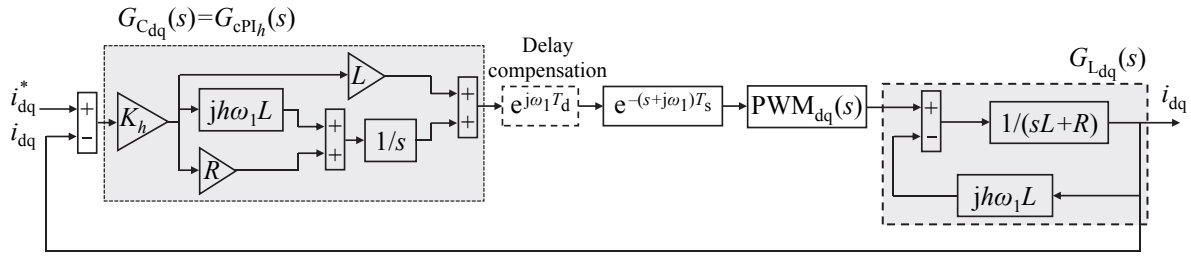

(c) Complex vector PI controller tuned according to IMC principle.

Figure 1.9: Complex vector block diagrams of the current closed loop with different PI controllers in SRF.

B) Complex Vector PI Controller

Instead of moving the plant pole to the real axis, as the classical PICCD does, it is also possible to match the complex pole of $G_{\mathrm{L}_{dq}}(s)$ by a complex zero in the controller. Thus, the complex vector PI controller was proposed [10, 92, 140, 141]:

$$G_{\mathrm{cPI}_h}(s) = \frac{s\,K_{\mathrm{P}_h} + K_{\mathrm{I}_h} + jh\omega_1 K_{\mathrm{P}_h}}{s} = K_h\,\frac{s\,L + R + jh\omega_1 L}{s}. \tag{1.26}$$

Note that in (1.26), the controller gains have been selected according to the IMC principle, as explained above. Fig. 1.9c illustrates the corresponding block diagram. If the delay effect were neglected and the plant parameters correctly identified, the resulting open-loop transfer function of the current loop would be identical to that obtained with the PICCD, i.e., $G_{\mathrm{OL}}(s) = K_h/s$, and so would be the closed-loop one, leading to an equivalent command tracking performance of both controllers [10, 92, 140].

Nonetheless, in case of plant parameter mismatches, the closed-loop frequency response with the PICCD would be more degraded around $h\,\omega_1$, i.e., at the vicinity of the frequency to

be controlled, whereas with $G_{\mathrm{cPI}_h}(s)$ it would be altered around 0 Hz, which is more favorable [10, 140]. Moreover, when implementing several controllers in parallel to regulate different harmonics and sequences, a much better performance, in terms of axes decoupling is achieved with $G_{\mathrm{cPI}_h}(s)$, especially at low gains [9, 85]. Regarding the disturbance rejection capability, the PICCD exhibits superior behavior than the complex vector alternative, even when L and R are correctly identified [10, 92].

1.2.7.3 Resonant Controllers

Resonant controllers present open-loop infinite gain at a certain frequency, called resonant frequency, which assures steady-state perfect tracking and disturbance rejection for components pulsating in closed loop at that frequency [27, 77, 79, 80, 114, 142, 144–148]. In this manner, ac currents can be regulated directly in stationary frame, avoiding Park transformations, and thus, reducing the computational burden [79, 80, 114, 144–146]. This also allows for a lower sensitiveness to errors and noise in synchronization [114, 144, 155]. Moreover, not only do they track the positive-sequence component, but also the negative-sequence one of the same harmonic order [77, 79, 80, 114, 144–146]. This is related to their equivalence to two identical PI regulators implemented in two SRFs simultaneously: one in a positive-sequence SRF and another one in a negative-sequence SRF [26, 42, 80, 114, 143, 144, 146]. Regulating the fundamental negative-sequence current is essential in grid-tied applications to compensate the grid imbalance. However, when using a resonant controller, achieving distortion-free saturation requires more complex schemes than in the case of a PI SRF regulator [156]. Besides, special care must be put on the discretization of the former in order to preserve the desired resonant frequency [79, 80].

Resonant controllers can be mainly grouped in PR and vector proportional-integral (VPI) controllers.

A) PR Controller

A PR controller can be expressed in the s-domain as follows:

$$G_{\mathrm{PR}_h}(s) = K_{\mathrm{P}h} + \frac{K_{\mathrm{I}h}s}{s^2 + h^2\omega_1^2} \tag{1.27}$$

where $K_{\mathrm{P}h}$ and $K_{\mathrm{I}h}$ denote the proportional and integral gains, respectively [77, 79, 146, 147, 157]. As shown in Fig. 1.10, this expression results from the addition of those of two identical classical PI controllers, one of them implemented in a positive-sequence SRF rotating at $h\omega_1$ and another one, in a negative-sequence SRF rotating at $-h\omega_1$, both translated to the stationary frame [by applying (1.4) to (1.23)]:

$$G_{\mathrm{PR}_h}(s) = \underbrace{\frac{K_{\mathrm{P}_h}}{2} + \frac{K_{\mathrm{I}_h}/2}{s - \mathrm{j}h\omega_1}}_{G^{+}_{\mathrm{PI}_h}(s)} + \underbrace{\frac{K_{\mathrm{P}_h}}{2} + \frac{K_{\mathrm{I}_h}/2}{s + \mathrm{j}h\omega_1}}_{G^{-}_{\mathrm{PI}_h}(s)}. \tag{1.28}$$

Superscripts $+$ and $-$ refer to the positive and negative SRFs, respectively. Note that in (1.28), as well as in Fig. 1.10, the gains of $G^{+}_{\mathrm{PI}_h}(s)$ and $G^{-}_{\mathrm{PI}_h}(s)$ are halved, so that the resulting ones after the addition correspond to those in (1.27) [85]. It is worth mentioning that adding state-feedback decoupling terms in both SRFs has no effect, as these terms are not altered by the transforms, and thus, they are canceled with each other (cf. Fig. 1.10) [9].

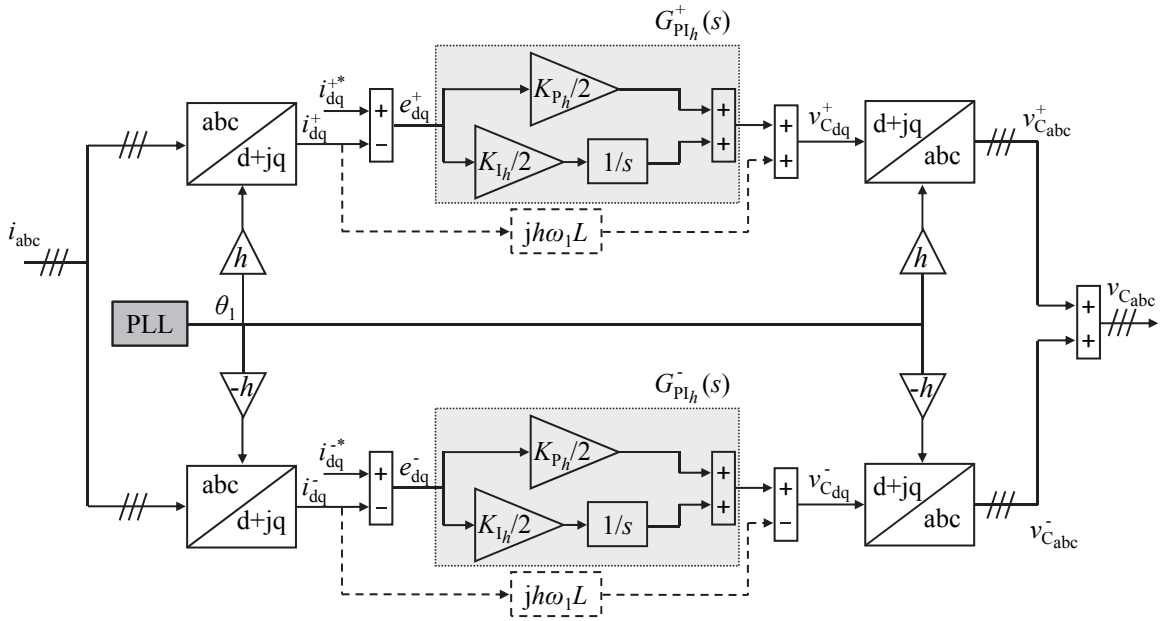

(a) Double SRF with classical PI controllers (with cross-coupling decoupling (PICCD)) and Park transforms.

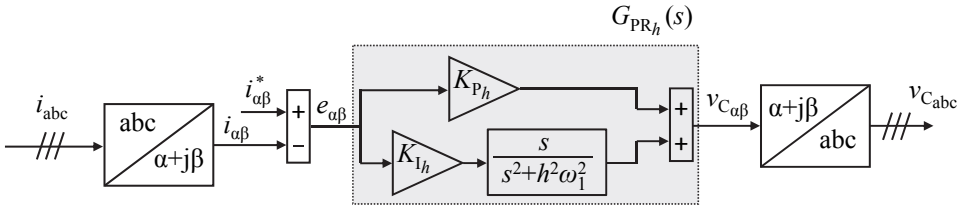

(b) PR controller and Clarke transforms.

Figure 1.10: Equivalence between double SRF PI controller and PR controller in stationary frame.

With the aim of regulating different harmonics, several PR controllers can be implemented in parallel [79, 111, 114, 143, 145, 146, 158–161], yielding to the following expression:

$$G_{\mathrm{PR}}(s) = K_{\mathrm{P_T}} + \sum_{h=1,5,7\ldots} K_{\mathrm{I}_h} \frac{s}{s^2 + h^2\omega_1^2} \tag{1.29}$$

where $K_{\mathrm{P_T}}$ is the addition of the individual proportional gains, i.e., $K_{\mathrm{P_T}} = \sum_{h=1,5,7\ldots} K_{\mathrm{P}_h}$.

In order to compensate the time delay at the vicinity of the resonant frequency, a delay compensation technique may also be added to these controllers [77, 79, 143, 147, 148, 159, 162]:

$$G^{\mathrm{d}}_{\mathrm{PR}_h}(s) = K_{\mathrm{P}_h} + K_{\mathrm{I}_h} \frac{s\cos(\phi'_h) - h\omega_1 \sin(\phi'_h)}{s^2 + h^2\omega_1^2}. \tag{1.30}$$

The superscript d indicates that delay compensation is included. This technique, which is equivalent to that applied to the PI regulators, consists in moving the zero of the PR controller in (1.27) to achieve a phase lead ϕ'_h around the resonant frequency. Note that for $\phi'_h = 0$, (1.30) equals (1.29).

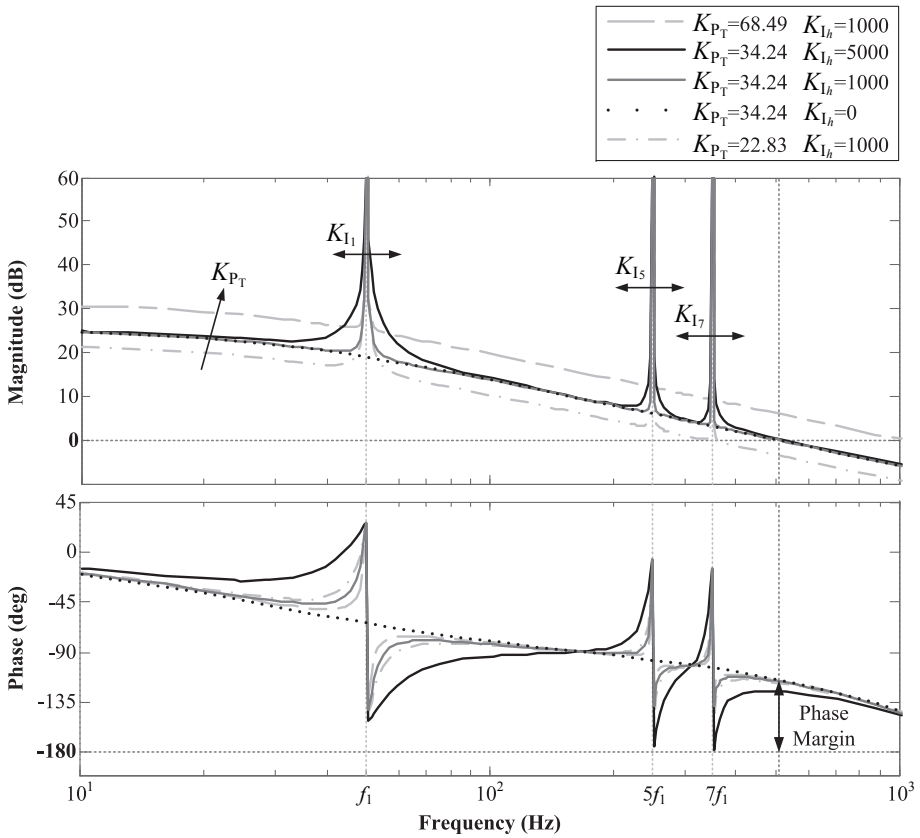

Figure 1.11: Open-loop Bode diagrams $G_{C_{\alpha\beta}}(z)z^{-1}G^{ZOH}_{L_{\alpha\beta}}(z)$ obtained with PR controllers without delay compensation, for different K_{P_T} and K_{I_h} values. The phase margin and crossover frequency is only indicated for those cases in which $K_{P_T} = 34.24$ (it is practically the same for the three K_{I_h} values). Parameters: $L = 10.9\,\text{mH}$, $R = 1.9\,\Omega$, $f_s = 10\,\text{kHz}$, $h \in \{1,5,7\}$, $f_1 = 50\,\text{Hz}$ and $K_{I_1} = K_{I_5} = K_{I_7} = K_{I_h}$.

A thorough study about the accuracy of the different methods to discretize resonant controllers has been contributed in [79]. According to it, the best choice is to apply the impulse invariant method to $G_{PR_h}(s)$ and $G^{d}_{PR_h}(s)$:

$$G_{PR_h}(z) = K_{P_h} + K_{I_h}T_s\frac{1-z^{-1}\cos(\omega_1 T_s)}{1-2z^{-1}\cos(\omega_1 T_s)+z^{-2}} \tag{1.31}$$

$$G^{d}_{PR_h}(z) = K_{P_h} + K_{I_h}T_s\frac{\cos(\phi'_h)-z^{-1}\cos(\phi'_h - h\omega_1 T_s)}{1-2z^{-1}\cos(h\omega_1 T_s)+z^{-2}}. \tag{1.32}$$

The tuning of ϕ'_h has been addressed in different works, with different objectives. E.g., in [77], the selection is targeted at sensitivity minimization, i.e., at maximizing the distance in the Nyquist curve to the critical point, which improves the stability, while in [7], it is aimed at a passivity-based design to prevent from system unknown instabilities.

Regarding the tuning of K_{P_T} and K_{I_h}, some guidelines can be found in the literature, mainly based on the observation of open-loop Bode diagrams, as the one shown in Fig. 1.11. The

crossover frequency (i.e., the frequency at which the gain is 0 dB) is mainly set by the proportional gain $K_{\mathrm{P_T}}$, and so are the phase margin and bandwidth [79, 80, 85, 111, 146, 161]. When delay compensation is not included, $K_{\mathrm{P_T}}$ usually also defines the maximum resonant frequency that can be controlled maintaining the stability [79, 85, 111, 146] (see [77] for exceptions). The reason is that resonant filters principally modify the frequency response only at the vicinity of the frequency to be controlled, i.e., $h\omega_1$ [65, 79, 85, 111, 146, 158, 161, 163, 164]. Consideration of delay compensation makes possible to control frequencies higher than the crossover one without losing the stability [77, 139, 147]. The width of the resonant peak at each resonant frequency is established by the corresponding integral gain K_{I_h}. This fact can be observed in Fig. 1.11, which includes curves with three different K_{I_h} values. Consequently, selection of integral gains implies a compromise between filter selectivity and settling time of command tracking and disturbance rejection of components rotating at $h\omega_1$ [79, 80, 85, 139, 144, 146, 160, 165, 166]. In general, the higher the K_{I_h}, the faster the dynamics, but the lower the filter selectivity, which implies that the current loop performs better in the presence of frequency deviations, but also, that is more sensitive to noise. On the contrary, the lower the K_{I_h}, the slower the settling time and the higher the filter selectivity. Nevertheless, these are mostly qualitative guidelines, which do not consider the delay effect. Furthermore, they are not aimed at the optimization of the disturbance rejection transient response, which is crucial to fulfill the LVRT requirements and, as proved in chapter §4, more demanding than the reference tracking one, as well as very dependent on the parameter tuning. Hence, an accurate assessment of the current loop, together with a tuning method for K_{I_h} is presented in chapter §4.

B) VPI Controller

VPI controllers are alternative resonant regulators to PR ones [77, 79, 142, 143, 147, 148, 157, 167–170] of the form

$$G_{\mathrm{VPI}_h}(s) = \frac{s^2 K_{\mathrm{P}h} + s K_{\mathrm{I}h}}{s^2 + h^2\omega_1^2}. \tag{1.33}$$

Hence, if the delay were neglected, the resulting open-loop transfer function of the current control loop in stationary frame would be

$$G_{\mathrm{OL}}(s) = G_{\mathrm{VPI}_h}(s)\, G_{\mathrm{L}_{\alpha\beta}}(s) = \frac{s^2 K_{\mathrm{P}h} + s K_{\mathrm{I}h}}{s^2 + h^2\omega_1^2} \frac{1}{sL+R}. \tag{1.34}$$

Therefore, cancellation of the plant pole may be achieved with the VPI controller as done with the PI regulators, i.e., by selecting its gains as $K_{\mathrm{P}h}/K_{\mathrm{I}h} = L/R$ [77, 79, 142, 143]. Thus, (1.33) can be rearranged as

$$G_{\mathrm{VPI}_h}(s) = K_h \frac{s(sL+R)}{s^2 + h^2\omega_1^2} \tag{1.35}$$

where $K_{\mathrm{P}h} = K_h L$ [77, 79, 142, 143, 147, 148, 157]. In this manner, in such conditions, (1.34) would be further simplified as $G_{\mathrm{OL}}(s) = sK_h/(s^2 + h^2\omega_1^2)$. Owing to this fact, despite not explicitly including ϕ'_h in (1.35), $G_{\mathrm{VPI}_h}(s)$ already provides certain phase compensation, of an angle $\arctan(h\omega_1 L/R)$. Nevertheless, when controlling high-order harmonic components ($h \geq 37$), delay compensation has to be included to guarantee the stability of the current loop [77, 143]:

$$G^{\mathrm{d}}_{\mathrm{VPI}_h}(s) = K_h \frac{(sL+R)\left[s\cos(\phi'_h) - h\omega_1 \sin(\phi'_h)\right]}{s^2 + h^2\omega_1^2} \tag{1.36}$$

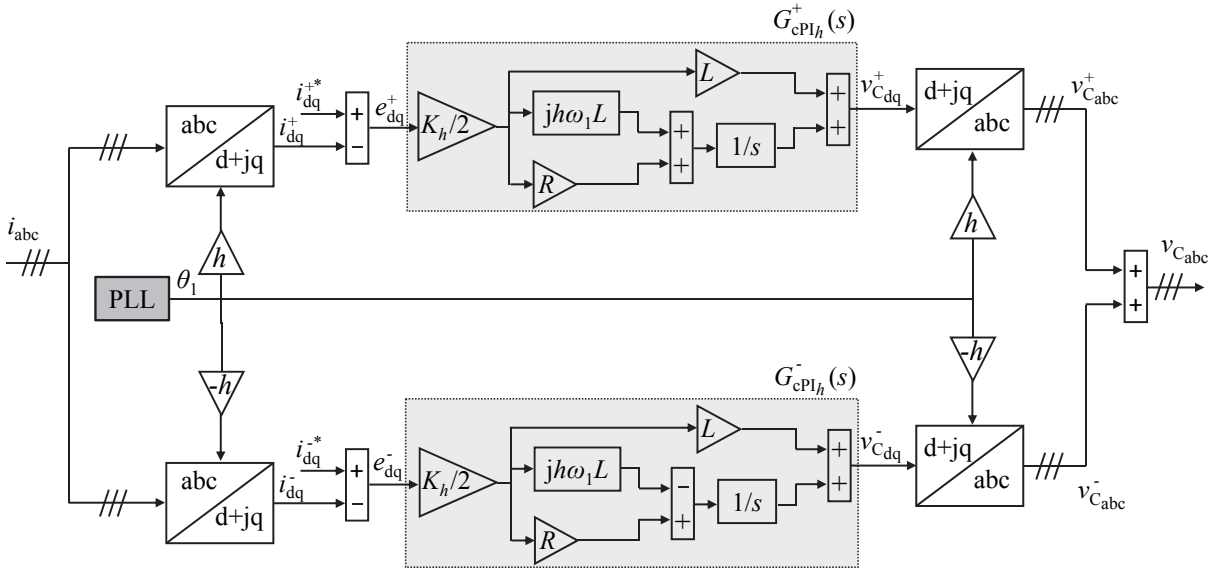

(a) Double SRF with complex vector PI controllers and Park transforms.

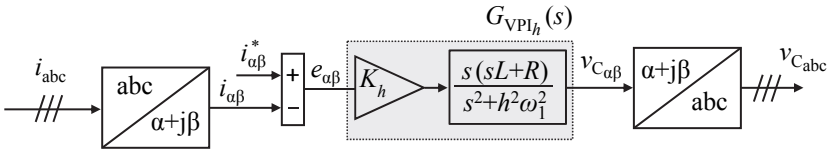

(b) VPI controller and Clarke transforms.

Figure 1.12: Equivalence between double SRF complex vector PI controller and VPI controller in stationary frame.

As in the case of PR controllers, several VPI regulators can be added in parallel to control different harmonics. VPI controllers provide very low gain for dc and for other components far from the ones to be regulated [142, 143]. Some recent works show that they could provide higher stability margins than PR ones, and hence, more damped responses [77, 79, 143, 157]. On the other hand, as illustrated in Fig. 1.12, a VPI controller is equivalent to the addition of two identical complex vector PI controllers, one of them implemented in a positive-sequence SRF rotating at $h\,\omega_1$ and another one, in a negative-sequence SRF rotating at $-h\,\omega_1$, both translated to the stationary frame [by applying (1.4) to (1.26)]:

$$G_{\mathrm{VPI}_h}(s) = \underbrace{\frac{K_h}{2}\frac{(s-\mathrm{j}h\omega_1)L+R+\mathrm{j}h\omega_1 L}{s-\mathrm{j}h\omega_1}}_{G^{+}_{\mathrm{cPI}_h}(s)} + \underbrace{\frac{K_h}{2}\frac{(s+\mathrm{j}h\omega_1)L+R-\mathrm{j}h\omega_1 L}{s+\mathrm{j}h\omega_1}}_{G^{-}_{\mathrm{cPI}_h}(s)} \tag{1.37}$$

The gain of each $G^{+}_{\mathrm{cPI}_h}(s)$ and $G^{-}_{\mathrm{cPI}_h}(s)$ is halved with respect to that in (1.26), so that the resulting K_h corresponds to that in (1.35) [85].

Discretization of VPI controllers has been also deeply analyzed in [79]. In such work, a separation of the controller into two different resonant terms is proposed:

$$G_{\mathrm{VPI}_h}(s) = K_h\left[L\underbrace{\frac{s^2}{s^2+h^2\omega_1^2}}_{\text{sine term}} + R\underbrace{\frac{s}{s^2+h^2\omega_1^2}}_{\text{cosine term}}\right]. \tag{1.38}$$

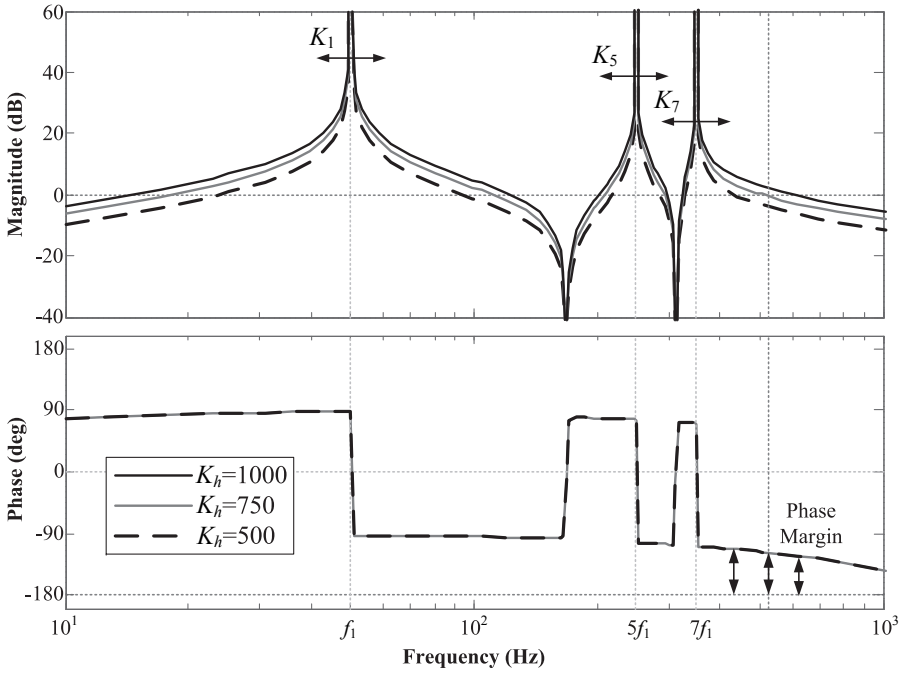

Figure 1.13: Open-loop Bode diagrams $G_{\mathrm{C}_{\alpha\beta}}(z)z^{-1}G^{\mathrm{ZOH}}_{\mathrm{L}_{\alpha\beta}}(z)$ obtained with VPI controllers without delay compensation, for different K_h values. Parameters: $L = 10.9\,\mathrm{mH}$, $R = 1.9\,\Omega$, $f_\mathrm{s} = 10\,\mathrm{kHz}$, $h \in \{1,5,7\}$, $f_1 = 50\,\mathrm{Hz}$ and $K_1 = K_5 = K_7 = K_h$.

Hence, a different discretization method can be applied to each term. For the cosine one, which coincides with that of the PR controller [cf. (1.29)], the same technique is recommended, i.e., the impulse invariant method, whereas for the sine term, either first-order hold, Tustin with prewarping or zero-pole matching are regarded as suitable options [79]. Thus, $G_{\mathrm{VPI}}(s)$ and $G^{\mathrm{d}}_{\mathrm{VPI}_h}(s)$ may be expressed in the z-domain as follows, when Tustin with prewarping discretization is applied to the sine term [79]:

$$G_{\mathrm{VPI}}(z) = K_h\left[\underbrace{L\cos^2\left(\frac{h\omega_1 T_\mathrm{s}}{2}\right)\frac{1-2z^{-1}+z^{-2}}{1-2z^{-1}\cos(h\omega_1 T_\mathrm{s})+z^{-2}}}_{\text{sine term}} + \underbrace{R\,T_\mathrm{s}\frac{1-z^{-1}\cos(h\omega_1 T_\mathrm{s})}{1-2z^{-1}\cos(h\omega_1 T_\mathrm{s})+z^{-2}}}_{\text{cosine term}}\right] \tag{1.39}$$

$$G^{\mathrm{d}}_{\mathrm{VPI}_h}(z) = K_h\left[\underbrace{L\frac{\frac{1}{2}(-1+z^{-2})\sin(\phi'_h)\sin(h\omega_1 T_\mathrm{s})+(1-2z^{-1}+z^{-2})\cos(\phi'_h)\cos^2\left(\frac{h\omega_1 T_\mathrm{s}}{2}\right)}{1-2z^{-1}\cos(h\omega_1 T_\mathrm{s})+z^{-2}}}_{\text{sine term}}\right.$$
$$\left. + \underbrace{R\,T_\mathrm{s}\frac{\cos(\phi'_h)-z^{-1}\cos(\phi'_h-h\omega_1 T_\mathrm{s})}{1-2z^{-1}\cos(h\omega_1 T_\mathrm{s})+z^{-2}}}_{\text{cosine term}}\right]. \tag{1.40}$$

As reported in [77, 142, 143], K_h tuning involves a tradeoff between selective filtering and settling time. From Fig. 1.13, the higher the K_h, the wider the resonant peak, and thus, the

lesser the selectivity. As demonstrated in [77], once K_h is determined, ϕ'_h can be adjusted independently to maximize the phase margin, i.e., $\phi'_h = 1.5h\omega_1 T_d$, without worsening the transient response.

Given the advantages of VPI controllers, and the lack of studies about their tuning oriented to grid-connected applications, in which settling time, overshoot and THD are the main constraints, a rigorous analysis and design of current loop is conducted in chapter §5. A comparison in those terms between PR and VPI controllers is also provided.

C) Resonant Controllers in SRF

Resonant controllers tuned at $h = 6k$, with $k \in \mathbb{N}$, can be implemented in an SRF rotating at the fundamental frequency, so that they regulate simultaneously a negative-sequence current harmonic of the form $6k-1$ and a positive-sequence one of the form $6k+1$ [3, 4, 7, 142, 143, 148, 160, 171, 172]. Thus, a single resonant filter is able to control two harmonic components, reducing the computational resources needed [171, 172]. This strategy can be adopted with both PR and VPI controllers [3, 4, 7, 142, 143, 148, 160, 171].

1.3 Major Results

The work in this dissertation is divided into four main chapters, which are followed by a fifth one that summarizes the conclusions and two appendices. While chapters §2 and §3 address the estimation of plant parameters, chapters §4 and §5 are focused on controller tuning.

Chapter 2: "Equivalent Loss Resistance Estimation of Grid-Tied Converters for Current Control Analysis and Design"

This chapter proposes a method to identify the VSC equivalent loss resistance in specific working conditions. This resistance reflects the influence of the power losses on the plant model and its estimation is essential to accurately analyze and design the current control loop. The developed estimation technique is based on the iterative evaluation of the closed-loop transient responses obtained with two different control loops: one with the actual plant and another one with a model. Regarding the implementation of the developed method, two options are possible: online or offline. Experimental results allow to identify the corresponding equivalent loss resistance of a three-phase grid-tied VSC working at different switching frequencies and power ratings.

Chapter 3: "A Method for Identification of the Equivalent Inductance and Resistance in the Plant Model of Current-Controlled Grid-Tied Converters"

In this chapter, a method to identify both the equivalent inductance and resistance in the plant model of the current loop is presented. Having reliable estimates of both parameters allows for an accurate analysis of the current loop dynamics, as well as for a precise tuning of the controller parameters. The proposed technique, which is an improvement of that in chapter §2, is also an iterative algorithm that minimizes the difference between the step responses obtained with two distinct current closed loops. It can either work online or offline. The corresponding inductance and resistance of a three-phase grid-tied VSC working at different switching frequencies and power ratings, with L and LCL filters, have been experimentally identified.

Chapter 4: "Assessment and Optimization of the Transient Response of Proportional-Resonant Current Controllers for Distributed Power Generation Systems"

In this chapter, a methodology to assess and optimize the transient response of PR current controllers is developed, which is based on the study of the error signal transfer function roots by means of root loci. The proposed controller tuning aims at minimizing the postfault and reference tracking settling times, so that power electronics converters in DPGSs can fulfill the most demanding GC requirements. The need of a tradeoff between reference and disturbance transients is identified. Experimental results obtained with a three-phase VSC prototype validate the approach.

Chapter 5: "Transient Response Evaluation of Stationary-Frame Resonant Current Controllers for Grid-Connected Applications"

This chapter presents a study about the convenience of employing VPI controllers in grid-tied applications. Their transient responses for reference tracking and disturbance rejection, which are assessed by the corresponding error signal roots, are compared with those obtained with the PR controller. It is demonstrated that at high sampling frequencies, the behavior of the PR controller is clearly superior. In the presence of both reference and disturbance changes, shorter settling times and smaller overshoot are attained, whereas a lower THD is achieved in steady state. Nevertheless, as the sampling frequency decreases, both controllers present more similarities. Experimental results corroborate the theoretical analysis.

Chapter 6: "Conclusions and Future Research"

The main conclusions of this dissertation are summarized in this chapter and some recommendations for future research topics are provided.

Appendix A: "Study of the Disturbance Rejection Capability of the Harmonics Caused by Dead Times in the Experimental Results of Chapter 2"

This appendix analyzes the capability of the current closed loop to reject the fifth and the seventh harmonics caused by dead times as a function of K and the resistance mismatch, in order to theoretically justify the differences in the amplitude of these oscillations in the experimental results from chapter §2.

Appendix B: "Mathematical Development of the Error Time-Domain Expressions for Chapter 4"

This appendix exposes the analytical development of the error time-domain expressions for chapter §4.

Chapter 2

Equivalent Loss Resistance Estimation of Grid-Tied Converters for Current Control Analysis and Design

Abstract *— Rigorous analysis and design of the current control loop in voltage source converters (VSCs) requires an accurate modeling. The loop behavior can be significantly influenced by the VSC working conditions. To consider such effect, converter losses should be included in the model, which can be done by means of an equivalent series resistance. This chapter proposes a method to identify the VSC equivalent loss resistance for proper tuning of the current control loop. It is based on analysis of the closed-loop transient response provided by a synchronous proportional-integral current controller, according to the internal model principle. The method gives a set of loss resistance values linked to working conditions, which can be used to improve the tuning of the current controllers, either by online adaptation of the controller gains or by open-loop adaptive adjustment of them according to pre-stored data. The developed identification procedure is tested in the laboratory at different specifications of power level and switching frequency.*

2.1 Introduction

Pulse-width modulated voltage source converters (VSCs) are employed for grid connection in multiple applications such as active power filters [77, 79, 81], microgrids [58, 173, 174] or distributed power generation from renewable energy sources [34, 78, 100, 111, 175–177]. In all of them, L or LCL filters are usually employed to mitigate the switching harmonics [34, 78, 100, 111, 173, 174, 177]. In such applications, stringent requirements are often demanded [34, 58, 76–78, 81, 111, 173–175, 177], so the control algorithms should be accurately adjusted in order to assure their fulfillment. Special attention must be paid to the inner loop, which is usually a current one [34, 78–81, 95, 100, 174], since it establishes the performance of the overall system in terms of transient response [10, 111]. Linear plant models permit the application of well-known linear analysis and design techniques [34, 75–78, 81]. In this manner, linear first-order time-averaged models are usually chosen for the filter admittance [76, 77, 79–81]. This assumption is also suitable for LCL filters provided that their behavior is similar to that of L ones at frequencies below the LCL resonance [77, 102, 111].

On the other hand, the VSC behavior is very influenced by power losses [93, 95, 175, 178,

179], so a good model should reflect the effects associated to them. Various approaches have addressed this topic, mainly based on the inclusion of resistances in the control loop models [76, 93, 95, 178–182]; in particular, a resistance is considered in parallel with the dc-link [95, 178, 181] or in series with the filter inductance [76, 93, 95, 178–182] depending on whether the dc-link voltage or the ac current is controlled, respectively. Each combination of demanded power, output voltage or switching frequency leads to different percentages of power losses [175, 178, 179, 183, 184] and, in turn, to different values of these resistances. As a result, the working conditions of the converter are reflected on the respective plant models.

Focusing on current control, although the inclusion of an equivalent resistance in series with the filter inductance and its parasitic resistance to model the effects associated to the VSC losses is commonly accepted [76, 93, 95, 178–181], there are few works aimed at current loop analysis and design that consider it, and the available information in this sense is scarce. In some references, the fact that this equivalent loss resistance is considered is briefly mentioned and then, a value is given as part of the plant parameters without much explanation [76, 93]. At best, a set of different values is provided at different power levels for a certain converter [179]. But, at this point, there is not a clear method explaining how to quantify the VSC equivalent loss resistance.

Knowledge of the inductance value is enough to guarantee a certain bandwidth quite approximately [76]. However, when specifications are given in terms of transient response (e.g., settling time and overshoot), an accurate estimation of the time constant, i.e., inductance and resistance, is essential [10, 80, 119]. It is also worth noting that knowing the resistance value permits to improve the disturbance rejection capability by means of the "active resistance" technique without altering the command tracking response [10, 154]. As shown in this chapter, the value of the converter equivalent loss resistance may be very significant depending on the working conditions. At light load and high switching frequencies, in our experimental setup, values as high as $4-10$ times the filter resistance are obtained. Thus, an erroneous estimation (or its omission) implies the utilization of certain controller gains that alter the time-domain response of the current control closed loop with respect to that expected from its theoretical design (e.g., different settling time and overshoot). Therefore, it is interesting to have a method to identify the VSC equivalent loss resistance, so that the actual current dynamics may be properly studied and the controller parameters can be precisely tuned.

Assuming the commonly-accepted low-order time-averaged plant model of the current loop [10, 76, 77, 79–81, 95, 140, 141], and including the converter equivalent resistance in it [76, 93, 95, 180, 181], a method is developed in this chapter to identify the VSC equivalent loss resistance in each specific working condition for current control design. The proposal has its basis on model reference adaptive systems (MRASs) [123], which have become really popular in drives applications to estimate, for example, the stator resistance value [130–136, 185]. The MRAS-based method developed in this chapter exploits the properties of the current closed-loop transient response that is obtained by implementing a synchronous PI controller with state-feedback cross-coupling decoupling (PICCD) [10, 34, 58, 78, 140, 141, 154], considering the internal model control (IMC) principle [10, 141]. It is an iterative algorithm that minimizes the error between the closed-loop step responses obtained with the real plant and with the plant model. Root-locus diagrams are analyzed to introduce the basis and to support the procedure. Regarding the implementation of the identified information, two options are possible: online or offline. The advantages and drawbacks of both alternatives, as well as the limitations of each one with the developed procedure, are discussed.

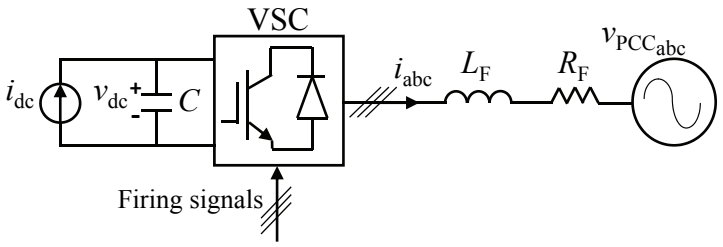

Figure 2.1: Scheme of a grid-connected VSC.

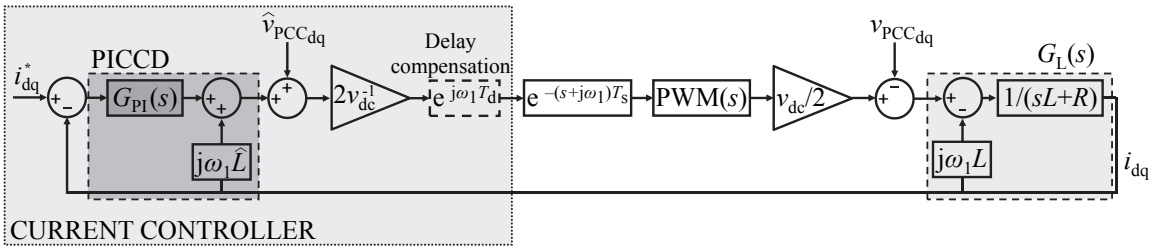

(a) In complete form and in the s-domain.

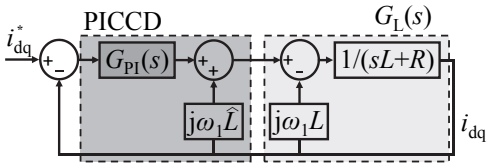

(b) In simplified form, neglecting the 1.5 sample delay and in the s-domain.

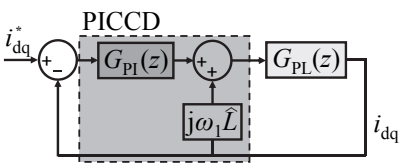

(c) In simplified form, including the 1.5 sample delay and in the z-domain.

Figure 2.2: Complex vector block diagrams of the current control closed loop in SRF (inverter operation).

The chapter is organized as follows. Section §2.2 reviews the current control closed-loop model. Section §2.3 introduces the theoretical basis of the proposal by means of an analysis of the influence of the total resistance in the root-locus diagrams and in the step response of the current loop. In section §2.4, the developed identification method is presented. Section §2.5 evaluates the sensitivity to the resistance estimate when a two degrees-of-freedom (2DOF) proportional-integral (PI) controller is implemented in the final application. Experimental results are provided in section §2.6. Finally, section §2.7 concludes the work.

2.2 Current Control Closed-Loop Model

Fig. 2.1 depicts a three-phase grid-connected VSC, where the voltage at the point of common coupling (PCC) and the current in phase n are denoted by v_{PCC_n} and i_n, respectively. L_F and R_F are respectively the inductance and resistance of the interface filter, while v_dc and C are respectively the dc-link voltage and capacitance. The direct current externally supplied to (or demanded from) the dc-link is represented by i_dc.

Fig. 2.2a shows the complex vector block diagram in the s-domain of the current control closed loop with respect to a synchronous reference frame (SRF) rotating at the fundamental frequency ω_1. The subscripts dq are used for complex vector notation with respect to the d and

q axes of the SRF (i.e., $i_{\mathrm{dq}} = i_{\mathrm{d}} + \mathrm{j}i_{\mathrm{q}}$ and $v_{\mathrm{PCC_{dq}}} = v_{\mathrm{PCC_d}} + \mathrm{j}v_{\mathrm{PCC_q}}$), an asterisk denotes reference signals and a hat is used for the estimated and measured values. The VSC introduces a gain equal to half v_{dc}, which is compensated by multiplying the output of the current controller by the inverse. A time delay $T_{\mathrm{d}} = 1.5T_{\mathrm{s}}$ in the stationary frame is considered [76, 80]. The computational delay (i.e., a delay of one sample [76, 80]) is represented in the SRF as $\mathrm{e}^{-(s+\mathrm{j}\omega_1)T_{\mathrm{s}}}$, with T_{s} being the sampling period, while a zero-order hold (ZOH) is used to model the regularly sampled pulse-width modulation (PWM), which introduces half a sample delay [76, 80]. A delay compensation term $\mathrm{e}^{\mathrm{j}\omega_1 T_{\mathrm{d}}}$ may be introduced in the control loop to cancel the phase lag caused by the delay at dc in the SRF (see the block with dashed lines in the center of Fig. 2.2a) [10]. The plant admittance is modeled in the SRF as [10, 81, 140]

$$G_{\mathrm{L}}(s) = \frac{1}{sL + R + \mathrm{j}\omega_1 L}. \tag{2.1}$$

Apart from R_{F}, the equivalent loss resistance of the converter R_{C} can also be included in R, i.e., $R = R_{\mathrm{F}} + R_{\mathrm{C}}$ [76, 93, 95, 180, 181]. The resistance and the inductance of the feeder cables are neglected.

It is worth mentioning that, as all the transfer functions defined along this chapter are expressed with respect to the SRF, subscripts dq are omitted for the sake of clarity, e.g., $G_{\mathrm{L}}(s)$ is adopted, instead of $G_{\mathrm{L_{dq}}}(s)$, which was employed in the introduction (cf. chapter §1).

A synchronous PI controller is used to regulate the current [10, 34, 81, 140, 154]:

$$G_{\mathrm{PI}}(s) = K_{\mathrm{P}} + \frac{K_{\mathrm{I}}}{s} \tag{2.2}$$

with K_{P} and K_{I} being the proportional and integral gains, respectively. To enhance the transient behavior, which degrades as ω_1 becomes greater due to the cross coupling between the d and q axes in (2.1) [10, 140, 141], a current feedback with a gain $\mathrm{j}\omega_1\widehat{L}$ is added to the controller output (cf. Fig. 2.2a). This modified PI controller is very popular and is often known as PICCD [10, 34, 58, 78, 140, 141, 154].

Since $v_{\mathrm{PCC_{dq}}}$ acts as a disturbance in the control loop, it can be measured ($\widehat{v}_{\mathrm{PCC_{dq}}}$) and fedforward in order to improve the transient behavior [34]. Making the assumption of perfect cancellation between each other, and neglecting the delay, Fig. 2.2a can be simplified, giving rise to Fig. 2.2b.

On the other hand, Fig. 2.2c illustrates the block diagram in the z-domain. The discretization of (2.1) with the ZOH method and the multiplication of the result by $z^{-1}\mathrm{e}^{-\mathrm{j}\omega_1 T_{\mathrm{s}}}$ permits to include in the plant expression in the SRF the delay of 1.5 samples:

$$G_{\mathrm{PL}}(z) = \frac{z^{-2}}{R}\,\frac{(1-\rho^{-1})\mathrm{e}^{-2\mathrm{j}\omega_1 T_{\mathrm{s}}}}{1 - z^{-1}\rho^{-1}\mathrm{e}^{-\mathrm{j}\omega_1 T_{\mathrm{s}}}} \tag{2.3}$$

where $\rho = \mathrm{e}^{RT_{\mathrm{s}}/L}$. $G_{\mathrm{PI}}(z)$ has been obtained by applying the Tustin transform to $G_{\mathrm{PI}}(s)$ following the indications in [79].

2.3 Theoretical Basis: Analysis of the Current Control Closed-Loop Step Response

Prior to the explanation of the proposed method, an analysis of the current control closed loop is conducted. In order to simplify the study, in sections §2.3.1 and §2.3.2, the time delay

is firstly neglected (cf. Fig. 2.2b), but it will be considered (cf. Fig. 2.2c) from section §2.3.3 until the end of the chapter.

2.3.1 Open-Loop Transfer Function in the Continuous Domain

Owing to the cancellation between the imaginary terms of $G_{\mathrm{L}}(s)$ and the PICCD in Fig. 2.2b, the open-loop transfer function of the current control loop is as follows:

$$G_{\mathrm{OL}}(s) = G_{\mathrm{PI}}(s)\,\frac{1}{sL+R} = \frac{sK_{\mathrm{P}}+K_{\mathrm{I}}}{s}\,\frac{1}{sL+R}. \tag{2.4}$$

According to the IMC principle, the PI controller gains are selected as $K_{\mathrm{P}}/K_{\mathrm{I}} = \widehat{L}/\widehat{R}$ and $K_{\mathrm{P}} = K\widehat{L}$ [10, 141], so that the plant pole is directly canceled by the real zero of the PI controller in SRF, provided that the estimated plant parameters ($\widehat{L}$ and $\widehat{R}$) match the real ones (L and R) [10, 81, 140, 141]. In this manner, the open-loop transfer function $G_{\mathrm{OL}}(s)$ can be simplified as [10, 141]

$$G'_{\mathrm{OL}}(s) = K\,\frac{1}{s}. \tag{2.5}$$

It can be observed that $G'_{\mathrm{OL}}(s)$ does not depend on the plant parameters, although they need to be known. Moreover, it has only one open-loop pole $p_1^{\mathrm{ol}} = 0$ and one closed-loop pole $p_1^{\mathrm{cl}} = -K$. In this situation, the closed-loop response to a step in the current reference i^* is an exponential function [75, 140]. Note that K becomes equal to the closed-loop bandwidth in $\mathrm{rad/s}$ [10, 141, 154].

Nevertheless, when the plant parameter estimates are wrong, i.e., $\widehat{L} \neq L$ or $\widehat{R} \neq R$, $G_{\mathrm{OL}}(s)$ cannot be simplified, leading to

$$G''_{\mathrm{OL}}(s) = K\,\frac{s\widehat{L}+\widehat{R}}{s}\,\frac{1}{sL+R}. \tag{2.6}$$

$G''_{\mathrm{OL}}(s)$ has one zero z_1, two open-loop poles p_1^{ol} and p_2^{ol} and two closed-loop poles p_1^{cl} and p_2^{cl}:

$$\begin{aligned} &z_1 = -\widehat{R}/\widehat{L}; \qquad p_1^{\mathrm{ol}} = 0; \qquad p_2^{\mathrm{ol}} = -R/L; \\ &p_{1,2}^{\mathrm{cl}} = \frac{-(R+K\widehat{L}) \pm \sqrt{(R+K\widehat{L})^2 - 4KL\widehat{R}}}{2L}. \end{aligned} \tag{2.7}$$

In this case, given that the number of poles is bigger than one, the closed-loop response to a step in i^* may be a double exponential function or the product of exponential and trigonometric functions, depending on whether both poles are real or complex [75].

Initially, L is assumed constant and equal to the filter inductance value that is measured offline (i.e., $\widehat{L} = L = L_{\mathrm{F}}$), as done in many other works [131–133, 136]. On the contrary, R strongly depends on the VSC losses [76, 93, 95, 178–181], so it should be identified (i.e., to find $\widehat{R} = R = R_{\mathrm{F}} + R_{\mathrm{C}}$), which is the purpose of this chapter.

2.3.2 Root-Locus Diagrams in the Continuous Domain

To facilitate the understanding of the previous subsection, as well as to link it to R_{C} identification, the complex vector root loci of the current control closed loop (in SRF, in the s-domain

and neglecting the delay, as in section §2.3.1) are studied in the following for three different situations.

The diagrams in Fig. 2.3 have been obtained using the parameters of the main case analyzed in the experimental setup section (cf. case A in Table 2.4 and $\omega_1 = 2\pi 50\,\mathrm{rad/s}$). Note that $R_C = 1.9\,\Omega$ is determined in the experiments (cf. section §2.6) as a result of the estimation process, so it is an unknown variable for the control designer when selecting the PICCD parameters (i.e., $\widehat{R}$, L and K); such $R_C = 1.9\,\Omega$ value is simply used here to generate the root-locus diagrams in order to study the different possibilities that may occur in reality depending on the current control parameters.

Under these circumstances, three different relations between $\widehat{R}$ and R are analyzed.

a) Underestimate of R, in Fig. 2.3a, considering it equal to R_F and neglecting R_C ($\widehat{R} = R_F = 0.4\,\Omega < R = 2.3\,\Omega$).

b) Correct identification of R, in Fig. 2.3b ($\widehat{R} = R = 2.3\,\Omega$).

c) Overestimate of R, in Fig. 2.3c ($\widehat{R} = 3\,\Omega > R = 2.3\,\Omega$).

From Figs. 2.3a, b and c, it can be checked how z_1 moves depending on the relation between $\widehat{R}$ and R, and how this affects the position of the closed-loop poles. The closed-loop poles corresponding to three representative K values ($0.4/L$ in red, $2.3/L$ in dark gray and $3/L$ in green) have been depicted, i.e., $K = \widehat{R}/L$ in each of the three cases. Further explanation for selecting these particular gains will be given in section §2.4. When $\widehat{R} = R_F < R$ (cf. Fig. 2.3a), there are two closed-loop poles that move along the real axis as K increases: p_1^{cl} moves towards z_1 and p_2^{cl} tends to negative infinity. As the estimate approaches the actual value, z_1 gets closer to p_2^{ol}, until achieving perfect cancellation at $\widehat{R} = R$, i.e., when R_C is correctly identified (cf. Fig. 2.3b). In this case, there is only one closed-loop pole p_1^{cl}, which is simply equal to the gain K [cf. (2.5)]. If R is overestimated (cf. Fig. 2.3c), p_1^{cl} and p_2^{cl} become complex for $K \in (K_{\gamma 1}, K_{\gamma 2})$, where

$$K_{\gamma 1,\gamma 2} = \frac{(2\widehat{R} - R) \mp 2\sqrt{\widehat{R}^2 - R\widehat{R}}}{L}. \tag{2.8}$$

Moreover, in this situation, p_1^{cl} and p_2^{cl} move along a circumference with radius rd and center ct:

$$rd = \frac{\sqrt{\widehat{R}^2 - R\widehat{R}}}{L}; \qquad ct = z_1 = -\frac{\widehat{R}}{L}. \tag{2.9}$$

In this manner, in situations a) and c), unlike in b), the dynamics differs from that expected from the design based on the IMC principle.

2.3.3 Current Step Response in the Discrete-Time Domain

This section studies the influence of the accuracy in R identification on the transient response. A step of amplitude I_{AMP} in the q-axis current reference i_q^* is commanded to the system described in Fig. 2.2c, i.e., this analysis considers the time delay, while i_d^* remains constant:

$$I_{dq}^*(z) = I_d^*(z) + \mathrm{j} I_{AMP} \frac{1}{1 - z^{-1}} \tag{2.10}$$

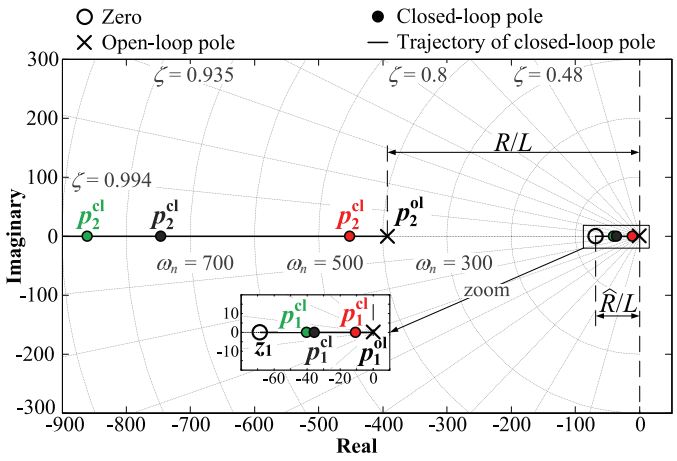

(a) $\widehat{R} = R_{\mathrm{F}} < R$.

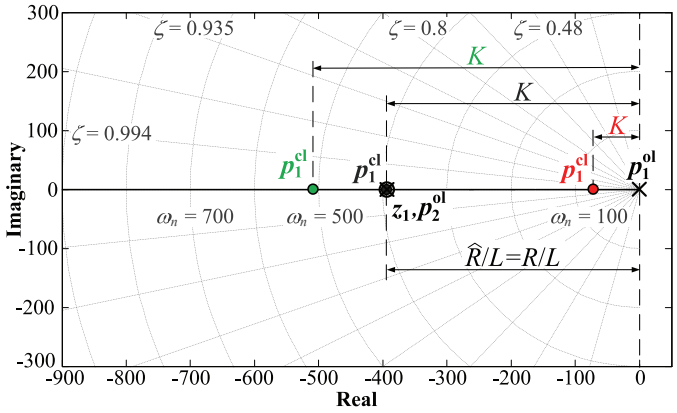

(b) $\widehat{R} = R$.

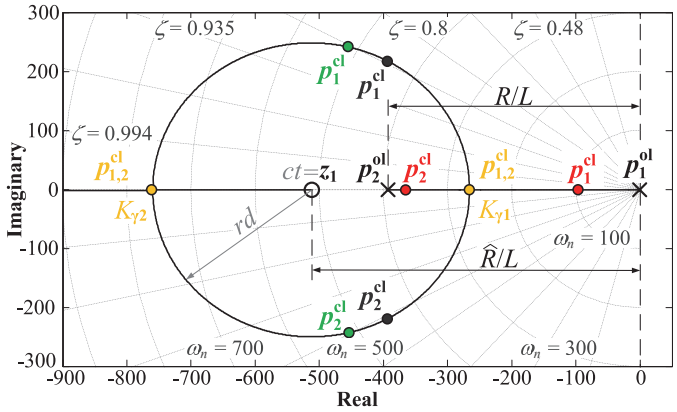

(c) $\widehat{R} > R$.

Figure 2.3: Root-locus diagrams of the current control loop with respect to the SRF and in the s-domain. Closed-loop poles in red are placed at $K = 0.4/L$; in dark gray, at $K = 2.3/L$ and in green, at $K = 3/L$. Additional closed-loop poles in orange are placed at $K_{\gamma 1}$ and $K_{\gamma 2}$ in (c).

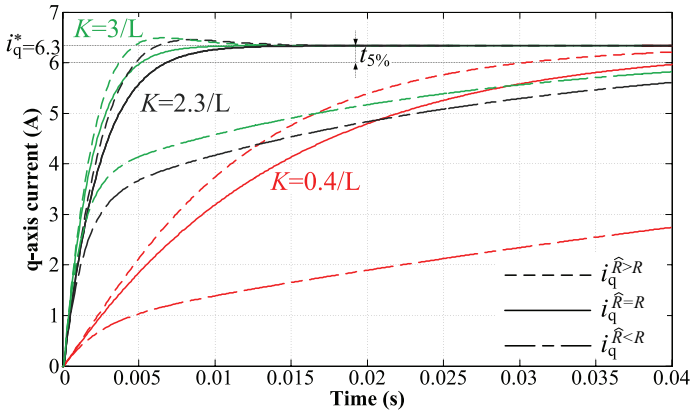

Figure 2.4: Step response of i_q. Effect of different values of K for $\widehat{R} = R_\mathrm{F} < R$, $\widehat{R} = R$ and $\widehat{R} > R$.

A sampling frequency $f_\mathrm{s} = 1/T_\mathrm{s}$ of 10 kHz is employed. The time-domain response of the current $i_\mathrm{q}(t)$ at each instant $t = \lambda T_\mathrm{s}$ ($\lambda \in \mathbb{N}$) to the step $I^*_\mathrm{q}(z)$ is

$$i_\mathrm{q}(t) = \mathfrak{Im}\left\{ \mathcal{Z}^{-1}\left[I^*_\mathrm{dq}(z) \underbrace{\frac{G_\mathrm{PI}(z)G_\mathrm{PL}(z)}{1+(G_\mathrm{PI}(z)-\mathrm{j}\omega_1\widehat{L})G_\mathrm{PL}(z)}}_{G_\mathrm{CL}(z)} \right] \right\} \tag{2.11}$$

where $G_\mathrm{CL}(z)$ is the closed-loop transfer function of the current loop in the z-domain.

The response to a step of $I_\mathrm{AMP} = 6.3\,\mathrm{A}$ (cf. case A in section §2.6) is evaluated for the same three $\widehat{R}$ cases as in the previous subsection. The results are shown in Fig. 2.4: the current response when R is underestimated $i_\mathrm{q}^{\widehat{R}<R}$, with a dashed line with unequal segments; the current response when R is correctly identified $i_\mathrm{q}^{\widehat{R}=R}$, with a continuous line, and the current response when R is overestimated $i_\mathrm{q}^{\widehat{R}>R}$, with a dashed line. Besides, the same K values ($0.4/L$ in red, $2.3/L$ in dark gray and $3/L$ in green) are considered. The resulting curves are in agreement with the root-locus diagrams in Fig. 2.3, as described in the following.

In the case that $\widehat{R} = R_\mathrm{F} < R$, the global step response $i_\mathrm{q}^{\widehat{R}<R}$ is the addition of two exponential curves, one that decays slower and another one that decays faster (caused by the two real closed-loop poles p_1^cl and p_2^cl, respectively). The overshoot is null, since there are no complex poles.

When R is correctly identified, the step response $i_\mathrm{q}^{\widehat{R}=R}$ is an exponential curve [there is a single real pole, cf. (2.5)]. The overshoot is null and the settling time $t_{5\%}$ is inversely proportional to K; a tolerance band of 5% is defined, which leads to $t_{5\%} = -\ln|0.05|/K$ [75]. For a given K, $t_{5\%}$ is significantly shorter than in the case of $\widehat{R} < R$.

In the case that $\widehat{R} > R$, for $K < K_{\gamma 1}$ (e.g., $K = 0.4/L < K_{\gamma 1}$ [cf. (2.8)]), the response $i_\mathrm{q}^{\widehat{R}>R}$ is similar to the case of $\widehat{R} < R$, but with a shorter $t_{5\%}$ (even shorter than in the case of $\widehat{R} = R$). On the contrary, from $K = K_{\gamma 1}$ to $K = K_{\gamma 2}$ (e.g., $K = 2.3/L$ and $K = 3/L$), ripple is superimposed to the exponential response (p_1^cl and p_2^cl are complex, so they excite different frequencies). As a consequence, for $\widehat{R} > R$ and $K_{\gamma 1} < K < K_{\gamma 2}$, there is certain overshoot. Besides, for these particular parameter values, $t_{5\%}$ is slightly shorter than for the case of $\widehat{R} = R$, but this may differ depending on the chosen tolerance band for the settling time. In any case, the rise time [75] is shorter for any L, R and $K \in (K_{\gamma 1}, K_{\gamma 2})$, provided that $\widehat{R} > R$.

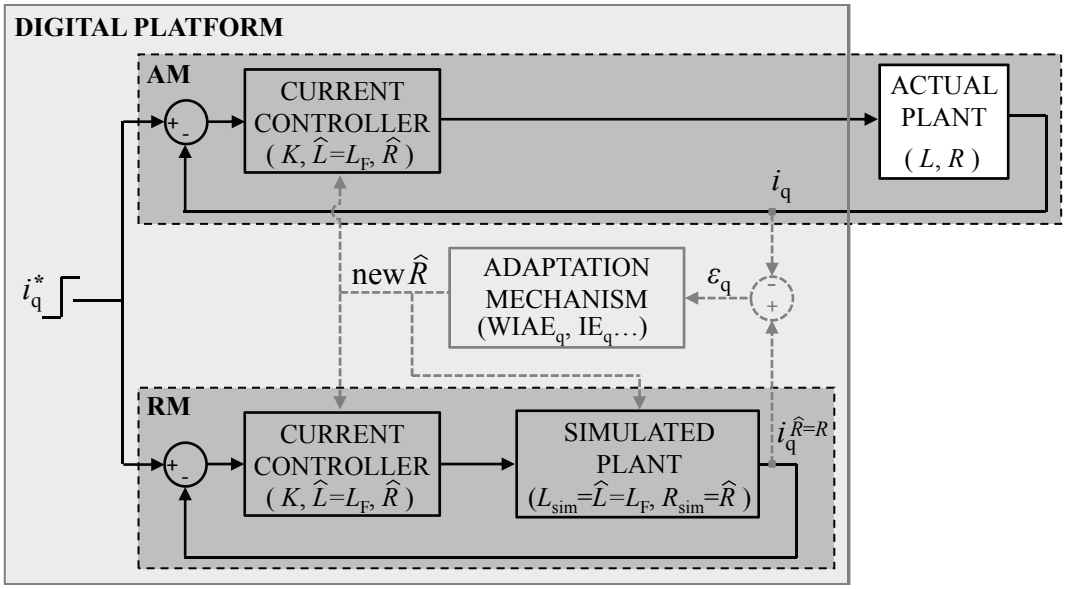

Figure 2.5: Block diagram of the proposed identification algorithm implementation, where the current control closed loop with the real plant (AM) and the one with the simulated plant (RM) are shown.

2.4 Developed Identification Method of the VSC Equivalent Loss Resistance

From the observations in the previous section, it can be concluded that the correct estimation of R, and consequently, of R_C, influences the transient behavior of the current loop, so a step test can be used to identify R. Based on these features, the developed MRAS-based identification method is presented in this section. Firstly, a brief overview of the classic MRAS technique, its applications and general information about the proposed scheme can be found in section §2.4.1. After that, section §2.4.2 describes in detail the developed technique. With the aim of assessing its estimation error and the speed of convergence, some other theoretical examples are included in section §2.4.3. Finally, implementation options are discussed in section §2.4.4, while section §2.4.5 studies the effect of uncertainties in $\widehat{L}$ on the resistance estimate.

2.4.1 Modifications of Previous MRAS Methods

As reported in section §1.2.6.2, classical MRAS techniques are founded on the premise that one variable in the model that is related to the parameter to be estimated can be calculated in two different ways: by means of an RM, in which the value of the parameter to be estimated does not need to be introduced by the designer, and by means of an AM, in whose equations it does [123, 130] (cf. Fig. 1.7). The error between the output of both models is employed to drive an adaptation mechanism that updates the AM and converges to zero as the estimated value of the parameter approaches the real one [123, 130–132].

The use of MRAS techniques to estimate the stator resistance in industrial drives, which shows certain similarities to the reported case of grid-connection in terms of plant model, has attracted much attention during the last years [130–136, 185]. In these proposals, the basic

scheme in Fig. 1.7 is adapted to each application and specifications: to the improvement of the behavior of the speed observer for sensorless control [130, 131, 133, 185], to condition monitoring [132, 134], or to precise current loop design [135, 136].

In this chapter, an MRAS-based adaptive control system in closed loop is proposed as a tool for identification of the VSC equivalent loss resistance. The block diagram in Fig. 2.5 presents the global structure of the developed estimator: AM, RM and adaptation mechanism, as well as the parameters involved in each block. Such identification is oriented to the design of the transient response of the current control closed loop. In this manner, the correct identification of R_C, which is achieved when the error signal between both models converges to zero (see Fig. 2.5), permits the real plant to obtain the desired closed-loop transient response, which is given by the RM. Since the accuracy of MRAS algorithms relies on that of the model [123], the basic MRAS structure has been modified in this chapter to consider the current closed-loop system, which includes controller, delays, converter and filter admittance, for both the AM and RM (cf. Fig. 2.5), so that the VSC equivalent loss resistance can be accurately identified. Thus, the model that contains the simulated plant (in this case, the RM) reproduces the behavior of the whole closed loop, instead of that of the filter admittance in isolation. Therefore, given that it is the closed-loop output the one that has to meet the transient constraints (e.g., settling time and overshoot), it can be said that the proposed MRAS structure is directly oriented to the fulfillment of time-domain specifications. All these aspects lead to an accurate estimation of the parameter values for the specific working conditions. It is worth mentioning that a current closed loop (different from the one in this chapter) has also been considered for both the AM and RM in [100], but in that work the effects associated to the VSC losses are not regarded, and it is oriented to an entirely different objective: to guarantee the damping of the LCL filter resonance in the presence of grid impedance variations.

2.4.2 Steps of the Developed Identification Method

The proposed iterative method is summarized in the steps below. The explanation is supported by a flowchart of the iterative process (cf. Fig. 2.6). The iteration number is denoted by k. In addition, an example of application of the proposed algorithm to case A of the experimental results, which is the same case that was considered in the previous section, is shown in Fig. 2.7.

Step 0) The controller parameters are set in both the AM and RM. $\widehat{L}$ and $\widehat{R}$ are chosen equal to the measured values of the interface filter, i.e., $\widehat{L} = L_F$, $\widehat{R}(1) = R_F$. In addition, the auxiliary boolean variable ***R_low_bound*** is initialized. According to case A, at the first iteration: $\widehat{L} = L_F = 5.86\,\text{mH}$ and $\widehat{R}(1) = R_F = 0.4\,\Omega$.

Step 1) Regarding the gain (which is the remaining controller parameter, see section §2.3), by inspection of Fig. 2.3, (2.7) and (2.9), it can be observed that by selecting

$$K = K^{\text{met}} = -ct = -z_1 = \frac{\widehat{R}}{L} \tag{2.12}$$

$p_{1,2}^{\text{cl}}$ are complex only if $\widehat{R} > R$. In this manner, provided that $\omega_1 << 2\pi f_s$ [186] and $K << 2\pi f_s$ [10, 76], it is guaranteed that the closed-loop poles have an imaginary term, which leads to overshoot, just in the case of R overestimation. Hence, by choosing $K(k) = \widehat{R}(k)/L$, it is possible to immediately know whether the transient response corresponds to an underestimate, correct

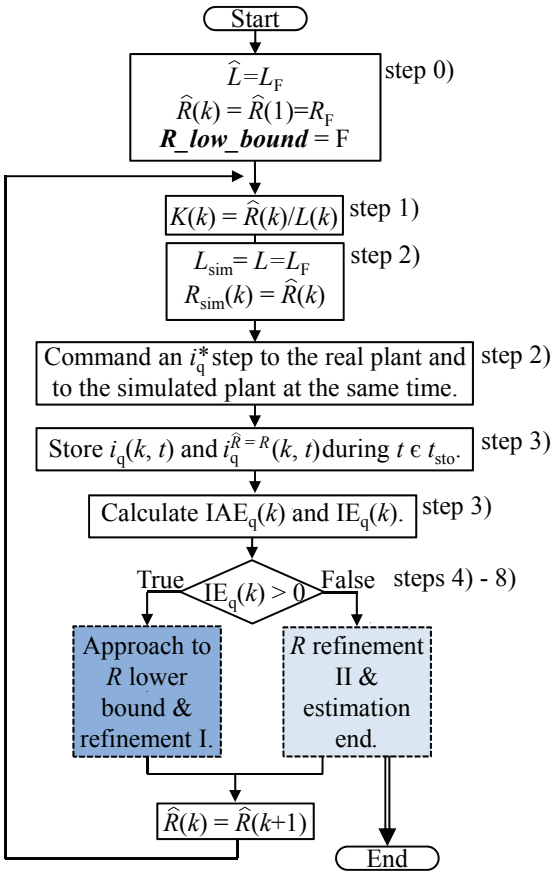

(a) Main diagram.

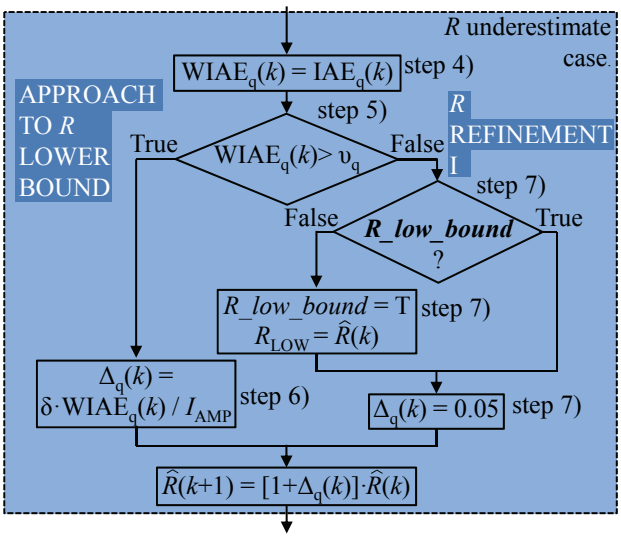

(b) Subdiagram of the underestimate case.

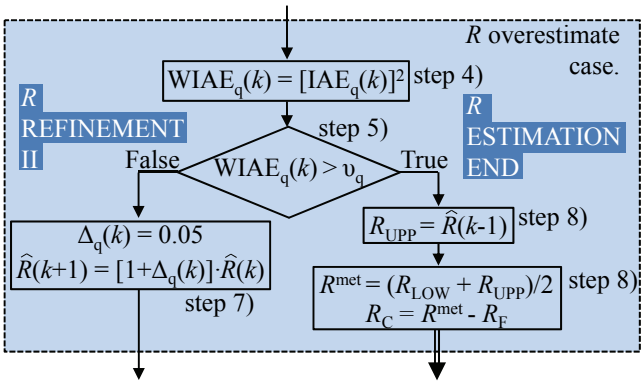

(c) Subdiagram of the overestimate case.

Figure 2.6: Flowchart of the developed identification method.

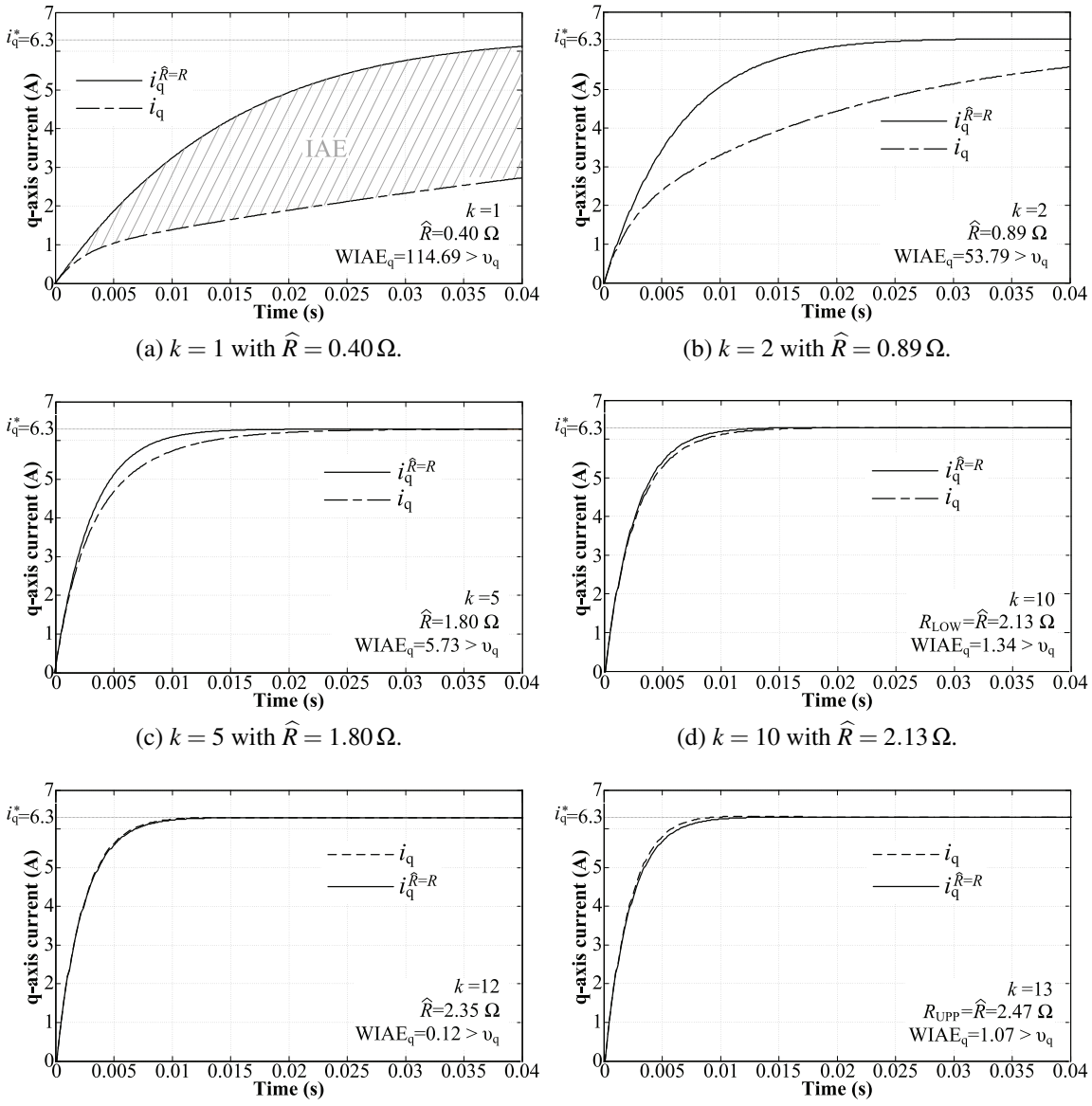

(a) $k = 1$ with $\widehat{R} = 0.40\,\Omega$.

(b) $k = 2$ with $\widehat{R} = 0.89\,\Omega$.

(c) $k = 5$ with $\widehat{R} = 1.80\,\Omega$.

(d) $k = 10$ with $\widehat{R} = 2.13\,\Omega$.

(e) $k = 12$ with $\widehat{R} = 2.35\,\Omega$.

(f) $k = 13$ with $\widehat{R} = 2.47\,\Omega$.

Figure 2.7: i_q step response for the theoretical example case A of the proposed identification method. Several iterations. The k values in each $\widehat{R}$ and in each WIAE$_q$ have been omitted for the sake of simplicity.

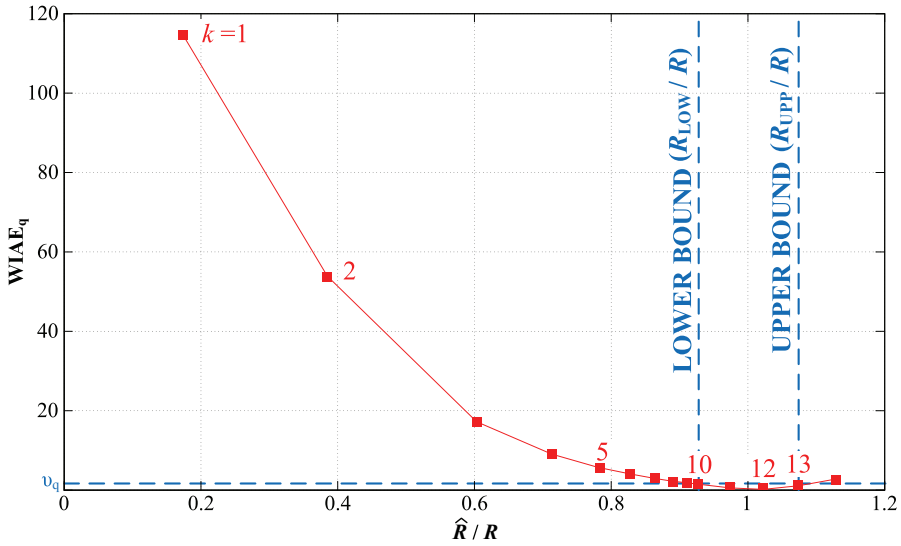

Figure 2.8: $\mathrm{WIAE_q}$ versus $\widehat{R}/R$ for the theoretical example case A of the proposed identification method. Note that the iteration number k is always increasing from left to right and only the number of those iterations that are detailed in Fig. 2.7 are indicated.

identification or overestimate of the actual resistance. Moreover, as (2.12) yields low K values, the condition $K << 2\pi f_s$ is satisfied even for relatively low sampling frequencies. It should be noted that these two assumptions ($\omega_1 << 2\pi f_s$ and $K << 2\pi f_s$) only affect the possibility of visual distinction among the three cases, but not the validity of the method, in which none of these simplifications is adopted when modeling the current loop. In the example, $K(1) = 0.4/(5.86 \cdot 10^{-3}) \approx 68$.

Step 2) A certain step response in i_q^* should be commanded to the actual converter, which is part of the AM. In the theoretical example, a step of amplitude $I_{AMP} = 6.3\,\mathrm{A}$ is ordered and the response corresponds to the dashed curve i_q in Fig. 2.7a.

At the same time, the same command i_q^* as in the actual loop is used as an input to simulate the behavior of the current control closed loop described in Fig. 2.2c, with the same controller as in the real loop, a PICCD, with the same parameters [$\widehat{L}$, $\widehat{R}(k)$ and $K(k)$], but assuming that the resistance and the inductance in the simulated plant [in the form of (2.3)] are $R_{sim}(k) = \widehat{R}(k)$ and $L_{sim} = \widehat{L} = L_F$. Thus, the simulated closed loop takes the role of RM: for each iteration k, the curve $i_q^{\widehat{R}=R}(k,t)$ is used as a target for $i_q(k,t)$. According to case A, at $k = 1$: $R_{sim}(1) = \widehat{R}(1) = R_F = 0.4\,\Omega$ and $L_{sim} = \widehat{L} = L_F = 5.86\,\mathrm{mH}$. In Fig. 2.7a, the corresponding $i_q^{\widehat{R}=R}$ is the continuous-line curve. The block diagram in Fig. 2.5 shows the simultaneous application of the same current step to both current control closed loops: the one with the actual plant (AM) and the one with the simulated plant (RM).

Step 3) The i_q and $i_q^{\widehat{R}=R}$ values are stored during the storing time $t_{sto} = t_{5\%} = -\ln|0.05|/K(1)$. In the conditions of case A, $t_{sto} \approx 44\,\mathrm{ms}$. It should be noticed that each iteration k happens every t_{sto}/T_s samples (e.g., in case A, every 440 samples). The error between both curves $\varepsilon_q(k,t) = i_q^{\widehat{R}=R}(k,t) - i_q(k,t)$ and the integral absolute error (IAE) [9, 187, 188] are computed: $\mathrm{IAE_q}(k) = \sum_{t=0}^{t_{sto}} \left|\varepsilon_q(k,t)\right| T_s$. In Fig. 2.7, the IAE corresponds to the area limited by the two curves $i_q^{\widehat{R}=R}$ and i_q (see the striped area in Fig. 2.7a). In addition, the sign of the error area is

obtained by checking whether the integral error (IE) $\mathrm{IE_q}(k) = \sum_{t=0}^{t_{\mathrm{sto}}} \varepsilon_{\mathrm{q}}(k,t) T_{\mathrm{s}}$ [10, 189] is bigger or smaller than zero.

Step 4) The main objective is the minimization of a cost function that should include information about the error in R estimation. The selected one is a modification of the IAE that attempts to weight the underestimate and overestimate cases. It should be noticed that the direct use of the IAE as the cost function could lead to a considerably higher R_{C} than the real one, since this indicator (area between $i_{\mathrm{q}}^{\widehat{R}=R}$ and i_{q}) is smaller when overestimating than when underestimating (e.g., according to case A, if $\widehat{R} = 0.8R$, $\mathrm{IAE_q} = 5.01$ Ams; however, if $\widehat{R} = 1.2R$, $\mathrm{IAE_q} = 2.23$ Ams). In this manner, the weighted IAE (WIAE) is defined as

$$\mathrm{WIAE_q}(k) = \begin{cases} \mathrm{IAE_q}(k) & \text{if} \quad \mathrm{IE_q}(k) \geq 0 \\ [\mathrm{IAE_q}(k)]^2 & \text{if} \quad \mathrm{IE_q}(k) < 0 \end{cases} \tag{2.13}$$

so a more symmetrical function with respect to the ratio $\widehat{R}/R$ is obtained (e.g., if $\widehat{R} = 0.8R$, $\mathrm{WIAE_q} = 5.01$ and if $\widehat{R} = 1.2R$, $\mathrm{WIAE_q} = 4.97$). This symmetric behavior can be observed in Fig. 2.8, which shows $\mathrm{WIAE_q}$ versus $\widehat{R}/R$ for all the iterations in case A. This graphic may also be helpful to understand all the steps of the identification process.

Step 5) Once the $\mathrm{WIAE_q}(k)$ is calculated, it should be checked whether it is smaller or larger than a threshold υ_{q}. This threshold is adjusted according to the desired resolution and to I_{AMP} (WIAE depends on the current amplitude); $\upsilon_{\mathrm{q}} = I_{\mathrm{AMP}}/4$ is recommended, based on tests performed with a wide range of inductance filter values. In the conditions of case A, $\upsilon_{\mathrm{q}} = 6.3/4 = 1.575$ is obtained; $\mathrm{WIAE_q}(1) = 114.69$.

Step 6) In the first iterations the common situation is that $\mathrm{IE_q}(k) > 0$ and $\mathrm{WIAE_q}(k) > \upsilon_{\mathrm{q}}$, since $\widehat{R}(k) << R$. In this case (labeled as "Approach to R lower bound" in Fig. 2.6b), the objective of the method is a quick reduction of the $\mathrm{WIAE_q}$ down to υ_{q}. Thus, $\widehat{R}$ for the next iteration is increased a percentage $\Delta_{\mathrm{q}}(k)$, which is calculated as a function of $\mathrm{WIAE_q}(k)$ and I_{AMP}: $\Delta_{\mathrm{q}}(k) = \delta\,\mathrm{WIAE_q}(k)/I_{\mathrm{AMP}}$, where $\delta = 1/15$. While $\mathrm{WIAE_q}(k)$ provides the new $\widehat{R}$ with information about how far its previous value was from R, I_{AMP} in the denominator permits to make the result independent from the current amplitude. Besides, the constant number 15, also in the denominator, has been chosen based on the results of tests that were made with a wide range of inductance filter values. In the theoretical example, at the first iteration (cf. Fig. 2.7a), $\mathrm{WIAE_q}(1) = 114.69 > \upsilon_{\mathrm{q}}$, so $\widehat{R}(2) = [1 + 1/(15 \cdot 6.3) \cdot 114.69] \cdot 0.4 = 0.89\,\Omega$ (cf. Fig. 2.7b); $\mathrm{WIAE_q}(2) = 53.79 > \upsilon_{\mathrm{q}}$, so $\widehat{R}(3) = 1.39\,\Omega$. In Fig. 2.7c, another iteration ($k = 5$) that exemplifies the approach to R lower bound is depicted.

Next, the process should be repeated from step 1).

Step 7) When $\mathrm{WIAE_q}(k) < \upsilon_{\mathrm{q}}$ [still $\mathrm{IE_q}(k) > 0$, i.e., this case corresponds to the path labeled as "R refinement I" in Fig. 2.6b], an underestimated value of R that leads to a resolution better than υ_{q} is obtained. The value of $\widehat{R}(k)$ in the first iteration at which this condition is verified is stored in R_{LOW} (subscript LOW refers to the lower bound in the identification process) and the refinement stage starts. $\widehat{R}(k+1)$ is increased a fixed percentage [in this case a 5% of $\widehat{R}(k)$]. In the example, this happens at $k = 10$ (cf. Fig. 2.7d), where $\mathrm{WIAE_q}(10) = 1.34 < \upsilon_{\mathrm{q}}$ and $R_{\mathrm{LOW}} = 2.13\,\Omega$, so $\widehat{R}(11) = 1.05\widehat{R}(10) = 2.24\,\Omega$.

Next, the process should be repeated from step 1), no matter the sign of $\mathrm{IE_q}(k)$. The new aim is to find R_{UPP} (subscript UPP refers to the upper bound), i.e., the overestimated value of R that

corresponds to a resolution better than υ_q. Therefore, at a certain k, $\mathrm{IE_q}(k) < 0$, so the refinement stage will be the one in Fig. 2.6c, instead of the one in Fig. 2.6b. An example of this case is represented in Fig. 2.7e, where $\mathrm{WIAE_q}(12) = 0.12 < \upsilon_q$, so $\widehat{R}(13) = 1.05\widehat{R}(12) = 2.47\,\Omega$.

Step 8) When $\mathrm{WIAE_q}(k) > \upsilon_q$ and $\mathrm{IE_q}(k) < 0$, the refinement stage ends. The value of $\widehat{R}(k-1)$ is stored in R_{UPP}. Then, $R_{\mathrm{C}}^{\mathrm{met}} = R^{\mathrm{met}} - R_{\mathrm{F}}$ is identified, with R^{met} being the average value of R_{LOW} and R_{UPP}, and the estimation process ends. According to case A, $\mathrm{WIAE_q}(14) = 2.61 > \upsilon_q$, so $R_{\mathrm{UPP}} = \widehat{R}(13) = 2.47\,\Omega$ (cf. Fig. 2.7f). Thus, $R^{\mathrm{met}} = (2.13 + 2.47)/2 = 2.30\,\Omega$ and $R_{\mathrm{C}}^{\mathrm{met}} = 2.30 - 0.4 = 1.90\,\Omega$.

2.4.3 Other Theoretical Examples

An evaluation of the estimation error and the speed of convergence is presented in Table 2.1. For this purpose, the developed method has been applied to different theoretical examples, with a wide range of values of rated power P_{rated}, rated line-to-line voltage $V_{\mathrm{LL_{rated}}}$, L_{F}, R_{F}, power level P_{level}, switching frequency f_{sw}, i_{q}^{*} and R_{C}, for both L and LCL filters. In case of the latter, the parameters L_{F} and R_{F} have been calculated as the addition of the corresponding ones of the grid- and converter-side inductors. The capacitor value has been selected so that the resonant frequency is $f_{\mathrm{s}}/8$ and a damping resistor of 0.28 per-unity (p.u.) has been added in series with it to guarantee the system stability [78, 102, 104]. As it can be checked in the table, for all the cases, either when an L or an LCL filter is employed to mitigate the switching harmonics, the equivalent loss resistance obtained with the method $R_{\mathrm{C}}^{\mathrm{met}}$ matches quite well R_{C}, in few iterations ($k_{\max}$ represents the number of iterations that are needed). Moreover, the results obtained with the L filters are identical to the ones with the LCL filters, except for some slight differences in the first of the cases (see the first two rows in Table 2.1). These observations are in agreement with the common assumption that an LCL filter can be usually modeled as an L one below the resonant frequency [77, 102, 111]. Those small differences in the first case can be expected, given that it is the most critical example (it has very low f_{sw}, f_{s} and resonant frequency).

2.4.4 Implementation Options

Regarding the implementation of the proposed identification method, two main options are possible: online and offline.

a) The developed algorithm can be understood as a tool for both closed-loop estimation and online tuning of the parameters K and $\widehat{R}$, the latter of which permits to transform (2.4) into (2.5), once the estimation process is completed. In that moment, the current controller is ready to work in normal operation, so K [the remaining parameter in (2.5)] could be modified according to different criteria from the one in this chapter, e.g., to minimize the settling time and overshoot with the simple equation proposed in [10]. Every time a certain condition is met, as, e.g., the command or detection of a load change, the estimation algorithm is reset to obtain the new resistance value. It should be noticed that this option is only valid in the case that a PICCD scheme as the one employed for the estimation is a suitable controller to meet the specifications of the application.

Table 2.1: Theoretical Examples of Application of the Proposed Method

P_{rated} ($V_{\text{LL}_{\text{rated}}}$)	L_{F}	R_{F}	P_{level} ($P_{\text{level}}/P_{\text{rated}}$)	f_{sw}	i_{q}^{*}	R_{C}	L		LCL	
							$R_{\text{C}}^{\text{met}}$	k_{max}	$R_{\text{C}}^{\text{met}}$	k_{max}
6 MW (3.3 kV)	2.08 mH	0.013 Ω	6 MW (100%)	1.05 kHz	1485 A	0.09 Ω	0.10 Ω	15	0.12 Ω	10
			1.5 MW (25%)	1.05 kHz	370 A	0.29 Ω	0.29 Ω	10	0.31 Ω	14
600 kW (690 V)	0.4 mH	0.01 Ω	500 kW (83%)	2.5 kHz	341 A	0.25 Ω	0.24 Ω	16	0.24 Ω	16
			500 kW (83%)	1.5 kHz	341 A	0.19 Ω	0.19 Ω	15	0.19 Ω	15
11 kW (400 V)	2.75 mH	0.12 Ω	9 kW (82%)	8 kHz	20 A	0.33 Ω	0.32 Ω	8	0.32 Ω	8
			4.9 kW (45%)	8 kHz	10 A	0.88 Ω	0.87 Ω	13	0.87 Ω	13
			4.9 kW (45%)	5 kHz	10 A	0.48 Ω	0.47 Ω	10	0.47 Ω	10
4.1 kW (400 V)	5 mH	0.11 Ω	3.9 kW (95%)	5 kHz	8 A	0.29 Ω	0.28 Ω	9	0.28 Ω	9
			2.4 kW (59%)	5 kHz	5 A	0.79 Ω	0.78 Ω	11	0.78 Ω	11

b) The developed algorithm is just a tool for closed-loop estimation, during a precommissioning stage. Thus, tuning and parameter adaptation of the controller that will be used in the final application have to be completed in other two different stages.

- First of all, in the case of a converter that works at different power levels, the VSC equivalent resistance should be identified for each condition following the proposed method. The different R_C values (as many as desired), each of them linked to the corresponding power level, should be stored in a table.
- Secondly, the information in the table should be employed to tune the current controller selected for the final application (which can be different from the one employed during the estimation), according to the constraints and objectives of each application [chapters §4 and §5] and [34, 76]. It should be remarked that most of the available methods for tuning of the current controller parameters need the inductance and the total resistance values [9, 76, 77, 81, 93, 100, 135, 140, 141]. Once the suitable gains are obtained for the different power levels, the table should be completed with them.
- Finally, an open-loop adaptive control should be implemented to update in real time the parameters of the controller used during normal operation as a function of the working conditions according to the lookup table, which works as the adaptation mechanism. This kind of algorithm is usually known as "gain-scheduling" technique [123–125]. One of the most challenging aspects of implementing a "gain-scheduling" scheme is to find a suitable relationship between environment measurements and controller parameters [123]. However, this is exactly what the systematic method proposed in this chapter does.
- Note that the accuracy of the R estimate provided by the proposed identification method is independent from the type of controller implemented in the final application, but some control alternatives may be more sensitive than others to R uncertainties. For instance, the case of the 2DOF PI controller, which also includes an "active resistance" [10, 92, 154, 190, 191], will be theoretically studied in section §2.5.

By comparing both options of implementation, it is worth noting that the second one permits to choose the most suitable current controller for each application (e.g., in case of voltage imbalance, a controller able to regulate the current negative sequence is preferred [chapters §4 and §5] and [9]). Moreover, the use of lookup tables allows a reduction in the number of operations of the final algorithm with respect to that of the first option [192]. Nevertheless, with estimation, tuning and "gain scheduling" in three different stages, a rigid relationship between the operating conditions and the parameter value is essential to guarantee the accuracy of the estimates. Although this requirement is fulfilled for the case of VSC equivalent loss resistance identification, the first option of implementation (online estimation and tuning in one stage) is more robust against unknown secondary causes of R_C variation. On the other hand, it should be mentioned that neither of both options requires the use of extra sensors, compared to the number needed in the common feedback control, which is a usual drawback in "gain-scheduling" solutions [123].

Table 2.2: Effect on R_C of Uncertainties in $\widehat{L}$.

Error in $\widehat{L}$	R_C^{met}	k_{max}
0%	1.9 Ω	14
+4%	1.92 Ω	14
−4%	1.88 Ω	14
+8%	1.89 Ω	13
−8%	1.87 Ω	14
+20%	1.84 Ω	11
−20%	1.82 Ω	15

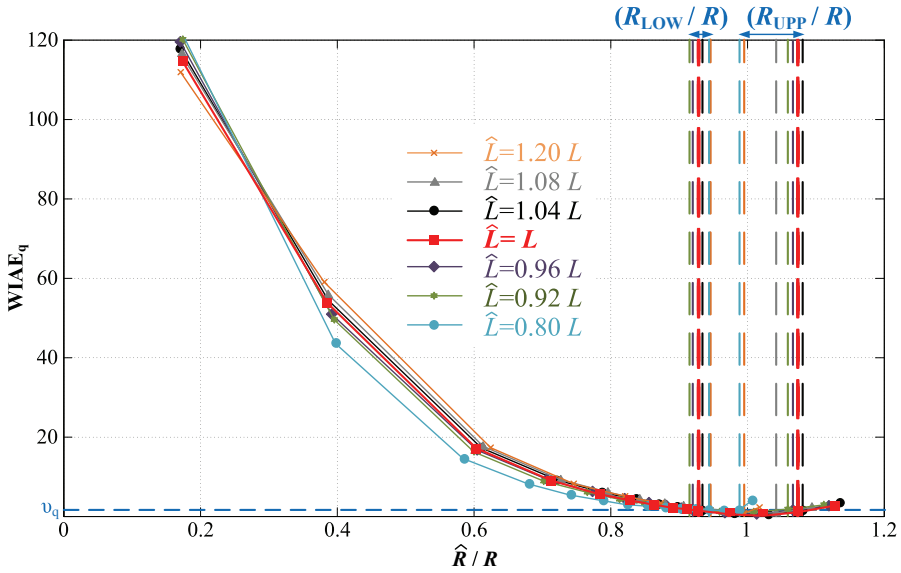

Figure 2.9: WIAE_q versus $\widehat{R}/R$ for the theoretical example case A of the proposed identification method. Effect on $\widehat{R}$ of different uncertainties in $\widehat{L}$.

2.4.5 Effect on the Resistance Estimation of Uncertainties in the Inductance Value

In the proposed method, L has been assumed constant up to this point. Nevertheless, as uncertainties or changes in its value might happen, as a consequence of factors such as temperature, soft saturation (abrupt saturation is disregarded) or errors in its measurement, their effect on the obtained $\widehat{R}$ should be assessed. In order to do that, errors of ±4%, ±8% and ±20% in $\widehat{L}$ have been evaluated for case A of the experimental results (cf. Table 2.2). Fig. 2.9 depicts the corresponding WIAE_q versus $\widehat{R}/R$ trajectories. From the results, it can be concluded that small uncertainties in $\widehat{L}$ (±4% and ±8%) have minimal impact on the obtained R_C (cf. Table 2.2). Moreover, even for $\widehat{L}/L = 1.20$ and $\widehat{L}/L = 0.80$, the error made in $\widehat{R}$ is irrelevant, especially compared to that caused by R mismatches due to the effects associated to converter losses, as, e.g., when considering $R = R_F$.

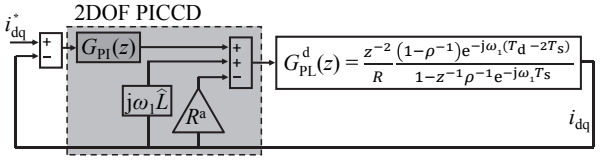

Figure 2.10: Complex vector block diagram of the current control closed loop in SRF when R^a is included. G^d_{PL} models the plant admittance together with the remaining delay after applying delay compensation.

2.5 Evaluation of the 2DOF PI Controller Case

A priori, adding a second degree of freedom to the current controller by means of the "active resistance" technique [10, 92, 154, 190, 191] would lower to a certain point the sensitivity of the current loop response in the presence of resistance uncertainties. However, it is convenient to evaluate whether knowing the resistance value permits to further enhance the current control closed-loop transient response for 2DOF PI controllers, as the one in Fig. 2.10, and to which extent. With that purpose, the analysis detailed below is performed for all the cases studied in the chapter, i.e., those in Tables 2.1 and 2.4. Note that the PI controller introduced in section §2.2 is usually known as one degree-of-freedom (1DOF) PI controller.

The step responses of the current control closed loop when an "active resistance" R^a is included (cf. Fig. 2.10) have been obtained in two different conditions.

a) When the total resistance of the plant besides R^a, i.e., $R = R_F + R_C$, is unknown and the gains of the PI controller are selected according to IMC and ignoring R:

$$G_{PI}(z) = K\Big[L + R^a \underbrace{\frac{T_s}{2}\frac{1+z^{-1}}{1-z^{-1}}}_{\text{Integrator}(z)}\Big] \tag{2.14}$$

b) When the total resistance of plant besides R^a, i.e., $R = R_F + R_C$, is known and the gains of the PI controller are selected according to IMC and taking into account both R and R^a, as recommended in the literature [10, 92, 190, 191]:

$$G_{PI}(z) = K\Big[L + (R^a + R) \underbrace{\frac{T_s}{2}\frac{1+z^{-1}}{1-z^{-1}}}_{\text{Integrator}(z)}\Big] \tag{2.15}$$

For both conditions [(2.14) and (2.15)], K has been tuned in order to achieve the minimum overshoot and settling time [10], i.e., $K = K_{opt} = 0.039 \cdot 2\pi f_s$, while R^a has been chosen as $R^a = KL = K_{opt}L$, so that the closed-loop poles are equivalent for both command tracking and disturbance rejection [10, 190, 191]. Table 2.3 summarizes the parameters of all the cases to be analyzed. For this study, R has been evaluated from zero up to the value that was the maximum of each case considered in the respective tables (cf. Tables 2.1 and 2.4).

The settling time $t_{2\%}$ versus R/R^a trajectories of the step responses for all the cases in Table 2.3 have been depicted in Figs. 2.11a and b. The former shows the trajectories that correspond to the cases in Table 2.1 (first six rows of Table 2.3) when R is ignored in the

Table 2.3: Parameters of the Different Cases for the 2DOF Analysis

$P_{\text{rated}}\,(V_{\text{LL}_{\text{rated}}})$	L_{F}	f_{sw}	P_{level}	$R\,(R_{\text{F}}+R_{\text{C}})$	f_{s}	K_{opt}	R^{a}	R/R^{a}	**Color (Figure)**
6 MW (3.3 kV)	2.08 mH	1.05 kHz	1.5 – 6 MW	0.01 – 0.303 Ω	2.1 kHz	514.59	1.07	0 – 0.28	Red (Fig. 2.11a)
600 kW (690 V)	0.4 mH	2.5 kHz	500 – 600 kW	0.01 – 0.26 Ω	5 kHz	1225	0.49	0 – 0.53	Black (Fig. 2.11a)
600 kW (690 V)	0.4 mH	1.5 kHz	500 – 600 kW	0.01 – 0.2 Ω	3 kHz	735	0.29	0 – 0.69	Blue (Fig. 2.11a)
11 kW (400 V)	2.75 mH	8 kHz	4.9 – 11 kW	0.01 – 1 Ω	8 kHz	1960	5.39	0 – 0.19	Cyan (Fig. 2.11a)
11 kW (400 V)	2.75 mH	5 kHz	4.9 – 11 kW	0.01 – 0.6 Ω	5 kHz	1225	3.37	0 – 0.18	Green (Fig. 2.11a)
4.1 kW (400 V)	5 mH	5 kHz	2.4 – 4.1 kW	0.01 – 0.9 Ω	10 kHz	2450	12.25	0 – 0.07	Orange (Fig. 2.11a)
25 kW (400 V)	5.86 mH	10 kHz	1.8 – 25 kW	0.01 – 4.2 Ω	10 kHz	2450	14.36	0 – 0.29	Blue (Fig. 2.11b)
25 kW (400 V)	9.56 mH	5 kHz	1.8 – 25 kW	0.01 – 3 Ω	5 kHz	1225	11.71	0 – 0.26	Red (Fig. 2.11b)
25 kW (400 V)	12.71 mH	2.5 kHz	1.8 – 25 kW	0.01 – 1.7 Ω	2.5 kHz	612.61	7.79	0 – 0.22	Green (Fig. 2.11b)

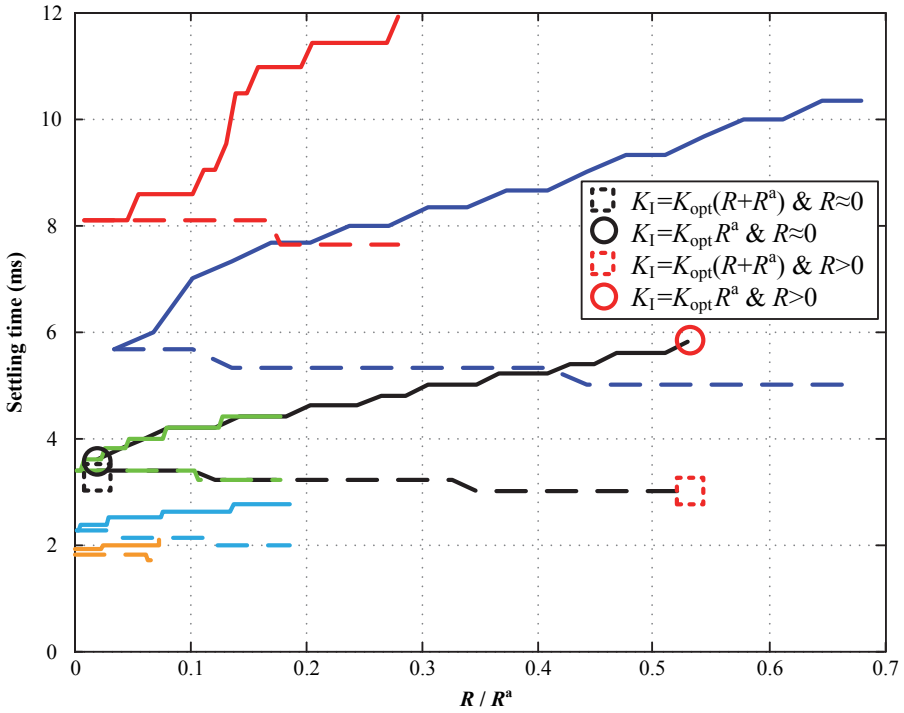

(a) First six cases in Table 2.3.

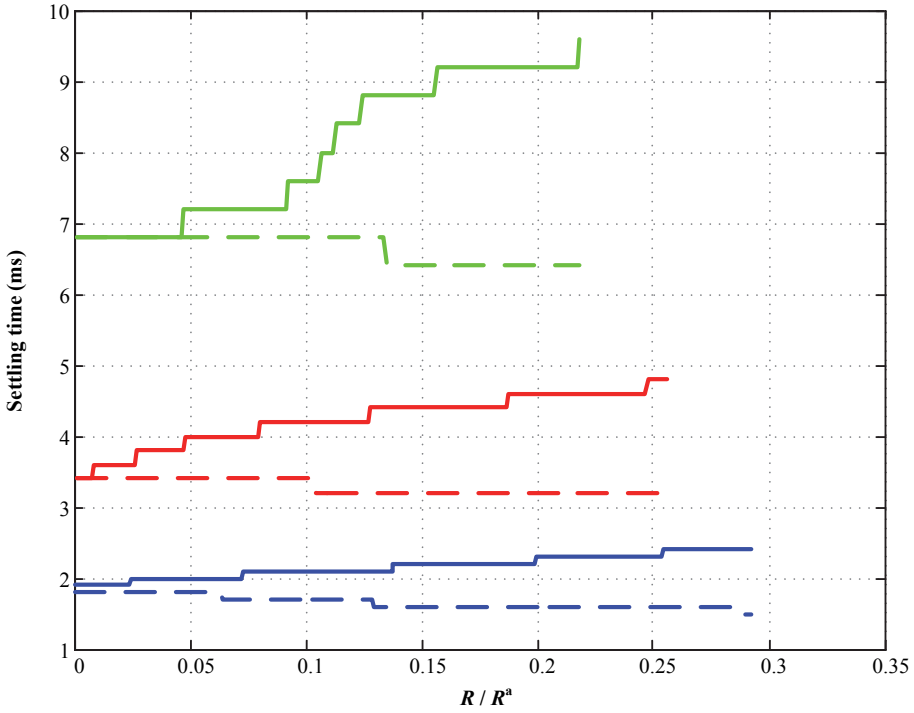

(b) Last three cases in Table 2.3.

Figure 2.11: Settling time $t_{2\%}$ versus R/R^{a} trajectories of i_{q} step responses for an R sweep. Solid lines are used when R is ignored in the PI tuning ($K_{\mathrm{I}} = K_{\mathrm{opt}}R^{\mathrm{a}}$); dashed lines are employed when R is included in the PI tuning [$K_{\mathrm{I}} = K_{\mathrm{opt}}(R+R^{\mathrm{a}})$].

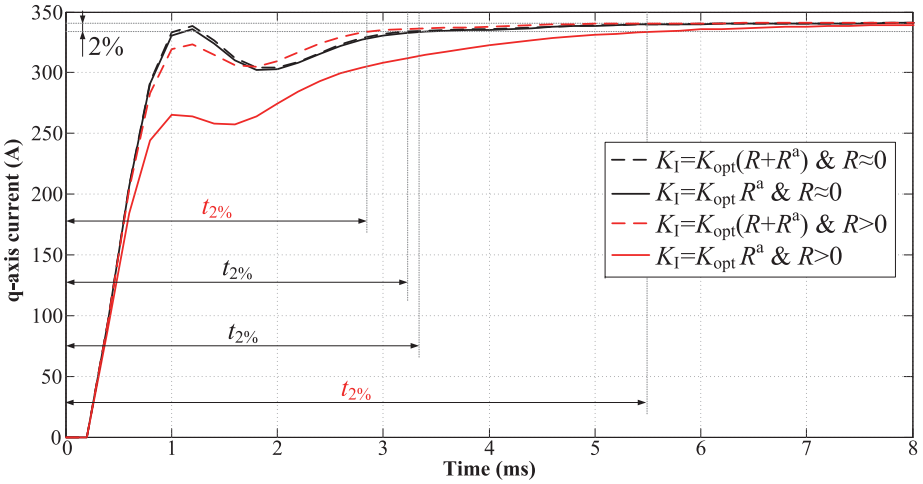

Figure 2.12: i_q step responses for the example of the second row in Table 2.3 (which coincides with the black trajectories in Fig. 2.11a).

controller tuning (solid lines) or when it is considered (dashed lines); Fig. 2.11b illustrates analogous curves for the cases in Table 2.4 (three last rows of Table 2.3). From these graphics, it can be observed that for very low R values, the difference between both trajectories (solid and dashed) is indeed negligible. Nevertheless, as R increases (R/R^a increases), both trajectories diverge: ignoring R in the controller tuning leads to an increase in the settling time of the step response for all the cases, while including a correct estimate of R permits to slightly reduce $t_{2\%}$ as R grows.

For illustrative purposes (the most relevant information is contained in Fig. 2.11a), the step responses of i_q for four different conditions of the second theoretical example in Table 2.3 are shown in Fig. 2.12. When R is negligible (see the black circle and the black square in the left part of the black trajectory in Fig. 2.11a), the transient responses in Fig. 2.12 are practically identical, no matter whether R is ignored or considered in the PI tuning (compare the solid and dashed black lines). Nevertheless, when R is significant (see the red circle and the red square in the right part of the black trajectory in Fig. 2.11a), either ignoring or considering R in the tuning leads to differences in the settling time (compare the solid and dashed red lines in Fig. 2.12). Consequently, even if a 2DOF PI controller is chosen for the final application, it is convenient to estimate the actual R value as proposed, so that the closed-loop performance can be improved.

On the other hand, it is worth highlighting that it is preferable to use a 1DOF controller rather than a 2DOF one during the estimation process, because the latter provides lower sensitivity to $\widehat{R}$ and modifies the transient response. In addition, the actual R value (and hence, its estimate, obtained with the 1DOF PI controller) is independent from whether R^a is included or not in the final application.

2.6 Experimental Results

2.6.1 Experimental Setup

The prototype is shown in Fig. 2.13 and its main parameters are specified in Table 2.4. A three-phase grid-connected VSC (of 25 kVA) working as a rectifier has been built to test

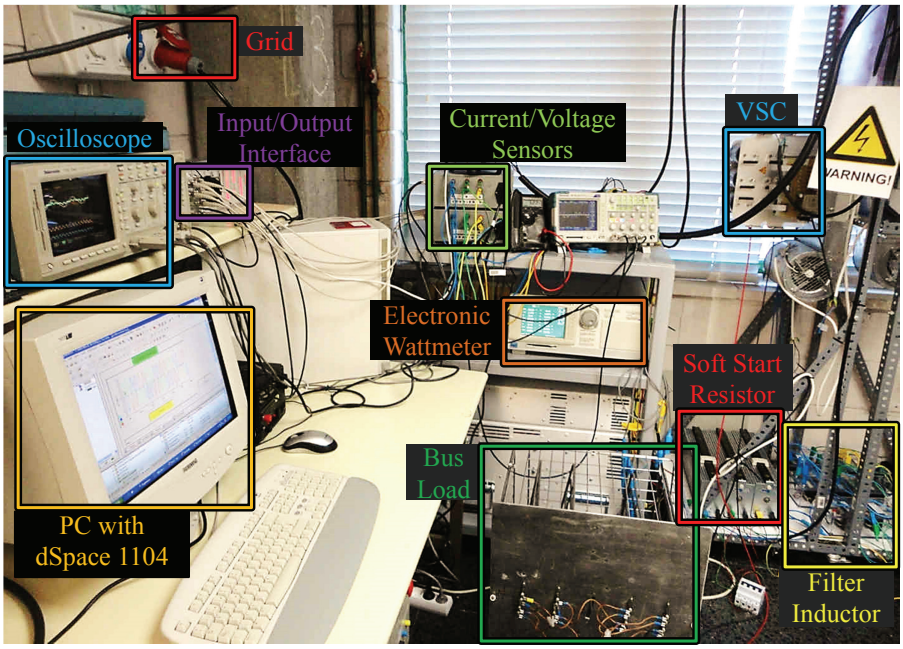

(a) Photograph.

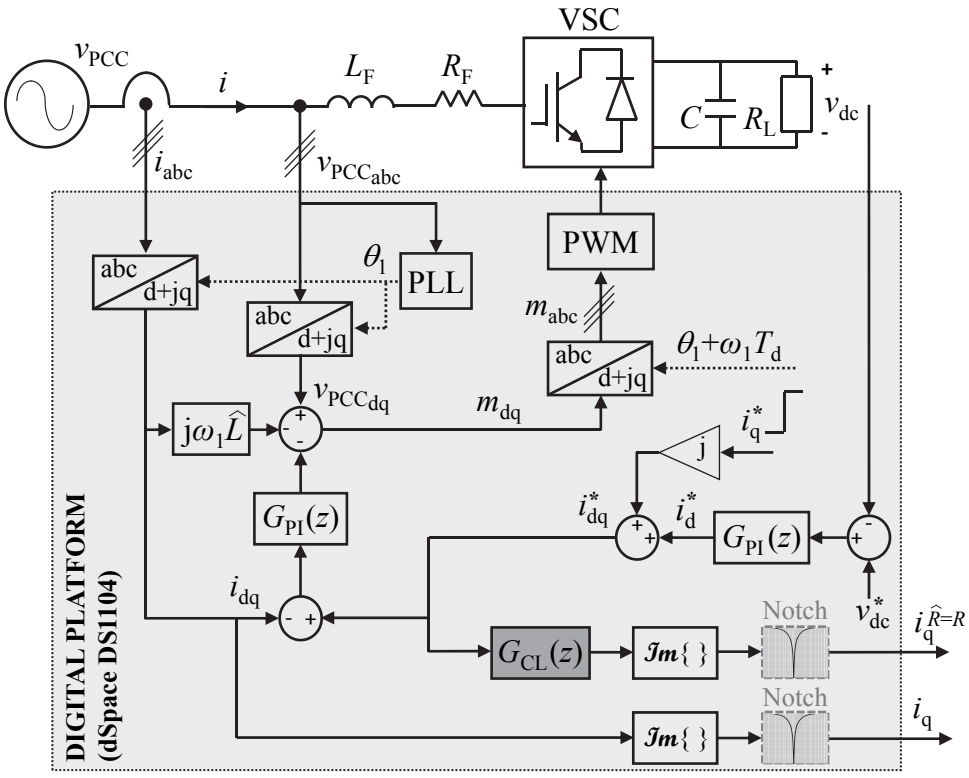

(b) Scheme.

Figure 2.13: Experimental setup.

Table 2.4: Experimental Setup Parameters of the Different Cases Tested

Case	P_{dc}	$f_{sw} = f_s$	L_F	R_F	i_d	i_q^*	v_{dc}	$v_{PCC_{rms}}$	R_C^{met}	k_{max}
A	4.3 kW	10 kHz	5.86 mH	0.4 Ω	9.7 A	6.3 A	750 V	230 V	1.9 Ω	14
B	2.8 kW	10 kHz	5.86 mH	0.4 Ω	6.3 A	6.3 A	750 V	230 V	2.6 Ω	16
C	1.8 kW	10 kHz	5.86 mH	0.4 Ω	4.25 A	4.25 A	750 V	230 V	3.8 Ω	22
D	1.8 kW	5 kHz	9.56 mH	0.4 Ω	4.25 A	4.25 A	750 V	230 V	2.7 Ω	13
E	1.8 kW	2.5 kHz	12.71 mH	0.35 Ω	4.25 A	4.25 A	750 V	230 V	1.3 Ω	9

the proposed methodology, which feeds a dc load R_L (cf. Fig. 2.13b). Note that with the objective of validating the VSC equivalent loss resistance, the power demanded during the experiments is significantly lower than the rated one. The digital control is implemented in the rapid prototyping platform dSpace DS1104. A classical PI controller is used to keep v_{dc} constant. Its output is i_d^*. To perform the required steps, i_q^* is set manually. A PICCD is used to regulate the current in the dq frame (cf. section §2.2). Its output m is driven to the PWM unit of the dSpace DS1104 platform. A phase-locked loop (PLL) tracks the grid phase angle θ_1, which is employed in the frame transformations [28]. The delay compensation term $e^{j\omega_1 T_d}$ from Fig. 2.2a is implemented by simply adding a phase lead $\omega_1 T_d$ to θ_1 before being input to the inverse transformation in Fig. 2.13b [10]. The actual i_q is internally calculated from the measured current waveforms, and then visualized in the oscilloscope through a digital-to-analog converter (DAC).

In agreement with section §2.4, the same i_q^* step as in the actual control loop has been applied to the simulated control loop [cf. (2.11), Fig. 2.5 and the shaded block in Fig. 2.13b] in the dSpace platform, i.e., to an identical PICCD that regulates the simulated plant $G_{PL}(z)$ and setting $L_{sim} = \widehat{L}$ and $R_{sim} = \widehat{R}$. The resulting waveform $i_q^{\widehat{R}=R}$ is extracted through another DAC.

Converter nonlinearities such as dead times cause low-order harmonics in the converter output voltage that lead to significant harmonics in the current [193], being the most important the fifth negative-sequence and the seventh positive-sequence ones. A usual solution in identification (which avoids complicating the plant model with extra dead-time compensation algorithms) is the inclusion of identical prefilters in the open-loop path of both signals to be compared i_q and $i_q^{\widehat{R}=R}$, so they do not alter the identification process [194]. In this experimental setup, narrow notch filters tuned at the sixth harmonic in the SRF have been selected (cf. Fig. 2.13b). It should be remarked that these filters remove the sixth harmonic from i_q and $i_q^{\widehat{R}=R}$ visualization and calculation, but they do not eliminate the harmonic content from the actual current i.

2.6.2 Evaluation of Results

2.6.2.1 Identification Method

Fig. 2.14 shows experimental results obtained with the proposed method in the conditions of case A in Table 2.4 (power demanded by the dc load $P_{dc} = 4.3\,\text{kW}$ and $f_{sw} = 10\,\text{kHz}$), which is the one analyzed in sections §2.3.2, §2.3.3 and §2.4. Besides i_q and $i_q^{\widehat{R}=R}$, v_{PCC_a} and i_a are also included in the oscilloscope captures. Results of the same iterations (same $\widehat{R}$ values) as in Fig. 2.7 are presented. Examples of the approach to R lower bound are shown in Figs. 2.14a, b

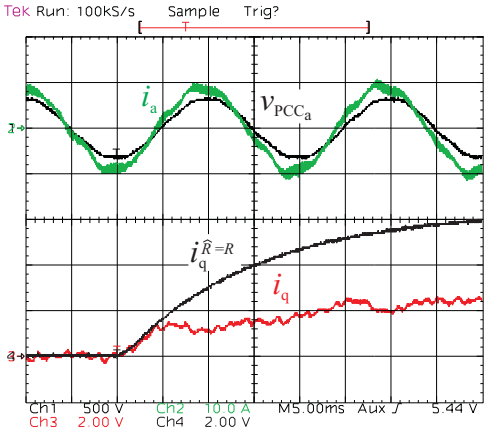

(a) $k = 1$ with $\widehat{R} = 0.40\,\Omega$.

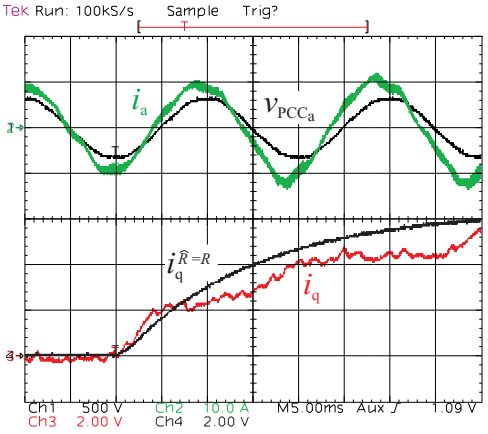

(b) $k = 2$ with $\widehat{R} = 0.89\,\Omega$

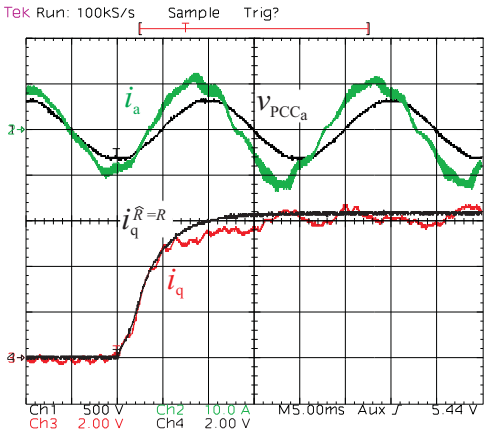

(c) $k = 5$ with $\widehat{R} = 1.80\,\Omega$

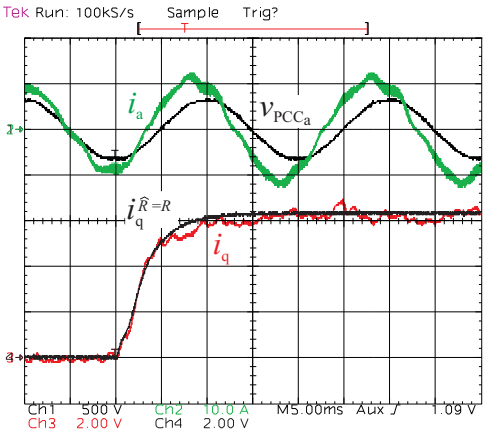

(d) $k = 10$ with $R_{\mathrm{LOW}} = \widehat{R} = 2.13\,\Omega$

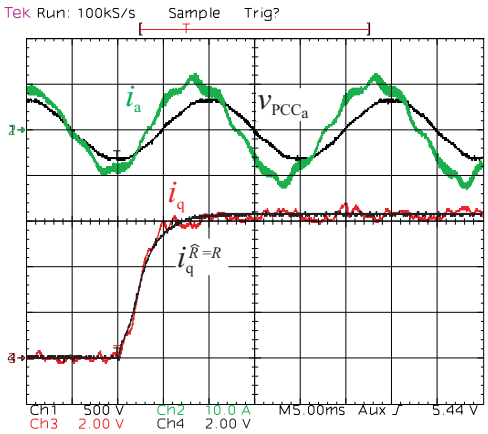

(e) $k = 12$ with $\widehat{R} = 2.35\,\Omega$

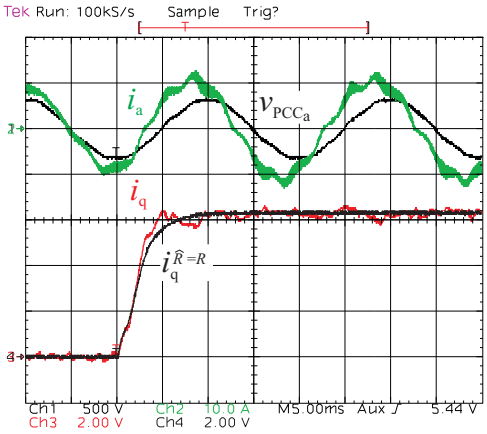

(f) $k = 13$ with $R_{\mathrm{UPP}} = \widehat{R} = 2.47\,\Omega$

Figure 2.14: Experimental results: step response of the actual and simulated current loops. Different iterations of the identification process in the conditions of case A ($P_{\mathrm{dc}} = 4.3\,\mathrm{kW}$ and $f_{\mathrm{sw}} = 10\,\mathrm{kHz}$). Scales: $v_{\mathrm{PCC_a}}$ in $500\,\mathrm{V/div}$, i_{a} in $10\,\mathrm{A/div}$, i_{q} and $i_{\mathrm{q}}^{\widehat{R}=R}$ in $2\,\mathrm{A/div}$, time in $5\,\mathrm{ms/div}$.

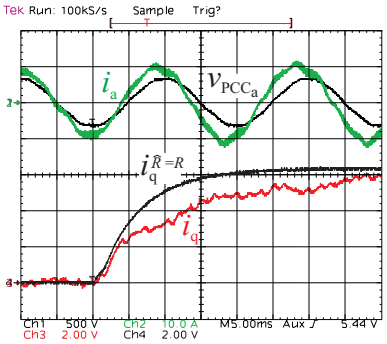

(a) $P_{dc} = 4.3\,\text{kW}$. $\widehat{R} = 1 < R$.

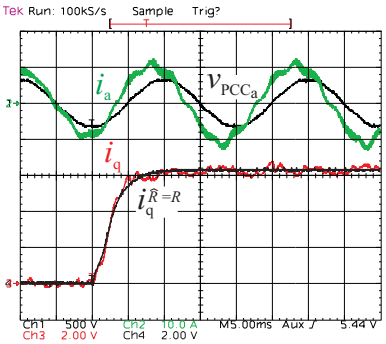

(b) $P_{dc} = 4.3\,\text{kW}$. $R^{\text{met}} = \widehat{R} = R = 2.3\,\Omega$.

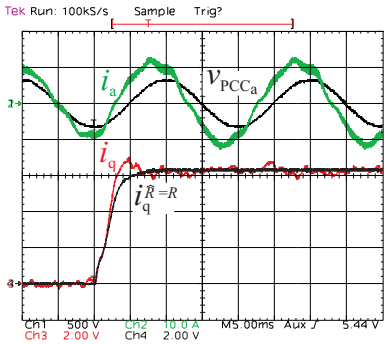

(c) $P_{dc} = 4.3\,\text{kW}$. $\widehat{R} = 3.5\,\Omega > R$.

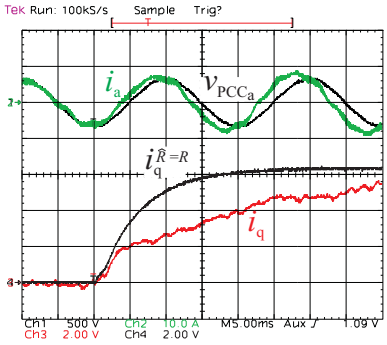

(d) $P_{dc} = 2.8\,\text{kW}$. $\widehat{R} = 1 < R$.

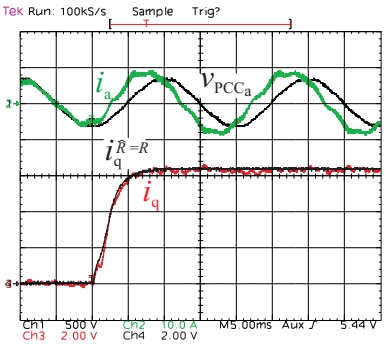

(e) $P_{dc} = 2.8\,\text{kW}$. $R^{\text{met}} = \widehat{R} = R = 3\,\Omega$.

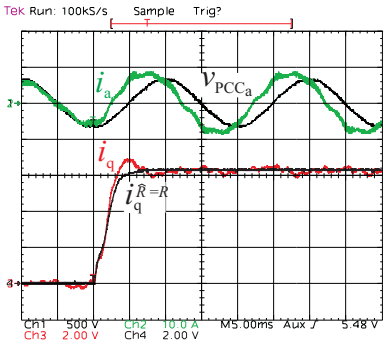

(f) $P_{dc} = 2.8\,\text{kW}$. $\widehat{R} = 4\,\Omega > R$.

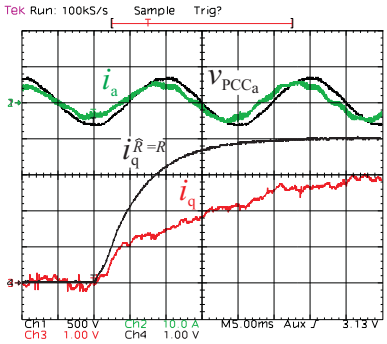

(g) $P_{dc} = 1.8\,\text{kW}$. $\widehat{R} = 1 < R$.

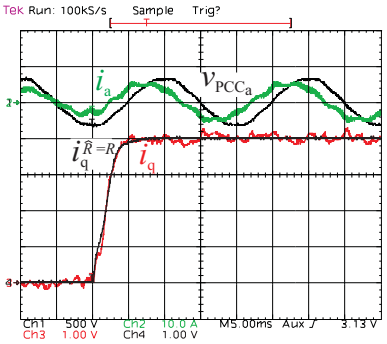

(h) $P_{dc} = 1.8\,\text{kW}$. $R^{\text{met}} = \widehat{R} = R = 4.2\,\Omega$.

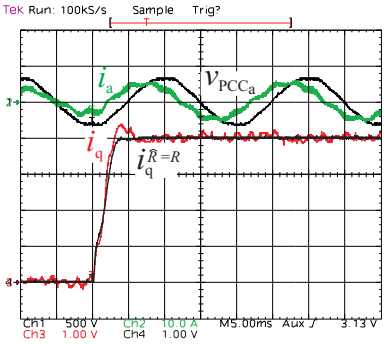

(i) $P_{dc} = 1.8\,\text{kW}$. $\widehat{R} = 5.5\,\Omega > R$.

Figure 2.15: Experimental results: step response of the actual and simulated current loops at three different P_{dc} and $f_{sw} = 10\,\text{kHz}$. Scales: v_{PCC_a} in $500\,\text{V/div}$, i_a in $10\,\text{A/div}$, i_q and $i_q^{\widehat{R}=R}$ in $2\,\text{A/div}$ for (a)-(f) and in $1\,\text{A/div}$ for (g)-(i), time in $5\,\text{ms/div}$.

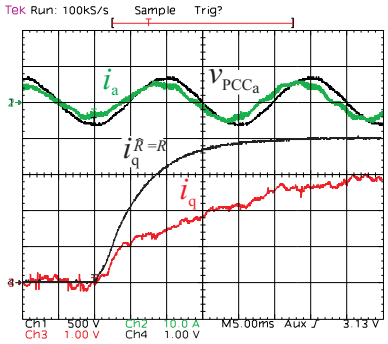

(a) $f_{sw} = 10\,\text{kHz}$. $\widehat{R} = 1 < R$.

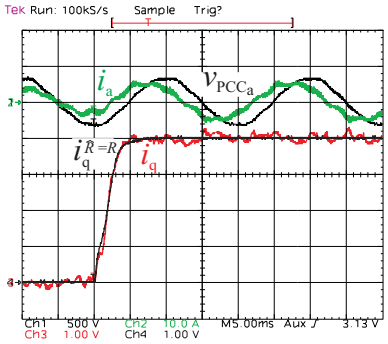

(b) $f_{sw} = 10\,\text{kHz}$. $R^{met} = \widehat{R} = R = 4.2\,\Omega$.

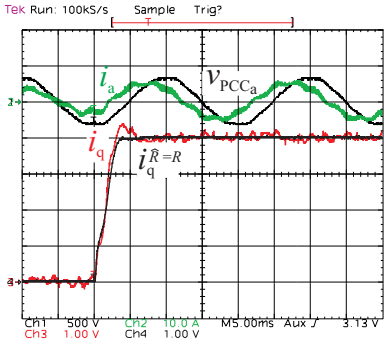

(c) $f_{sw} = 10\,\text{kHz}$. $\widehat{R} = 5.5\,\Omega > R$.

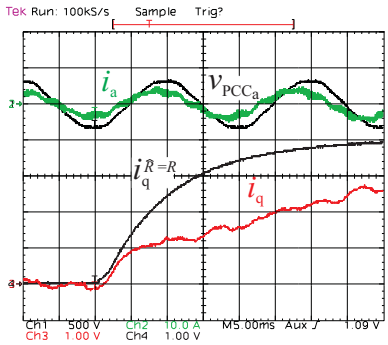

(d) $f_{sw} = 5\,\text{kHz}$. $\widehat{R} = 1 < R$.

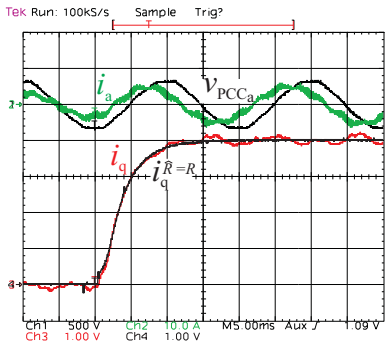

(e) $f_{sw} = 5\,\text{kHz}$. $R^{met} = \widehat{R} = R = 3\,\Omega$.

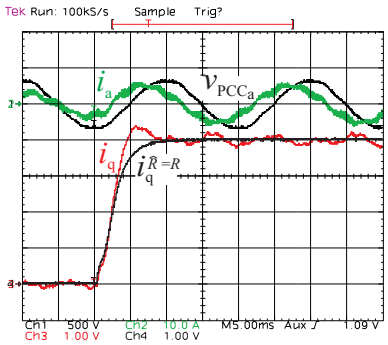

(f) $f_{sw} = 5\,\text{kHz}$. $\widehat{R} = 4.5\,\Omega > R$.

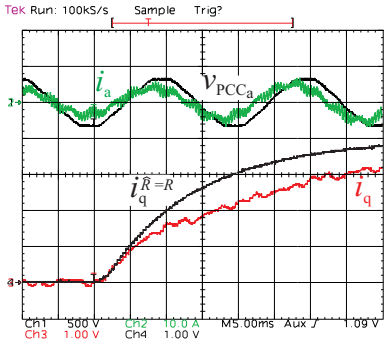

(g) $f_{sw} = 2.5\,\text{kHz}$. $\widehat{R} = 1 < R$.

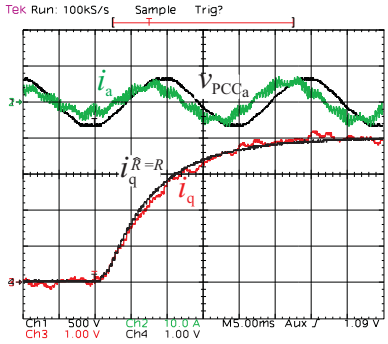

(h) $f_{sw} = 2.5\,\text{kHz}$. $R^{met} = \widehat{R} = R = 1.65\,\Omega$.

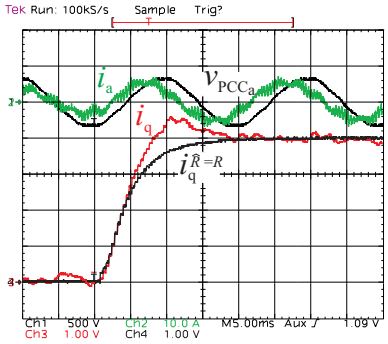

(i) $f_{sw} = 2.5\,\text{kHz}$. $\widehat{R} = 3\,\Omega > R$.

Figure 2.16: Experimental results: step response of the actual and simulated current loops at three different f_{sw} and $P_{dc} = 1.8\,\text{kW}$. Scales: v_{PCC_a} in $500\,\text{V/div}$, i_a in $10\,\text{A/div}$, i_q and $i_q^{\widehat{R}=R}$ in $1\,\text{A/div}$, time in $5\,\text{ms/div}$.

and c, at $k = 1$ with $\widehat{R} = R_F = 0.40\,\Omega$, at $k = 2$ with $\widehat{R} = 0.89\,\Omega$ and at $k = 5$ with $\widehat{R} = 1.80\,\Omega$, respectively. Examples of the refinement stage are shown in Figs. 2.14d, e and f, at $k = 10$ with $R_{LOW} = \widehat{R} = 2.13\,\Omega$, at $k = 12$ with $\widehat{R} = 2.35\,\Omega$ and at $k = 13$ with $R_{UPP} = \widehat{R} = 2.47\,\Omega$, respectively. Good matching between theoretical (cf. Fig. 2.7) and experimental (cf. Fig. 2.14) results is observed. Clearly, in spite of the fact that $R = R_F$ is a usual assumption in the existing literature [34, 77, 79, 81, 140, 141, 173, 176, 177], the parasitic resistance of the interface filter is far from being the actual resistance in the current loop. $R^{met} = 2.3\,\Omega$ is established, leading to $R_C^{met} = 1.9\,\Omega$.

A study of the disturbance rejection capability of the harmonics caused by dead times in the conditions of Fig. 2.14 can be found in the Appendix §A.

2.6.2.2 Effect of the Power Level

The developed method is employed to experimentally identify R_C at $f_{sw} = 10\,\text{kHz}$ and at different specifications of power level (cf. cases A, B and C in Table 2.4). The results are shown in Fig. 2.15. The top row corresponds to case A ($P_{dc} = 4.3\,\text{kW}$). Examples of R underestimate, correct identification and overestimate are shown in Figs. 2.15a, b and c, respectively. The obtained i_q are in agreement with the analysis (and curves) in section §2.3.3 for $\widehat{R} < R$, $\widehat{R} = R$ and $\widehat{R} > R$. $R_C^{met} = 1.9\,\Omega$ is determined for case A (cf. Fig. 2.15b), i.e., more than 4 times R_F.

The middle row in Fig. 2.15 corresponds to case B ($P_{dc} = 2.8\,\text{kW}$). Figs. 2.15d, e and f are examples of $\widehat{R} < R$, $\widehat{R} = R$ and $\widehat{R} > R$, respectively. As it could be expected, since a lower power is demanded by the dc load, the percentage of losses increases, and a bigger R_C than in case A ($R_C^{met} = 2.6\,\Omega$) is obtained, i.e., 6.5 times R_F.

Figs. 2.15g, h and i, in the bottom row, show the results of case C ($P_{dc} = 1.8\,\text{kW}$). In these conditions, $R_C^{met} = 3.8\,\Omega$ is identified (cf. Fig. 2.15h), i.e., 9.5 times R_F.

The obtained R_C values are in agreement with the fact that the percentage of losses increases for VSCs working under rated conditions [179, 183, 184]. An increase in the number of iterations as the power level of a specific experimental setup decreases (and losses increase) is observed, owing to the fact that $\widehat{R}(1) = R_F$, is farther from the actual R.

2.6.2.3 Effect of the Switching Frequency

The proposed method is applied to the test bench working at three different f_{sw}, while the power level is maintained constant at 1.8 kW (cf. cases C, D and E in Table 2.4). The results are shown in Fig. 2.16. It should be noticed that the top row in this figure, which corresponds to case C ($f_{sw} = 10\,\text{kHz}$), is exactly the same as the bottom row in Fig. 2.15, but it is repeated here to ease the comparison. Hence, Figs. 2.16a, b and c are equal to Figs. 2.15g, h and i, respectively, and $R_C^{met} = 3.8\,\Omega$ is determined.

Figs. 2.16d, e and f, in the middle row, show the results of case D ($f_{sw} = 5\,\text{kHz}$). At this lower f_{sw}, $R_C^{met} = 2.7\,\Omega$ is obtained (cf. Fig. 2.16e), i.e., around 6.5 times R_F.

The results at $f_{sw} = 2.5\,\text{kHz}$ (cf. case E) are included in Figs. 2.16g, h and i in the bottom row. From Fig. 2.16h, an even lower R_C^{met} ($1.3\,\Omega$) is identified, i.e., around 3 times R_F, much lower than the ones for cases C and D.

The obtained R_C values are in agreement with the fact that losses decrease as the f_{sw} reduces [100, 175, 179, 183, 184].

2.7 Conclusions

In this chapter, a method to identify the VSC equivalent loss resistance in specific working conditions has been proposed. The VSC equivalent loss resistance reflects the influence of the power losses on the plant model. As demonstrated, an incorrect estimation of it leads to a degraded behavior of the current control closed loop, different from the theoretical one (e.g., in terms of settling time and overshoot). Hence, its identification is essential for a rigorous analysis and design of this loop. It is also proved that, although adding a second degree of freedom to the current controller by means of the "active resistance" technique lowers to a certain point the sensitivity to resistance uncertainties, accurate knowledge of the actual resistance value permits to further enhance the transient response.

The developed method is based on the iterative minimization of a cost function that quantifies the error between the current control closed-loop step responses of the real system and the one of a simulated plant, with the current controllers tuned according to the IMC principle. Thus, it is particularly oriented to the fulfillment of transient response constraints. This estimation method works in closed loop, and may be implemented either offline, during a pre-commissioning stage, or online. Moreover, it can be run at any sampling frequency.

It has been shown that the proposal is able to provide a good estimation of the VSC equivalent loss resistance at different sampling and switching frequencies or in systems that work at very variable load conditions, reaching at high switching frequencies and light load a significant value with respect to the one of the interface filter parasitic resistance; e.g., in our tests, values between 4 and 10 times the filter resistance have been obtained.

Contributions of this chapter have been published in the journal IEEE Transactions on Power Electronics [5] and presented at an international conference [19].

Chapter 3

A Method for Identification of the Equivalent Inductance and Resistance in the Plant Model of Current-Controlled Grid-Tied Converters

Abstract *— Precise knowledge of the plant time constant L/R is essential to perform a thorough analysis and design of the current control loop in voltage source converters (VSCs). From the perspective of the current controller dynamics in the low frequency range, such plant time constant is also suitable for most cases in which an LCL filter is used. As the loop behavior can be significantly influenced by the VSC working conditions, the effects associated to converter losses should be included in the model, through an equivalent series resistance. In addition, the plant inductance may also present important uncertainties with respect to the value of the VSC L/LCL interface filter measured at rated conditions. Thus, in this work, a method is presented to estimate both parameters of the plant time constant, i.e., the equivalent inductance and resistance in the plant model of current-controlled VSCs. The proposed technique is based on the evaluation of the closed-loop transient responses of both axes of the synchronous reference frame when a proportional-integral current controller is implemented. The method gives a set of resistance and inductance values that should be employed for a rigorous design of the current controllers. Experimental results validate the approach.*

3.1 Introduction

The connection of different sources and loads to the grid is often carried out through pulse-width modulated voltage source converters (VSCs) [58, 77, 81, 86–88, 106, 111, 154]. In order to fulfill the stringent limits set by the standards, rigorous analysis and design of the control loops becomes essential [77, 86–88, 111]. Regarding those requirements that are related to the transient response, special attention must be paid to the inner loop, which is usually a current one [10, 58, 76, 81, 86–88, 111]. The use of linear plant models allows to apply the well-known linear analysis and design methods [10, 76, 81, 88, 106]. Thus, in these applications, linear first-order time-averaged models are commonly chosen for the filter admittance [10, 76, 77, 80, 81, 85]. This assumption is also suitable in the case that LCL filters are employed to mitigate the switching harmonics, provided that their behavior is similar to that of L filters at frequencies

below the LCL resonance [77, 85, 102, 106, 111].

Focusing on the current control loop, a certain bandwidth can be set by using the inductance value for the gain tuning [76, 106]. Nevertheless, when specifications are established in terms of transient response (settling time and overshoot), the plant time constant L/R should be accurately known (i.e., both inductance L and resistance R) [10, 80, 86, 119]. Moreover, the time constant should include the VSC equivalent loss resistance, which reflects the effects related to converter losses on the plant model [76, 93–95]. These, in turn, are linked to the VSC working conditions (power level with respect to the rated one and switching frequency) [cf. chapter §2].

A method has been developed in chapter §2 to estimate the plant time constant in different working conditions for current control design. The commonly-accepted low-order time-averaged plant model was adopted [10, 76, 77, 80, 81, 85, 95, 140, 141], and the converter equivalent loss resistance was included in it [76, 93–95]. However, in such work, the inductance value was considered as known and constant, attributing uncertainties in the plant constant to the resistance. Extra inductance (and resistance) may be present in the electric circuit due to the existence of additional elements, such as the coupling transformer, the grid impedance or long wires [4, 7, 58, 86–89, 102, 106, 111, 154]. Besides, several phenomena, such as saturation, can cause significant variations in the inductance value [86, 87, 89, 195, 196]. Inaccuracy in the identification of the plant time constant may affect the stability [88, 106] and, as proved in chapter §2, it also alters the transient response. Considering that both the inductance and the resistance are unknown and depend on the operating conditions, some methods have been developed aimed at the estimation of the two parameters in grid-connected applications [86, 87]. These proposals, which are based on neural networks, include real time simulation results, but they have not been tested with an actual converter [86, 87].

In this chapter, a method to estimate the equivalent inductance and resistance in the plant model of current-controlled VSCs is proposed. The technique has its basis on model reference adaptive systems (MRASs), which are very popular in drives applications [134, 185]. In the MRAS-based technique developed in this work, which is an improvement of that presented in chapter §2, an iterative algorithm minimizes the difference between the current step responses that are obtained with two distinct current closed loops: one including the actual plant, and one in which it is replaced by a plant model. On the other hand, the current controller consists in a synchronous PI controller with state-feedback cross-coupling decoupling (PICCD) [10, 58, 78, 140, 141, 154]; its gains are set according to the internal model control (IMC) principle [10, 141]. Unlike in the method of chapter §2, here both real and imaginary components (i.e., the projections on the two orthogonal axes d and q) of the complex current response are taken into account. In this manner, the information related to the axes cross coupling is exploited to estimate the inductance. Identification of both parameters, and not only of the resistance, is a significant contribution with respect to chapter §2, as most of the tuning methods for current controllers employed in the literature need a correct estimate of the two of them, or at least, of the inductance [9, 10, 76–78, 80, 81, 86–88, 93, 106, 119, 140, 141, 186], [cf. chapters §4 and §5]. Regarding the implementation, two options are possible: online or offline.

The chapter is organized as follows. Section §3.2 reviews the current control closed-loop model. An analysis of the effect of the parameter mismatches on the root-locus diagrams of the current loop and on the time-domain step response is conducted in section §3.3. After that, the developed identification method is presented in section §3.4. Experimental results are provided in section §3.5 and finally, section §3.6 concludes the work.

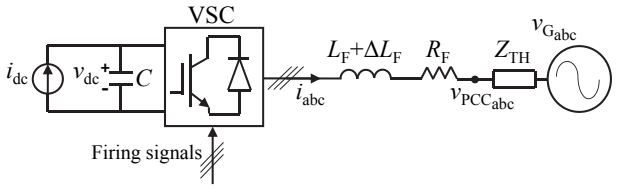

Figure 3.1: Scheme of a grid-tied VSC.

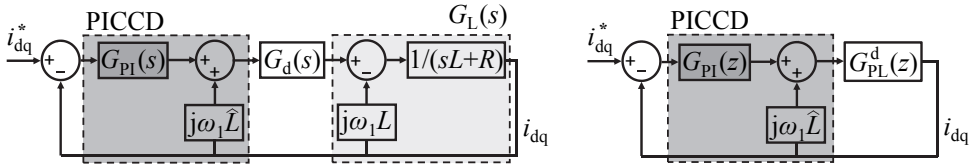

(a) In the s-domain. (b) In the z-domain.

Figure 3.2: Complex vector block diagram of the current control loop in SRF for the VSC working in inverter operation.

3.2 Model and Control of the Current Loop

Fig. 3.1 illustrates a three-phase grid-tied VSC. The variables i_{dc}, v_{dc} and C denote the direct current delivered to (or demanded from) the dc-link, its voltage and its capacitance, respectively. The filter inductance that the designer knows a priori (e.g., from offline measurements or from the supplier) and its parasitic resistance are represented by L_F and R_F, respectively. ΔL_F symbolizes uncertainties in the inductance with respect to L_F, which can be attributed to the variations of its value with the operating point, as the ones caused by saturation [86, 87, 89, 195, 196]. Besides, they could also represent errors in the original measurements. Thus, the actual value of the filter inductance in certain conditions is the addition of these two, i.e., $L_F + \Delta L_F$. The complex variable Z_{TH} refers to the Thevenin equivalent impedance seen from point of common coupling (PCC), which is a combination of passive elements [4, 7]. Such impedance is mainly due to the coupling transformer and to the grid and, as done in other works, it has been assumed to be principally inductive and resistive [58, 86–89, 106]. Finally, v_{PCC_n}, i_n and v_{G_n} stand for the n-phase voltage at the PCC, current and grid voltage, respectively.

The block diagram of the current control loop of the aforementioned VSC is depicted in Fig. 3.2a. It is expressed in the s-domain and with respect to an SRF rotating at the fundamental frequency ω_1. The disturbance v_{PCC} is not included because approximate cancellation is assumed to be achieved through its measurement and feedforward [10]. A hat defines parameter estimates and an asterisk, reference signals. Complex vector notation [140] with respect to the SRF is expressed by the subscript dq. Computation and modulation imply a time delay T_d of one and a half samples in the stationary frame, i.e., $T_d = 1.5T_s$, with T_s being the sampling period [10, 76, 77, 80, 106, 197]. Such delay is represented in the SRF as $e^{-(s+j\omega_1)T_d}$ [10]. A delay compensation according to [10, 186] is considered, which permits to cancel the phase lag at dc in the SRF caused by T_d, by adding a phase lead equal to $\omega_1 T_d$, i.e., $e^{j\omega_1 T_d}$. Hence, the remaining delay after applying delay compensation in the SRF is $G_d(s) = e^{-sT_d}$. On the other hand, the plant admittance can be modeled in the SRF as [10, 81]

$$G_L(s) = \frac{1}{sL + R + j\omega_1 L}. \tag{3.1}$$

L represents the equivalent inductance in the plant model of the current loop, which is defined as $L = L_\mathrm{F} + \Delta L_\mathrm{F} + L_\mathrm{TH}$, with $L_\mathrm{TH} = \mathfrak{Im}\{Z_\mathrm{TH}\}/\omega$. In addition to R_F, the equivalent resistance of the loop $R = R_\mathrm{F} + R_\mathrm{TH} + R_\mathrm{C}$ also includes $R_\mathrm{TH} = \mathfrak{Re}\{Z_\mathrm{TH}\}$ and the equivalent loss resistance of the converter R_C [76, 93–95].

It is worth mentioning that, as all the transfer functions defined along this chapter are expressed with respect to the SRF, subscripts dq are omitted for the sake of clarity, e.g., $G_\mathrm{L}(s)$ is adopted, instead of $G_{\mathrm{L_{dq}}}(s)$, which was employed in the introduction (cf. chapter §1).

In Fig. 3.2a, a synchronous proportional-integral (PI) controller is used to regulate the current:

$$G_\mathrm{PI}(s) = K_\mathrm{P} + \frac{K_\mathrm{I}}{s} = \frac{K(s\widehat{L} + \widehat{R})}{s} \tag{3.2}$$

where the proportional and integral gains K_P and K_I have been selected according to IMC [10, 141]. Hence, the real term of the plant pole is canceled by the zero of the PI controller, provided that the plant parameter estimates ($\widehat{L}$ and $\widehat{R}$) match the actual ones (L and R) [10, 81, 140, 141]. Cancellation of the plant pole imaginary term is addressed by means of a current feedback with a gain $\mathrm{j}\omega_1\widehat{L}$, added to the controller output (cf. Fig. 3.2a) [10, 58, 140, 141, 154]. The PI controller with this kind of decoupling is often known as PICCD [78, 140].

Fig. 3.2b depicts the block diagram of the current loop in the z-domain. G_PL^d models the effect of the plant admittance and the remaining delay after applying delay compensation [10, 186]

$$G_\mathrm{PL}^\mathrm{d}(z) = \frac{z^{-2}}{R}\,\frac{(1-\rho^{-1})\mathrm{e}^{\mathrm{j}\omega_1(T_\mathrm{d}-2T_\mathrm{s})}}{1-z^{-1}\rho^{-1}\mathrm{e}^{-\mathrm{j}\omega_1 T_\mathrm{s}}}, \text{with } \rho = \mathrm{e}^{T_\mathrm{s}/\tau} \tag{3.3}$$

where $\tau = L/R$ denotes the plant time constant. This expression has been obtained by applying the zero-order hold (ZOH) discretization method to (3.1) and multiplying the result by the computational delay $z^{-1}\mathrm{e}^{-\mathrm{j}\omega_1 T_\mathrm{s}}$ and by the delay compensation term $\mathrm{e}^{\mathrm{j}\omega_1 T_\mathrm{d}}$ [10, 186]. Note that (3.3) also considers the slight decrease in gain caused at high frequencies by the introduction of the ZOH prior to the pulse-width modulation (PWM) [10]. Finally, the Tustin discretization method has been employed to obtain $G_\mathrm{PI}(z)$.

3.3 Analysis of the Current Control Closed Loop

The developed estimation algorithm, which will be explained in detail in section §3.4, is based on the evaluation of the current step response. In this section, the current control closed-loop dynamics is studied first by means of root-locus diagrams, taking into account L and R parameter mismatches. In order to evaluate the validity of the plant model described in Fig. 3.2 when LCL filters are employed as the interface between the grid and the converter instead of L ones, diagrams of both cases are included in sections §3.3.1 (with an L filter) and §3.3.2 (with an LCL filter). In addition, the root-loci analysis permits to study the stability of the loop, to establish a proper gain K for the PI controller and to corroborate that when the plant parameters are correctly identified, the transient response of the current loop is better in terms of overshoot and settling time. Finally, the time-domain current step responses of both axes i_d and i_q are assessed in section §3.3.3, with the objective of relating them with the mismatches in L and R.

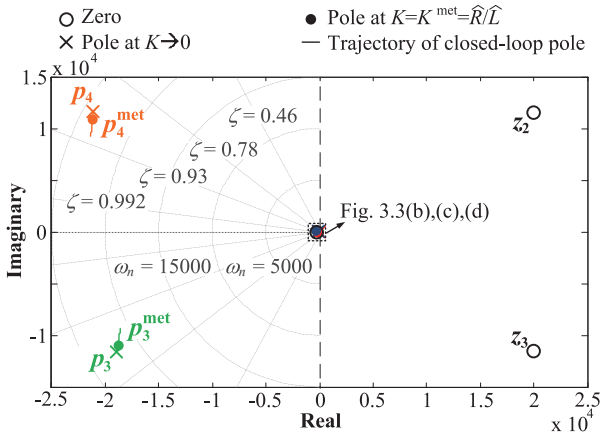

(a) General view when $\widehat{L} = L = 10.9\,\text{mH}$ and $\widehat{R} = R = 1.9\,\Omega$.

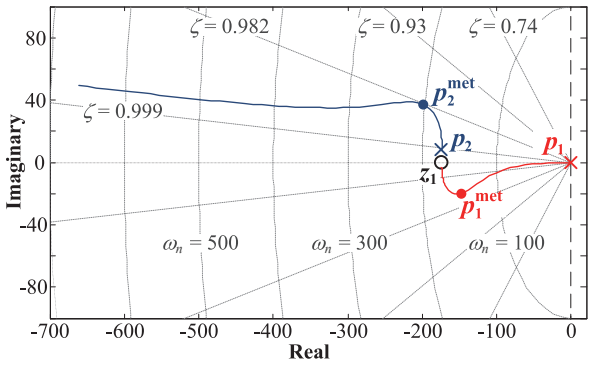

(b) Closer view of the dominant poles when $\widehat{L} = L = 10.9\,\text{mH}$ and $\widehat{R} = R = 1.9\,\Omega$.

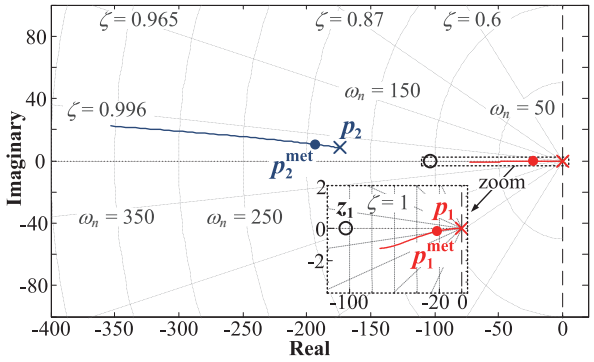

(c) Closer view of the dominant poles when $\widehat{L} = 4.36\,\text{mH} < L$ and $\widehat{R} = 0.45\,\Omega < R$.

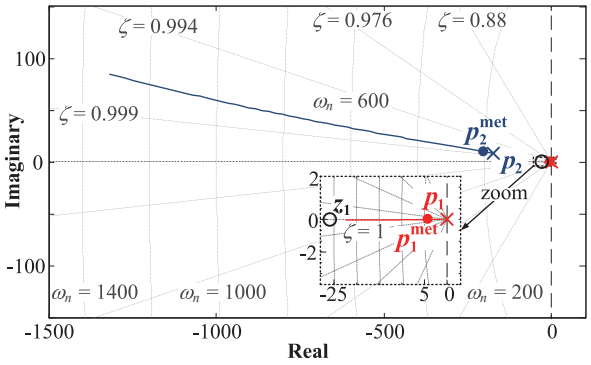

(d) Closer view of the dominant poles when $\widehat{L} = 17.44\,\text{mH} > L$ and $\widehat{R} = 0.45\,\Omega < R$.

Figure 3.3: Root-locus diagrams of $G_{\text{CL}}(s)$ when an L filter is employed.

3.3.1 Root-Locus Diagrams with L Filters

This analysis is conducted in the continuous domain, with the remaining delay $G_{\text{d}}(s)$ after the compensation being approximated with good accuracy by a second-order Padé expansion [10]:

$$G_{\text{d}}(s) = \text{e}^{-sT_{\text{d}}} \approx \frac{1 - s\frac{1}{2}T_{\text{d}} + s^2\frac{1}{12}T_{\text{d}}^2}{1 + s\frac{1}{2}T_{\text{d}} + s^2\frac{1}{12}T_{\text{d}}^2}. \tag{3.4}$$

From Fig. 3.2a, the closed-loop transfer function of the current control loop is

$$G_{\text{CL}}(s) = \frac{I_{\text{dq}}(s)}{I_{\text{dq}}^*(s)} = \frac{G_{\text{PI}}(s)G_{\text{d}}(s)G_{\text{L}}(s)}{1 + [G_{\text{PI}}(s) - \text{j}\omega_1\widehat{L}]G_{\text{d}}(s)G_{\text{L}}(s)}. \tag{3.5}$$

This transfer function can be simplified as $G_{\text{CL}}(s) = K/(s+K)$, if $\widehat{R} = R$, $\widehat{L} = L$ and T_{d} is negligible, i.e., $\omega_1 << 2\pi f_{\text{s}}$. Without considering such simplification, $G_{\text{CL}}(s)$ has four poles p_1-p_4 and three zeros z_1-z_3.

Fig. 3.3 shows different root-locus diagrams for $L = 10.9\,\text{mH}$, $R = 1.9\,\Omega$ and $f_{\text{s}} = 10\,\text{kHz}$. These inductance and resistance correspond to those of case B in Table 3.3 (one of the cases that has been tested experimentally), even though in this section an L filter is considered, instead of

an LCL one. Three distinct relations between the estimated and actual values of the parameters are evaluated:

a) Correct identification of both parameters, i.e., $\widehat{L} = L = 10.9\,\text{mH}$ and $\widehat{R} = R = 1.9\,\Omega$ in Figs. 3.3a and b.

b) Inductance and resistance underestimates, i.e., $\widehat{L} = 4.36\,\text{mH} < L$ and $\widehat{R} = 0.45\,\Omega < R$ in Fig. 3.3c.

c) Inductance overestimate and resistance underestimate, i.e., $\widehat{L} = 17.44\,\text{mH} > L$ and $\widehat{R} = 0.45\,\Omega < R$ in Fig. 3.3d.

It should be noted that the relations labeled as a) and c) correspond to the last and the first iterations of case B, respectively [cf. section §3.5.2], whereas b) exemplifies an equivalent mismatch in the inductance to that in c), i.e., also a 60%, but with L being underestimated. Analogous results to the ones presented in this section have been found when analyzing these three relations in different cases.

From Fig. 3.3a, it can be concluded that the poles p_3 and p_4 have a scarce influence on the transient response, given their distant position with respect to the imaginary axis. This happens regardless of the relation between the actual values of the parameters and their estimates. Therefore, the study will focus on p_1 and p_2. Closer views of their trajectories for cases a), b) and c) are shown in Fig. 3.3b, c and d, respectively.

When the plant parameters are correctly identified (cf. Fig. 3.3b), for all the K values considered (i.e., for $K \leq 610\,\text{rad/s}$), the dominant pole p_1 is faster than in the other two cases (cf. Figs. 3.3c and d). Regarding the other pole p_2, it becomes less oscillating, but slower, as $\widehat{L}/L$ decreases, within the same K range. Having a correct identification of the plant parameters leads to a better transient response (in terms of overshoot and settling time) from the current controller viewpoint, as expected [140, 141].

The two poles p_1^{met} and p_2^{met}, which are obtained for $K = K^{\text{met}} = \widehat{R}/\widehat{L}$, have been depicted in the corresponding diagrams: for $K^{\text{met}} = 174$ in Fig. 3.3b, for $K^{\text{met}} = 103$ in Fig. 3.3c and for $K^{\text{met}} = 26$ in Fig. 3.3d. In the three cases, these poles are stable and result in a relatively slow transient response, which favors the estimation based on the step response (due to a higher robustness to noise). In fact, all the poles are stable within the range of K values considered ($K \leq 610\,\text{rad/s}$). This maximum gain to be evaluated has been calculated as $K = (1.4R)/(0.4L)$, and represents a worst case of K^{met} [in which the inductance is underestimated a 60%, as in 2), but with the resistance being overestimated a 40%, so that K is significantly larger than the corresponding K^{met} in any of the cases analyzed].

3.3.2 Validity of the Plant Model for LCL Filters

With the aim of evaluating the validity of the plant model detailed in Fig. 3.2 when an LCL filter is selected to mitigate the switching harmonics, equivalent situations to those in the previous section are studied, considering also the capacitor branch, with a capacitance $C_{\text{F}} = 6\,\mu\text{F}$. In this manner, $L = 10.9\,\text{mH}$ and $R = 1.9\,\Omega$ are divided between the grid and the converter sides [102, 106] (cf. case B in Table 3.3). A damping resistor $R_{\text{D}} = 10\,\Omega$ [0.28 per-unity (p.u.)] has been considered in series with C_{F} to guarantee the system stability [78, 102, 104]. It should be noted that all the parameter values used in this section coincide with those of the experimental test labeled as case B, which is specified in section §3.5.2.

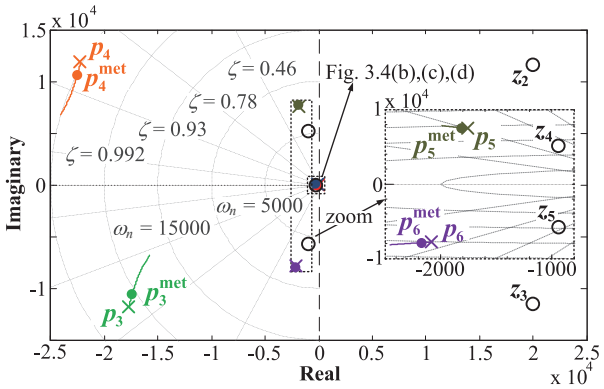

(a) General view when $\widehat{L} = L = 10.9\,\text{mH}$ and $\widehat{R} = R = 1.9\,\Omega$.

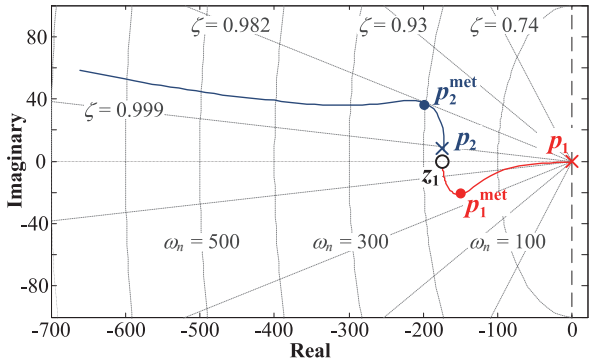

(b) Closer view of the dominant poles when $\widehat{L} = L = 10.9\,\text{mH}$ and $\widehat{R} = R = 1.9\,\Omega$.

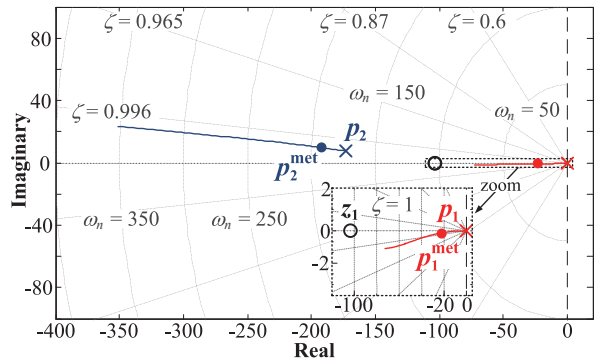

(c) Closer view of the dominant poles when $\widehat{L} = 4.36\,\text{mH} < L$ and $\widehat{R} = 0.45\,\Omega < R$.

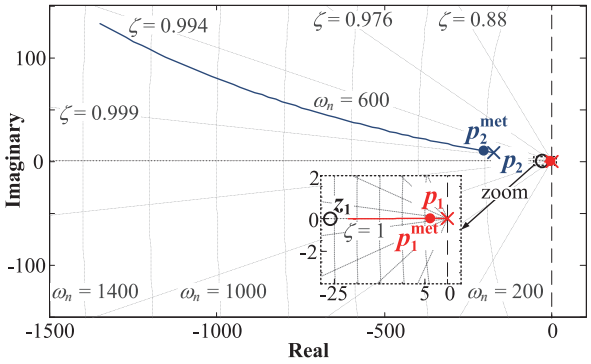

(d) Closer view of the dominant poles when $\widehat{L} = 17.44\,\text{mH} > L$ and $\widehat{R} = 0.45\,\Omega < R$.

Figure 3.4: Root-locus diagrams of $G_{\text{CL}}(s)$ when an LCL filter is employed.

In order to obtain the corresponding closed-loop transfer function, $G_{\text{L}}(s)$ in (3.5) should be substituted by $G_{\text{LCL}}(s)$, which, when the converter-side current i is controlled, is as follows:

$$G_{\text{LCL}}(s) = \frac{Y_{\text{CS}}(s)\,[1 + Y_{\text{GS}}(s)\,Z_{\text{D}}(s)]}{1 + Y_{\text{CS}}(s)\,Z_{\text{D}}(s) + Y_{\text{GS}}(s)\,Z_{\text{D}}(s)} \tag{3.6}$$

where $Y_{\text{GS}}(s)$ and $Y_{\text{CS}}(s)$ are the plant admittances [in the form of (3.1)] of the converter and grid sides, respectively, and $Z_{\text{D}}(s) = 1/(sC_{\text{F}} + \text{j}\omega_1 C_{\text{F}}) + R_{\text{D}}$ is the impedance offered by the capacitor and the damping resistor, with the three transfer functions being expressed with respect to the SRF.

The resulting root loci are displayed in Fig. 3.4. Figs. 3.4a and b depict the pole trajectories for $\widehat{L} = L$ and $\widehat{R} = R$, while Figs. 3.4c and d illustrate those for $\widehat{L} < L$ and $\widehat{L} > L$, respectively, with $\widehat{R} < R$ in both of them.

As expected, given the order of $G_{\text{LCL}}(s)$, when an LCL filter is employed, there are two more poles p_5 and p_6 and two more zeros z_4 and z_5 with respect to the case of L filters (compare Fig. 3.4a with Fig. 3.3a). Nevertheless, these additional poles are significantly farther from the imaginary axis than p_1 and p_2 (although closer than p_3 and p_4). With the aim of saving space, this general view of the root-locus diagram has been only included for the case of correct identification of the plant parameters, but an equivalent behavior of z_4, z_5, p_5 and p_6 is observed in the presence of parameter mismatches. Both the zeros and the poles when $K \to 0$ (represented

by crosses) are located at the same position for the three cases evaluated. Moreover, as K raises, p_5 and p_6 increase their real and imaginary parts. Concerning their exact trajectories, irrelevant discrepancies are found among them. Consequently, regardless of the relation between the parameter estimates and their actual values, p_5 and p_6 will have little impact on the transient response, so the analysis is focused on p_1 and p_2 subsequently, whose trajectories are shown in detail in Figs. 3.4b, c and d for the same three situations as in section §3.3.1.

When both L and R are correctly identified, the root-locus diagram in case of an LCL filter, which is displayed in Fig. 3.4b, is very similar to that of an L one, depicted in Fig. 3.3b. No differences are observed in the trajectory of the dominant pole p_1. Concerning p_2, as K increases, its imaginary part becomes slightly more oscillating when the higher-order filter is used. Similar observations can be drawn for the cases of inductance underestimate (by comparing Figs. 3.4c and 3.3c) and of inductance overestimate (by contrasting Figs. 3.4d and 3.3d). Moreover, the poles p_1^{met} and p_2^{met} obtained with $K = K^{\text{met}}$ in Figs. 3.4b-d match with very good accuracy those in Figs. 3.3b-d. In this manner, it can be concluded that for not very large bandwidths (as the ones employed in this proposal) the current closed loop detailed in Fig. 3.2 is also valid when LCL filters are used as the interface between the grid and the converter.

3.3.3 Influence of L and R Mismatches on the Time-Domain Current Step Responses

In this section, transfer functions in the discrete-time domain are considered, i.e., those indicated in the closed loop of Fig. 3.2b. In order to assess the effect of L and R mismatches, a step of amplitude $I_{\text{AMP}} = 6\,\text{A}$ is commanded to the q-axis component of the current reference, while the d-axis one is maintained constant, in the following situations.

- Correct identification of R, with $\widehat{R} = R = 1.9\,\Omega$, to evaluate the effect of $\widehat{L}$ (cf. Figs. 3.5a and b).
  - Correct identification of L, with $\widehat{L} = L = 10.9\,\text{mH}$.
  - Underestimate of L, with $\widehat{L} = 0.4L < L$.
  - Overestimate of L, with $\widehat{L} = 1.6L > L$.
- Correct identification of L, with $\widehat{L} = L = 10.9\,\text{mH}$, to study the influence of $\widehat{R}$ (Figs. 3.5c, d and e).
  - Correct identification of R, with $\widehat{R} = R = 1.9\,\Omega$.
  - Underestimate of R, with $\widehat{R} = 0.4R < R$.
  - Overestimate of R, with $\widehat{R} = 1.6R > R$.

Three different gains are considered $K = 69$ (in red), $K = 432$ (in green) and $K = 173$ (in black), which respectively correspond to the most extreme values of K^{met} in the situations detailed above, and to the intermediate one. It should be noticed that an equivalent detuning in both parameters has been contemplated in this section to facilitate the comparison.

As it can be checked from Figs. 3.5a, c and e, the step commanded to i_{q}^* causes some transient on i_{d}, despite having maintained i_{d}^* constant. By comparing Figs. 3.5a and c, it can be observed that such coupling is significantly larger in the presence of L mismatches than when

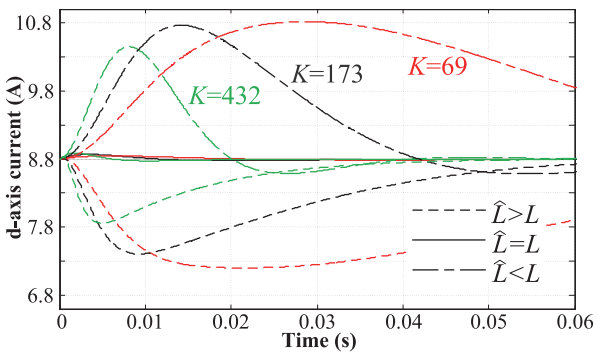

(a) Effect of $\widehat{L}$ on i_{d}.

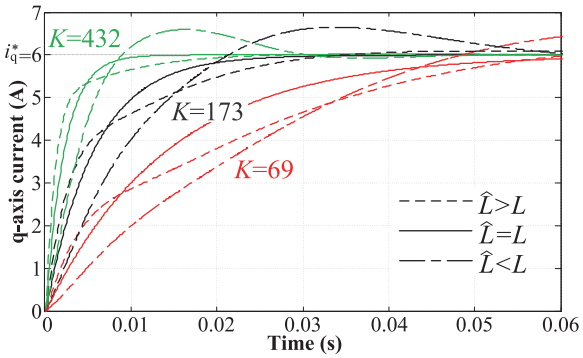

(b) Effect of $\widehat{L}$ on i_{q}.

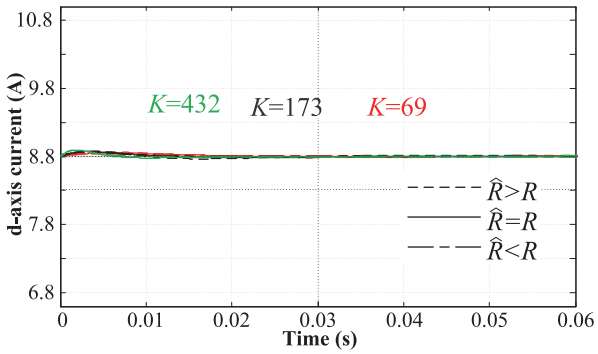

(c) Effect of $\widehat{R}$ on i_{d}.

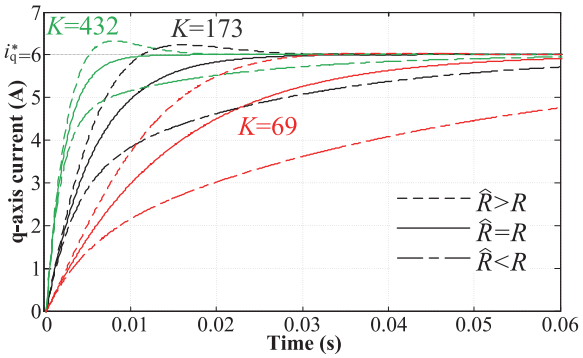

(d) Effect of $\widehat{R}$ on i_{q}.

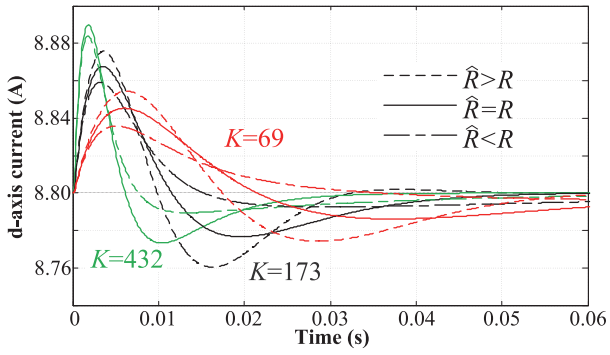

(e) Closer view of (c).

Figure 3.5: Influence of parameter mismatches on the current step response.

R is misestimated. Moreover, from the i_d response in Fig. 3.5a, it is possible to distinguish whether the inductance is underestimated or overestimated. Considering the curves corresponding to a correct parameter estimate $i_\mathrm{d}^{\widehat{\tau}=\tau}$ as a target, the sign of the area encircled by them and the respective curves obtained for $\widehat{L} < L$ is negative, no matter the value of K (cf. Fig. 3.5a). On the contrary, when $\widehat{L} > L$, the sign of the error area is positive. However, this is not fulfilled for the resistance, as it may be checked from Fig. 3.5e, which illustrates a closer view of Fig. 3.5c.

From the comparison of Figs. 3.5b and d, analogous conclusions can be drawn for the resistance estimate and the q-axis response. Similarly, it is also possible to discern whether R is underestimated or overestimated from i_q (cf. Fig. 3.5d), by checking the sign of the error area encircled by the output corresponding with a correct parameter estimation $i_\mathrm{q}^{\widehat{\tau}=\tau}$ and the output with a detuning. When $\widehat{R} < R$ the sign of the error area is positive, whereas when $\widehat{R} > R$ it is negative. This is not satisfied for the inductance, as it can be observed in Fig. 3.5b.

3.4 Identification Method

As demonstrated, L and R mismatches have a significant influence on the complex current step response. Thus, an identification method based on this concept is developed, in which the d-axis response is employed to update L, while the q-axis one is used for R, owing to the advantages commented in the previous section.

A block diagram of the global structure of the estimation method is depicted in Fig. 3.6. In this scheme, the adjustable model (AM) can be distinguished, which is the current control closed loop with the actual plant, as well as the reference model (RM), which is another current closed loop that contains a simulated plant [in the form of (3.3)], and the adaptation mechanism. Hence, the same organization that has led to an accurate estimation of R in chapter §2 is maintained, but in this work both orthogonal components of the plant output i_dq are considered to estimate the two parameters. It is worth remarking that the two control loops have identically tuned PICCD to regulate the current [in the form of (3.2), with the same K, $\widehat{L}$ and $\widehat{R}$]. Furthermore, these parameters also coincide with those of the simulated plant in the RM, so that its output $i_\mathrm{dq}^{\widehat{\tau}=\tau}$ can be used as a target for the actual plant (cf. section §3.3.3). In this manner, the proposal is based on an iterative minimization of the area encircled by $i_\mathrm{dq}^{\widehat{\tau}=\tau}$ and the output of the actual plant i_dq, when successive steps are commanded in i_q^*. The d-axis current reference, which is usually set by an outer loop that regulates the active power transfer, is maintained constant, so that the dynamics of such loop remains practically unaltered (only the effect of the axes decoupling ineffectiveness will be noticed). Thus, a correct identification of L and R is achieved when the complex error signal between both models ε_dq converges to zero. Nevertheless, as in practice unmodeled dynamics such as noise, or nonlinearities may affect the process, when the area is iteratively reduced down to a threshold, instead of stopping the identification process, a refinement stage is started, with the aim of improving the accuracy of the estimates. It should be noticed that, since the method is based on the step response, the resulting estimates are valid for frequencies within the controller bandwidth.

Within each iteration k, two main indicators are calculated from the error between both curves $\varepsilon_a(k,t) = i_a^{\widehat{\tau}=\tau}(k,t) - i_a(k,t)$, for $a = \mathrm{d},\mathrm{q}$. Firstly, in order to distinguish between the underestimate and overestimate cases, the sign of the error area (cf. section §3.3.3) is established by evaluating whether the integral error (IE) $\mathrm{IE}_a(k) = \sum_{t=0}^{t_\mathrm{sto}} \varepsilon_a(k,t) T_\mathrm{s}$ [189] is greater or lower than zero. Secondly, a modified integral absolute error (IAE) $\mathrm{IAE}_a(k) = \sum_{t=0}^{t_\mathrm{sto}} |\varepsilon_a(k,t)|\, T_\mathrm{s}$ [9]

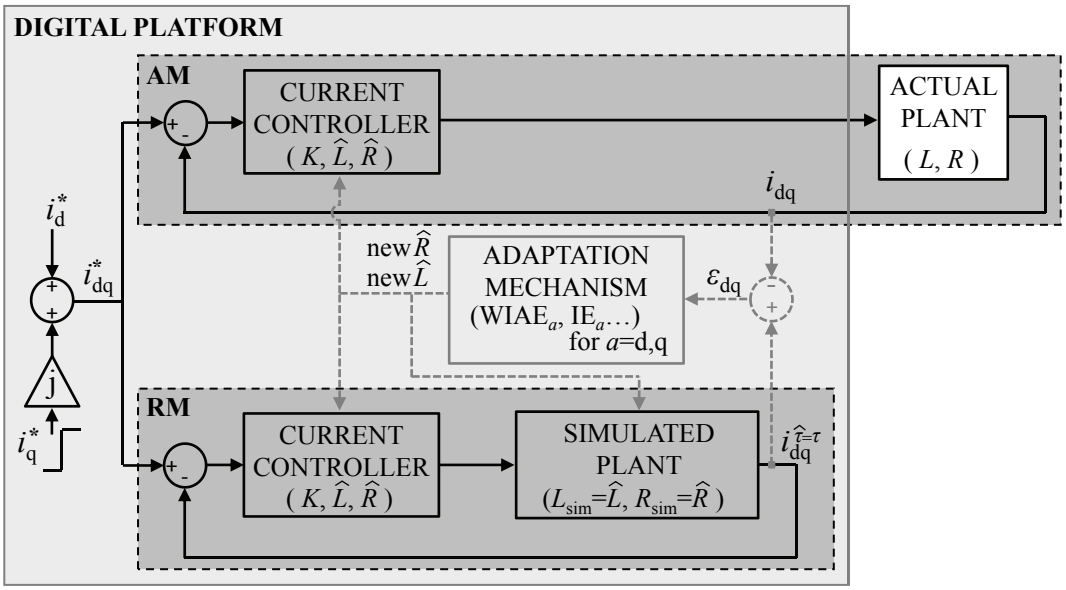

Figure 3.6: Block diagram of the proposed identification algorithm, where the current control closed loop with the actual plant (i.e., AM) and the one with the simulated plant (i.e., RM) are shown.

that weights these two cases quantifies the area, so that it can be directly employed to correct the parameter mismatch, as it will be explained below. Note that the method is not constrained to work only with certain sampling frequencies $f_s = 1/T_s$, as it will be demonstrated with the examples included in Tables 3.2 and 3.3. The same f_s and switching frequency f_{sw} as the ones that the setup was designed for can be employed.

Based on all these features, the developed identification method is summarized in the following steps. The explanation is supported by a detailed flowchart of the iterative process (cf. Fig. 3.7), as well as by an example of application of the proposed algorithm (cf. Fig. 3.8), which corresponds to the first row in Table 3.2 (such conditions are also equivalent to those of case C of the experimental results, as it will be explained in section §3.5).

Step 0) As shown in Fig. 3.7a, initial values for the controller parameters are chosen in the AM and RM. $\widehat{L}(1) = L_F$ and $\widehat{R}(1) = R_F$ are recommended, although the designer can alternatively select any other criteria considering the setup conditions. In addition, the auxiliary boolean variables ***R_low_bound***, ***L_low_bound*** and ***L_upp_bound*** are initialized, and so are the numeric variables L^{met} and R^{met}, which will contain the equivalent inductance and the equivalent resistance identified with the method, respectively. In this example, $\widehat{L}(1) = L_F = 3.8\,\text{mH}$ and $\widehat{R}(1) = R_F = 0.4\,\Omega$ are established.

Step 1) The remaining parameter in (3.2), K, is calculated as $K(k) = K^{met}(k) = \widehat{R}(k)/\widehat{L}(k)$ (cf. section §3.3). The parameters of the simulated plant are set as $L_{sim}(k) = \widehat{L}(k)$ and $R_{sim}(k) = \widehat{R}(k)$. A step of amplitude I_{AMP} in the q-axis current reference i_q^* must be simultaneously commanded to both current control closed loops as indicated in Fig. 3.6, i.e., to the AM and to the RM. The d- and q-components of such curves are shown in Fig. 3.8 for $i_q^* = 4\,\text{A}$ in the theoretical example. At $k = 1$, $K(1) \approx 105$ in Fig. 3.8a.

Step 2) The i_{dq} and $i_{dq}^{\widehat{\tau}=\tau}$ values must be stored during a storing time equal to the settling time $t_{sto} = -\ln|0.01|/K(1)$. The $\text{IE}_a(k)$ and $\text{IAE}_a(k)$ are computed for both axes, i.e., for $a = \text{d},\text{q}$.

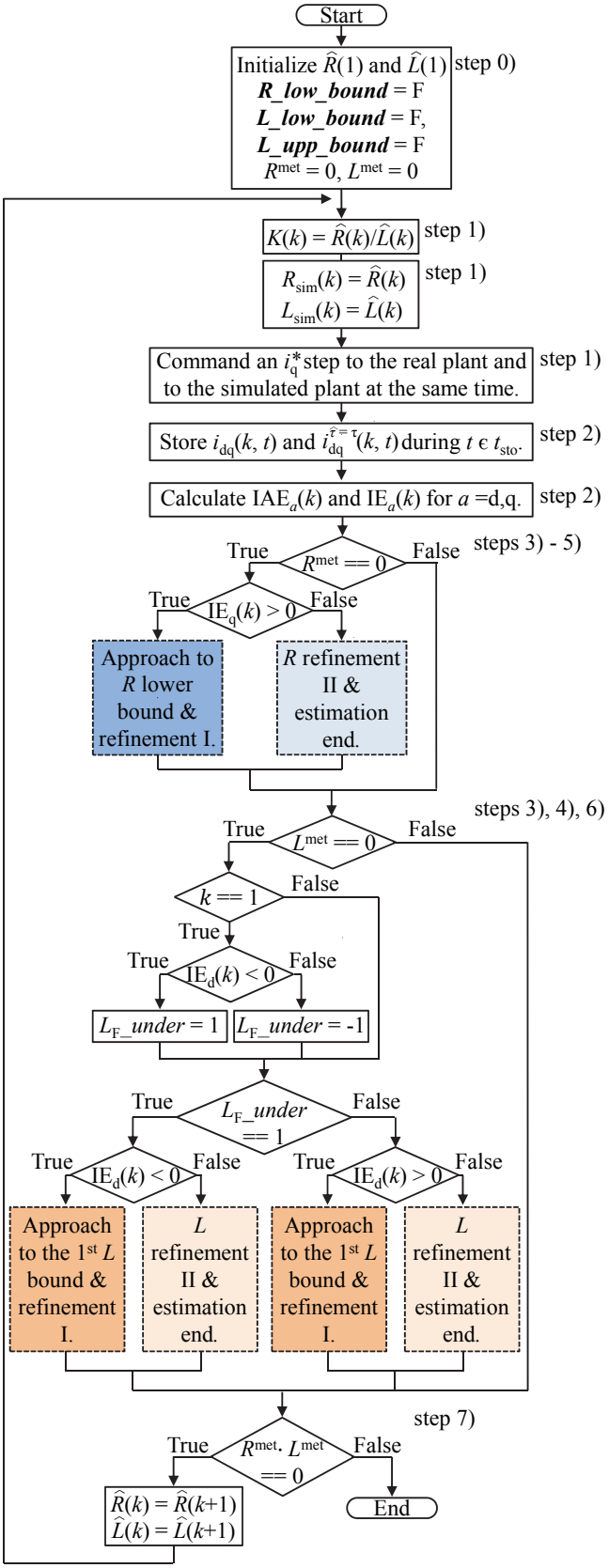

(a) Main diagram.

Figure 3.7: Continued on next page.

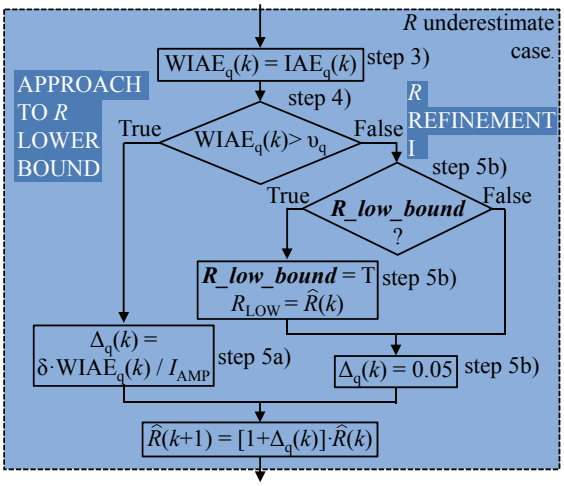

(b) Subdiagram of approach to R lower bound and refinement I.

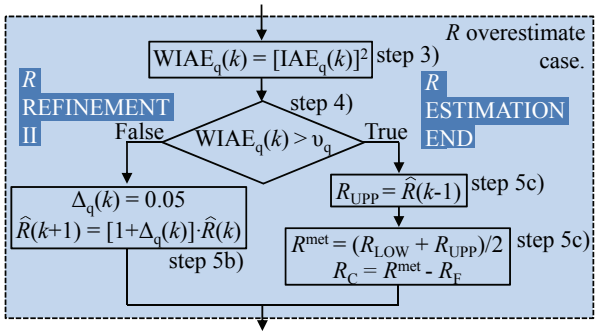

(c) Subdiagram of R refinement II and estimation end.

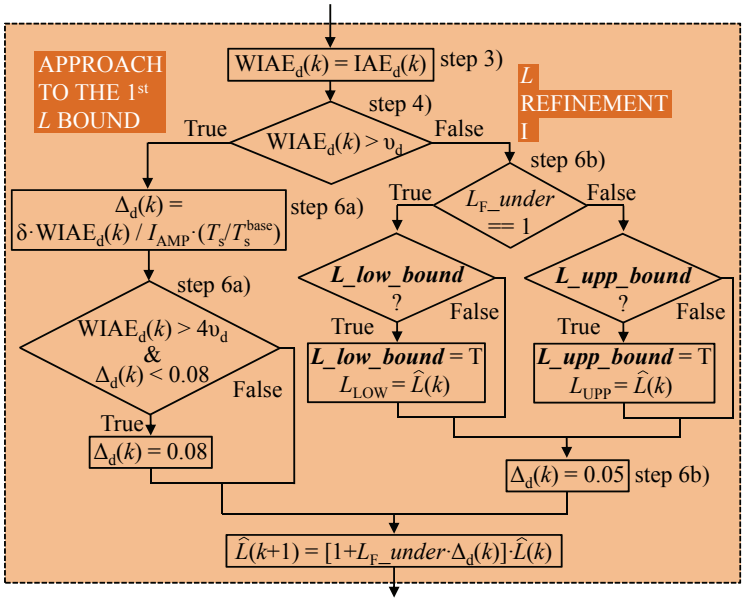

(d) Subdiagram of approach to the 1st L bound and refinement I.

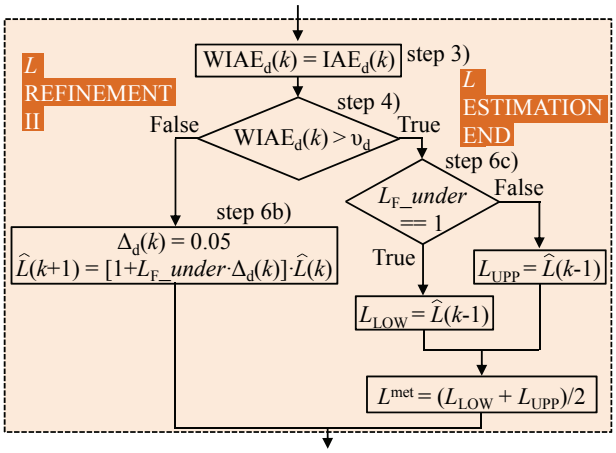

(e) Subdiagram of L refinement II and estimation end.

Figure 3.7: Flowchart of the developed identification method. This figure is continued from previous page.

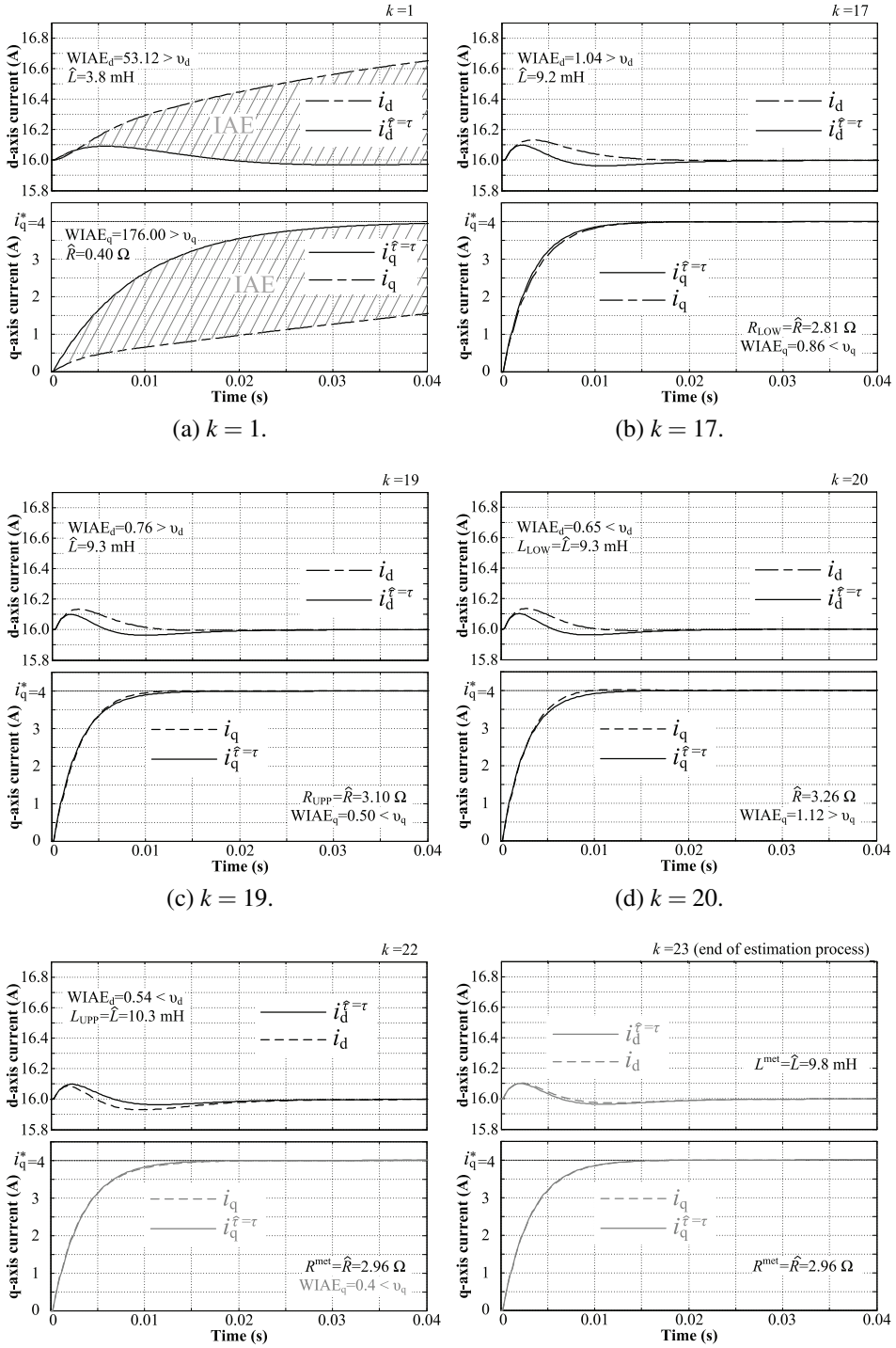

(a) $k = 1$. (b) $k = 17$.

(c) $k = 19$. (d) $k = 20$.

(e) $k = 22$. (f) $k = 23$, at which the identification process ends.

Figure 3.8: i_q step response for the theoretical example (first row in Table 3.2) of the proposed identification method. The k values in each $\widehat{R}$, $\widehat{L}$ and WIAE_a have been omitted for the sake of simplicity. Gray lines and labels are employed in those iterations at which the parameter has already been estimated.

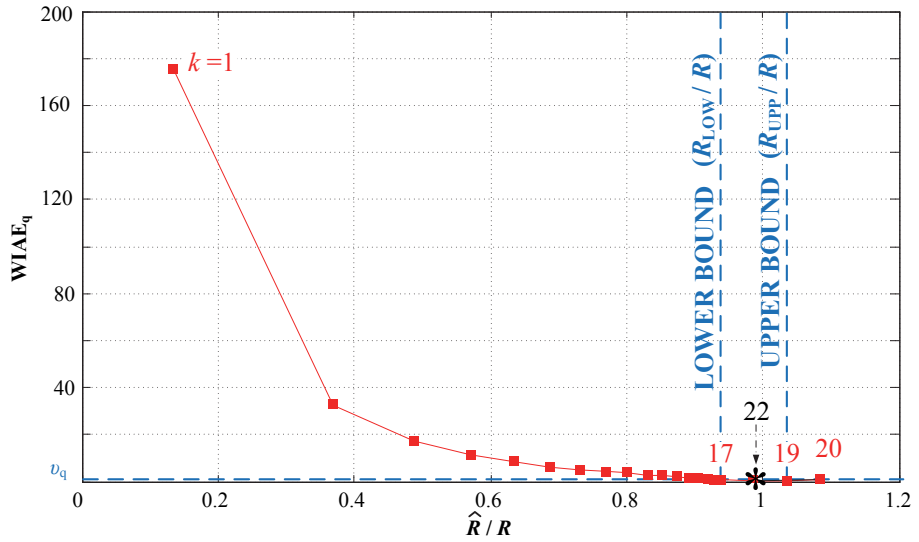

(a) WIAE$_q$ versus $\widehat{R}/R$.

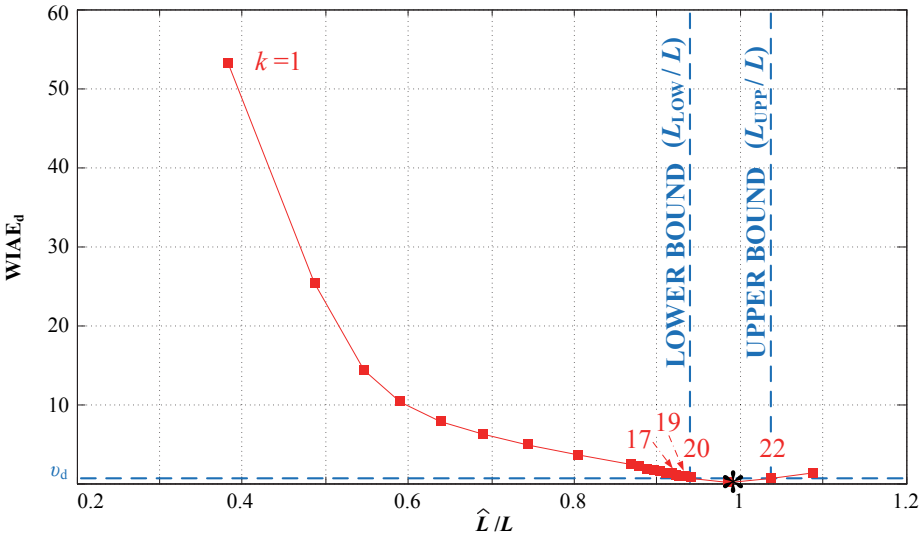

(b) WIAE$_d$ versus $\widehat{L}/L$.

Figure 3.9: Theoretical example of the proposed identification method. Note that the iteration number k increases from left to right and only the number of those iterations that are displayed in Fig. 3.8 are indicated. A black asterisk is employed in those iterations at which the respective parameter has already been estimated.

In Fig. 3.8, the IAE corresponds to the area limited by each pair of curves, i.e., between $i_a^{\widehat{\tau}=\tau}$ and i_a (see the striped area in Fig. 3.8a). In the example, $t_{\text{sto}} \approx 44\,\text{ms}$.

Step 3) The weighted IAE_a (WIAE_a) is calculated:

$$\text{WIAE}_\text{d}(k) = \text{IAE}_\text{d}(k) \tag{3.7}$$

$$\text{WIAE}_\text{q}(k) = \begin{cases} \text{IAE}_\text{q}(k) & \text{if} \quad \text{IE}_\text{q}(k) \geq 0 \\ [\text{IAE}_\text{q}(k)]^2 & \text{if} \quad \text{IE}_\text{q}(k) < 0. \end{cases} \tag{3.8}$$

From Fig. 3.9, which shows WIAE_q versus $\widehat{R}/R$ and WIAE_d versus $\widehat{L}/L$ for all the iterations in the theoretical example, it can be observed that WIAE_a exhibits a symmetric behavior around $\widehat{R}/R = 1$ and $\widehat{L}/L = 1$, weighting the underestimated and overestimated cases. This graphic is also helpful to understand all the steps of the identification process. Note that the weighted IAE (WIAE) convergence to zero in both axes is achieved at the end of the process.

Step 4) Then, it should be checked whether the $\text{WIAE}_a(k)$ is smaller or larger than a threshold υ_a. In the example, $\upsilon_\text{q} = 1$ and $\upsilon_\text{d} = 0.67$ are obtained.

Step 5) Focusing on R estimation ($a = \text{q}$).

Step 5a) In the first iterations the common situation is that $\text{IE}_\text{q}(k) > 0$ and $\text{WIAE}_\text{q}(k) > \upsilon_\text{q}$, since $\widehat{R}(k) \ll R$. During this stage (labeled as "Approach to R lower bound" in Fig. 3.7b), the objective is a quick reduction of WIAE_q down to υ_q. $\widehat{R}$ for the next iteration is increased a percentage $\Delta_\text{q}(k)$, which is calculated as $\Delta_\text{q}(k) = \delta\text{WIAE}_\text{q}(k)/I_\text{AMP}$. While usage of $\text{WIAE}_\text{q}(k)$ for $\Delta_\text{q}(k)$ calculation provides the new $\widehat{R}$ with information about how far its previous value was from R, that of I_AMP permits to make $\Delta_\text{q}(k)$ independent from the current amplitude. In Fig. 3.8a of the theoretical example, i.e., at the first iteration, $\text{WIAE}_\text{q}(1) = 176.00 > \upsilon_\text{q}$, so $\widehat{R}(2) = 1.1\,\Omega$. Next, the process continues with step 6).

Step 5b) When $\text{WIAE}_\text{q}(k) < \upsilon_\text{q}$ [still $\text{IE}_\text{q}(k) > 0$, i.e., this case corresponds to the path labeled as "R refinement I" in Fig. 3.7b], an underestimated value of R that leads to a greater precision than υ_q is obtained. The value of $\widehat{R}(k)$ in the first iteration at which this condition is satisfied is stored in R_LOW (subscript LOW refers to the lower bound in the identification process) and the refinement stage starts. $\widehat{R}(k+1)$ is increased a fixed percentage (cf. section §3.4.1). In the example, this happens at $k = 17$, as depicted in Fig. 3.8b, where $\text{WIAE}_\text{q}(17) = 0.86 < \upsilon_\text{q}$, $R_\text{LOW} = \widehat{R}(17) = 2.81\,\Omega$ and $\widehat{R}(18) = 2.96\,\Omega$.

Next, the process should continue with L estimation, i.e., step 6). Concerning R estimation, the new aim will be finding R_UPP (subscript UPP refers to the upper bound), i.e., the overestimated value that corresponds to a precision better than υ_q. Therefore, at a certain k, $\text{IE}_\text{q}(k) < 0$, so the refinement stage will be the one in Fig. 3.7c, instead of that in Fig. 3.7b. An example of this case is represented in Fig. 3.8c, where $\text{WIAE}_\text{q}(19) = 0.50 < \upsilon_\text{q}$ and $\widehat{R}(19) = 3.10\,\Omega$, so $\widehat{R}(20) = 3.26\,\Omega$.

Step 5c) When $\text{WIAE}_\text{q}(k) > \upsilon_\text{q}$ and $\text{IE}_\text{q}(k) < 0$, the refinement stage ends. The value of $\widehat{R}(k-1)$ is stored in R_UPP. Then, R^met is obtained as the average value of R_LOW and R_UPP and the process of R identification has ended. In the example, this happens at $k = 20$ (cf. Fig. 3.8d), where $\text{WIAE}_\text{q}(20) = 1.12 > \upsilon_\text{q}$, so $R_\text{UPP} = \widehat{R}(19) = 3.10\,\Omega$ (cf. Fig. 3.8c). Thus, $R^\text{met} = (2.81 + 3.10)/2 = 2.96\,\Omega$.

Step 6) Subsequently, a similar process to the one described in steps 5a)-5c) is executed for L identification ($a = \text{d}$).

Step 6a) "Approach to the 1st L bound", detailed in Fig. 3.7d (Figs. 3.8a, b and c show examples of this stage).

Step 6b) "L refinement", specified in Figs. 3.7d and e (Figs. 3.8d and e, with $L_{\mathrm{LOW}} = \widehat{L}(20) = 9.3\,\mathrm{mH}$ and with $L_{\mathrm{UPP}} = \widehat{L}(22) = 10.3\,\mathrm{mH}$, respectively, are examples of this stage).

Step 6c) "L estimation end", explained in Fig. 3.7e [at $k = 23$ with $L^{\mathrm{met}} = (9.3 + 10.3)/2 = 9.8\,\mathrm{mH}$].

After any of the steps 6a), 6b) or 6c), the process should be repeated from step 1).

***Step 7*)** Once both final parameter estimates R^{met} and L^{met} are obtained, the iterative process ends. The corresponding step response with the identified parameters for the theoretical example is the one in Fig. 3.8f.

It should be noticed that relevant modifications are made in step 6) with respect to the process of R estimation. Firstly, initial overestimation of L is also regarded. A priori, whether the inductance is underestimated or overestimated is unknown by the designer. By the evaluation of $\mathrm{IE_d}(1)$ sign, both cases are discerned (cf. Fig. 3.7a). Secondly, as the delay has an important influence in the axes cross coupling [197], i.e., in i_{d} when a step is commanded to i_{q}, $\Delta_{\mathrm{d}}(k)$ should be weighted by T_{s}. Hence, during the stage of "Approach to the 1st L bound", $\Delta_{\mathrm{d}}(k) = \delta\mathrm{WIAE_d}(k)/I_{\mathrm{AMP}} \cdot (T_{\mathrm{s}}/T_{\mathrm{s}}^{\mathrm{base}})$, with $T_{\mathrm{s}}^{\mathrm{base}} = 100\,\mu\mathrm{s}$ (cf. Fig. 3.7d). Finally, with the aim of accelerating the reduction of $\mathrm{WIAE_d}$ down to υ_{d}, a new condition has been included in Fig. 3.7d, which sets a minimum Δ_{d} for those cases in which the indicator is very far from the threshold. This permits a decrease in the number of iterations, especially when very low $\widehat{L}(1)$ are employed.

3.4.1 Parameter Tuning Guidelines

- υ_{d} and υ_{q}. The threshold values must be calculated as a function of I_{AMP}. From Fig. 3.2, the coupling on the d-axis when a step is commanded to i_{q} depends on the amplitude of the latter, i.e., on I_{AMP}. As both $\mathrm{WIAE_d}$ and $\mathrm{WIAE_q}$ are calculated from $\mathrm{IAE_d}$ and $\mathrm{IAE_q}$ [see (3.7) and (3.8)], which in turn are obtained from the d- and q-axis errors between the outputs of the real and simulated loops, $\mathrm{WIAE_d}$ and $\mathrm{WIAE_q}$ depend on I_{AMP}, and so should the thresholds. In addition, it may be taken into account that large values of υ_{d} and υ_{q} lead to a worse precision in the estimates, whereas low values result in a better one.

- Minimum Δ_{d} and Δ_{q}. The lower the value of these parameters, the better the precision of the estimates, but also the higher the number of iterations needed during the refinement stages (cf. Figs. 3.7b-e). Therefore, a tradeoff should be reached. As they are set as percentages, the same Δ_{d} and Δ_{q} can be employed independently from the order of magnitude of the inductance and resistance, even the same value for both parameters, as long as they lead to a good enough precision and a reasonable number of iterations.

- I_{AMP}. Two main points should be considered. On the one hand, the magnitude of the commanded step has to be large enough, so that the estimation is not polluted by the electric noise or by any kind of unmodeled dynamics (e.g., harmonics caused by nonlinearities, such as dead times [193]). On the other hand, during such transient, the normal behavior of the system should not be altered (e.g., by triggering the protections, by unintentionally producing saturation or by preventing the usual control objective from being fulfilled during a significant period of time). It is worth mentioning that, provided that

Table 3.1: Recommended Estimation Method Parameters.

Parameter	Recommended Value
υ_{d}	$I_{\mathrm{AMP}}/6$
υ_{q}	$I_{\mathrm{AMP}}/4$
Minimum Δ_{d} and Δ_{q}	$0.05(5\%)$
I_{AMP}	$0.25\,i_{\mathrm{d}}$
δ	$1/25$

these two premises are fulfilled, the proposed estimation algorithm has been designed to be practically independent from I_{AMP} by its consideration in the adjustment of υ_a (see the first paragraph of this subsection), as well as in $\Delta_{\mathrm{d}}(k)$ and $\Delta_{\mathrm{q}}(k)$ [see steps 5a) and 6a) of the estimation algorithm].

Apart from these guidelines, recommended values for the different parameters involved in the estimation method are included in Table 3.1. Such values have been chosen after having obtained satisfactory results in all the cases tested, which cover a wide range of rated powers P_{rated}, rated line-to-line voltages V_{LLrated}, power levels P_{level}, currents, f_{sw}, f_{s} and equivalent inductances and resistances in the current loop, either with L or with LCL filters (see Tables 3.2 and 3.3). Note that setting $I_{\mathrm{AMP}} = 0.25\,i_{\mathrm{d}}$ implies just a 3% increase in the total amplitude. It is suggested to employ these same values the first time that the estimation is applied in some specific conditions. In a second approach, the designer may change them, according to the guidelines given above and the obtained results.

3.4.2 Implementation Aspects

Two implementation options are possible: the developed algorithm could be used online, with some restrictions, or it may be employed offline, during a precommissioning stage.

Regarding the former alternative, a PICCD must be adopted to regulate the positive-sequence fundamental component of the current. This fact does not mean that other controllers cannot be added in parallel with the aim of regulating the negative-sequence one (e.g., a resonant controller tuned at $2\omega_1$ in the SRF [65]) or of rejecting some harmonic components (e.g., resonant controllers in the stationary or in the SRF [4, 7, 58, 77, 81, 111]). Nevertheless, while the estimation process is working, such controllers should be disabled momentarily. Otherwise, the system dynamics would be more complicated than the one modeled in Fig. 3.2b, and the transient response would not correspond with the expected one, which could lead to errors in the estimates. Once the plant parameters L and R are identified, such controllers can be reestablished.

On the other hand, when opting for an offline implementation, the current controller in the final application may be different from that used during the identification (precommissioning stage), i.e., distinct from a PICCD. Thus, e.g., controllers able to regulate the positive and the negative sequences of the fundamental component, such as resonant ones [58, 65, 77, 111], or double SRF PI controllers [9, 58, 65] can be selected with no need to cancel their effect momentarily, as the estimation has been previously completed. In the same manner, harmonic regulators may also be added [4, 7, 58, 77, 81, 111].

During the identification process, it is necessary to command steps in the q-axis current reference. Hence, in case that such current reference has to be set by an outer loop that regulates the voltage [58, 198], the application of the proposal is limited to a precommissioning stage (during which, the elimination of this outer loop is possible).

On the other hand, it is assumed that Z_{TH} and I_{AMP} are small enough to disregard their effect on the phase-locked loop (PLL) through the PCC voltage, and hence, the effect of the PLL on L^{met} and R^{met}. If this were not the case, grid synchronization should be implemented by extracting the phase from the grid frequency estimation provided, e.g., by a filtered and transient-free version of a PLL frequency intermediate signal [91].

3.4.3 Other Theoretical Examples

With the aim of evaluating the estimation errors and the speed of convergence in a wide range of conditions, the developed method has been applied to several theoretical examples, which are illustrative cases in different applications. Thus, distinct P_{rated}, $V_{\mathrm{LL\,rated}}$, P_{level}, f_{sw} and f_{s} have been adopted, for both L and LCL filters, as indicated in Table 3.2. Moreover, different L and R values are regarded, due to distinct L_{F}, ΔL_{F} and L_{TH} and to distinct R_{F}, R_{C} and R_{TH}, respectively. In other words, some of these examples illustrate operation under the rated conditions, some others over them; some cases include significant grid impedances, while some others do not. In the examples with LCL filters, the parameters L_{F} and R_{F} have been calculated as the addition of the corresponding ones of the grid- and converter-side inductors, as done in section §3.3.2, i.e., $L_{\mathrm{F}} = L_{\mathrm{GS}} + L_{\mathrm{CS}}$ and $R_{\mathrm{F}} = R_{\mathrm{GS}} + R_{\mathrm{CS}}$ [102, 106]. C_{F} has been selected so that the LCL resonant frequency is $f_{\mathrm{s}}/8$ and $R_{\mathrm{D}} = 0.28$ p.u. has been added in series with it to guarantee the system stability [78, 102, 104]. In all these cases, the initial conditions are set as $\widehat{L}(1) = L_{\mathrm{F}}$ and $\widehat{R}(1) = R_{\mathrm{F}}$, following the recommendations given at the beginning of this section. The parameters of the estimation method have been tuned according to Table 3.1.

As it can be checked from Table 3.2, L^{met} and R^{met} match with good accuracy L and R, respectively, in few iterations ($k_{\max}$ represents the number of iterations that results from the application of the method) for all the examples. Therefore, the performance of the estimation method in terms of speed of convergence and error in the estimates is demonstrated for a wide range of conditions. In addition, no significant differences can be observed between the results obtained with both types of filters, corroborating that the method is also valid when LCL ones are employed, as expected from section §3.3.2.

On the other hand, a study of the regions of convergence as a function of the parameter mismatches is conducted for the five cases in Table 3.2. Fig. 3.10 summarizes the results. For such analysis, the parameters of the estimation method have been tuned according to Table 3.1. The initial estimates have been set as $\widehat{L}(1) = L_{\mathrm{F}}$ and $\widehat{R}(1) = R_{\mathrm{F}}$ and the effect of different ratios $\widehat{L}(1)/L$ and $\widehat{R}(1)/R$ has been assessed by varying L and R, respectively, which a priori are unknown by the designer. Sixteen different ratios have been considered for the inductance, from 0.1 to 10, and eight for the resistance, from 0.1 to 0.8. Note that some of the values tested correspond to very large mismatches, difficult to appear in practice (e.g., in the example of the first row, in which $\widehat{L}(1) = L_{\mathrm{F}} = 3.8\,\mathrm{mH}$ and $\widehat{R}(1) = R_{\mathrm{F}} = 0.4\,\Omega$, variations of L from 38 mH to 0.38 mH and of R up to $4\,\Omega$ are regarded). From Fig. 3.10, it can be observed that the regions of convergence cover the majority of the areas under analysis, especially in the examples corresponding to the first, second and third rows of the table (these only diverge in some cases in which $\widehat{L}(1) = 10L$, also with a resistance mismatch). As expected due to the low f_{s} and f_{sw},

Table 3.2: Theoretical Examples of Application of the Proposed Method

P_{rated} ($V_{\text{LL}_{\text{rated}}}$)	P_{level} ($P_{\text{level}}/P_{\text{rated}}$)	f_{sw} (f_{s})	L $= L_{\text{F}} + \Delta L_{\text{F}} + L_{\text{TH}}$	R $= R_{\text{F}} + R_{\text{C}} + R_{\text{TH}}$	L			LCL		
					L^{met}	R^{met}	k_{max}	L^{met}	R^{met}	k_{max}
25 kW	8 kW	5 kHz	9.9 mH	3 Ω	9.8 mH	2.96 Ω	23	9.8 mH	2.98 Ω	26
(400 V)	(32%)	(5 kHz)	$= 3.8 + 0.4 + 5.7$ mH	$= 0.4 + 1.4 + 1.2$ Ω						
11 kW	9 kW	8 kHz	3.37 mH	1.73 Ω	3.4 mH	1.77 Ω	25	3.4 mH	1.77 Ω	24
(400 V)	(82%)	(8 kHz)	$= 2.75 + 0.1 + 0.52$ mH	$= 0.12 + 0.33 + 1.28$ Ω						
4.1 kW	5 kW	5 kHz	7 mH	0.32 Ω	7 mH	0.32 Ω	15	7 mH	0.32 Ω	15
(400 V)	(122%)	(10 kHz)	$= 5 - 1 + 3$ mH	$= 0.11 + 0.11 + 0.1$ Ω						
600 kW	650 kW	2.5 kHz	0.3 mH	0.11 Ω	0.3 mH	0.10 Ω	17	0.3 mH	0.11 Ω	17
(690 V)	(108%)	(5 kHz)	$= 0.4 - 0.1 + 0$ mH	$= 0.01 + 0.1 + 0$ Ω						
6 MW	1.5 MW	1.05 kHz	2.2 mH	0.31 Ω	2 mH	0.32 Ω	10	2 mH	0.32 Ω	7
(3.3 kV)	(25%)	(2.1 kHz)	$= 2.08 + 0.12 + 0$ mH	$= 0.01 + 0.3 + 0$ Ω						

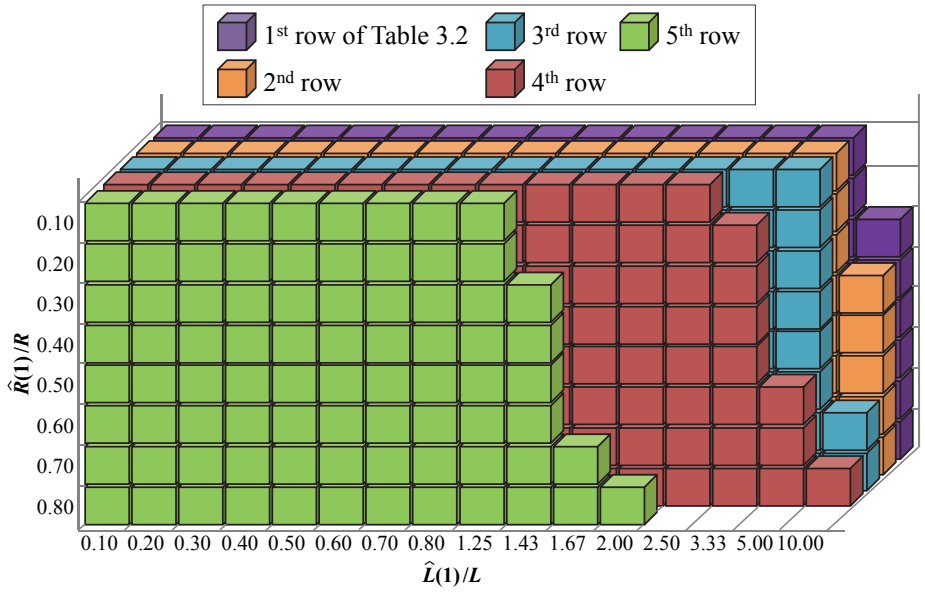

Figure 3.10: Regions of convergence as a function of L and R mismatches for the examples in Table 3.2.

the example of the fifth row is the most critical one. In all the cases, the convergence worsens with L and R mismatches, with the former being overestimated. In conclusion, the developed method converges in most of the cases under analysis. Nevertheless, there is certain tendency to divergence in those conditions in which there are very large initial mismatches between the estimated and real values of the parameters, particularly when the sampling frequency is very low.

3.5 Experimental Results

In order to experimentally validate the developed estimation technique, a three-phase grid-tied VSC (of 25 kVA) working as a rectifier has been built, which feeds a dc load R_{L} (cf. Fig. 3.11). Its main parameters are specified in Table 3.3, in addition to $v_{\mathrm{dc}} = 750\,\mathrm{V}$ and $v_{\mathrm{PCC\,rms}} = 230\,\mathrm{V}$. The digital control is executed in a dSPACE MABXII DS1401 platform. As illustrated in the scheme of Fig. 3.11b, the current is regulated by an SRF PICCD, whose reference i_{d}^{*} is generated by an outer loop, which controls v_{dc}. The other current component i_{q}^{*} is set directly, to command the required steps (cf. section §3.4). The actual i_{d} and i_{q} are internally calculated from the measured currents, and then visualized in the oscilloscope through digital-to-analog converters (DACs). The delay compensation term $\mathrm{e}^{\mathrm{j}\omega_1 T_{\mathrm{d}}}$ is implemented by the addition of a phase lead $\omega_1 T_{\mathrm{d}}$ to θ_1 before being input to the inverse transformation [10]. The same i_{q}^{*} step as in the actual control loop is commanded to the simulated control loop $G_{\mathrm{CL}}(z)$ in the digital platform, which is composed of an identical SRF PICCD that in this case regulates the simulated plant $G_{\mathrm{PL}}(z)$, whose parameters are $L_{\mathrm{sim}} = \widehat{L}$ and $R_{\mathrm{sim}} = \widehat{R}$ [cf. (3.3), section §3.4 and the shaded block in Fig. 3.11b]. The outputs of the simulated plant $i_{\mathrm{d}}^{\widehat{\tau}=\tau}$ and $i_{\mathrm{q}}^{\widehat{\tau}=\tau}$ are extracted through another two DACs.

[1] Inductance values for $i_{\mathrm{d}} = 9\,\mathrm{A}$.

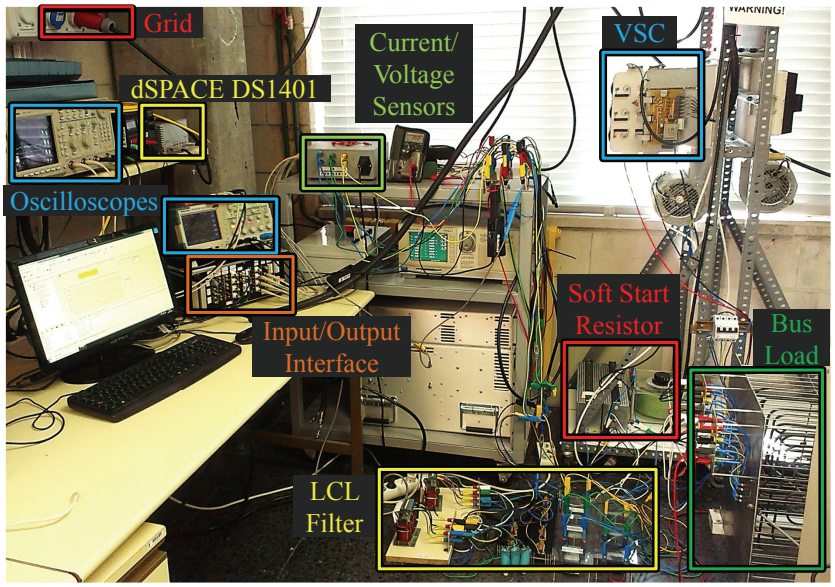

(a) Photograph.

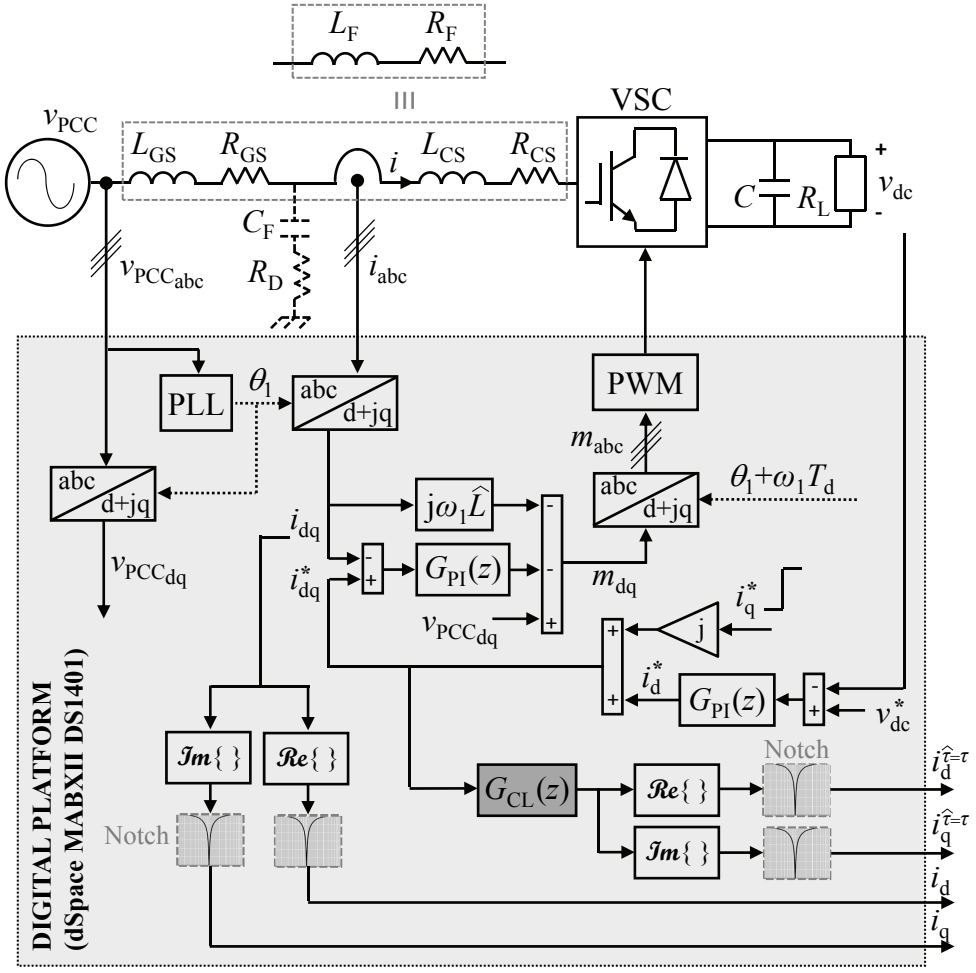

(b) Scheme.

Figure 3.11: Experimental setup.

Table 3.3: Experimental Setup Parameters of the Different Cases Tested

Case (filter)	P_{dc}	f_{sw}	f_{s}	i_{d}	i_{q}^{*}	L_{F}[1] ($L_{\mathrm{GS}}+L_{\mathrm{CS}}$)	$R^{[14]}$	$\widehat{L}(1)$	$\widehat{R}(1)=R_{\mathrm{F}}$ ($R_{\mathrm{GS}}+R_{\mathrm{CS}}$)	L^{met}	R^{met}	k_{max}
A (L)	4.3 kW	10 kHz	10 kHz	9 A	6 A	5.9 mH	2.3 Ω	$1.6L_{\mathrm{F}}=9.4$ mH	0.4 Ω	5.9 mH	2.29 Ω	20
B (LCL)	4.3 kW	5 kHz	10 kHz	8.8 A	6 A	10.9 mH (5 mH + 5.9 mH)	1.9 Ω	$1.6L_{\mathrm{F}}=17.4$ mH	0.45 Ω (0.05 Ω + 0.4 Ω)	11 mH	1.88 Ω	15
C (L)	2 kW	5 kHz	5 kHz	4.5 A	4 A	9.5 mH	3 Ω	$0.4L_{\mathrm{F}}=3.8$ mH	0.4 Ω	9.8 mH	2.96 Ω	23
D (L)	2 kW	2.5 kHz	2.5 kHz	4.5 A	4 A	12.1 mH	1.7 Ω	$0.4L_{\mathrm{F}}=4.8$ mH	0.4 Ω	12.6 mH	1.77 Ω	10

As it can be checked from Table 3.3, some of the conditions in which the method proposed in this chapter is tested are analogous to those in chapter §2. These are the cases A, C and D, which consist in identifying the plant parameters under different conditions of power level and switching frequency. Additionally, in this work, experiments with an LCL filter have been also carried out (cf. case B in Table 3.3).

In order to test the performance of the method when the inductance is initially overestimated, i.e., $\widehat{L}(1) > L$, if $\widehat{L}(1) = L_{\mathrm{F}}$ is established as in section §3.4, the inductor should be saturated, i.e., $(\Delta L_{\mathrm{F}} + L_{\mathrm{TH}}) < 0$. As the electric installation cannot handle as much current as it would be needed to saturate the inductors, the following procedure has been adopted, which permits to perform the tests in equivalent conditions from the algorithm viewpoint. Instead of considering $\widehat{L}(1) = L_{\mathrm{F}}$, initial mismatches in the inductance estimate are set with respect to L_{F}, to represent such overestimation: $\widehat{L}(1) = 1.6 L_{\mathrm{F}}$ in cases A and B of Table 3.3. Analogously, the same idea is applied to test the proposal under initial inductance underestimates: $\widehat{L}(1) = 0.4 L_{\mathrm{F}}$, in cases C and D of Table 3.3. An equivalent procedure has been adopted to validate the proposals of [55, 100, 107, 120, 126]. In addition, initial mismatches of the same (or smaller) value have been contemplated in the related bibliography [86–89, 106].

The equivalence between both alternatives can be further verified by comparing the theoretical example used to support the method explanation (1st row in Table 3.2) and case C in the experimental results (3rd row in Table 3.3). In both, $\widehat{L}(1) = 3.8\,\mathrm{mH}$ and $L = 9.9\,\mathrm{mH}$, although $L = L_{\mathrm{F}} + \Delta L_{\mathrm{F}} + L_{\mathrm{TH}} = 3.8\,\mathrm{mH} + 0.4\,\mathrm{mH} + 5.7\,\mathrm{mH}$ in the former, while $L_{\mathrm{F}} = 9.5\,\mathrm{mH}$ and $(\Delta L_{\mathrm{F}} + L_{\mathrm{TH}}) = 0.4\,\mathrm{mH}$ in the latter. Regarding the resistance, $\widehat{R}(1) = R_{\mathrm{F}} = 0.4\,\Omega$ and $R = 3\,\Omega$ in both, but $R_{\mathrm{C}} + R_{\mathrm{TH}} = 1.4\,\Omega + 1.2\,\Omega$ in the theoretical example, whereas $(R_{\mathrm{C}} + R_{\mathrm{TH}}) = 2.6\,\Omega$ in the experiments. Note that $i_{\mathrm{d}} = 16\,\mathrm{A}$ is flowing in the former, while $i_{\mathrm{d}} = 4.5\,\mathrm{A}$ in the latter, so R_{C} is actually larger in the real test than in the simulated one; i.e., the current limit imposed by the installation makes impossible to test substantial changes in L, but not in R.

It can be noted that in the experiments, the magnitude of the commanded steps is relatively large, with respect to the current that is circulating before the step, as it can be checked from Table 3.3. Such step magnitude has been set with the aim of fulfilling the first premise, immunizing from noise and unmodeled dynamics (cf. section §3.4.1), which are larger than usual, since the experimental setup is working at very low power levels, with respect to the nominal one. Owing to this same fact, selecting such amplitude does not lead to any problem with respect to the second premise, as there is not risk of triggering the converter protections or of producing saturation.

3.5.1 Estimation Method

The developed method is employed to experimentally identify the plant parameters R and L in the conditions of case A in Table 3.3 ($P_{\mathrm{dc}} = 4.3\,\mathrm{kW}$ and $f_{\mathrm{sw}} = f_{\mathrm{s}} = 10\,\mathrm{kHz}$). Results of the most significant iterations during the estimation process are included in Fig. 3.12. Starting from $\widehat{R}(1) = 0.4\,\Omega$ and $\widehat{L} = 9.4\,\mathrm{mH}$ (cf. Fig. 3.12a), $R^{\mathrm{met}} = 2.29\,\Omega$ and $L^{\mathrm{met}} = 5.9\,\mathrm{mH}$ are determined in 20 iterations (cf. Fig. 3.12f). Intermediate iterations are also depicted in Figs. 3.12b-e. Fig. 3.12a exemplifies the approach to the first bound stage in the identification of both parameters. A few iterations later, at $k = 8$ (cf. Fig. 3.12b), the refinement stage starts for L, since $L_{\mathrm{UPP}} = \widehat{L} = 6.1\,\mathrm{mH}$ is established, while the estimation of R remains in the previous stage. At $k = 10$, L_{LOW} is identified to be that of the previous iteration $k = 9$ (cf. Fig. 3.12c), i.e., $L_{\mathrm{LOW}} = \widehat{L} = 5.8\,\mathrm{mH}$, and $L^{\mathrm{met}} = 5.9\,\mathrm{mH}$ is obtained. From Figs. 3.12d and e, the refine-

ment stage in R estimation begins at $k = 16$, with the detection of $R_{\mathrm{LOW}} = \widehat{R} = 2.12\,\Omega$ and ends at $k = 20$, when R_{UPP} is set to be that of $k = 19$, i.e., $R_{\mathrm{UPP}} = \widehat{R} = 2.45\,\Omega$. Therefore, at $k = 20$, $R^{\mathrm{met}} = 2.29\,\Omega$ and $L^{\mathrm{met}} = 5.9\,\mathrm{mH}$ are identified and the estimation process ends (see how each pair of curves $i_{\mathrm{d}}^{\widehat{\tau}=\tau} - i_{\mathrm{d}}$ and $i_{\mathrm{q}}^{\widehat{\tau}=\tau} - i_{\mathrm{q}}$ overlaps).

3.5.2 Estimation with an LCL filter

The performance of the proposed method when an LCL filter is employed to mitigate the switching harmonics rather than an L one should be experimentally validated, as these filters are widely employed in many grid-tied applications [78, 88, 102, 104, 106, 111, 154]. Thus, a test according to the conditions labeled as case B in Table 3.3 is conducted. Note that $L_{\mathrm{F}} = L_{\mathrm{GS}} + L_{\mathrm{CS}}$ and $R_{\mathrm{F}} = R_{\mathrm{GS}} + R_{\mathrm{CS}}$ are considered [102, 106], as indicated in section §3.4.3 and Fig. 3.11b. In addition, $C_{\mathrm{F}} = 6\,\mu\mathrm{F}$ and $R_{\mathrm{D}} = 10\,\Omega$ (0.28 p.u.) have been selected (cf. section §3.4.3 and Fig. 3.11b). Fig. 3.13 shows the results. Figs. 3.13a and b depict two representative iterations: the first one (with $\widehat{R} = 0.45\,\Omega$ and $\widehat{L} = 1.6L_{\mathrm{F}} = 17.4\,\mathrm{mH}$) and that at which the first refinement stage starts (in this case, L refinement stage, with $\widehat{R} = 0.89\,\Omega$ and $L_{\mathrm{UPP}} = \widehat{L} = 11.5\,\mathrm{mH}$). Fig. 3.13c illustrates the transient response obtained with the final parameter estimates $R^{\mathrm{met}} = 1.88\,\Omega$ and $L^{\mathrm{met}} = 11\,\mathrm{mH}$ after 15 iterations. This same experimental test, i.e., case B, has been repeated with an L filter and the same R^{met} and L^{met} were identified, validating the conclusions of section §3.3.2.

3.5.3 Effect of Power Level and Switching Frequency

Similarly to the experiments in chapter §2, the proposed method is applied to the test bench working at two different f_{sw} and at a power level of 2 kW, both distinct from those in case A (cf. cases C and D in Table 3.3). In these two cases, an initial underestimate of L [$\widehat{L}(1) = 0.4L_{\mathrm{F}}$] has been regarded. As commented at the beginning of this section, the conditions of case C, in which $f_{\mathrm{sw}} = 5\,\mathrm{kHz}$, are equivalent to those of the example used to support the explanation of the developed method, i.e., to those detailed in the first row of Table 3.2 and employed in Figs. 3.8 and 3.9. Figs. 3.14a, b and c show the results at three significant iterations (the same three as in Figs. 3.8a, b and f, respectively). More specifically, these iterations correspond to the first one, to that at which the first refinement stage starts (in this case, that of R) and to the end of the process, once $R^{\mathrm{met}} = 2.96\,\Omega$ and $L^{\mathrm{met}} = 9.8\,\mathrm{mH}$ are established at $k = 23$, respectively. Good matching between theoretical (cf. Figs. 3.8a, b and f) and experimental (cf. Figs. 3.14a, b and c) results is observed.

Figs. 3.15a, b and c depict analogous iterations in the conditions of case D, with $f_{\mathrm{sw}} = 2.5\,\mathrm{kHz}$. After 10 iterations, $R^{\mathrm{met}} = 1.77\,\Omega$ and $L^{\mathrm{met}} = 12.6\,\mathrm{mH}$ are identified (cf. Fig. 3.15c).

3.6 Conclusions

In this chapter, a method to identify the plant time constant of VSCs at certain working conditions has been proposed. With such algorithm, both the equivalent inductance and resistance seen by the current loop can be estimated, even in the presence of significant variations of any of them or of important initial misestimates. In this manner, the dynamics of the actual loop may be properly studied and the controller parameters can be precisely tuned. In addition, the

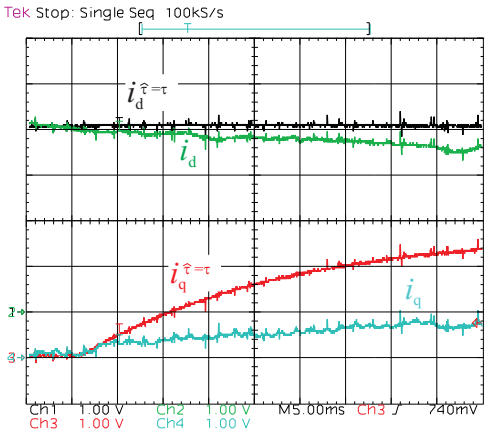

(a) $k = 1$ with $\widehat{R} = 0.4\,\Omega$ and $\widehat{L} = 9.4\,\text{mH}$.

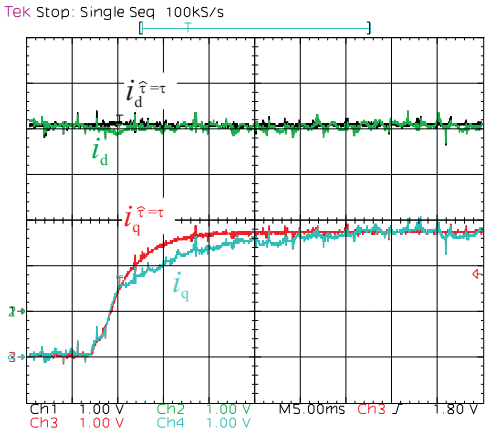

(b) $k = 8$ with $\widehat{R} = 1.8\,\Omega$ and $L_{\text{UPP}} = \widehat{L} = 6.1\,\text{mH}$.

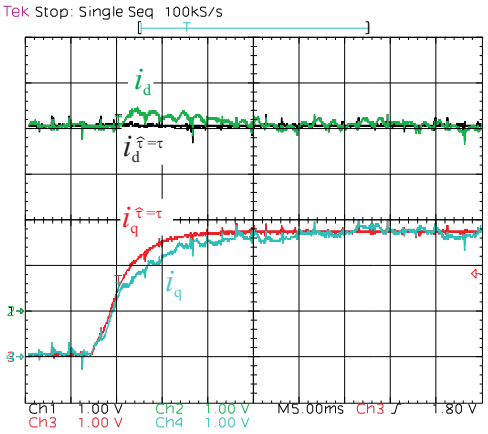

(c) $k = 9$ with $\widehat{R} = 1.87\,\Omega$ and $L_{\text{LOW}} = \widehat{L} = 5.8\,\text{mH}$.

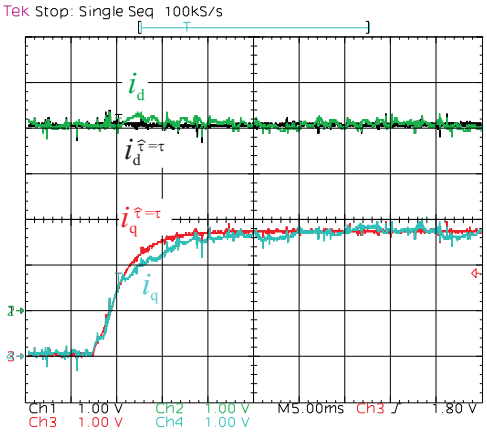

(d) $k = 16$ with $R_{\text{LOW}} = \widehat{R} = 2.12\,\Omega$ and $L^{\text{met}} = \widehat{L} = 5.9\,\text{mH}$.

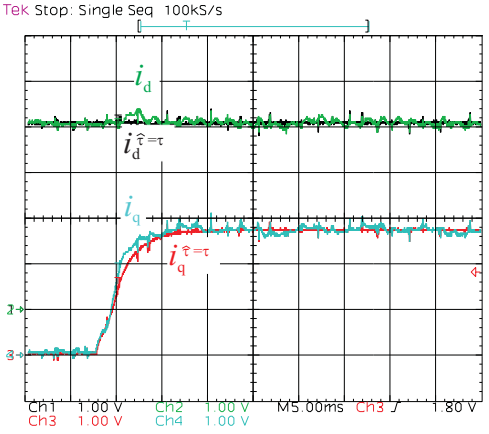

(e) $k = 19$ with $R_{\text{UPP}} = \widehat{R} = 2.45\,\Omega$ and $L^{\text{met}} = \widehat{L} = 5.9\,\text{mH}$.

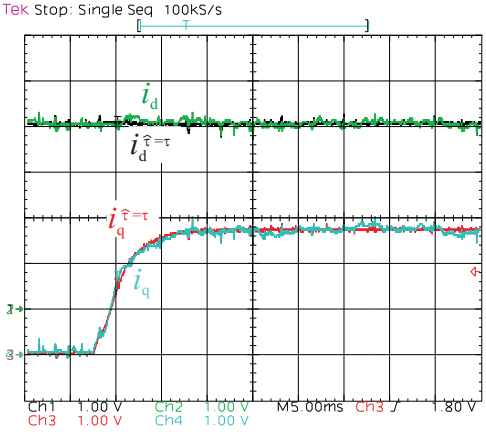

(f) end of estimation process at $k = 20$ with $R^{\text{met}} = \widehat{R} = 2.29\,\Omega$ and $L^{\text{met}} = \widehat{L} = 5.9\,\text{mH}$.

Figure 3.12: Experimental results: step response of the actual and simulated current loops. Different iterations of the estimation process in the conditions of case A. Scales: $i_d^{\widehat{\tau}=\tau}$, i_d, $i_q^{\widehat{\tau}=\tau}$ and i_q in $2.19\,\text{A/div}$, time in $5\,\text{ms/div}$.

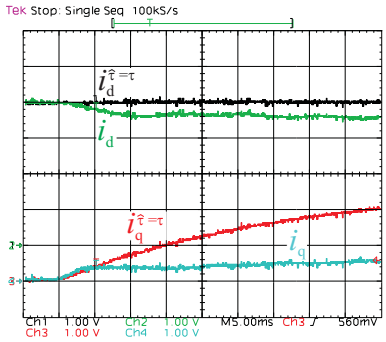

(a) First iteration with $\widehat{R} = 0.45\,\Omega$ and $\widehat{L} = 17.4\,\text{mH}$.

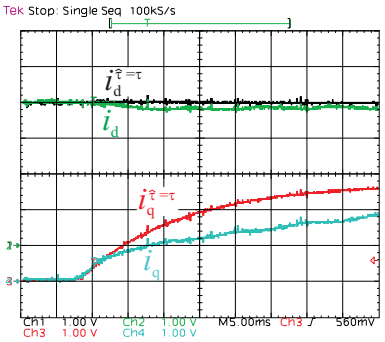

(b) $k = 3$, with $\widehat{R} = 0.89\,\Omega$ and $L_{\text{UPP}} = \widehat{L} = 11.5\,\text{mH}$.

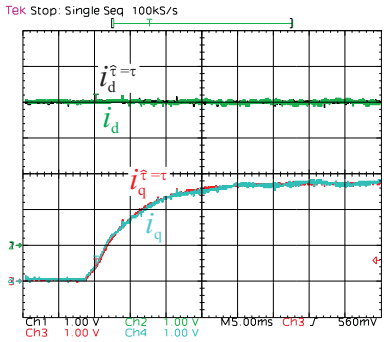

(c) End of estimation process at $k = 15$ with $R^{\text{met}} = \widehat{R} = 1.88\,\Omega$ and $L^{\text{met}} = \widehat{L} = 11\,\text{mH}$.

Figure 3.13: Experimental results: step response of the actual and simulated current loops. Different iterations of the estimation process in the conditions of case B. Scales: $i_d^{\hat{\tau}=\tau}$, i_d, $i_q^{\hat{\tau}=\tau}$ and i_q in $2.19\,\text{A/div}$, time in $5\,\text{ms/div}$.

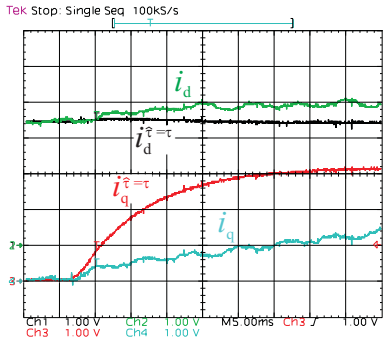

(a) First iteration with $\widehat{R} = 0.4\,\Omega$ and $\widehat{L} = 3.8\,\text{mH}$.

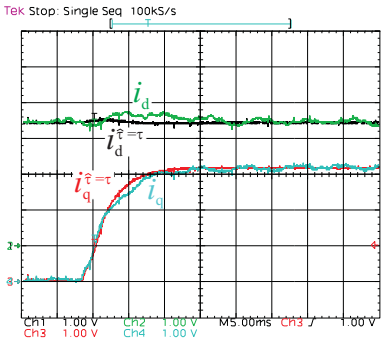

(b) Start of the first refinement stage, in this case at $k = 17$, with $R_{\text{LOW}} = \widehat{R} = 2.81\,\Omega$ and $\widehat{L} = 9.2\,\text{mH}$.

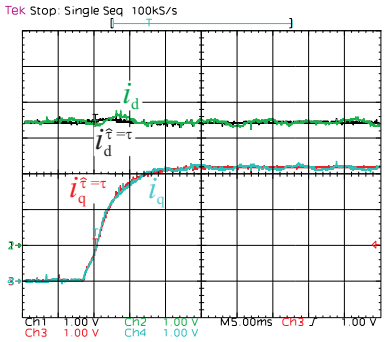

(c) End of estimation process at $k = 23$ with $R^{\text{met}} = \widehat{R} = 2.96\,\Omega$ and $L^{\text{met}} = \widehat{L} = 9.8\,\text{mH}$.

Figure 3.14: Step response of the actual and simulated current loops. Different iterations of the estimation process in the conditions of case C. Scales: $i_d^{\hat{\tau}=\tau}$, i_d, $i_q^{\hat{\tau}=\tau}$ and i_q in $1.25\,\text{A/div}$, time in $5\,\text{ms/div}$.

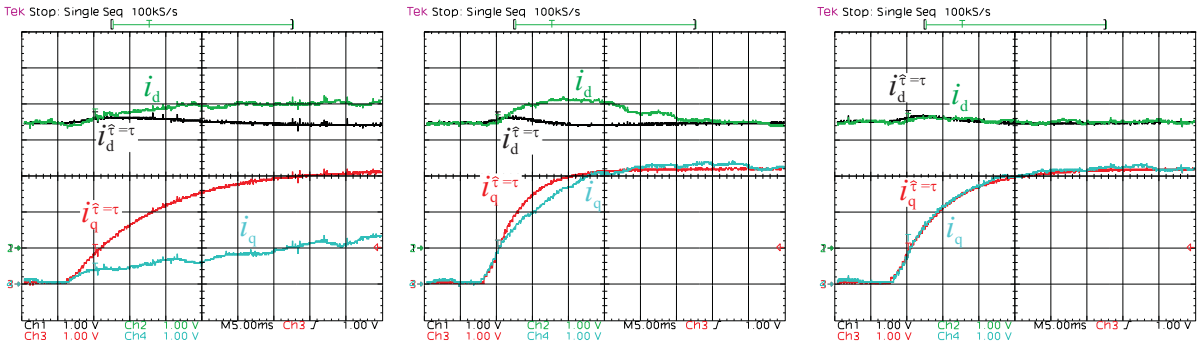

(a) First iteration with $\widehat{R} = 0.4\,\Omega$ and $\widehat{L} = 4.8\,\text{mH}$.

(b) $k = 3$, with $R_{\text{LOW}} = \widehat{R} = 1.67\,\Omega$ and $\widehat{L} = 8.0\,\text{mH}$.

(c) End of estimation process at $k = 10$ with $R^{\text{met}} = \widehat{R} = 1.77\,\Omega$ and $L^{\text{met}} = \widehat{L} = 12.6\,\text{mH}$.

Figure 3.15: Experimental results: step response of the actual and simulated current loops. Different iterations of the estimation process in the conditions of case D. Scales: $i_{\text{d}}^{\hat{\tau}=\tau}$, i_{d}, $i_{\text{q}}^{\hat{\tau}=\tau}$ and i_{q} in $1.25\,\text{A/div}$, time in $5\,\text{ms/div}$.

validity of modeling an LCL filter as an L one from the point of view of the current loop is analyzed in detail, as a function of the gain value. As a result, it is demonstrated that the method is also valid when LCL filters are employed.

The developed algorithm is based on the iterative minimization of a cost function that quantifies the complex difference between the current control closed-loop step responses of the actual system and the one including a simulated plant, with the current controllers tuned according to IMC. Hence, it is particularly designed to satisfy time-domain specifications. It works in closed loop, at the same sampling frequency as the rest of the control, and may be implemented either online or offline. The corresponding inductance and resistance of a VSC working at different power ratings and switching frequencies, with L and LCL filters, have been experimentally identified, considering important initial mismatches in both parameters.

Contributions of this chapter have been published in the journal IEEE Transactions on Power Electronics [1] and presented at an international conference [13].

Chapter 4

Assessment and Optimization of the Transient Response of Proportional-Resonant Current Controllers for Distributed Power Generation Systems

Abstract *— The increasing number of distributed power generation systems (DPGSs) is changing the traditional organization of the electrical network. An important part of these DPGSs is based on renewable energy sources. In order to guarantee an efficient integration of renewable based generation units, grid codes must be fulfilled. Their most demanding requirements, such as low-voltage ride through and grid support, need a really fast transient response of the power electronics devices. In this manner, the current controller speed is a key point. This chapter develops a methodology to assess and optimize the transient response of proportional-resonant current controllers, which is based on the study of the error signal transfer function roots by means of root loci. Controller gains are set to achieve fast and nonoscillating transient responses; i.e., to minimize the settling time. It is proved that optimal gain selection results from a tradeoff between transients caused by reference changes and transients due to alterations at the point of common coupling (PCC). Experimental results obtained with a three-phase voltage source converter prototype validate the approach. Short transient times are achieved even when tests emulate very demanding realistic conditions: a* $+90^\circ$ *phase-angle jump in the current reference and a "type C" voltage sag at the PCC.*

4.1 Introduction

Nowadays, there is a large penetration of renewable energy sources into the power system. Their connection to the utility network leads to problems to maintain voltage and frequency within the operating limits. In order to deal with them, the different countries (or even areas) have defined their own grid codes (GCs) [37–41]. The dynamic requirements from GCs force generation systems to remain connected to the network even when grid faults occur, which is known as low-voltage ride-through (LVRT) capability [60, 61, 199–201]. In addition, the most demanding of them also require grid support during these events by means of reactive current

injection [37, 39–41].

On the other hand, the traditional organization of the power system is changing, as distributed power generation systems (DPGSs) are increasingly being integrated at the distribution level [33, 43]. In the near future, it is expected that the amount of power from these DPGSs based on renewable sources will be really significant. Concerns about their operation together with the traditional power units in terms of guaranteeing the stability and reliability of the power system have to be regarded [202–204]. Therefore, it is essential to investigate the transient response during faults of the power converters connected to DPGSs.

In DPGSs, the control of the grid-side converter is usually based on dual loops: outer loops, with slow dynamics, regulate the reactive power delivered to the grid and the dc-link voltage; they generate the references for the inner loops, with faster dynamics, which control the current [34, 200, 205]. However, when a fault is detected [206, 207], GCs force generation systems to inject a certain percentage of reactive current within a maximum delay. In this manner, two main tasks are critical: new reference generation and current control [65, 68, 69, 207–210]. Firstly, reference generation for the current control loop through outer power controllers with slow dynamics has to be disregarded, to cope with these demanding requirements [205, 209]. Secondly, a thorough analysis and design of the current controllers is crucial to attain an enhanced transient response. This chapter addresses this second task. Besides, high-bandwidth grid synchronization algorithms able to deal with distorted conditions are needed for the inner loop [28].

Resonant regulators have been proved to be a good choice in current control loops. They allow to achieve equivalent transient and steady-state performance to synchronous reference frame (SRF) proportional-integral (PI) controllers. Moreover, they are an interesting alternative in terms of computational burden, since some Park transformations can be saved [144, 146]. In this manner, they are widely used in multiple applications such as active power filters [79, 114, 143, 145, 146, 158–160], wind turbines [34, 163], water turbines [211], photovoltaic inverters [161, 204], motor drives [144, 212], fuel-cell inverters [213] and dynamic voltage restorers [214].

A proportional-resonant (PR) controller has a gain associated to the proportional part and another one for each resonant filter [34, 144, 204, 213]. An accurate adjustment of these parameters is key to achieve the best possible transient response. Regarding the proportional gain, there is a well-accepted criterion for its selection, based on guaranteeing a crossover frequency at least a decade below the sampling frequency [80]. In relation to the integral gains for the resonant filters, several authors point that a higher value results in faster dynamics at the cost of worse filtering and stability [79, 80, 139, 144, 146, 160, 165, 166]. In [80] and [139], an expression for the time constant of the current control loop (just considering the dominant pole) is given. Despite being very insightful, this information is not enough to optimize the transient response in the new DPGS scenario, where the GC requirements related to transient stability are becoming more and more restrictive. More specifically, in the presence of voltage sags at the point of common coupling (PCC), the current controller should track fast the new control references and also reject quickly the disturbance (i.e., the grid fault). As shown in this chapter, the latest constraint is more demanding in practice and very dependent on the parameter tuning.

A novel approach to assess and design the transient response of PR controllers is developed in this chapter; this methodology is based on the inspection of root loci of the error signals in the z-domain, which are obtained from the controller, plant, reference and disturbance transfer functions. Two error signals are studied: the error signal due to a change in the current command

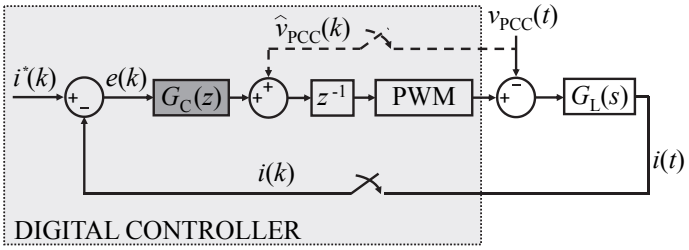

Figure 4.1: Block diagram of the current control closed loop.

(reference change Δi^*) and the one caused by a voltage sag at the PCC (disturbance change Δv_{PCC}). Controller gains are selected in order to minimize the postfault settling time.

A three-phase voltage source converter (VSC) working as a rectifier has been built confirm the suitability of the proposal. PR controllers with filters only at the fundamental frequency or also contemplating harmonic frequencies have been tested. Besides, the effect of different sampling frequencies has been studied. Transients in the current reference and sags at the PCC have been regarded in all these situations.

The chapter is organized as follows. Section §4.2 reviews some basic concepts about the current control loop and PR controllers. General information about the proposed error root-locus analysis is given in section §4.3. Section §4.4 specifies the controllers and tests to be analyzed and shows the root-locus diagrams in these different situations. Finally, the experimental results of section §4.5 validate the theoretical approach and the chapter ends with some conclusions (see section §4.6).

4.2 Basic Concepts of Current Control

Fig. 4.1 illustrates a block diagram of a digital current control loop [80, 112]. The different signals and transfer functions are detailed below.

- i stands for the actual value of the current.
- i^* is the current reference.
- $e = i^* - i$ denotes the error signal.
- $G_C(z)$ represents a discrete-time domain current controller, in this chapter, a PR one.
- z^{-1} models the computational delay, which is equal to one sample.
- PWM(s) is the delay of half a sample introduced by the regularly sampled pulse-width modulation (PWM), which can be modeled by a zero-order hold (ZOH).
- v_{PCC} symbolizes the voltage at the PCC, a disturbance for the current control loop.
- $G_L(s)$ is the continuous-domain transfer function of the plant admittance. A first-order model

$$G_L(s) = \frac{1}{sL+R} \tag{4.1}$$

may be used in most cases. As described in chapters §2 and §3, not only does R include the parasitic resistance of the interface filter R_{F}, but also the equivalent loss resistance of the converter. On the other hand, the actual inductance of the current loop L can also differ from the interface filter inductance L_{F} (see chapter §3). Equation (4.1) also includes LCL filters assuming that they can be modeled as L filters at frequencies below the LCL resonance [55, 77, 111].

- A feedforward of v_{PCC} ($\widehat{v}_{\mathrm{PCC}}$) may be included in order to improve the transient response in the presence of grid faults [34, 65, 113].

It is worth mentioning that, as all the transfer functions defined along this chapter are expressed with respect to the stationary frame, subscripts $\alpha\beta$ are omitted for the sake of clarity, e.g., $G_{\mathrm{L}}(s)$ is adopted, instead of $G_{\mathrm{L}_{\alpha\beta}}(s)$, which was employed in the introduction (cf. chapter §1).

4.2.1 Background on PR Controllers

As reported in section §1.2.7.3, PR controllers are linear regulators that have resonant poles at specific frequencies. A simple PR controller can be expressed in the z-domain as

$$G_{\mathrm{PR}}(z) = K_{\mathrm{P}_1} + K_{\mathrm{I}_1} T_{\mathrm{s}} \frac{1 - z^{-1}\cos(\omega_1 T_{\mathrm{s}})}{1 - 2z^{-1}\cos(\omega_1 T_{\mathrm{s}}) + z^{-2}} \tag{4.2}$$

with K_{P_1} and K_{I_1} being the proportional and integral gains, respectively, at the resonant frequency ω_1 and with T_{s} being the sampling period. Equation (4.2) has been obtained by using the impulse invariant discretization method [79]. By $G_{\mathrm{PR}}(z)$ inspection, some interesting features of PR controllers in comparison with other linear regulators are highlighted.

- $G_{\mathrm{PR}}(z)$ has infinite gain at the resonant frequency, which assures steady-state perfect tracking and disturbance rejection for components pulsating at ω_1. Other basic schemes based on linear regulators such as simple proportional and dead-beat controllers (unless more complex estimators are included) do not achieve zero steady-state error at ω_1 [80, 144–146].

- $G_{\mathrm{PR}}(z)$ can be designed to have a high bandwidth, provided that resonant peaks do not affect the cut-off frequency (which is the case when low integral gains are used) [144, 146].

- PR controllers in the $\alpha\beta$ frame are equivalent to a pair of PI controllers implemented in a positive- and a negative-sequence SRF simultaneously [80, 144, 146]. Under the discrete implementation point of view, PR controllers are an interesting alternative to reduce computational burden [144, 146].

Equation (4.2) can be extended to include more resonant filters:

$$G_{\mathrm{PR}}(z) = K_{\mathrm{P_T}} + \sum_{h=1,5,7\ldots} K_{\mathrm{I}_h} T_{\mathrm{s}} \frac{1 - z^{-1}\cos(h\omega_1 T_{\mathrm{s}})}{1 - 2z^{-1}\cos(h\omega_1 T_{\mathrm{s}}) + z^{-2}}. \tag{4.3}$$

where $K_{\mathrm{P_T}}$ is the addition of the individual proportional gains, i.e., $K_{\mathrm{P_T}} = \sum_{h=1,5,7\ldots} K_{\mathrm{P}_h}$ and K_{I_h} is the integral gain at the harmonic resonant frequency $h\,\omega_1$. This structure is exploited in some applications for harmonic reference tracking [79, 114, 143, 145, 146, 158–160], while in some others, for harmonic rejection [111, 161].

4.3 Error Root-Locus Analysis for Transient Optimization

According to the scheme in Fig. 4.1, as a linear system, the overall transfer function of the current loop is defined as [76]

$$I(z) = \frac{G_{\mathrm{C}}(z)z^{-1}G_{\mathrm{L}}^{\mathrm{ZOH}}(z)}{1+G_{\mathrm{C}}(z)z^{-1}G_{\mathrm{L}}^{\mathrm{ZOH}}(z)}I^*(z) - \frac{G_{\mathrm{L}}^{\mathrm{Tustin}}(z)}{1+G_{\mathrm{C}}(z)z^{-1}G_{\mathrm{L}}^{\mathrm{ZOH}}(z)}V_{\mathrm{PCC}}(z) \tag{4.4}$$

where $G_{\mathrm{L}}^{\mathrm{Tustin}}(z)$ and $G_{\mathrm{L}}^{\mathrm{ZOH}}(z)$ are obtained by discretization of (4.1) with Tustin and ZOH methods, respectively:

$$G_{\mathrm{L}}^{\mathrm{Tustin}}(z) = \frac{1+z^{-1}}{(R+\frac{2L}{T_{\mathrm{s}}})+z^{-1}(R-\frac{2L}{T_{\mathrm{s}}})} \tag{4.5}$$

$$G_{\mathrm{L}}^{\mathrm{ZOH}}(z) = \frac{z^{-1}}{R}\frac{1-e^{-\rho}}{1-z^{-1}e^{-\rho}} \tag{4.6}$$

with $\rho = \mathrm{e}^{RT_{\mathrm{s}}/L}$. The Tustin method is chosen in (4.5) because it provides an accurate discretization at low frequencies [79], while the ZOH discretization method in (4.6) permits to include in (4.1) the effect of the PWM, i.e., half a sample delay [77, 80, 112, 114].

From (4.4) and Fig. 4.1, the global error signal $E(z) = I^*(z) - I(z)$ can be expressed as the addition of the errors caused by each of the inputs, i.e., the error caused by reference changes $E_{\Delta i^*}(z)$ and the error caused by disturbance changes $E_{\Delta v_{\mathrm{PCC}}}(z)$:

$$E(z) = E_{\Delta i^*}(z)|_{\Delta v_{\mathrm{PCC}}=0} + E_{\Delta v_{\mathrm{PCC}}}(z)|_{\Delta i^*=0} \tag{4.7}$$

In this manner, both errors can be studied separately, being:

$$E_{\Delta i^*}(z)|_{\Delta v_{\mathrm{PCC}}=0} = \frac{1}{1+G_{\mathrm{C}}(z)z^{-1}G_{\mathrm{L}}^{\mathrm{ZOH}}(z)}\Delta i^*(z) \tag{4.8}$$

$$E_{\Delta v_{\mathrm{PCC}}}(z)|_{\Delta i^*=0} = \frac{G_{\mathrm{L}}^{\mathrm{Tustin}}(z)}{1+G_{\mathrm{C}}(z)z^{-1}G_{\mathrm{L}}^{\mathrm{ZOH}}(z)}\Delta v_{\mathrm{PCC}}(z). \tag{4.9}$$

Equation (4.8) represents the error when the reference is modified:

$$\Delta i^*(z) = i^*_{\mathrm{new}}(z) - i^*_{\mathrm{old}}(z) \tag{4.10}$$

with i^*_{new} and i^*_{old} being the current and previous sinusoidal input references (with a given amplitude and phase). These references are of the form

$$i^*(z) = A\underbrace{\frac{1-z^{-1}\cos(\omega_1' T_{\mathrm{s}})}{1-2z^{-1}\cos(\omega_1' T_{\mathrm{s}})+z^{-2}}}_{\text{cosine term}} + B\underbrace{\frac{z^{-1}\sin(\omega_1' T_{\mathrm{s}})}{1-2z^{-1}\cos(\omega_1' T_{\mathrm{s}})+z^{-2}}}_{\text{sine term}} \tag{4.11}$$

where A and B are the amplitude of the cosine and sine terms, respectively. From (4.10) and (4.11), any amplitude or phase change in the current reference can be modeled as

$$\Delta i^*(z) = (A_{\text{new}} - A_{\text{old}}) \underbrace{\frac{1 - z^{-1}\cos(\omega_1' T_s)}{1 - 2z^{-1}\cos(\omega_1' T_s) + z^{-2}}}_{\text{cosine term}} + (B_{\text{new}} - B_{\text{old}}) \underbrace{\frac{z^{-1}\sin(\omega_1' T_s)}{1 - 2z^{-1}\cos(\omega_1' T_s) + z^{-2}}}_{\text{sine term}} . \tag{4.12}$$

A priori, (4.8) is sixth-ordered when $G_C(z)$ takes the form of (4.2), i.e., $G_C = G_{PR}$. Nevertheless, when the input frequency ω_1', in this case, the fundamental frequency, is equal to the PR controller resonant frequency ω_1, the order is reduced to four: the poles of Δi^* are canceled by the zeros introduced by $G_{PR}(z)$. The error caused by the remaining roots decays, so zero steady-state error is achieved. Maximizing the speed of such decay (the decay rate) means optimizing the transient response in terms of settling time $t_{2\%}$ (a tolerance band of 2% is defined for this chapter).

Once the error function is obtained, as in (4.8), one can graphically represent their roots (poles and zeros). Root loci give information about the main characteristics, such as stability, decay rate and damping. Thus, the controller parameters can be adjusted so that the dominant poles are as fast and as damped as possible. Based on the residues calculation (numerators of the terms obtained by partial-fraction expansion of the z-domain function), the time expression of the error signal is obtained. Further justification of this process is included in the Appendix §B. A similar methodology is applied to study the error signal caused by disturbance changes $E_{\Delta v_{PCC}}$ in (4.9).

In conclusion, following this approach, an accurate prediction of the error waveform during transients can be obtained and hence, the regulator may be precisely adjusted. Controller parameters can be selected to achieve the best result in most situations, considering reference changes and grid disturbances. It should be noticed that, even though this analysis focuses on PR controllers, the proposed methodology may be applied to other linear controllers.

4.4 Design Study

The methodology proposed in the previous section is particularized for the laboratory equipment. The experimental setup is depicted on Fig. 4.2, with $L = L_F = 5\,\text{mH}$ and $R_F = 0.5\,\Omega$.

This section focuses on the tuning of the current controller parameters considering different cases:

- a PR controller with a single resonant filter at the fundamental frequency [see (4.2)] for a sampling frequency $f_s = 10\,\text{kHz}$ and a switching frequency $f_{sw} = 10\,\text{kHz}$ in section §4.4.1 and for $f_s = f_{sw} = 2.5\,\text{kHz}$ in section §4.4.3;

- a PR controller with several resonant filters [see (4.3)] for $f_s = f_{sw} = 10\,\text{kHz}$ in section §4.4.2.

Since the goal is to optimize the transient response in the presence of reference or disturbance changes, two transient tests have been selected considering very critical scenarios:

- test I: a phase reference change of $+90^\circ$ in the positive-sequence current vector;

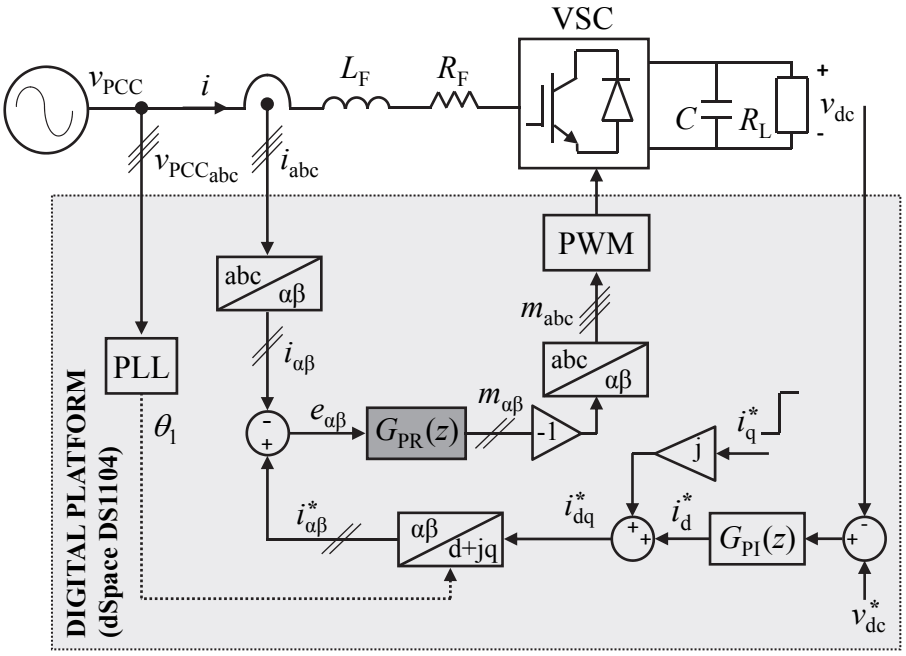

Figure 4.2: Scheme of the laboratory prototype.

- test II: a typical sag in wind power installations categorized as "type C" with a characteristic voltage of the dip of 40% in amplitude, which implies both amplitude and phase jumps [215] [$\Delta v_{\mathrm{PCC_{abc}}} = (122.57\,\mathrm{V}\angle -2.618\,\mathrm{rad}, 122.57\,\mathrm{V}\angle 2.618\,\mathrm{rad}, 0\,\mathrm{V}\angle 0\,\mathrm{rad})$ and hence, $\Delta v_{\mathrm{PCC}_{\alpha\beta 0}} = (122.57\,\mathrm{V}\angle -2.618\,\mathrm{rad}, 70.77\,\mathrm{V}\angle 0.523\,\mathrm{rad}, 0\,\mathrm{V}\angle 0\,\mathrm{rad})$].

Regarding tests at $f_s = f_{sw} = 10\,\mathrm{kHz}$, a fixed proportional gain, $K_{P_T} = 25$, has been selected to set a bandwidth of about 850 Hz, a value below $1/10 f_s$, which is a typical design constraint [76, 80, 141]. In a similar way, $K_{P_T} = 6.25$ has been chosen for $f_s = f_{sw} = 2.5\,\mathrm{kHz}$. In general, the crossover frequency is little affected by resonant terms unless really high K_{I_h} values are used [144].

In the following, this study focuses on selecting the optimal values for K_{I_h}, while keeping constant K_{P_T}, as above justified. In general, the transient response can be optimized either by making the poles as fast as possible (which results in bigger exponential coefficients, i.e., larger decay rates) or by placing them next to zeros that cancel their effect (which results in smaller residues) [216]. More details about the relationship between the pole positions and the error time-domain expressions are given in the Appendix §B.

4.4.1 PR Controller only at Fundamental Frequency

Fig. 4.3 depicts root-locus diagrams of $E_{\Delta i^*}(z)$ and $E_{\Delta v_{PCC}}(z)$ at $f_s = 10\,\mathrm{kHz}$, with $R = 4\,\Omega$ (cf. chapter §2). They represent the trajectories of the poles with an increasing K_{I_1} in case of reference change (test I) and disturbance change (test II), respectively. Regarding Fig. 4.3a, there are six poles and five zeros.

- The zero z_1 depends on the input and it is defined as follows:

$$z_1 = \cos(\omega_1' T_s) - \frac{(B_{new} - B_{old})}{(A_{new} - A_{old})} \sin(\omega_1' T_s) \tag{4.13}$$

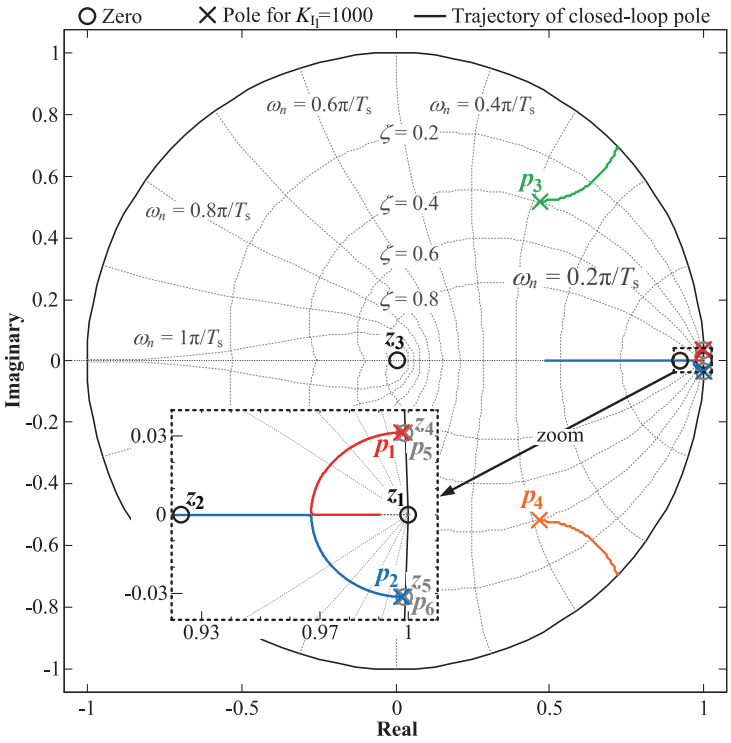

(a) Test I. Roots of $E_{\Delta i^*}(z)$.

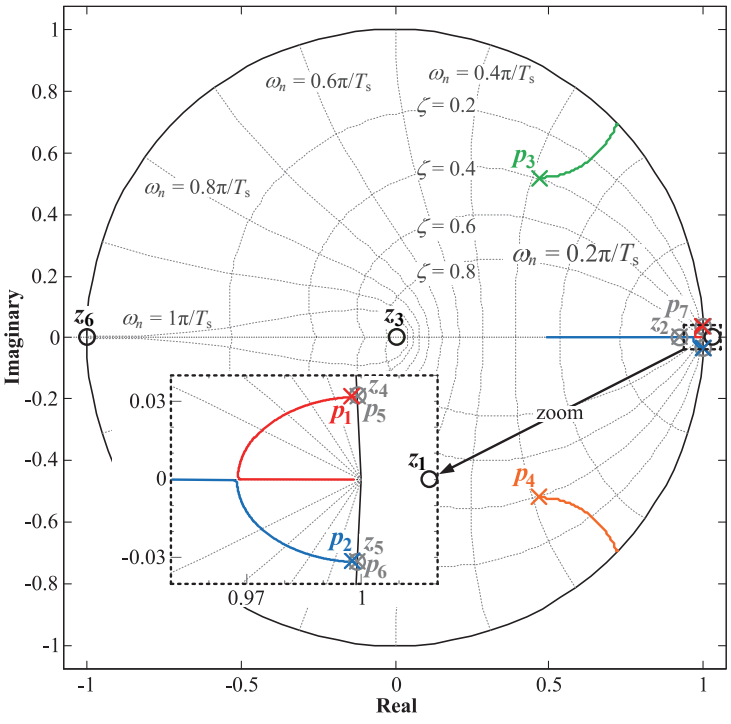

(b) Test II. Roots of $E_{\Delta v_{\mathrm{PCC}}}(z)$.

Figure 4.3: Root-locus diagrams of the error signal during transients when using a PR controller with a single resonant filter at $h = 1$ and $f_s = 10\,\mathrm{kHz}$. K_{I_1} is increased from 1000 to 150000 and $K_{P_1} = 25$. The poles and zeros that are canceled with each other are shown in gray.

when $A_{\text{new}} \neq A_{\text{old}}$. Otherwise, z_1 does not influence the system dynamics. Analyzing (4.13), it can be drawn that, in most situations, $\omega_1' T_s$ is really small so that the cosine term is much more significant than the sine term. In this manner, z_1 is located in most cases next to $z = 1$. In general, this is advantageous, as it will be commented afterward.

- The zero $z_2 = \rho^{-1} = e^{-RT_s/L}$ is actually the plant pole [that of $G_L^{\text{ZOH}}(z)$)].

- As the input is a sinusoidal waveform like (4.12), another zero appears at $z_3 = 0$.

- The zeros z_4 and z_5 [due to $G_{\text{PR}}(z)$] cancel the poles p_5 and p_6 [owing to $\Delta i^*(z)$]. In fact, this is the aim of resonant controllers, which is verified in these root loci.

- The poles p_1 and p_2 depend on all the system parameters. When K_{I_1} is low, p_1 and p_2 are the dominant poles. Since they are close to $z = 1$, they are slower. As K_{I_1} increases, they approach the real axis, i.e., they reduce their oscillating terms. Once there, both poles move along the real axis in opposite directions, making p_1 slower and p_2 faster.

- The other pair of poles, p_3 and p_4, increase their module, being moved towards the unit circle boundary, as K_{I_1} grows.

The root-locus diagram of $E_{\Delta v_{\text{PCC}}}(z)$ is depicted in Fig. 4.3b. In this case, one more pole and one more zero appear, while the other roots are the same as in Fig. 4.3a. These roots remain exactly at the same place as in case of transients in the current reference, except z_1, which depends on the input that is tested. The additional roots in case of transients in v_{PCC} are the following.

- A new pole appears at $p_7 = \rho^{-1} = e^{-RT_s/L}$, which corresponds to the plant pole [owing to $G_L^{\text{Tustin}}(z)$] and it is canceled by z_2.

- There is also a new zero $z_6 = -1$ due to the numerator of $G_L^{\text{Tustin}}(z)$ [cf. (4.5)]. Since it is really far from the dominant poles, this zero is not important for the system dynamics.

Once how the roots move is explained, four significant values for K_{I_1} are analyzed. The resulting root loci are illustrated in Figs. 4.4, 4.5, 4.6 and 4.7, respectively. The canceled roots, namely $p_5 - z_4$, $p_6 - z_5$ and $p_7 - z_2$, are no longer depicted. These K_{I_1} values are as follows.

a) A $K_{I_1} = 2000$ that makes the dominant poles p_1 and p_2 oscillate (cf. Fig. 4.4). In addition, this gain represents typical values in the range $[1000 - 2000]$, which are widely employed in the literature for current-loop plants with comparable values [77, 79, 114, 143, 161].

b) A $K_{I_1} = 17645$, for which the dominant poles are located at the same place in the real axis, i.e., $p_1 = p_2$ (cf. Fig. 4.5).

c) A $K_{I_1} = 34000$ that places the dominant poles at the real axis, but with p_2 being faster than p_1, i.e., $p_1 > p_2$ (cf. Fig. 4.6).

d) A $K_{I_1} = 100000$, for which p_3 and p_4 become dominant, instead of p_1 and p_2 (cf. Fig. 4.7).

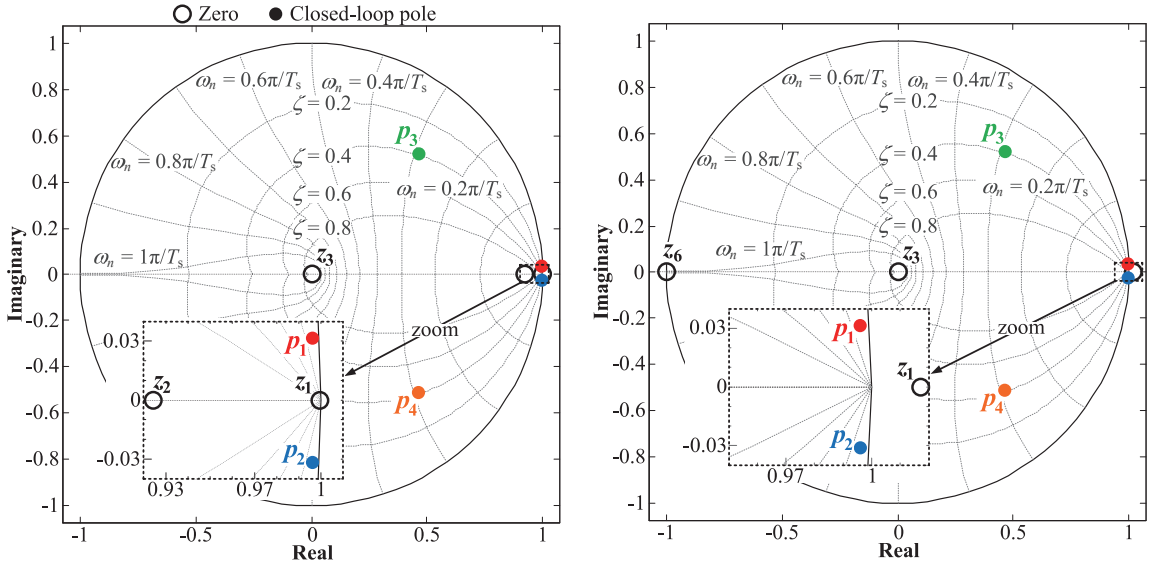

(a) Test I. Roots of $E_{\Delta i^*}(z)$. $K_{\mathrm{I}_1} = 2000$.

(b) Test II. Roots of $E_{\Delta v_{\mathrm{PCC}}}(z)$. $K_{\mathrm{I}_1} = 2000$.

Figure 4.4: Root-locus diagrams of the error signal during transients when using a PR controller with a single resonant filter at $h = 1$ for $f_{\mathrm{s}} = 10\,\mathrm{kHz}$, with $K_{\mathrm{P}_1} = 25$ and $K_{\mathrm{I}_1} = 2000$.

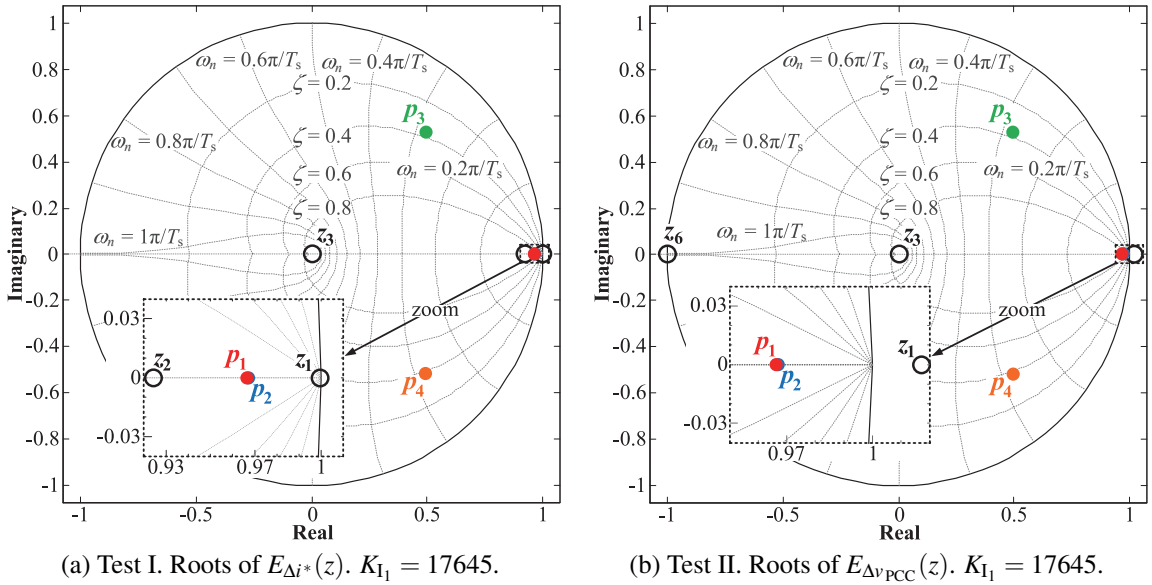

(a) Test I. Roots of $E_{\Delta i^*}(z)$. $K_{\mathrm{I}_1} = 17645$.

(b) Test II. Roots of $E_{\Delta v_{\mathrm{PCC}}}(z)$. $K_{\mathrm{I}_1} = 17645$.

Figure 4.5: Root-locus diagrams of the error signal during transients when using a PR controller with a single resonant filter at $h = 1$ for $f_{\mathrm{s}} = 10\,\mathrm{kHz}$, with $K_{\mathrm{P}_1} = 25$ and $K_{\mathrm{I}_1} = 17645$.

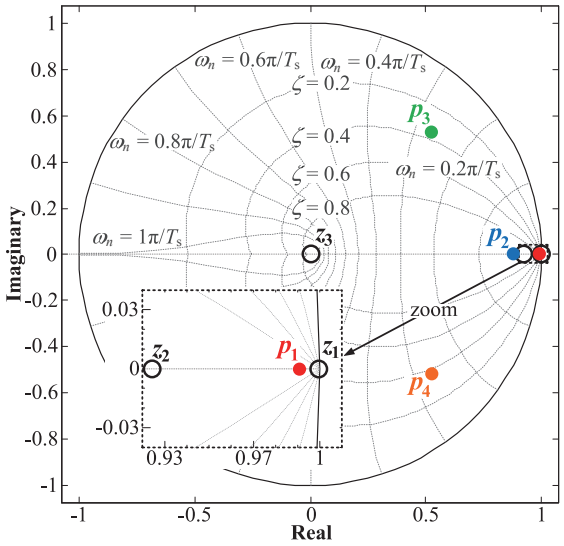

(a) Test I. Roots of $E_{\Delta i^*}(z)$. $K_{\mathrm{I}_1} = 34000$.

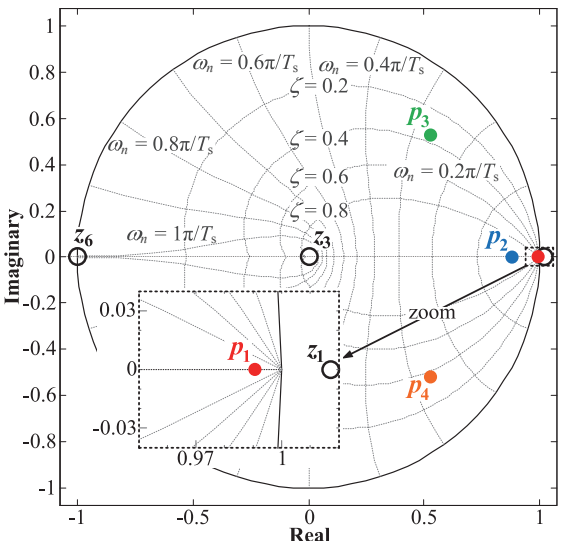

(b) Test II. Roots of $E_{\Delta v_{\mathrm{PCC}}}(z)$. $K_{\mathrm{I}_1} = 34000$.

Figure 4.6: Root-locus diagrams of the error signal during transients when using a PR controller with a single resonant filter at $h = 1$ for $f_s = 10\,\mathrm{kHz}$, with $K_{\mathrm{P}_1} = 25$ and $K_{\mathrm{I}_1} = 34000$.

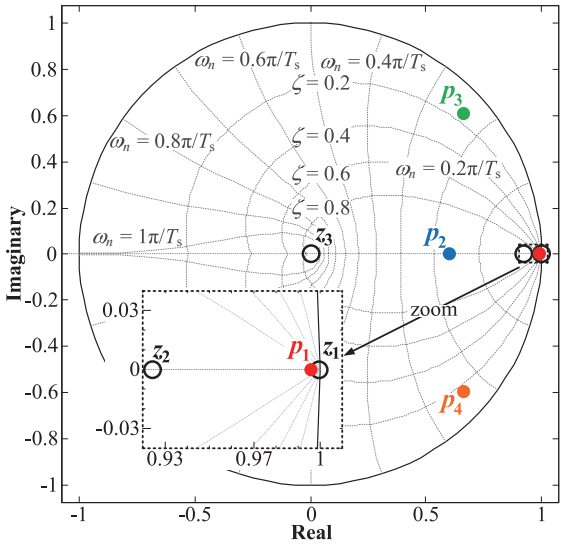

(a) Test I. Roots of $E_{\Delta i^*}(z)$. $K_{\mathrm{I}_1} = 100000$.

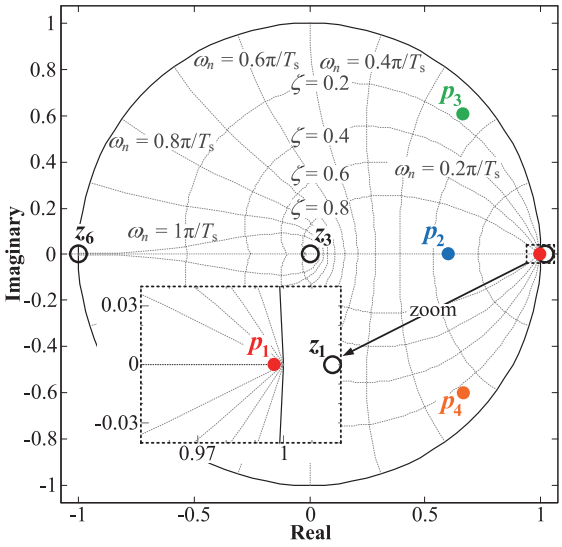

(b) Test II. Roots of $E_{\Delta v_{\mathrm{PCC}}}(z)$. $K_{\mathrm{I}_1} = 100000$.

Figure 4.7: Root-locus diagrams of the error signal during transients when using a PR controller with a single resonant filter at $h = 1$ for $f_s = 10\,\mathrm{kHz}$, with $K_{\mathrm{P}_1} = 25$ and $K_{\mathrm{I}_1} = 100000$.

Figs. 4.4a and b show the root loci of $E_{\Delta i^*}(z)$ and $E_{\Delta v_{\mathrm{PCC}}}(z)$ when $K_{\mathrm{I}_1} = 2000$. It can be observed that, by using a low value for the integral gain, the dominant poles p_1 and p_2 are slow and oscillating in both tests. The other poles p_3 and p_4 are faster, but oscillating too. Given that the main goal is to achieve a fast transient response, $K_{\mathrm{I}_1} = 2000$ is not a suitable value.

In Figs. 4.5a and b, $K_{\mathrm{I}_1} = 17645$ is used. Modifications in the fast poles p_3 and p_4 are not important with respect to $K_{\mathrm{I}_1} = 2000$. However, the dominant poles p_1 and p_2 are placed now in the real axis, at the same point, i.e., $p_1 = p_2$. In case of reference change, p_1 and p_2 are between z_1 and z_2. This location is really advantageous since z_1 and z_2 tend to minimize the residues of p_1 and p_2 (pole-zero cancellation), so their time responses are very damped. Regarding changes in v_{PCC}, the situation is a little different (cf. Fig. 4.5b) because z_1 is farther now and there is no z_2. In this case, p_1 and p_2 residues are higher as there is only one zero and it is farther from the dominant poles. Hence, the corresponding time-domain response is not as damped as in the previous case. In conclusion, $K_{\mathrm{I}_1} = 17645$ is optimal for changes in the disturbance when the goal is to reduce the settling time because p_1, which is not canceled by z_1 (it was in the case of reference change), is as far as possible from the unit circle boundary.

With $K_{\mathrm{I}_1} = 34000$, p_1 and p_2 in Fig. 4.6a have no oscillating terms either (i.e., imaginary part). Besides, they are close to z_1 and z_2, so their residues are small, which decreases their effect on the error time-domain response. Thus, this condition is optimal for changes in the current reference. Nevertheless, it should be noticed that when $A_{\mathrm{new}} \approx A_{\mathrm{old}}$ [cf. (4.13)], z_1 does not affect the dynamics, since its position is really far from the dominant poles. In this particular case, the residue of p_1 is more significant, leading to a slower transient response. Therefore, in this situation, $K_{\mathrm{I}_1} = 17645$ would be a better option than $K_{\mathrm{I}_1} = 34000$ because p_1 is as far as possible from the unit circle boundary. However, as the instant at which a current reference change is commanded is generally controlled, this scenario might be easily avoided from the reference generation block. In relation to changes in v_{PCC} (cf. Fig. 4.6b), z_1 does not cancel p_1, the slowest pole, and there is no cancellation for p_2 either. This fact leads to a transient response a bit slower than that of Fig. 4.5b, but still very fast compared to that with $K_{\mathrm{I}_1} = 2000$. Regarding the other pair of poles, p_3 and p_4, no significant changes are observed with respect to the two previous gain selections.

Finally, Figs. 4.7a and b, depict the root-locus diagrams for $K_{\mathrm{I}_1} = 100000$. With this gain, the slowest pole p_1 is even closer to the zero z_1. Moreover, p_2 is now the fastest pole. The poles p_3 and p_4 have moved towards the unit circle boundary, becoming dominant. This is an unwanted situation because p_3 and p_4 may lead to important high-frequency oscillations owing to their large imaginary terms.

In conclusion, for a given K_{P_1}, the optimal value of K_{I_1} results from a balance between that for changes in i^* and that for transients in v_{PCC}. Since the settling time of $e_{\Delta v_{\mathrm{PCC}}}(t)$ tends to be much larger, the proposed criterion is to minimize it at the cost of longer $e_{\Delta i^*}(t)$ transients. As proved forward, this tradeoff, achieved with $K_{\mathrm{I}_1} = 17645$, is very suitable for the compliance of the most demanding GC requirements. Anyway, with $K_{\mathrm{I}_1} = 34000$, $e_{\Delta v_{\mathrm{PCC}}}(t)$ is more damped, which could also be an interesting feature.

4.4.2 PR Controller at Fundamental and Harmonic Frequencies

Real applications usually need harmonic control either for reference tracking [27, 79, 146] or for rejection [27, 28, 34, 111]. In such case, additional resonant filters tuned to follow these frequencies are included in the current control loop as in (4.3). The proposed methodology is

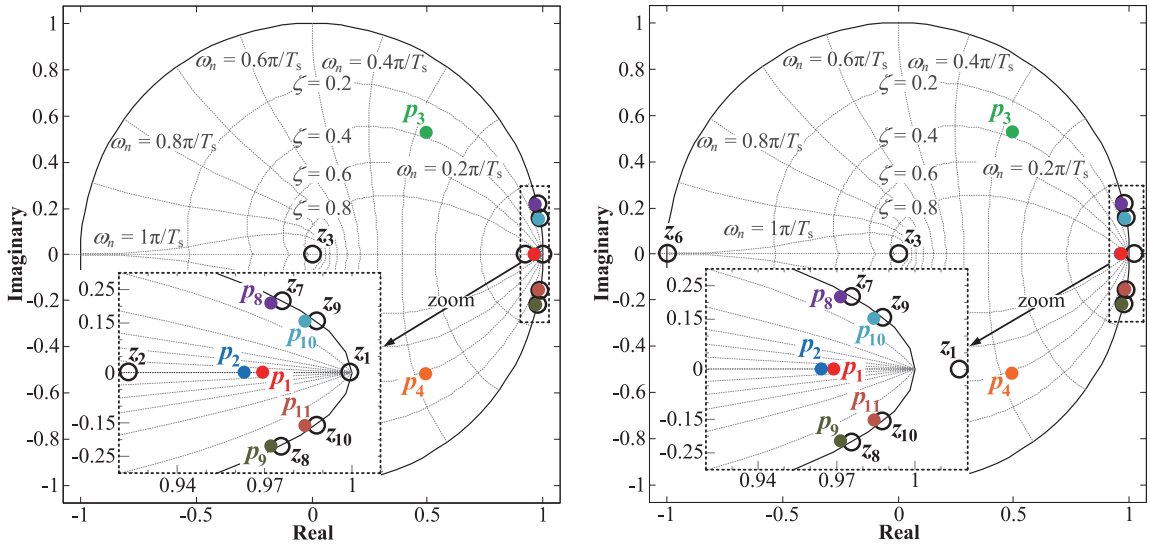

(a) Test I. Roots of $E_{\Delta i^*}(z)$.

(b) Test II. Roots of $E_{\Delta v_{\mathrm{PCC}}}(z)$.

Figure 4.8: Root-locus diagrams of the error signal during transients when using a PR controller with resonant filters at $h = 1,5,7$ for $f_s = 10\,\mathrm{kHz}$, with $K_{\mathrm{P_T}} = 25$, $K_{\mathrm{I_1}} = 17645$ and $K_{\mathrm{I_5}} = K_{\mathrm{I_7}} = 2000$.

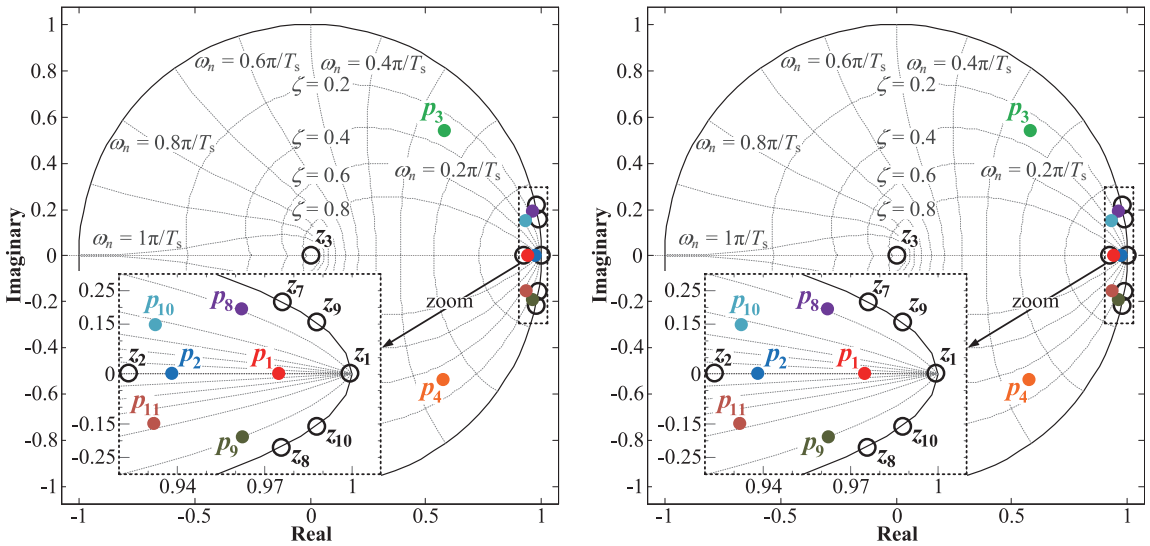

(a) Test I. Roots of $E_{\Delta i^*}(z)$.

(b) Test II. Roots of $E_{\Delta v_{\mathrm{PCC}}}(z)$.

Figure 4.9: Root-locus diagrams of the error signal during transients when using a PR controller with resonant filters at $h = 1,5,7$ for $f_s = 10\,\mathrm{kHz}$, with $K_{\mathrm{P_T}} = 25$, $K_{\mathrm{I_1}} = 17645$ and $K_{\mathrm{I_5}} = K_{\mathrm{I_7}} = 17645$.

Table 4.1: Parameters of the Error Time-Domain Expressions for the Real Poles in Figs. 4.8 and 4.9

Test	$K_{I_5} = K_{I_7}$	$r_1(p_1)$	$p'_1(p_1)$	$t_{2\%}(p_1)$	$r_2(p_2)$	$p'_2(p_2)$	$t_{2\%}(p_2)$
I	**2000**	$-1.02 \cdot 10^4$	$0.30 \cdot 10^3$	**14** ms	$1.09 \cdot 10^4$	$0.39 \cdot 10^3$	**11** ms
I	**17645**	$-0.34 \cdot 10^4$	$0.25 \cdot 10^3$	**16** ms	$0.22 \cdot 10^4$	$0.65 \cdot 10^3$	**6.2** ms
II	**2000**	$-2.97 \cdot 10^5$	$0.29 \cdot 10^3$	**14** ms	$3.63 \cdot 10^5$	$0.39 \cdot 10^3$	**10** ms
II	**17645**	$-1.06 \cdot 10^5$	$0.26 \cdot 10^3$	**16** ms	$2.52 \cdot 10^5$	$0.65 \cdot 10^3$	**6.2** ms

Table 4.2: Parameters of the Error Time-Domain Expressions for the Main Conjugate Pole Pairs in Figs. 4.8 and 4.9

Test	$K_{I_5} = K_{I_7}$	$d'_8(p_8 - p_9)$, $f'_8(p_8 - p_9)$	σ'_8 $(p_8 - p_9)$	$t_{2\%}$ $(p_8 - p_9)$	d'_{10} $(p_{10} - p_{11},)$ $f'_{10}(p_{10} - p_{11})$	σ'_{10} $(p_{10} - p_{11})$	$t_{2\%}$ $(p_{10} - p_{11})$
I	**2000**	$-5.53 \cdot 10^2$, $1.42 \cdot 10^2$	$0.04 \cdot 10^3$	**101** ms	$-5.29 \cdot 10^2$, 82.83	$0.04 \cdot 10^3$	**108** ms
I	**17645**	$3.30 \cdot 10^3$, $3.35 \cdot 10^3$	$0.19 \cdot 10^3$	**20** ms	$-1.95 \cdot 10^4$, $5.25 \cdot 10^3$	$0.61 \cdot 10^3$	**6.5** ms
II	**2000**	$-3.09 \cdot 10^2$, $2.13 \cdot 10^3$	$0.04 \cdot 10^3$	**101** ms	$-1.03 \cdot 10^3$, $2.52 \cdot 10^3$	$0.04 \cdot 10^3$	**108** ms
II	**17645**	$-8.39 \cdot 10^3$, $1.87 \cdot 10^4$	$0.19 \cdot 10^3$	**20** ms	$-5.08 \cdot 10^4$, $1.05 \cdot 10^5$	$0.61 \cdot 10^3$	**6.5** ms

applied to obtain suitable values for K_{I_h}, starting from $K_{I_1} = 17645$ at $f_s = 10\,\text{kHz}$.

New examples with resonant filters for the fifth and the seventh harmonics, as well as for the fundamental frequency, are analyzed. As it can be observed in Figs. 4.8 and 4.9, two new pair of poles ($p_8 - p_9$ and $p_{10} - p_{11}$) and two new pair of zeros ($z_7 - z_8$ and $z_9 - z_{10}$) appear in the root loci. For simplicity, identical K_{I_5} and K_{I_7} are chosen. The methodology is applied for two values: $K_{I_5} = K_{I_7} = 2000$ and $K_{I_5} = K_{I_7} = 17645$.

Figs. 4.8a and b show the root-locus diagrams of $E_{\Delta i^*}(z)$ and $E_{\Delta v_{PCC}}(z)$, respectively, with $K_{I_5} = K_{I_7} = 2000$. Figs. 4.9a and b do the same with $K_{I_5} = K_{I_7} = 17645$. Observing all of them, it is noticed that p_3 and p_4 are a bit closer to the unit circle boundary when $K_{I_5} = K_{I_7} = 17645$ is selected. On the other hand, comparing these graphics with those of Figs. 4.5a and b, it may be asserted that including more resonant filters, and the value of the respective resonant gains, affects the position of p_1 and p_2. Regarding the additional poles (p_8, p_9, p_{10} and p_{11}), it is difficult to draw immediate conclusions from the root loci in Figs. 4.8 and 4.9. The zeros z_7, z_8, z_9 and z_{10} are located at the unit circle boundary, so the two options to optimize the transient response cannot be fulfilled at the same time: placing the poles far from the unit circle boundary and next to zeros that cancel their effect (see section §4.4). In this situation, the error time-domain expressions for the main poles should be calculated (indications about how to do it are given in the Appendix §B). Tables 4.1 and 4.2 display the values of the main parameters in (B.3) and the respective settling times $t_{2\%}$ for the real poles and for the main conjugate pole pairs in the four cases analyzed in Figs. 4.8 and 4.9. Settling times are calculated as the time at which the error has entered and remained within the 2% of the residue for each of the poles and pole pairs. From these tables, it can be concluded that the effect of the majority of the poles (p_2,

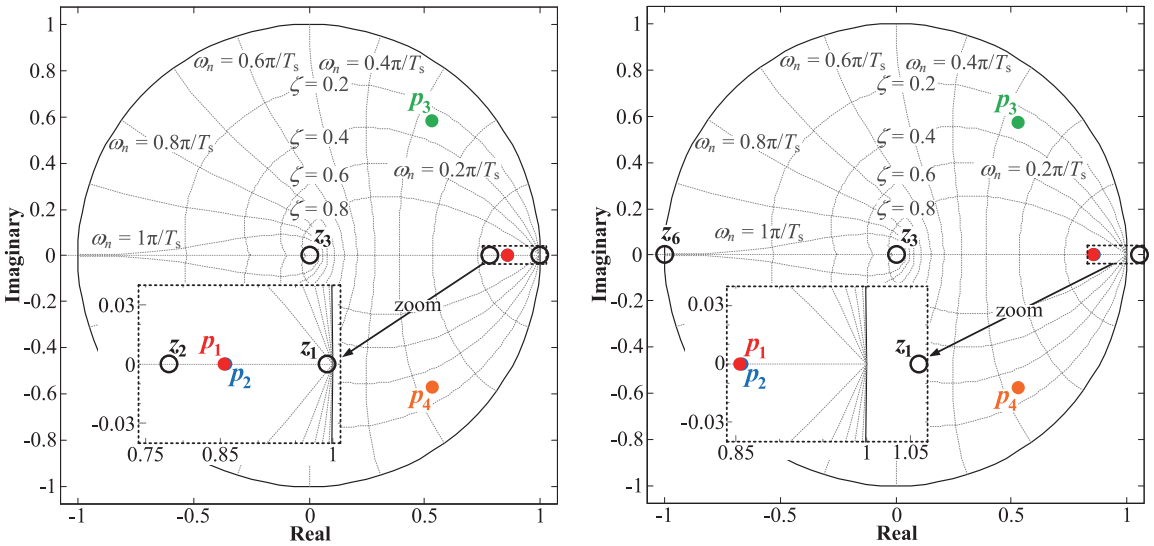

(a) Test I. Roots of $E_{\Delta i^*}(z)$.

(b) Test II. Roots of $E_{\Delta v_{\mathrm{PCC}}}(z)$.

Figure 4.10: Root-locus diagrams of the error signal during transients when using a PR controller with a single resonant filter at $h = 1$ and $f_{\mathrm{s}} = 2.5\,\mathrm{kHz}$, with $K_{\mathrm{P}_1} = 6.25$ and $K_{\mathrm{I}_1} = 5738$.

p_8, p_9, p_{10} and p_{11}) is canceled much faster when $K_{\mathrm{I}_5} = K_{\mathrm{I}_7} = 17645$ is employed, either in test I or in test II, especially the effect of p_8, p_9, p_{10} and p_{11}. On the contrary, the effect of p_1 lasts longer for $K_{\mathrm{I}_5} = K_{\mathrm{I}_7} = 17645$, although the difference is not important (the settling time of this pole for both gains is always lower than 20 ms, as indicated in Table 4.1). The overshoot caused by p_8, p_9, p_{10} and p_{11} is a lightly larger with $K_{\mathrm{I}_5} = K_{\mathrm{I}_7} = 17645$ (bigger values of the residues d'_8, f'_8, d'_{10} and f'_{10}) and slightly smaller for p_1 and p_2 (minor values of the residues r_1 and r_2). As the main objective is to minimize $t_{2\%}$, $K_{\mathrm{I}_5} = K_{\mathrm{I}_7} = 17645$ is chosen as the best option.

4.4.3 Effect of Sampling Frequency

Wind power installations of hundreds of kilowatts or megawatts usually work at lower f_{sw}, and therefore, at lower f_{s}. The aim of this section is to demonstrate the suitability of the proposed methodology when a lower $f_{\mathrm{s}} = f_{\mathrm{sw}} = 2.5\,\mathrm{kHz}$ is used, with $R = 3.1\,\Omega$ (cf. chapter §2). A PR controller with a single resonant filter at the fundamental frequency is employed. Figs. 4.10a and b depict the root-locus diagrams of $E_{\Delta i^*}(z)$ and $E_{\Delta v_{\mathrm{PCC}}}(z)$ in these conditions. As justified in section §4.4.1, transients caused by disturbance changes (sags at the PCC) are more critical, so that gain selection has been made in order to enhance their settling time. A resonant gain $K_{\mathrm{I}_1} = 5262$ places the dominant poles p_1 and p_2 as far as possible from the unit circle boundary (i.e., it makes $p_1 = p_2$, see section §4.4.1). Comparing these figures to those obtained with $f_{\mathrm{s}} = 10\,\mathrm{kHz}$ (cf. Figs. 4.5a and b), it can be observed that the faster poles p_3 and p_4 have now more impact as they are closer to the unit circle boundary. Short settling times can be achieved at the cost of bigger initial oscillations since the dominant poles p_1 and p_2 may be placed at the optimal position. However, at really low f_{s}, the effect of the delay will make p_3 and p_4 dominant (or even unstable). Hence, it seems very difficult to achieve the same design constraints ($t_{2\%} < 20\,\mathrm{ms}$) by only tuning the PR controller parameters. Alternatives

and enhancements for very low f_s scenarios (e.g., multi-megawatt applications [46, 104]) is a challenging topic for future works, but out of the scope of this chapter.

4.4.4 Comparison with Previous Assessments

As commented along the chapter, the influence of integral gains in the transient response has been approached in several works [79, 80, 139, 144, 146, 160, 165, 166]. Most of them give qualitative guidelines that can be summarized as follows.

a) As K_{I_1} increases, the transient response enhances, but filtering and stability worsen.

b) Coupling between resonant terms results in higher oscillations.

It is worth mentioning that an expression for the main time constant is given in [80, 139] as $\tau = K_{P_1}/K_{I_1}$, which closely matches the inverse of the real part of p_2. Therefore, it is a suitable approximation for current loop tuning when resonant gains are low ("narrow bandpass filters"), which is not the case when the main goal is to minimize the settling time. In this situation, delay should not be disregarded (it modifies p_3 and p_4, pushing them towards the unit circle boundary). Furthermore, as explained in section §4.4.1, the information given in [80, 139] is not enough to optimize $e_{\Delta v_{PCC}}(t)$, which is more critical than $e_{\Delta i^*}(t)$. Some advantages of the proposed methodology with respect to [80, 139] are the following.

- It is possible to choose K_{I_1} so that $p_1 = p_2$, the main guideline given for an optimal design.
- It allows to assess the damping of the dominant roots.
- It permits to calculate the gain at which p_3 and p_4 become significant/dominant.
- If multiple resonant filters are considered, cross couplings between the different terms may be evaluated.

4.5 Experimental Results

Fig. 4.11 is a photograph of the real implementation described in Fig. 4.2. A three-phase VSC working as a rectifier has been built to test the proposed methodology. The rectifier application has been selected because it allows to test very demanding transients with the available laboratory equipment. Nevertheless, results are equivalent to those of an inverter due to the bidirectionality of this converter [165]. Real-time implementation is achieved through the prototyping platform dSpace DS1104, which includes a Power PC MPC8240 and a Texas Instruments TMS320F240 digital signal processor (DSP). A Pacific 360-AMX three-phase linear power source is used to supply the ac source voltages and to program the voltage sags.

The rectifier digital controller from Fig. 4.2 works as follows.

- A PI controller keeps constant the dc-link voltage v_{dc}. Its output is the current reference for the d axis of an SRF i_d^*.
- The current reference for the q axis of the SRF i_q^* is set manually. This permits a degree of freedom to perform the tests (i_d^* is the actuation of the outer loop, so it cannot be modified). The most demanding transient in the reference that can be tested is a $+90^\circ$ phase jump.

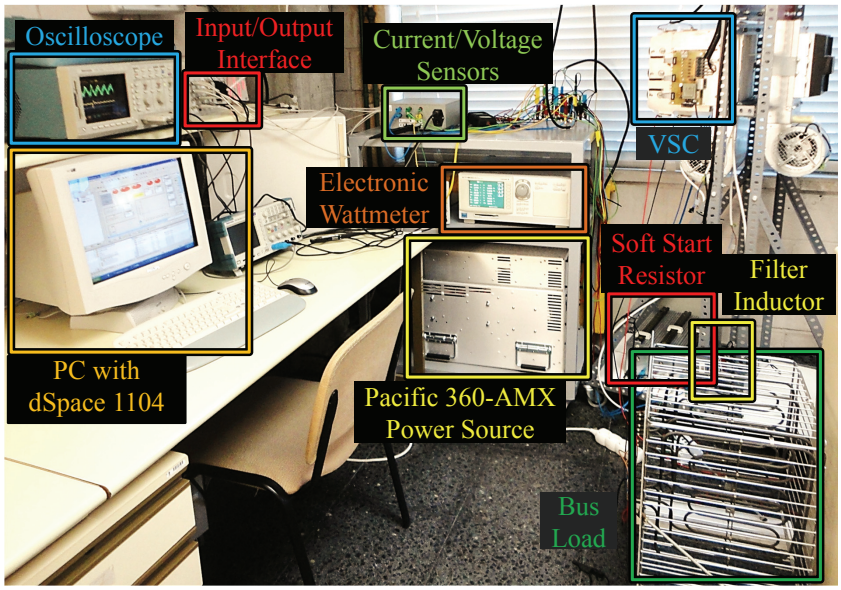

Figure 4.11: Photo of the laboratory prototype.

Table 4.3: Power Rate of the Different Tests

$f_s = f_{sw}$	Test	P_{rated}
10 kHz	I	3 kVA
10 kHz	II	2.1 kVA
2.5 kHz	I	1.7 kVA
2.5 kHz	II	1.5 kVA

- A phase-locked loop (PLL) is used to track the phase angle of the power source θ_1. This angle is employed in the dq $-$ $\alpha\beta$ transformation of the current reference.
- A pair of PR controllers is employed to regulate the current in the $\alpha\beta$ frame (one in each of the axes). Their output m is driven to the PWM unit of the DSP.

The experimental evaluation of the controllers studied in the previous section is made for transients caused by i^* changes (test I) and by v_{PCC} changes (test II). In addition, another subsection is included, which discusses the effect of the sampling frequency. Table 4.3 indicates the power rate P_{rated} of the different experiments.

4.5.1 PR Controller only at the Fundamental Frequency

The same values as in section §4.4.1 are used in these experimental tests ($K_{I_1} = 2000$, 17645, 34000 and 100000, $K_{P_1} = 25$ and $f_s = 10$ kHz). Oscilloscope captures depict the a-phase PCC voltage v_{PCC_a}, the a-phase current i_a and the actual error in α axis e_α. Besides, the estimated error is also depicted $\hat{e}_\alpha$.

This error estimation has been obtained from the respective root loci (Figs. 4.4, 4.5, 4.6 and 4.7) following the steps detailed in the Appendix §B. It should be noticed that e_α and $\hat{e}_\alpha$ are internal signals of the control that have been read through digital-to-analog converters (DACs).

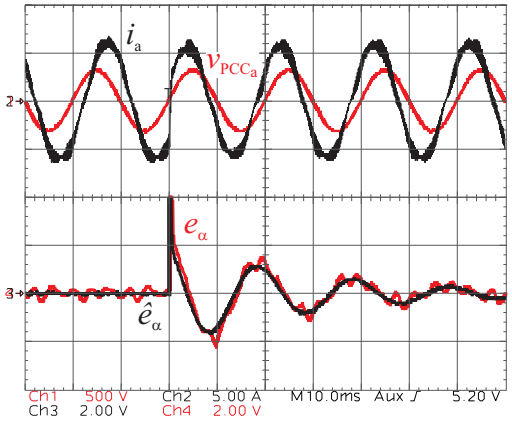

(a) Test I. Reference change. $K_{I_1} = 2000$.

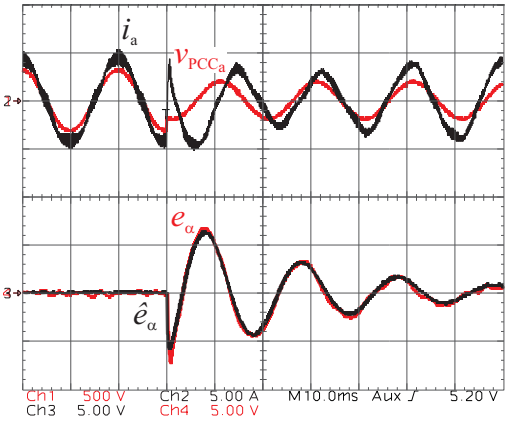

(b) Test II. Disturbance change.$K_{I_1} = 2000$.

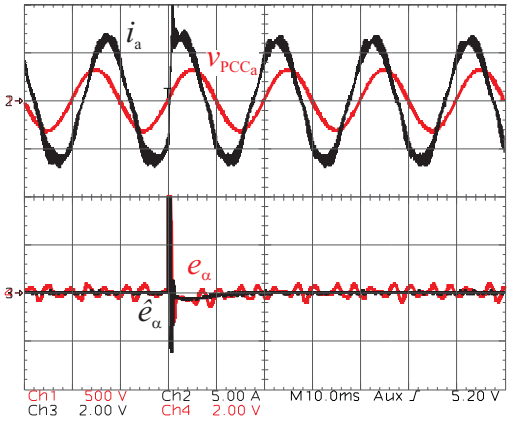

(c) Test I. Reference change.$K_{I_1} = 17645$.

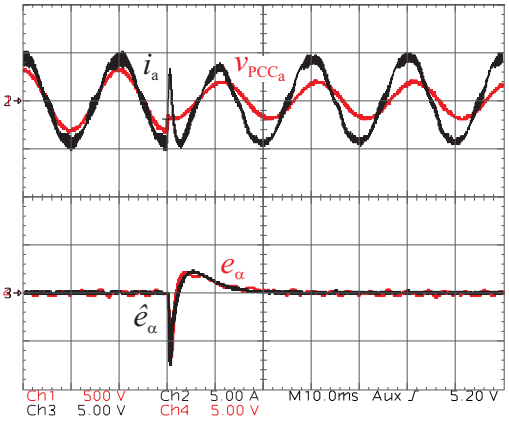

(d) Test II. Disturbance change. $K_{I_1} = 17645$.

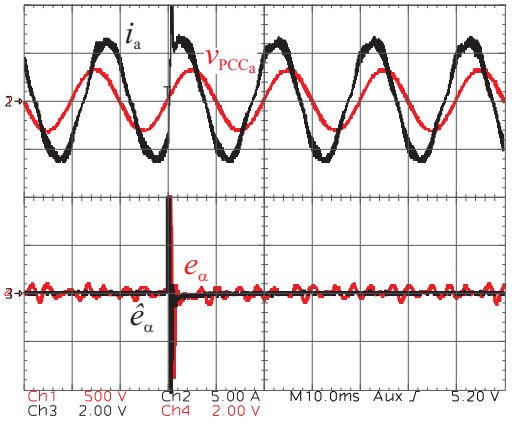

(e) Test I. Reference change. $K_{I_1} = 34000$.

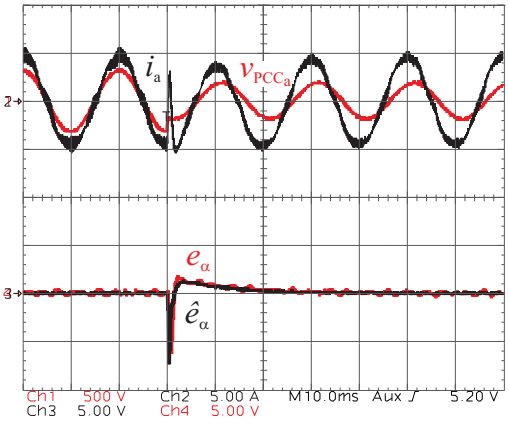

(f) Test II. Disturbance change.$K_{I_1} = 34000$.

Figure 4.12: Continued on next page.

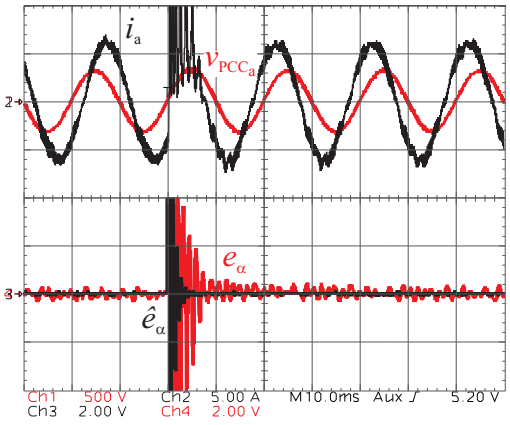

(g) Test I. Reference change. $K_{I_1} = 100000$.

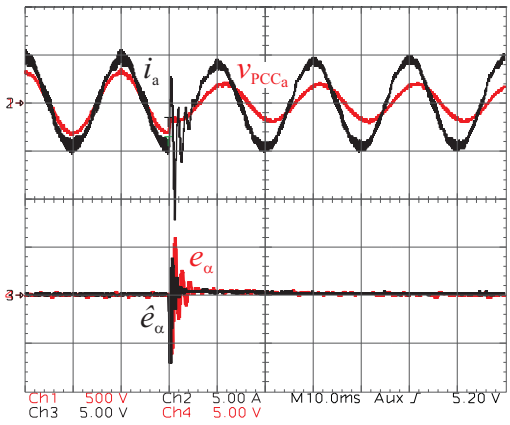

(h) Test II. Disturbance change. $K_{I_1} = 100000$.

Figure 4.12: Transient response when using a PR controller with a single resonant filter at $h = 1$ and $f_s = 10\,\text{kHz}$, with $K_{P_1} = 25$. Comparison of different K_{I_1} values. Scales: v_{PCC_a} in $500\,\text{V/div}$, i_a in $5\,\text{A/div}$, $\hat{e}_\alpha$ and e_α in $0.9\,\text{A/div}$ for (a), (c), (e) and (g) and in $3\,\text{A/div}$ for (b), (d), (f) and (h), time in $10\,\text{ms/div}$. This figure is continued from previous page.

Figs. 4.12a and b show the experimental results for $K_{I_1} = 2000$. The initial peaks are high-frequency oscillations caused by p_3 and p_4 (cf. Figs. 4.4a and b). As these poles are much faster than p_1 and p_2, their influence in the error response disappears quickly. It can also be observed that these initial oscillations are more important for transients in the current reference than for transients in v_{PCC}, i.e., the residues of p_3 and p_4 are larger in the former. The reason is that the dominant poles p_1 and p_2 have minor relative importance when testing transients in the current reference (smaller residues, but still bigger than those of p_3 and p_4) because they are more easily canceled by z_1 and z_2 (cf. Fig. 4.4a). In case of disturbance changes, there is no z_2 and z_1 is farther from p_1 (cf. Fig. 4.4b). Going back to Figs. 4.12a and b, it may be observed that $K_{I_1} = 2000$ leads to an oscillating and slow error decay (longer than 70 ms) in both tests.

On the one hand, with $K_{I_1} = 17645$, the transient response is significantly improved for both $e_{\Delta i^*}$ and $e_{\Delta v_{PCC}}$, as it can be checked from Figs. 4.12c and d. In relation to the initial higher-frequency oscillations, no relevant differences are discerned with respect to the previous graphics, Figs. 4.12a and b. Regarding the settling times, in case of a change in the current reference, e_α is canceled in a time shorter than 20 ms. For the disturbance change, e_α decays in around 20 ms. Transients are much shorter and less oscillating than with $K_{I_1} = 2000$, corroborating the conclusion drawn from the error transfer function analysis (see in Figs. 4.5a and b that p_1 and p_2 are located in the real axis, farther from the unit circle boundary).

On the other hand, with $K_{I_1} = 34000$, the transient error also decays quickly and with no oscillations, as illustrated in Figs. 4.12e and f, like it did in the previous case, with $K_{I_1} = 17645$. The initial oscillations are also similar. Transients caused by reference changes are even faster (corroborating the results obtained from the root loci analysis of Fig. 4.6a), with settling times shorter than 5 ms. Nevertheless, in case of disturbance changes, e_α decays slightly slower than in Fig. 4.12d, although the overshoot is smaller with $K_{I_1} = 34000$ (see in Fig. 4.6b how p_2 is not canceled by any zero).

Finally, from Figs. 4.12g and h, the transient response worsens for $K_{I_1} = 100000$. High-frequency oscillations are really significant and lead to an undesired response. This happens

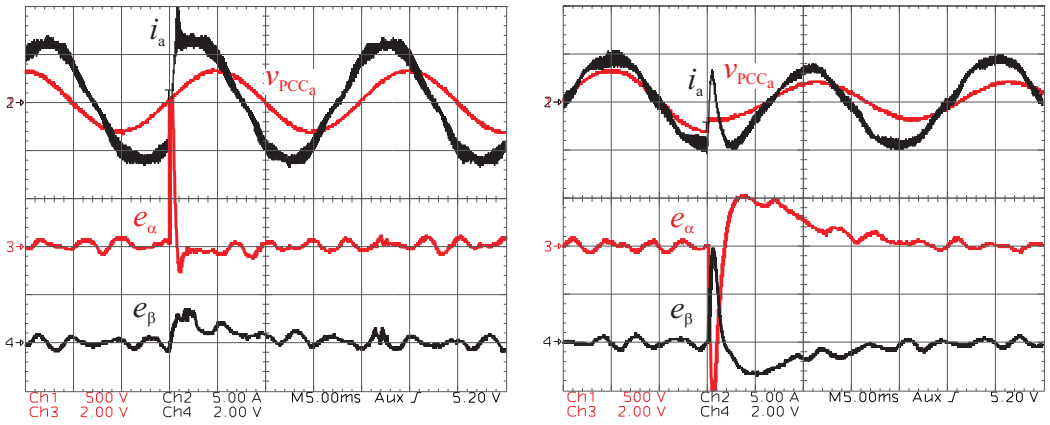

(a) Test I. Reference change.

(b) Test II. Disturbance change.

Figure 4.13: Detailed transient response when using a PR controller with a single resonant filter at $h = 1$ and $f_s = 10\,\text{kHz}$, with $K_{P_1} = 25$ and $K_{I_1} = 17645$. Scales: v_{PCC_a} in $500\,\text{V/div}$, i_a in $5\,\text{A/div}$, e_α and e_β in $0.9\,\text{A/div}$ for (a) and in $1.8\,\text{A/div}$ for (b), time in $5\,\text{ms/div}$.

because p_3 and p_4 are now the dominant poles (cf. Figs. 4.7a and b). From Fig. 4.12, it can be noticed that $\hat{e}_\alpha$ matches e_α in all the tests, strengthening the suitability of the proposed methodology. However, some differences are observed when $K_{I_1} = 100000$ is employed (cf. Figs. 4.12g and h). Real responses exhibit larger high-frequency oscillations, which permits to understand that the real plant has a delay bigger than the one considered (i.e., the imaginary terms of p_3 and p_4 are actually larger). Such little increase in the delay may be caused by the filters that adapt the sensed signals. This fact happens no matter the value of K_{I_1}, but the difference is more obvious when p_3 and p_4 are the dominant poles, as they have more influence in the error time-domain response.

As a conclusion, as reported in section §4.4.1, the optimal value for K_{I_1} implies a tradeoff between reference and disturbance transients. Regarding the settling time, for the selected K_{P_1}, $K_{I_1} = 34000$ is proved to be the most suitable value in reference changes and $K_{I_1} = 17645$, in disturbance changes, even though it causes a larger overshoot, corroborating the results drawn from the root loci analysis. It should be noticed that either of these two gains is a proper option in this kind of applications where the transient response is crucial, leading to much better results than those obtained with $K_{I_1} = 2000$.

Since transients caused by disturbances tend to be much longer, $K_{I_1} = 17645$ is proposed as the best tradeoff value according to the LVRT and grid support requirements of GCs (specified in terms of response times to follow the new reference commands): when a grid fault occurs, the system should be fast both recovering from the fault and tracking the new reference. This $K_{I_1} = 17645$ allows to attain settling times of about 20 ms in both situations, fulfilling the conditions specified in the most demanding GCs [39–41].

Fig. 4.13 illustrates in detail the error in both α and β axes e_α and e_β for $K_{I_1} = 17645$. It should be highlighted that this study analyzes each axis separately. In previous figures, e_α is shown, owing to the fact that the longest transient takes place in this component (they have been selected this way).

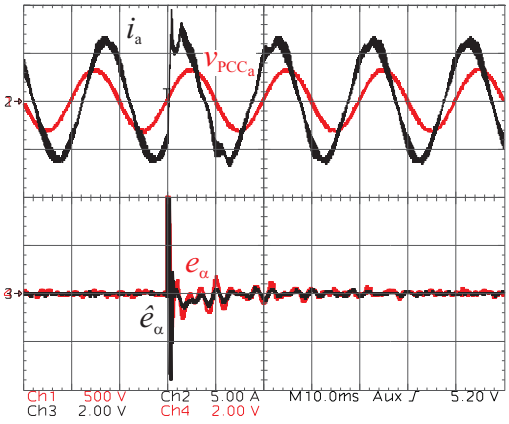

(a) Test I. Reference change. $K_{I_5} = K_{I_7} = 2000$.

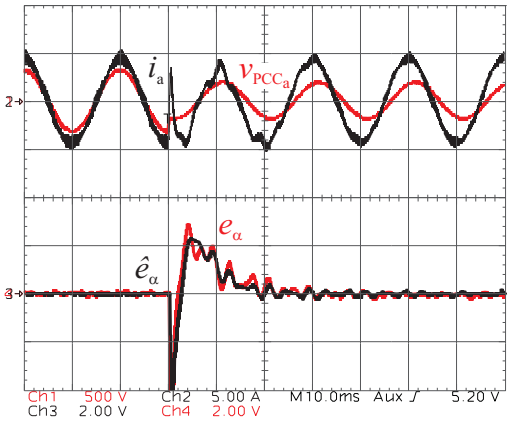

(b) Test II. Disturbance change. $K_{I_5} = K_{I_7} = 2000$.

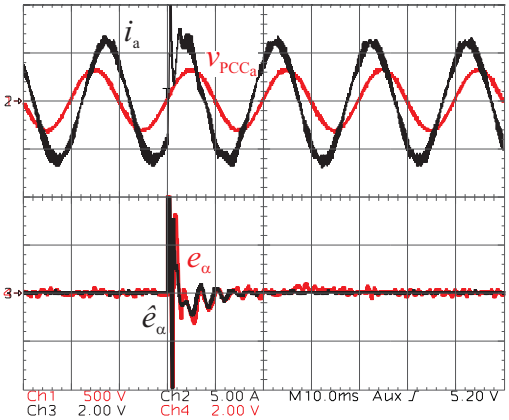

(c) Test I. Reference change. $K_{I_5} = K_{I_7} = 17645$.

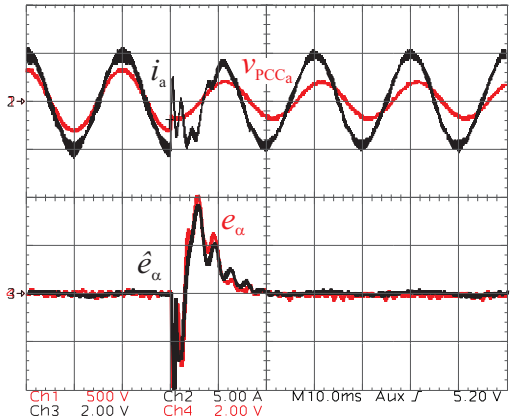

(d) Test II. Disturbance change. $K_{I_5} = K_{I_7} = 17645$.

Figure 4.14: Transient response when using a PR controller with resonant filters at $h = 1, 5, 7$ and $f_s = 10\,\text{kHz}$, with $K_{P_T} = 25$ and $K_{I_1} = 17645$. Comparison between different $K_{I_5} = K_{I_7}$ values. Scales: v_{PCC_a} in $500\,\text{V/div}$, i_a in $5\,\text{A/div}$, $\hat{e}_\alpha$ and e_α in $0.9\,\text{A/div}$ for (a) and (c) and in $1.8\,\text{A/div}$ for (b) and (d), time in $10\,\text{ms/div}$.

4.5.2 PR Controller at Fundamental and Harmonic Frequencies

The same two values of K_{I_5} and K_{I_7} as in section §4.4.2 are employed in these experimental tests in which $K_{I_1} = 17645$, $K_{P_T} = 25$ and $f_s = 10\,\text{kHz}$. Figs. 4.14a and b show e_α with $K_{I_5} = K_{I_7} = 2000$ and Figs. 4.14c and d, with $K_{I_5} = K_{I_7} = 17645$. Slightly larger initial high-frequency oscillations are observed for $K_{I_5} = K_{I_7} = 17645$. This is because, with these gains, the poles p_3 and p_4 are a bit closer to the unit circle boundary (compare Figs. 4.8 and 4.9). Nevertheless, the cancellation of harmonic fluctuations in the error signal is slower for $K_{I_5} = K_{I_7} = 2000$ (the poles from the harmonic resonant filters $p_8 - p_{11}$ are closer to the unit circle boundary). On the other hand, the error caused by the resonant filter tuned at the fundamental frequency is hidden by the harmonic oscillations, making difficult to distinguish its decay rate. The overshoot is bigger for $K_{I_5} = K_{I_7} = 17645$. If the goal is to achieve the shortest settling times, $K_{I_5} = K_{I_7} = 17645$ is proved to be the most suitable option, although there are no

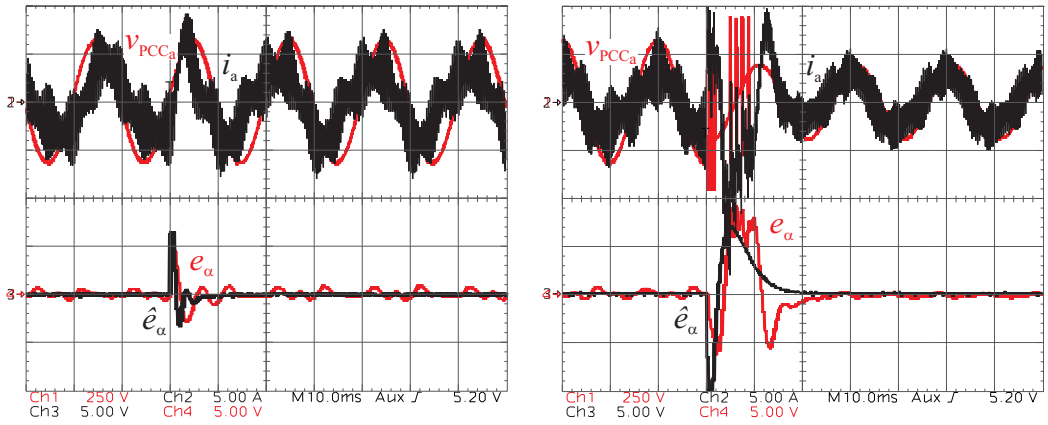

(a) Test I. Reference change.

(b) Test II. Disturbance change.

Figure 4.15: Transient response when using a PR controller with a single resonant filter at $h = 1$ and $f_s = 2.5\,\text{kHz}$, with $K_{P_1} = 6.25$ and $K_{I_1} = 5262$. Scales: v_{PCC_a} in $500\,\text{V/div}$, i_a in $5\,\text{A/div}$, $\hat{e}_\alpha$ and e_α in $2.6\,\text{A/div}$ for (a) and in $6\,\text{A/div}$ for (b), time in $10\,\text{ms/div}$.

relevant differences with respect to those of $K_{I_5} = K_{I_7} = 2000$.

4.5.3 Effect of Sampling Frequency

The same values $K_{I_1} = 5262$ and $K_{P_1} = 6.25$ as in section §4.4.3 are used in these experimental tests at a lower $f_s = 2.5\,\text{kHz}$. Figs. 4.15a and b display the transient responses caused by a current reference change and by a disturbance change, respectively. Although at this f_s, the initial oscillations are bigger than those of Figs. 4.12c and d (p_3 and p_4 are closer to the unit circle boundary, see section §4.4.3), settling times lower than 20 ms are achieved in both tests. Therefore, even at low f_s, transients due to changes in i^* and transients due to changes in v_{PCC} can be canceled in a shorter time than that requested in the most demanding GCs [39–41]. Figs. 4.16a and b illustrate in detail the error behavior in both α and β axes.

4.6 Conclusions

This chapter has developed a methodology to assess and optimize the transient response of PR controllers. Controller tuning aims at minimizing the postfault and new reference tracking settling times, so that power electronics converters in DPGSs can fulfill the most demanding GC requirements (LVRT and grid support). The developed technique is based on the modeling and study of the error signal transfer function roots caused either by transients in the reference (modifications of the current command) or by changes in the disturbance (voltage sags at the PCC). Both error signals are independent from each other, since the proposed approach is based on linear control analysis. Different significant situations considering very demanding scenarios have been analyzed and tested. The obtained experimental results prove that the theoretical expressions accurately estimate the real behavior of the current loop and hence, they are suitable for a precise adjustment of its parameters.

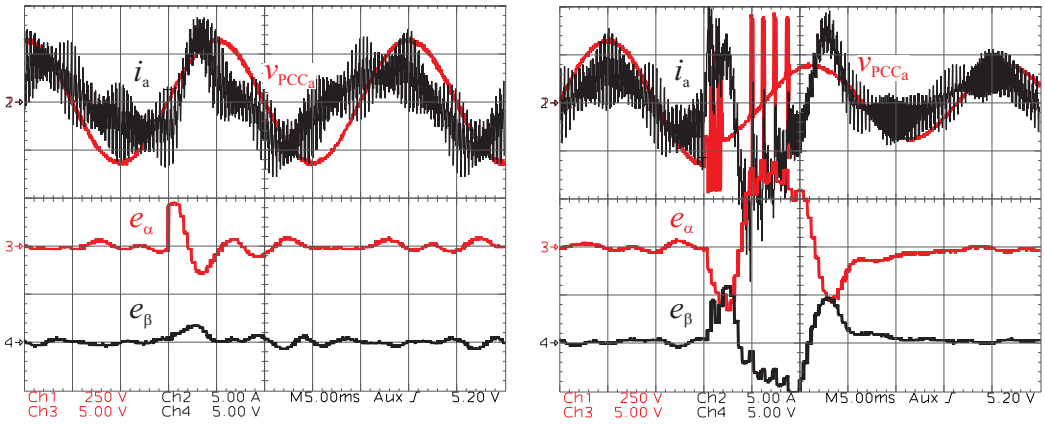

(a) Test I. Reference change.

(b) Test II. Disturbance change.

Figure 4.16: Detailed transient response when using a PR controller with a single resonant filter at $h = 1$ and $f_s = 2.5\,\text{kHz}$, with $K_{P_1} = 6.25$ and $K_{I_1} = 5262$. Scales: v_{PCC_a} in $500\,\text{V/div}$, i_a in $5\,\text{A/div}$, e_α and e_β in $2.6\,\text{A/div}$ for (a) and in $6\,\text{A/div}$ for (b), time in $5\,\text{ms/div}$.

In addition to the proposed design methodology, some specific results and considerations are important contributions of this study. They are summarized in the following.

- As expected from previous works, it is possible to get a very fast current reference tracking if high resonant gains are employed [79, 80, 139, 144, 146, 160, 165, 166]. However, this study demonstrates that this is achieved at the cost of longer transients when there is a change in the disturbance, i.e., a voltage sag at the PCC. By particularizing to the DPGS scenario, and more specifically, to LVRT and grid support requirements of GCs, both response times should be minimized. When a fault occurs at the PCC, the current controller should reject it; at the same time, the voltage sag has to be characterized to assess the new current command according to GC indications (which usually involves more reactive current to support the grid). Once the new current reference is available, the current controller should track it as fast as possible. Since GC specifications are in terms of response times to follow the new current references, the proposed tuning is a tradeoff that minimizes the most critical transient, i.e., the one due to disturbance changes. This optimal tuning is achieved by selecting the gains so that the dominant poles are $p_1 = p_2$.

- The most demanding LVRT and grid support requirements, such as those from Germany [39–41], require response times of 20 ms to follow the new reference command. On the other hand, it should also be taken into account the time necessary to characterize the voltage sag amplitude, which is around 20 ms (one fundamental cycle) according to the standards [206, 207]. During this task, it seems very desirable to totally cancel $e_{\Delta v_{PCC}}$. Once the sag is characterized, the new references for the current controller according to GCs must be calculated (current references from the outer loops, which have slower dynamics, are disregarded). Experimental results prove that, with the proposed methodology, settling times lower than 20 ms are achieved for both errors ($K_{I_1} = 17645$: Figs. 4.12d, 4.13b and 4.14d for $e_{\Delta v_{PCC}}$ and Figs. 4.12c, 4.13a and 4.14c for $e_{\Delta i^*}$). Hence, the proposed approach is suitable to fulfill the most demanding GC requirements in terms of transient response.

- It is demonstrated that the initial phase at which the step is commanded influences the transient response seen in the stationary frame, which is not possible to distinguish from the SRF analysis. On the other hand, the proper tuning of the PR controller parameters is not as dependent on f_s as it may be intuitively expected. The limits in the response are imposed by the effect of the delay and its associated roots p_3 and p_4, but the delay does not affect much the dominant poles p_1 and p_2. In practice, it is proved that settling times lower than 20 ms are attained even for a low sampling frequency $f_s = 2.5$ kHz (cf. Figs. 4.15a, b, 4.16a and b). In this manner, the proposed tuning for PR current controllers is also suitable for high power generation units with low f_s.

Contributions of this chapter have been published in the journal IEEE Transactions on Industrial Electronics [14].

Chapter 5

Transient Response Evaluation of Stationary-Frame Resonant Current Controllers for Grid-Connected Applications

Abstract *— This chapter provides a thorough analysis of the vector proportional-integral (VPI) controller transient response and compares it with that of the popular proportional-resonant (PR) controllers for grid-connected applications. The employed methodology is based on the study of the error signal roots: both reference tracking and disturbance rejection abilities are considered for proper gain tuning. It is proved that PR controllers lead to shorter settling times than VPI controllers at high sampling frequencies. However, as the sampling frequency decreases, the transient response of both controllers presents more similarities. A three-phase voltage source converter prototype has been implemented. Experimental results comparing the transient behavior of VPI and PR controllers in different conditions are provided: a* $+90^\circ$ *phase-angle jump in the current reference and a "type C" voltage sag at the PCC.*

5.1 Introduction

The increasing amount of renewable energy sources connected to the power system leads to problems to maintain voltage and frequency within the operating limits. In order to guarantee the stability and reliability of the utility network, the transmission system operators of the different countries have developed specific regulations called grid codes (GCs) [37, 39–41]. Modern GCs force generation systems to remain connected to the network even when grid faults occur, which is known as low-voltage ride-through (LVRT) [48, 60, 61, 209, 217–219]. Moreover, during these events, the most demanding ones also require generators to support the grid by supplying a certain amount of reactive current, which depends on the voltage drop [37, 39–41].

In renewable energy applications, the grid-side converter is usually based on dual-loop controllers [34, 48, 209, 217–220]. Inner loops with fast dynamics control the current according to the references given by the outer loops. These outer loops, which have slower dynamics, often regulate the reactive power and the dc-link voltage [34, 217–219]. In addition, according to GCs, once a fault is detected, a certain amount of reactive current must be injected by the generation unit within a maximum delay [39–41]. To fulfill this challenging requirement, two

main tasks are critical: new reference generation and current control [35, 209, 218]. Focusing on the first point, the new references for the current control loop need to be updated really fast, so reference generation through outer power controllers with slower dynamics has to be disregarded. In this manner, some works propose to substitute the steady-state outer controllers by new blocks during the fault [48, 209]. Besides, a rigorous analysis and design of the current controller transient response has to be conducted in order to achieve fast new reference tracking and disturbance [i.e., voltage sag at the point of common coupling (PCC)] rejection.

Regarding this second task, a methodology to assess and optimize the transient response of proportional-resonant (PR) controllers has been proposed in chapter §4. It is based on studying the roots of the error signal transfer function by means of root-locus diagrams. Suitable gains are set to achieve fast and nonoscillating transient responses; i.e., to minimize the settling time. It is proved that the optimal gain selection results from a tradeoff between transients caused by reference changes and transients caused by changes at the PCC. The effect of different sampling frequencies is also discussed. According to this study, an accurate tuning of PR controllers makes them suitable to fulfill the demanding GC requirements in terms of transient response.

The so-called vector proportional-integral (VPI) controllers have been presented as alternative resonant regulators to PR ones [77, 79, 142, 143, 147, 148, 157, 167–170]. Some recent works show that VPI controllers could provide higher stability margins than PR ones, and hence, more damped responses [77, 79, 143, 157]. Given these advantages of VPI controllers, and the lack of studies about their utilization for current control in renewable energy applications, the methodology proposed in chapter §4 is applied to them in this chapter, and, once the VPI controller is accurately adjusted, the results are compared with those of the PR controller in terms of settling time and overshoot. Experimental results where the transient response of both controllers is contrasted are included, regarding both reference and disturbance changes, as well as the effect of different sampling frequencies.

The chapter is organized as follows. Section §5.2 summarizes the fundamental aspects of the methodology to be used. Section §5.3 specifies the controllers and tests to be analyzed and shows the root-locus diagrams in these significant situations. Finally, the experimental results of section §5.4 verify the outcomes of the theoretical study, which are highlighted in section §5.5.

5.2 Transient Assessment Based on the Error Signal Roots

The methodology proposed in chapter §4 is based on the inspection of the root loci of the current error signal caused by transients. Therefore, the first step is to obtain the discrete-time expression of the global current error $E(z) = I^*(z) - I(z)$, which can be drawn from the current control loop model. The same block diagram as that in Fig. 4.1 is considered and, as done in the previous chapter, since all the transfer functions defined along this one are expressed with respect to the stationary frame, subscripts $\alpha\beta$ are omitted for the sake of clarity. As a linear system, the global current error is the addition of the partial errors:

$$E(z) = E_{\Delta i^*}(z)|_{\Delta v_{\mathrm{PCC}}=0} + E_{\Delta v_{\mathrm{PCC}}}(z)|_{\Delta i^*=0} \tag{5.1}$$

so that the error caused by changes in the current reference $E_{\Delta i^*}(z)$ and the error caused by changes in the disturbance, i.e., in the voltage at the PCC, $E_{\Delta v_{\mathrm{PCC}}}(z)$ can be analyzed separately. The discrete-time domain transfer functions that represent the error in both situations are

deduced:

$$E_{\Delta i^*}(z)|_{\Delta v_{\mathrm{PCC}}=0} = \frac{1}{1+G_{\mathrm{C}}(z)z^{-1}G_{\mathrm{L}}^{\mathrm{ZOH}}(z)}\Delta i^*(z) \tag{5.2}$$

$$E_{\Delta v_{\mathrm{PCC}}}(z)|_{\Delta i^*=0} = \frac{G_{\mathrm{L}}^{\mathrm{Tustin}}(z)}{1+G_{\mathrm{C}}(z)z^{-1}G_{\mathrm{L}}^{\mathrm{ZOH}}(z)}\Delta v_{\mathrm{PCC}}(z). \tag{5.3}$$

$G_{\mathrm{L}}^{\mathrm{Tustin}}(z)$ and $G_{\mathrm{L}}^{\mathrm{ZOH}}(z)$ are obtained by discretization of the plant model $G_{\mathrm{L}}(s) = 1/(sL+R)$ with Tustin and zero-order hold (ZOH) methods, respectively [79]. Apart from the resistance of the filter R_{F}, the equivalent loss resistance of the converter may also be considered in R, as explained in chapters §2 and §3. On the other hand, L represents the actual inductance of the current loop, which may differ from that of the interface filter L_{F} (see chapter §3). The discretization of the plant model with the ZOH method, i.e., $G_{\mathrm{L}}^{\mathrm{ZOH}}(z)$, implicitly includes the half a sample delay introduced by the regularly sampled pulse-width modulation (PWM) in (5.2) and (5.3), while z^{-1} represents the computational delay [80]. $\Delta i^*(z)$ is discrete-time expression of a change (either in amplitude or in phase) in the current reference:

$$i^*(z) = (A_{\mathrm{new}} - A_{\mathrm{old}})\underbrace{\frac{1-z^{-1}\cos(\omega_1 T_{\mathrm{s}})}{1-2z^{-1}\cos(\omega_1 T_{\mathrm{s}})+z^{-2}}}_{\text{cosine term}} + (B_{\mathrm{new}} - B_{\mathrm{old}})\underbrace{\frac{z^{-1}\sin(\omega_1 T_{\mathrm{s}})}{1-2z^{-1}\cos(\omega_1 T_{\mathrm{s}})+z^{-2}}}_{\text{sine term}} \tag{5.4}$$

where $(A_{\mathrm{new}} - A_{\mathrm{old}})$ and $(B_{\mathrm{new}} - B_{\mathrm{old}})$ are the amplitude changes of the cosine and sine terms, respectively, T_{s} denotes the sampling period and ω_1 is the fundamental frequency. The same expression can be used for $\Delta v_{\mathrm{PCC}}(z)$, which models a voltage change at the PCC.

$G_{\mathrm{C}}(z)$ is the discrete-time domain expression of a current controller implemented in the $\alpha\beta$ frame. For the PR controller, it has been obtained by applying the impulse invariant discretization method [79]:

$$G_{\mathrm{PR}_h}(z) = K_{\mathrm{P}_h} + K_{\mathrm{I}_h}T_{\mathrm{s}}\frac{1-z^{-1}\cos(h\omega_1 T_{\mathrm{s}})}{1-2z^{-1}\cos(h\omega_1 T_{\mathrm{s}})+z^{-2}} \tag{5.5}$$

where h is the harmonic order and K_{P_h} and K_{I_h} are the controller gains [77, 79, 146, 147, 157].

In the case of the VPI controller, discretization has been performed by decomposing the continuous-domain equation as the sum of two resonant terms (the Laplace transforms of a sine and a cosine term) and employing a different discretization method for each of them: Tustin with prewarping and impulse invariant methods, respectively [79]:

$$G_{\mathrm{VPI}_h}(z) = K_h\left[\underbrace{L\cos^2\left(\frac{h\omega_1 T_{\mathrm{s}}}{2}\right)\frac{1-2z^{-1}+z^{-2}}{1-2z^{-1}\cos(h\omega_1 T_{\mathrm{s}})+z^{-2}}}_{\text{sine term}} + \underbrace{R\,T_{\mathrm{s}}\frac{1-z^{-1}\cos(h\omega_1 T_{\mathrm{s}})}{1-2z^{-1}\cos(h\omega_1 T_{\mathrm{s}})+z^{-2}}}_{\text{cosine term}}\right] \tag{5.6}$$

where $K_{\mathrm{P}_h}/K_{\mathrm{I}_h} = L/R$ and $K_h = K_{\mathrm{P}_h}/L$ have been selected in order to achieve plant pole cancellation through internal model control (IMC) [77, 79, 142, 143, 147, 148, 157]. Further analysis about the influence of the discretization technique at low sampling frequencies f_{s} is given in section §5.3.3.

Once the error expressions are defined, one can graphically represent their roots and study their movement with gain variation, as well as the effects of their position in terms of transient response. The error transient response is, in this manner, optimized by making poles fast (large decay rates) and by placing them next to zeros that cancel their effect (small residues).

5.3 Design Study

The transient responses of PR and VPI controllers are assessed considering the following tests: a phase change of $+90^\circ$ in the current reference (test I) and a typical sag in wind power installations categorized as "type C" with a characteristic voltage of the dip of 40% (test II) [221]. These two transients have been applied to:

- single resonant controllers tuned at the fundamental frequency $\omega_1 = 2\pi 50\,\mathrm{rad/s}$, in section §5.3.1. with $f_s = 10\,\mathrm{kHz}$ and a switching frequency $f_{sw} = 10\,\mathrm{kHz}$ and with $f_s = f_{sw} = 2.5\,\mathrm{kHz}$ in section §5.3.3;
- several resonant controllers tuned at the fundamental and harmonic frequencies, in section §5.3.2, with $f_s = f_{sw} = 10\,\mathrm{kHz}$.

Root-locus diagrams have been depicted for $L = L_F = 4.51\,\mathrm{mH}$ and $R_F = 0.5\,\Omega$, which correspond with the parameters of the experimental setup (see section §5.4). On the other hand, it should be noticed that each VPI controller has only one gain to be tuned, K_h [cf. (5.6)], unlike the PR one, which has two of them, K_{P_h} and K_{I_h} [cf. (5.5)].

5.3.1 Resonant Controllers only at Fundamental Frequency

Fig. 5.1 depicts root-locus diagrams at $f_s = 10\,\mathrm{kHz}$, with $R = 4\,\Omega$ (cf. chapter §2) as a function of K_1 (K_h with $h = 1$) in case of a reference change [(5.2), test I] and a disturbance change [(5.3), test II]. For the PR controller, equivalent diagrams are detailed in Fig. 4.3. The study of the VPI controller (with respect to that of the PR one conducted in the previous chapter) implies to change only $G_C(z)$, so just the roots that depend on it are different. As the numerators and denominators of PR and VPI controllers are of the same order [see (5.5) and (5.6)], the number of zeros and poles in (5.2) and (5.3) is the same for both controllers. Thus, an analogous root numbering to that described in chapter §4 is applied with the VPI controller. In this manner, the roots that depend on the controller transfer function are p_1, p_2, p_3, p_4, z_4 and z_5. However, the zeros z_4 and z_5 cancel the poles p_5 and p_6 from the input, as it happened for PR controllers, so further analysis is focused on the poles p_1, p_2, p_3 and p_4.

- The poles p_1 and p_2 are the dominant ones. From Fig. 5.1, their behavior is similar to those in the case of PR controllers (see chapter §4). When K_1 is low, they are close to $z = 1$ and they are slower than the other poles. As K_1 increases, they approach the real axis, i.e., they reduce their oscillating terms. Once there, both poles move along the real axis in opposite directions, making p_1 slower and p_2 faster.
- Nevertheless, the other pair of poles p_3 and p_4 behaves differently from that in PR controllers. Both poles are placed in the real axis, p_4 next to z_3 and p_3 next to z_2, the latter of which is associated to the plant. This fact corresponds to the ability of VPI controllers to cancel the plant dynamics [see (4.1) and (5.6)]. As K_1 grows, p_3 and p_4 move along the real axis, getting separated from the respective zeros, and hence worsening the plant cancellation. It should be remarked that, for transients in v_{PCC} (Fig. 5.1b), the zero z_2 is already canceling the pole p_7, due to the numerator in (5.3).

Once the roots movement has been understood, it can be concluded that the value of K_1 that satisfies $p_1 = p_2$, which is the criterion selected as the most suitable in chapter §4 for PR

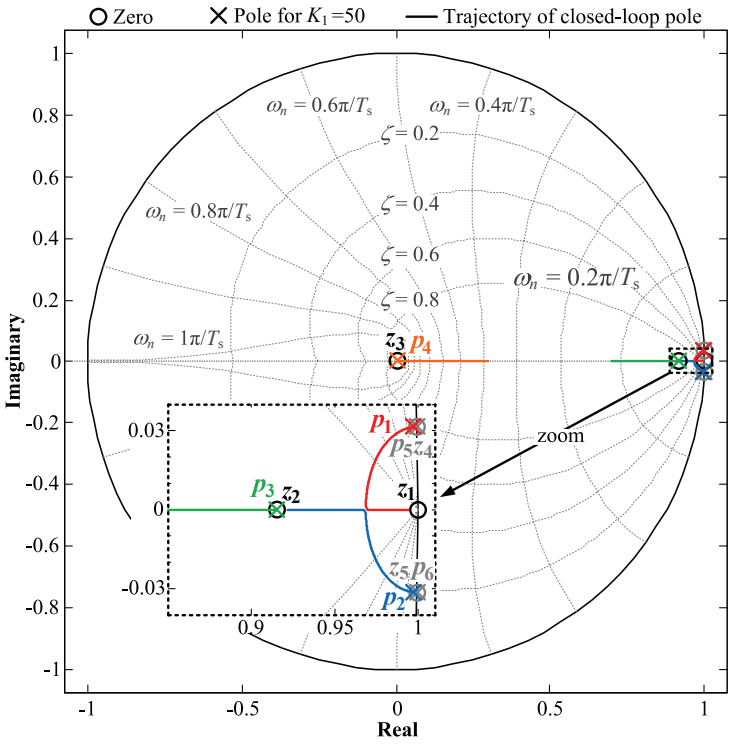

(a) Test I. Roots of $E_{\Delta i^*}(z)$.

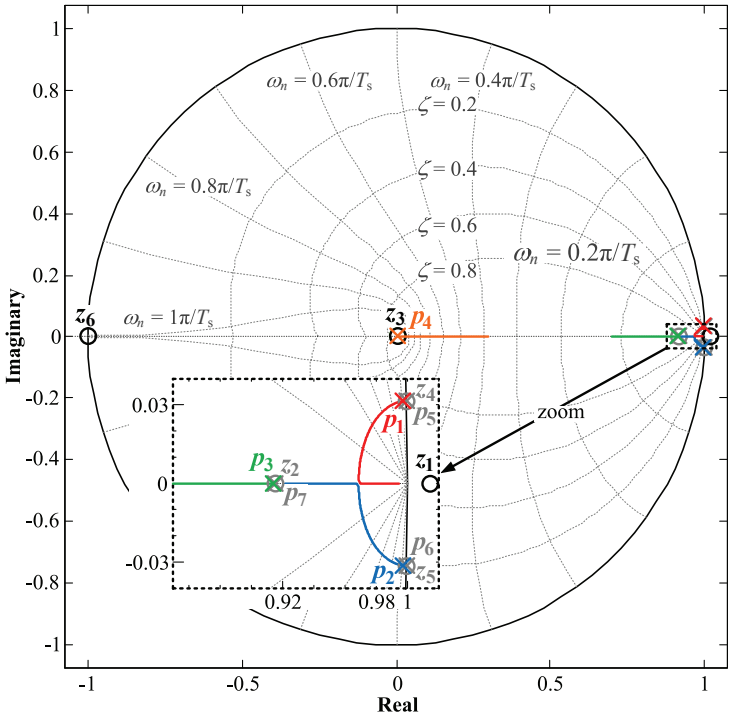

(b) Test II. Roots of $E_{\Delta v_{\mathrm{PCC}}}(z)$.

Figure 5.1: Root-locus diagrams of the error signal during transients when using a single VPI controller at $h = 1$ and $f_s = 10\,\mathrm{kHz}$. K_1 is increased from 50 to 2000. The poles and zeros that are canceled with each other are shown in gray.

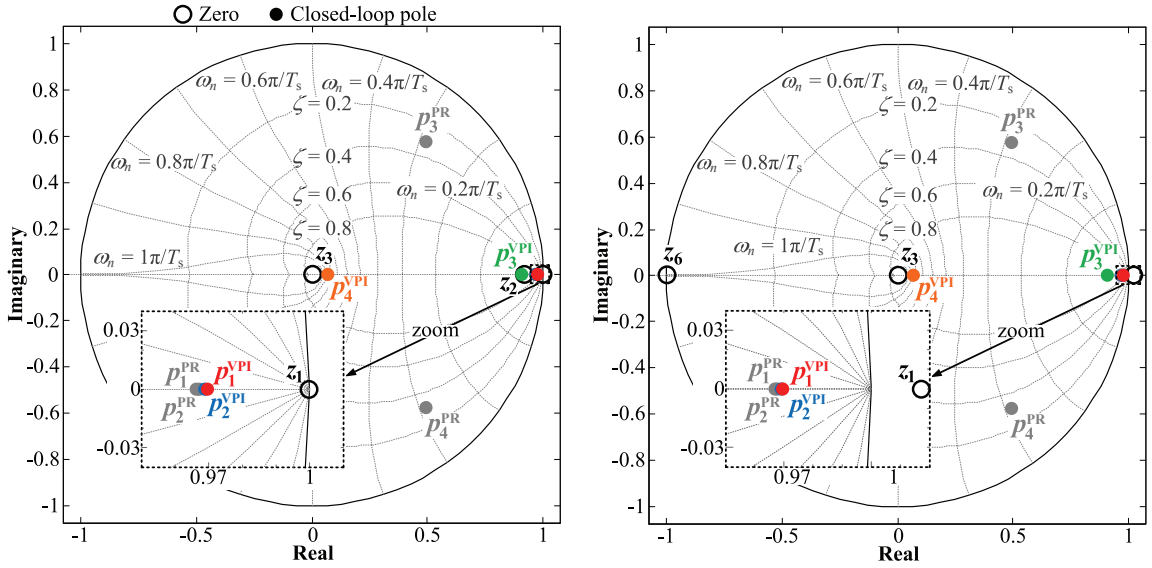

(a) Test I. Roots of $E_{\Delta i^*}(z)$.

(b) Test II. Roots of $E_{\Delta v_{\mathrm{PCC}}}(z)$.

Figure 5.2: Root-locus diagrams of the error signal during transients for gain values such that $p_1 = p_2$ when using a VPI and a PR controller. Resonant filters at $h = 1$ and $f_s = 10\,\mathrm{kHz}$.

controllers, is also the optimum for VPI ones, in terms of settling time $t_{2\%}$ (a tolerance band of 2% is defined for this chapter, as well). The corresponding root loci, at a high f_s (10 kHz) are shown in Figs. 5.2a and b for transients in the current reference and in the disturbance, respectively. It should be noticed that the canceled roots ($p_5 - z_4$, $p_6 - z_5$ and $p_7 - z_2$) are no longer illustrated. In order to facilitate the comparison, poles that correspond to the PR controller are also included (p^{PR} in gray), apart from those of the VPI controller (p^{VPI} in different colors). The roots in common have no superscript and are depicted in black.

A gain $K_1 = 629.5$ is used for the VPI controller to place the dominant poles at the same location in the real axis, i.e., $p_1 = p_2$, while for the PR controller, $K_{\mathrm{P}_1} = 25$ and $K_{\mathrm{I}_1} = 17740$ are employed to achieve the same condition. This tuning criterion assures a fair comparison between both controllers since the decay rate (distance to the boundary circle) of their respective dominant poles is maximized. Comparing the positions of the VPI controller dominant poles to the corresponding ones of the PR controller, it may be observed that they are slightly closer to the boundary circle with the former, which makes them slower. This fact happens because by varying the quotient $K_{\mathrm{P}_1}/K_{\mathrm{I}_1}$, the real-axis point at which $p_1 = p_2$ is modified. For the VPI controller, $K_{\mathrm{P}_1}/K_{\mathrm{I}_1} = L/R$ has been chosen [see (5.6)], but for the PR one, K_{P_1} and K_{I_1} have no direct relation with the plant parameters; they have been tuned separately to achieve a faster transient response while guaranteeing a certain bandwidth (see chapter §4). The other poles p_3 and p_4 are faster than p_1 and p_2 for both PR and VPI controllers. However, in the case of the PR controller, they are oscillating, with p_3 being faster and p_4 slower than in the case of the VPI controller.

Regarding the residues, i.e., the proximity between poles and zeros, in case of reference changes (cf. Fig. 5.2a), the zero z_2 is closer to p_3 than to p_1 and p_2, which are the dominant poles, with the VPI controller. On the contrary, the opposite happens with the roots of the PR regulator, i.e., z_2 is closer to p_1 and p_2 than to p_3. This fact makes p_1 and p_2 have more effect

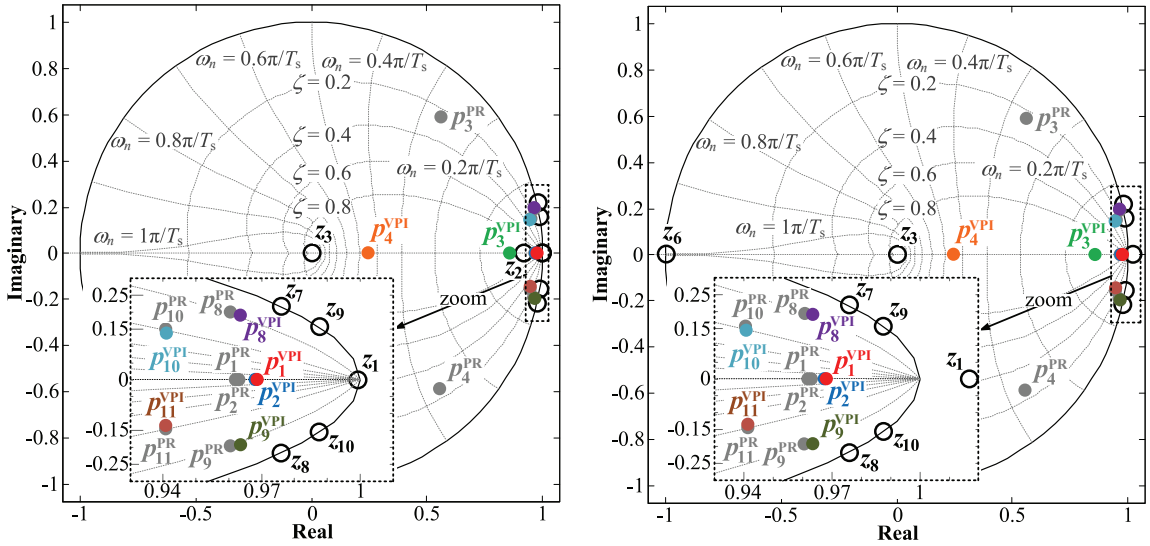

(a) Test I. Roots of $E_{\Delta i^*}(z)$. .

(b) Test II. Roots of $E_{\Delta v_{\mathrm{PCC}}}(z)$.

Figure 5.3: Root-locus diagrams of the error signal during transients for gain values such that $p_1 = p_2$ when using a VPI and a PR controller. Resonant filters at $h = 1, 5, 7$ and $f_s = 10\,\mathrm{kHz}$.

on the VPI controller transient response than on the PR one; whereas p_3 and p_4 present a bigger influence on the PR controller transient response than on the VPI one, leading to initial high-frequency oscillations in the former. A similar situation to the one of the reference change with the VPI regulator (cf. Fig. 5.2a) happens with the PR one in case of disturbance changes (cf. Fig. 5.2b): the poles p_1 and p_2 are more dominant in the transient response because there is no z_2. On the other hand, from Fig. 5.2b, the position of p_3 is especially relevant for disturbance changes with the VPI controller since there is no z_2 to minimize its impact, so the transient response will present even greater overshoot than in the previous two cases.

In summary, from the root loci, it may be concluded that a faster transient response will be achieved with the PR controller in both tests: reference and disturbance changes. In case of reference changes, initial high-frequency oscillations are expected with the PR controller, leading to a larger overshoot than with the VPI one. On the contrary, in case of disturbance changes, the response will be more damped with the PR regulator.

5.3.2 Resonant Controllers at Fundamental and Harmonic Frequencies

Current harmonic control, either for tracking [27, 81, 146, 220] or for rejection [27, 28, 34, 35, 111, 170], is usually needed in real applications. Regarding the latter case, undesired current harmonics may be caused by grid distortion or by nonlinear effects such as voltage source converter (VSC) dead times [193, 222, 223]. Consequently, additional resonant filters tuned to cancel the fifth and the seventh harmonics are included in both PR and VPI resonant controllers. Thus, VPI controllers like the one in (5.6) are implemented at $h = 5$ and $h = 7$, apart from the one at $h = 1$; the same is done with the PR controller in (5.5). Identical gain values for the fundamental and each harmonic controller, chosen to satisfy $p_1 = p_2$, are employed: $K_1 = K_5 = K_7 = 590$ for the VPI controller and $K_{\mathrm{P_T}} = \sum_{h=1,5,7} K_{\mathrm{P}_h} = 25$ and $K_{\mathrm{I}_1} = K_{\mathrm{I}_5} = K_{\mathrm{I}_7} = 16900$

for the PR one. The corresponding root loci at $f_s = 10\,\text{kHz}$ are depicted in Figs. 5.3a and b for $E_{\Delta i^*}(z)$ and $E_{\Delta v_{\text{PCC}}}(z)$, respectively.

By contrasting these results to those obtained with no harmonic control (section §5.3.1), it may be observed that smaller values for K_1 and K_{I_1} are needed here to achieve $p_1 = p_2$ with both PR and VPI controllers. From this fact, it can be concluded that adding more resonant filters with high gains affects the position of the dominant poles with both controllers [81]. From the comparison between Figs. 5.3a and b with Figs. 5.2a and b, the poles p_3 and p_4 are influenced as well; with the PR controller, they are slightly closer to the unit circle boundary when harmonic control is included, while with the VPI controller, p_3 and p_4 are moved slightly farther from the respective zeros. Both effects are equivalent to an increase in their respective gains, K_{I_1} and K_1 (see sections §4.4.1 and §5.3.1). As analogous consequences are noticed for the poles p_1, p_2, p_3 and p_4 of the VPI controller and the PR one, the observations of section §5.3.1 are repeated here: the dominant poles are slower with the VPI controller and they have more effect on the transient response, which will lead to a longer settling time and larger overshoot, respectively, than in the case of the PR controller (with the exception of the high-frequency oscillations in case of reference change, which increase the overshoot of the latter).

Additionally, two new pairs of poles and two new pairs of zeros appear in the root-locus diagrams of Figs. 5.3a and b. They are related to the additional resonant controllers included to reject the fifth and the seventh harmonics ($p_{10} - p_{11}$ and $z_9 - z_{10}$ result from the resonant controller at $h = 5$, while $p_8 - p_9$ and $z_7 - z_8$ result from the resonant controller at $h = 7$, maintaining the same root numbering as in chapter §4). The zeros z_7, z_8, z_9 and z_{10} are placed at the unit circle boundary and their positions are identical with both PR and VPI controllers (as it happened with the other zeros). However, the positions of p_8, p_9, p_{10} and p_{11} are slightly different. On the one hand, the poles which correspond to the VPI controller are a bit closer to the unit circle boundary, so harmonic attenuation will be marginally slower with this controller than with the PR one. On the other hand, p_8, p_9, p_{10} and p_{11} are placed a little closer to their corresponding zeros with the VPI controller than with the PR one. This fact will result in marginally smaller overshoot in the harmonic oscillations during transients with the VPI controller. Nevertheless, since these differences are quite small and these additional poles are not the dominant ones, they will not lead to significant differences in the transient responses, which will be practically the same as those in section §5.3.1.

5.3.3 Effect of Sampling Frequency

As f_s decreases, the delay effects caused by the discrete-time implementation become more noticeable. Moreover, the discretization method applied to the resonant controllers affects the system dynamics [79]. As an example, different discretization methods have been applied to the VPI controller at $f_s = 2.5\,\text{kHz}$. Figs. 5.4a and b show the root-locus diagrams of $E_{\Delta i^*}(z)$ with an increasing K_1 (from 50 to 800) when the cosine term of the VPI controller [see (5.6)] is discretized with first-order hold or Tustin with prewarping methods (labeled as D1 methods) and with the impulse invariant method (labeled as D2 methods), respectively. The poles obtained with a gain K_1 that satisfies $p_1 = p_2$ are marked with colored bullets. Besides, Fig. 5.4c presents the error transient response to a step in the current reference for the different discretization methods in such conditions. From these graphics, D2 methods are selected for discretization of VPI controllers, since they lead to a smaller overshoot and similar $t_{2\%}$ (with respect to D1 methods).

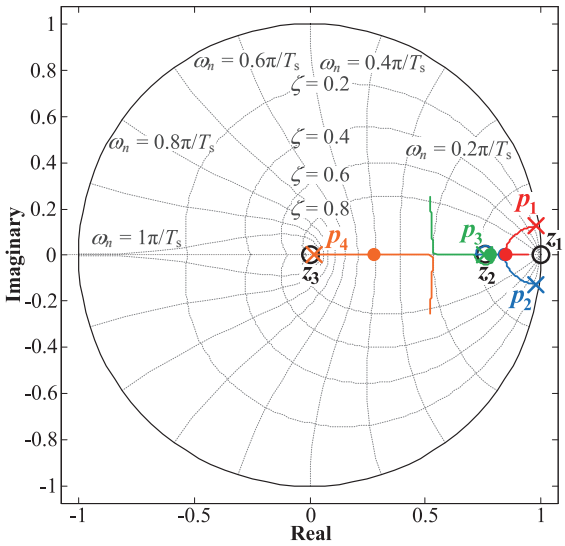

(a) Root-locus diagram of $E_{\Delta i^*}(z)$ with an increasing K_1. The VPI controller is discretized with an D1 method.

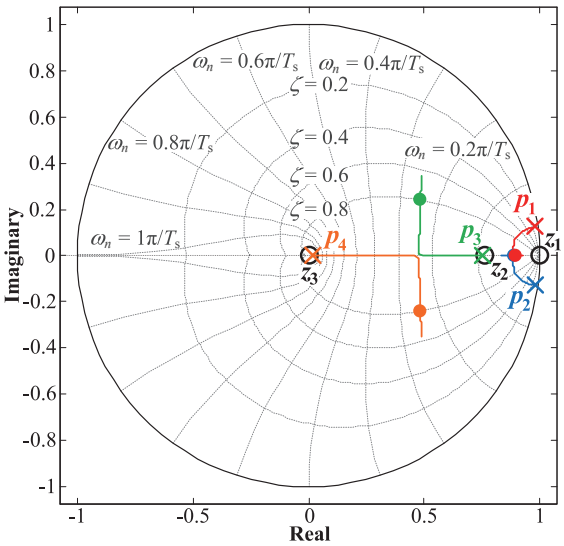

(b) Root-locus diagram of $E_{\Delta i^*}(z)$ with an increasing K_1. The VPI controller is discretized with a D2 method.

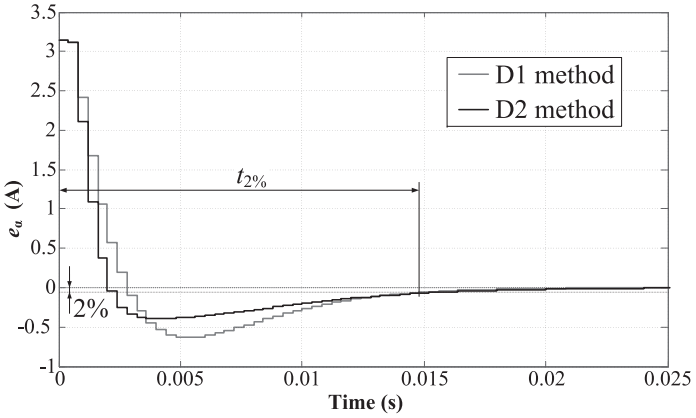

(c) Error transient response in case of reference change when VPI controllers are discretized with different methods (D1 or D2). K_1 has been tuned to satisfy $p_1 = p_2$.

Figure 5.4: Effect of the discretization method on the behavior of the VPI controller when K_1 is increased from 50 to 800 at $f_s = 2.5\,\text{kHz}$. In (a) and (b), the poles that correspond with a gain that satisfies $p_1 = p_2$ are indicated by colored bullets, while the poles at $K_1 = 50$ are marked with crosses.

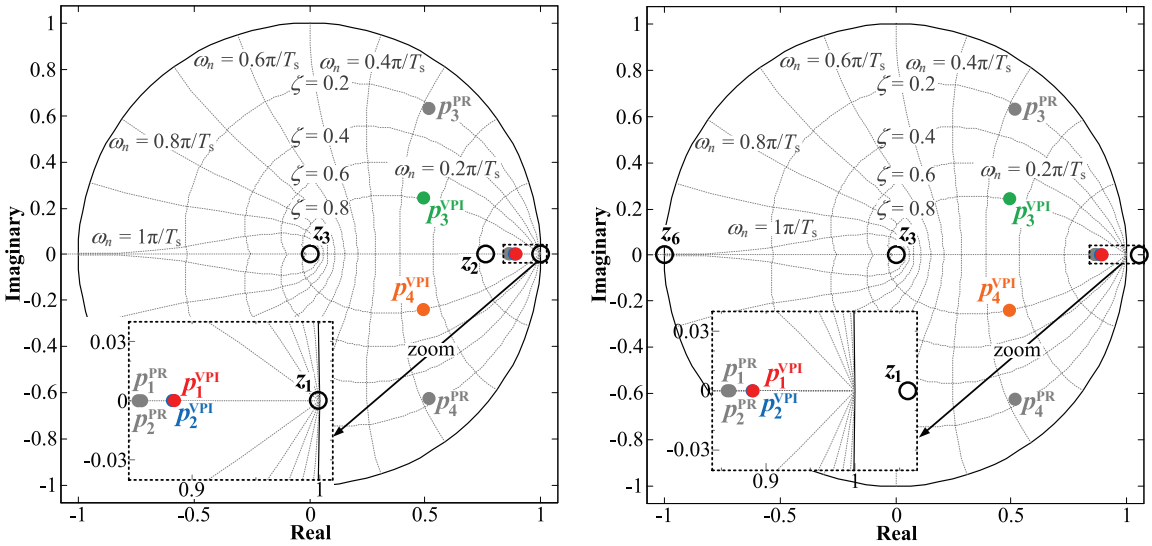

(a) Test I. Roots of $E_{\Delta i^*}(z)$.

(b) Test II. Roots of $E_{\Delta v_{\mathrm{PCC}}}(z)$.

Figure 5.5: Root-locus diagrams of the error signal during transients for gain values such that $p_1 = p_2$ when using a VPI and a PR controller. Resonant filters at $h = 1$ and $f_s = 2.5\,\mathrm{kHz}$.

Focusing on the comparison between PR and VPI controllers, resonant filters tuned to follow the fundamental frequency are employed at $f_s = 2.5\,\mathrm{kHz}$. Figs. 5.5a and b depict the root loci of $E_{\Delta i^*}(z)$ and $E_{\Delta v_{\mathrm{PCC}}}(z)$, respectively. A gain $K_1 = 690$ is selected for the VPI controller to achieve $p_1 = p_2$, while $K_{\mathrm{P}_1} = 6.25$ and $K_{\mathrm{I}_1} = 5372$ are chosen for the PR controller to satisfy the same condition. Comparing the positions of the dominant poles p_1 and p_2 to those in Figs. 5.2a and b, it may be observed that they are faster at a lower f_s, independently from the employed controller. However, like in the case of higher f_s, p_1 and p_2 are slightly slower with the VPI controller than with the PR one, which results in a slower transient response for both transient and disturbance changes. In addition, owing to the selected discretization method, at this f_s, the poles p_3 and p_4 are oscillating with the VPI controller too, although less than with the PR one, i.e., they are closer to the zeros that cancel their effect. The two previous facts make p_1 and p_2 have more effect on the VPI controller transient responses than on the PR ones. In the same way, the poles p_3 and p_4 will have bigger impact on the reference change response of the PR controller, leading to larger initial high-frequency oscillations. On the other hand, in case of disturbance changes (cf. Fig. 5.5b), the effect of p_1 and p_2 is just attenuated by z_1 (there is no z_2), so their position also results in greater overshoot (owing to larger residues) than in the case of reference changes for both PR and VPI controllers.

According to the previous analysis, it can be concluded that a faster transient response will be achieved by the PR controller, although as f_s decreases, the behavior of both controllers becomes more similar.

5.3.4 Effect of a Feed-Forward Path

In order to avoid steady-state error, there is no need of feedforward because $E_{\Delta i^*}$ and $E_{\Delta v_{\mathrm{PCC}}}$ decay to zero owing to the resonant controllers [145]. However, as commented in section §4.2, it

Table 5.1: THD, Overshoot and Settling Time of the Different Tests.

Controller	f_s	h	THD	Reference change		Disturbance change	
				Overshoot	Settling Time	Overshoot[1]	Settling Time[1]
VPI	10 kHz	1	8.29%	14%	17 ms	8.6 A	27 ms
PR	10 kHz	1	2.65%	28%	9 ms	4.4 A	20 ms
VPI	10 kHz	1,5,7	1.10%	49%	16 ms	8.8 A	26 ms
PR	10 kHz	1,5,7	0.92%	57%	12 ms	4.4 A	19 ms
VPI	2.5 kHz	1	4.75%	13%	16 ms	12.1 A	28 ms
PR	2.5 kHz	1	4.63%	40%	10 ms	10.9 A	22 ms

may be included to improve the transient response in the presence of grid faults [34, 65, 69, 113].

Fig. 4.1 considers the possibility of adding a feed-forward path $\widehat{v}_{\mathrm{PCC}}$. $E_{\Delta\widehat{v}_{\mathrm{PCC}}}(z)$ is the error due to changes in the feedforward $\Delta\widehat{v}_{\mathrm{PCC}}$ and is defined as:

$$E_{\Delta\widehat{v}_{\mathrm{PCC}}}(z) = \frac{z^{-1}G_{\mathrm{L}}^{\mathrm{ZOH}}(z)}{1+G_{\mathrm{PR}}(z)z^{-1}G_{\mathrm{L}}^{\mathrm{ZOH}}(z)}\Delta\widehat{v}_{\mathrm{PCC}}(z). \tag{5.7}$$

From (4.9) and (5.7), $E_{\Delta\widehat{v}_{\mathrm{PCC}}}(z)$ can be obtained as:

$$E_{\Delta\widehat{v}_{\mathrm{PCC}}}(z) = -z^{-1}\,\mathrm{PWM}\,E_{\Delta v_{\mathrm{PCC}}}(z) \tag{5.8}$$

which shows that the error caused by the feedforward counteracts the effect of $E_{\Delta v_{\mathrm{PCC}}}$ with a certain delay (equal to the computational and modulation ones). In this manner, it accelerates the error decay when transients are caused by disturbances in the grid. Nevertheless, it has to be taken into account that a direct feedforward is not always suitable. For example, considering very weak grids, v_{PCC} would be influenced by i so that the controller of Fig. 4.1 would have to be expanded with an external loop to regulate v_{PCC} [78, 224]. This scenario is out of the scope of this chapter.

5.4 Experimental Results

Fig. 5.6a shows a photograph of the real implementation described in Fig. 5.6b. A three-phase VSC working as a rectifier has been built to test the VPI controller, and to compare it with the PR one. Real-time implementation is achieved through the prototyping platform dSpace DS1104. A Pacific 360-AMX three-phase linear power source is used to supply the ac voltages and to program the voltage sags (test II). The rectifier digital controller from Fig. 5.6b uses a proportional-integral (PI) controller to keep constant the dc-link voltage v_{dc}. Its output is the current reference in the d axis of a synchronous reference frame (SRF) i_{d}^{*}. The current reference in the q axis of the SRF i_{q}^{*} is set manually, which permits to perform transients in

[1] In the case of a disturbance change, the steady-state current value is zero, so the overshoot is not expressed as a percentage of its final value, but as the maximum absolute peak of the error signal. In this manner, its unit is A. Similarly, the width of the tolerance band that is employed to calculate the settling time is here also defined in absolute terms (0.05 A) rather than as a percentage.

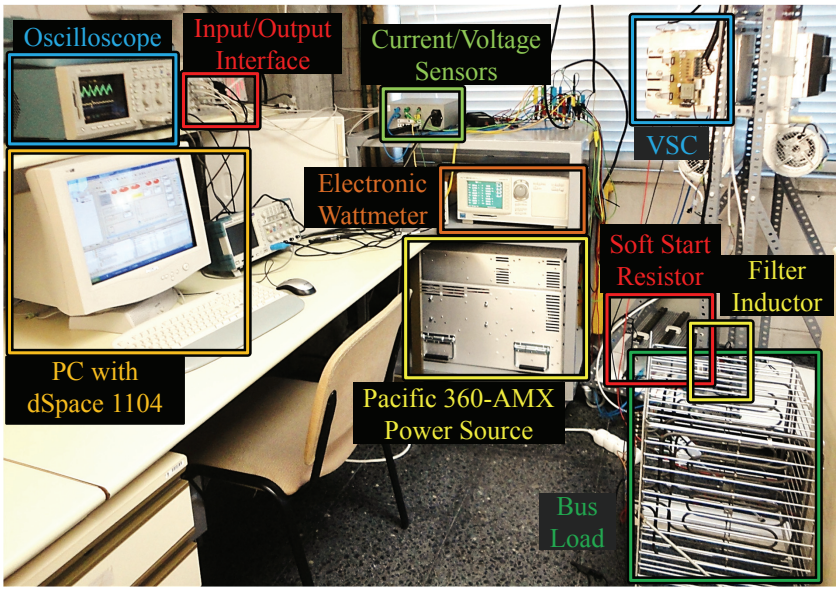

(a) Photograph.

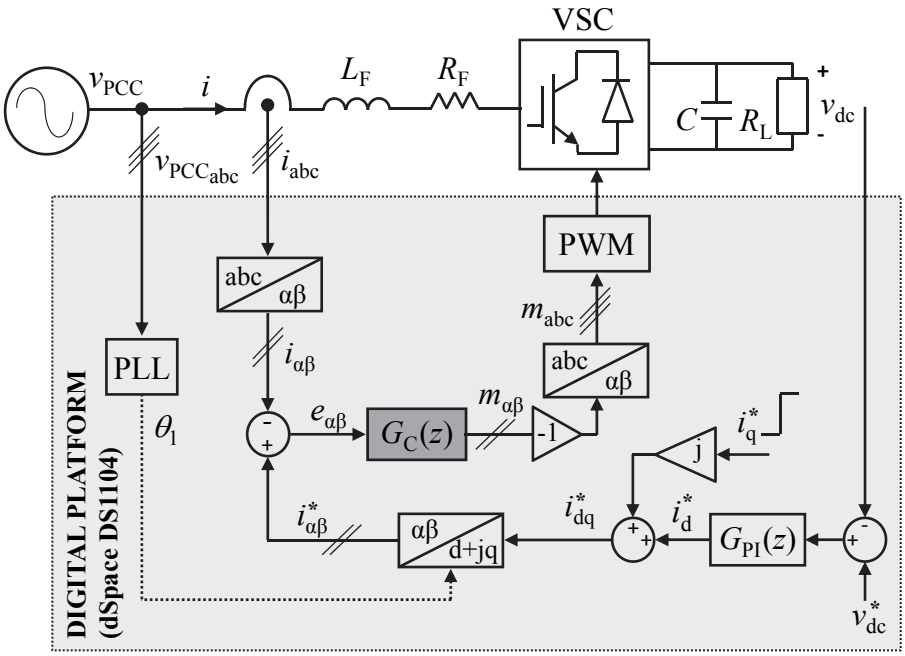

(b) Scheme.

Figure 5.6: Experimental setup.

the current reference (test I). A typical phase-locked loop (PLL) able to reject the influence of the negative sequence is used to track the phase angle of the power source θ_1 [216]. A pair of resonant controllers regulate the current in stationary frame (one in each of the axes). Their output m is driven to the PWM unit of the dSpace DS1104.

The experimental evaluation of the PR and VPI controllers is made following the same structure as in section §5.3. Additionally, an analysis of the total harmonic distortion (THD) in each of those cases is also provided (cf. section §5.4.4). Section §5.4.6 includes a discussion of the effect of the PLL on the disturbance rejection response. Apart from the experimental figures, Table 5.1 summarizes the obtained results, facilitating the comparison between PR and VPI controllers in terms of transient response (overshoot and settling time) and THD.

5.4.1 Resonant Controllers only at Fundamental Frequency

The same values as in section §5.3.1 are used in these experimental tests ($K_1 = 629.5$, $K_{P_1} = 25$, $K_{I_1} = 17740$ and $f_s = 10\,\text{kHz}$). Figs. 5.7a and b present the corresponding transient responses with the VPI controller, caused by a reference change and by a disturbance change, respectively. These oscilloscope captures show the a-phase PCC voltage v_{PCC_a}, the a-phase current i_a, the actual error in the α axis e_α and the estimated error $\hat{e}_\alpha$. This error estimation has been obtained from the respective root loci (Fig. 5.2) by the the residues calculation method (see Appendix §B). Note that e_α and $\hat{e}_\alpha$ are internal signals of the control that have been read through digital-to-analog converters (DACs) with a range of $\pm 10\,\text{V}$. On the other hand, it should be noticed that the negative-sequence current component is reflected on both e_α and the actual error in the β axis e_β. Hence, when either e_α or e_β become zero, it implies that the current imbalance has been compensated. To further demonstrate this fact, more oscilloscope captures of the disturbance rejection response are included in Figs. 5.9a and b, which display i_a, i_b, i_c and e_α with the VPI and with the PR controller, respectively. In all these tests, the α-axis signals are shown rather than the β-axis ones because the programmed sag (a "type C" sag that affects a- and b-phases) has a much bigger impact on the α-axis component of v_{PCC} than on the β one.

Comparing Figs. 5.7a and b to the corresponding ones with the PR controller (Figs. 5.8a and b), it can be observed that the VPI one leads to longer settling times (cf. Table 5.1). Regarding the overshoot, it is larger with the PR controller in case of a reference change, due to the initial high-frequency oscillations (see section §4.5.1 for more details); on the contrary, in case of a disturbance change, the overshoot is smaller with the PR controller than with the VPI one. These aspects are consistent with two observations made in section §5.3.1: with the VPI controller, the poles $p_1 = p_2$ are slower and the residues of the main poles (p_1, p_2 and p_3) are bigger. In these conditions, the settling times provided by the VPI controller are approximately 17 ms in case of a reference change and 27 ms for the disturbance change, while with the PR controller are 9 ms and 20 ms, respectively. It should be noticed that the response to reference change of the VPI controller (cf. Fig. 5.7a) is quite similar to the response to disturbance change of the PR controller (cf. Fig. 5.8b), corroborating the observations in section §5.3.1.

5.4.2 Resonant Controllers at Fundamental and Harmonic Frequencies

In order to improve the distortion, more resonant filters in parallel tuned at the fifth and the seventh harmonics [i.e., $h = 5$ and $h = 7$ in (5.5) or in (5.6)] are included in the current control loop for both resonant controllers. The same values as in section §5.3.3 are employed in these

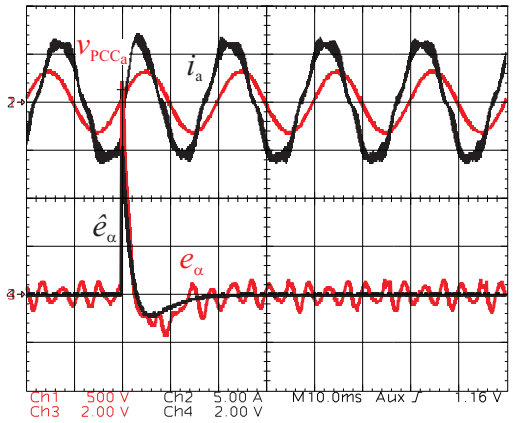

(a) Test I. Reference change. $f_s = 10\,\text{kHz}$ and $K_1 = 629.5$.

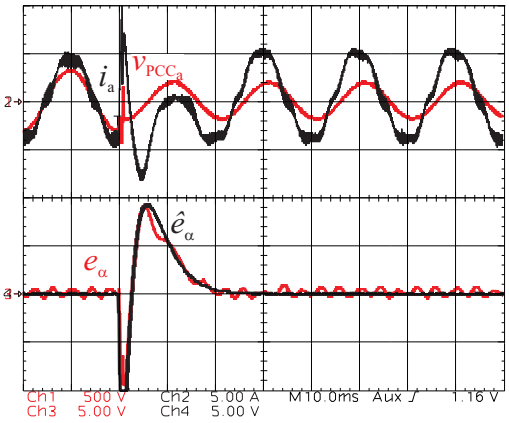

(b) Test II. Disturbance change. $f_s = 10\,\text{kHz}$ and $K_1 = 629.5$.

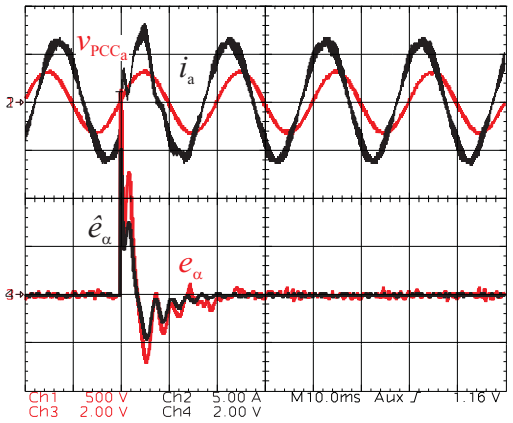

(c) Test I. Reference change. $f_s = 10\,\text{kHz}$ and $K_1 = K_5 = K_7 = 590$.

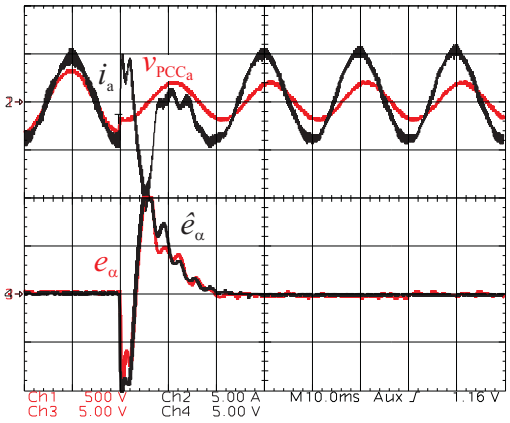

(d) Test II. Disturbance change. $f_s = 10\,\text{kHz}$ and $K_1 = K_5 = K_7 = 590$.

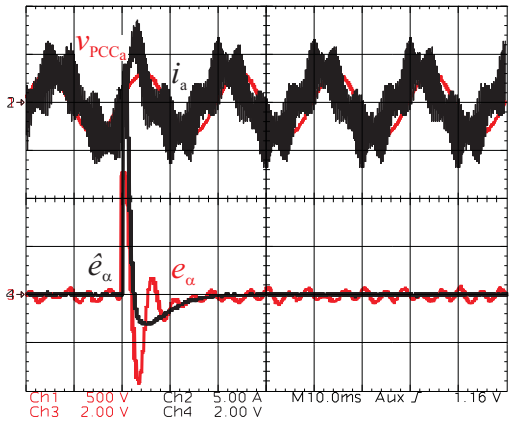

(e) Test I. Reference change. $f_s = 2.5\,\text{kHz}$ and $K_1 = 669$.

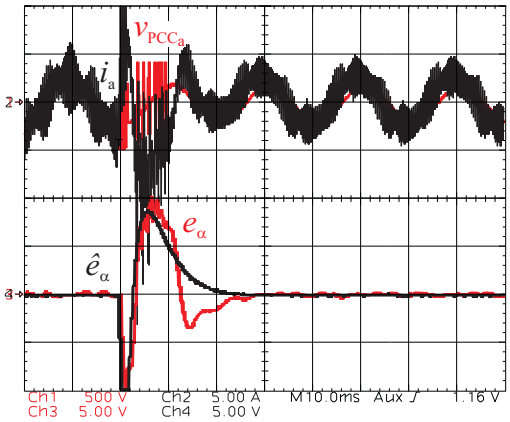

(f) Test II. Disturbance change. $f_s = 2.5\,\text{kHz}$ and $K_1 = 669$.

Figure 5.7: Transient response with VPI controllers: effects of f_s and of adding more resonant filters. Scales: v_{PCC_a} in $500\,\text{V/div}$, i_a in $5\,\text{A/div}$, $\hat{e}_\alpha$ and e_α in $2\,\text{A/div}$ for (a), (c), in $6\,\text{A/div}$ for (b), (d) and (f) and in $1\,\text{A/div}$ for (e), time in $10\,\text{ms/div}$.

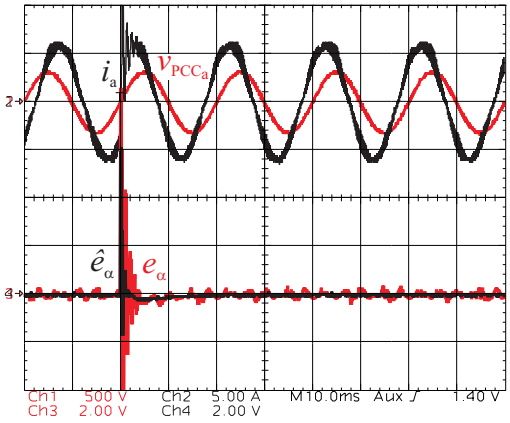

(a) Test I. Reference change. $f_s = 10\,\text{kHz}$, $K_{P_1} = 25$ and $K_{I_1} = 17740$.

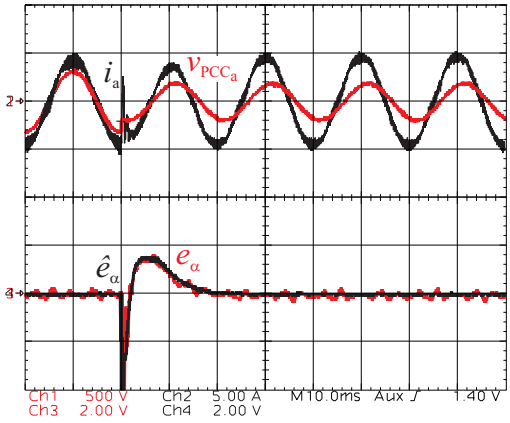

(b) Test II. Disturbance change. $f_s = 10\,\text{kHz}$, $K_{P_1} = 25$ and $K_{I_1} = 17740$.

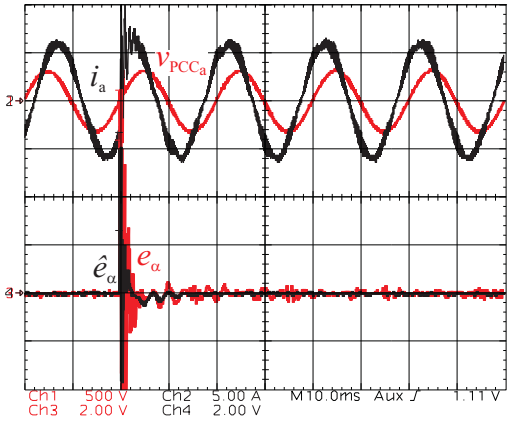

(c) Test I. Reference change. $f_s = 10\,\text{kHz}$, $K_{P_T} = \sum_{h=1,5,7} K_{P_h} = 25$ and $K_{I_1} = K_{I_5} = K_{I_7} = 16900$.

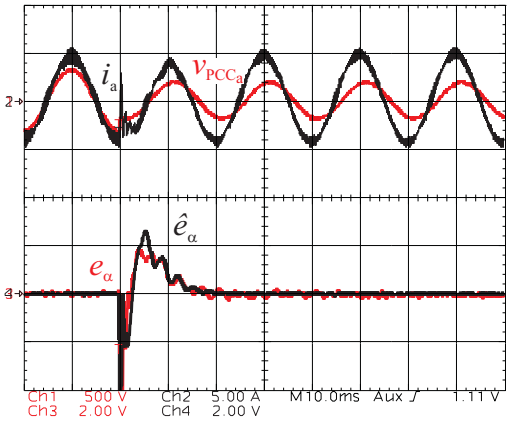

(d) Test II. Disturbance change. $f_s = 10\,\text{kHz}$, $K_{P_T} = \sum_{h=1,5,7} K_{P_h} = 25$ and $K_{I_1} = K_{I_5} = K_{I_7} = 16900$.

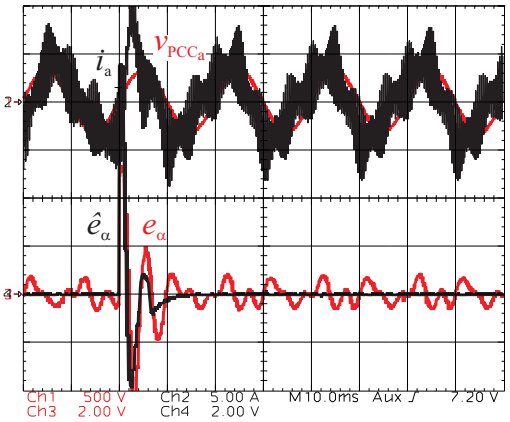

(e) Test I. Reference change. $f_s = 2.5\,\text{kHz}$, $K_{P_1} = 6.25$ and $K_{I_1} = 5372$.

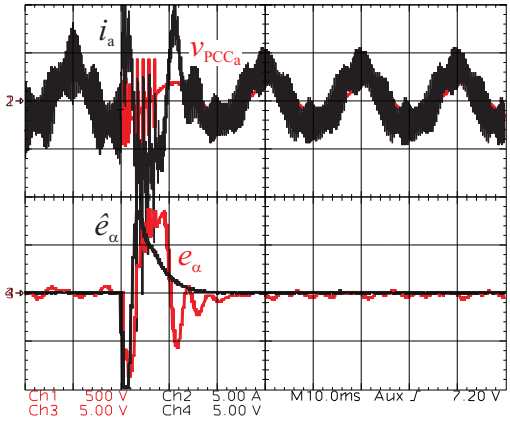

(f) Test II. Disturbance change. $f_s = 2.5\,\text{kHz}$, $K_{P_1} = 6.25$ and $K_{I_1} = 5372$.

Figure 5.8: Transient response with PR controllers: effects of f_s and of adding more resonant filters. Scales: v_{PCC_a} in $500\,\text{V/div}$, i_a in $5\,\text{A/div}$, $\hat{e}_\alpha$ and e_α in $2\,\text{A/div}$ for (a)-(d), in $1\,\text{A/div}$ for (e) and in $6\,\text{A/div}$ for (f), time in $10\,\text{ms/div}$.

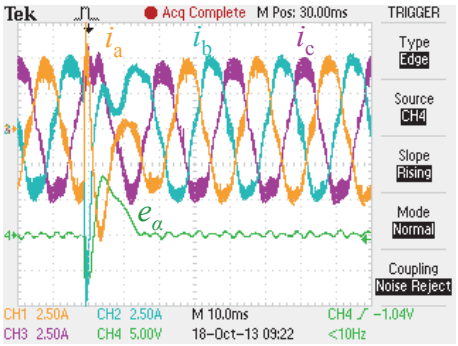

(a) VPI controllers with no harmonic compensation.

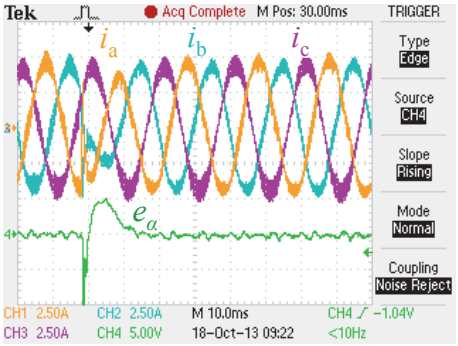

(b) PR controllers with no harmonic compensation.

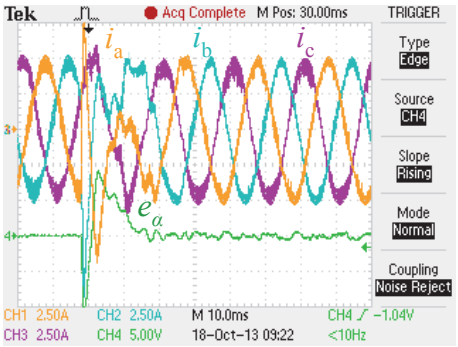

(c) VPI controllers with harmonic compensation of 5th and 7th harmonics.

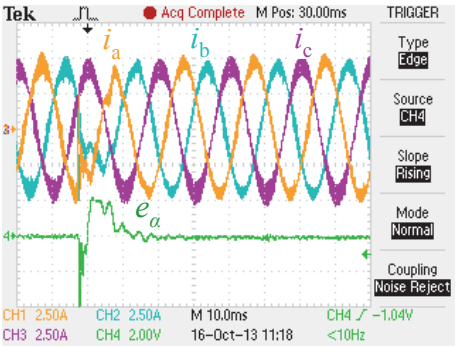

(d) PR controllers with harmonic compensation of 5th and 7th harmonics.

Figure 5.9: 3-phase currents and α-axis error in the disturbance rejection response at $f_s = 10\,\text{kHz}$. Scales: i_a, i_b, i_c in $2.5\,\text{A/div}$ and e_α in $5\,\text{A/div}$ in (a) and (c) and in $2\,\text{A/div}$ in (b) and (d), time in $10\,\text{ms/div}$.

experimental tests ($K_1 = K_5 = K_7 = 590$, $K_{P_T} = 25$, $K_{I_1} = K_{I_5} = K_{I_7} = 16900$ and $f_s = 10\,\text{kHz}$). Figs. 5.7c and d show the corresponding results with the VPI controller for transients in the current reference and transients in the disturbance, respectively. It can be observed that steady-state ripple (first 20 ms) has been significantly improved with respect to that of Figs. 5.7a and b. Additionally, analogously to the previous subsection, Figs. 5.9c and d display i_a, i_b, i_c and e_α in case of a disturbance change with the VPI and with the PR controller, respectively.

Regarding the transient behavior of the VPI controller, it may also be noticed in Figs. 5.7c and d that more oscillations appear as a consequence of the additional poles p_8, p_9, p_{10} and p_{11}. Comparing these two figures with the respective ones of the PR controller (cf. Figs. 5.8c and d), the observations included in section §5.4.1 are also verified when additional controllers are implemented in parallel: the VPI controller leads to slower error decay and larger overshoot (except for the high-frequency oscillations in case of reference change), which makes the PR controller a more suitable option (cf. Table 5.1). In relation to the transient harmonic fluctuations in the error signal, no big differences are observed between both controllers.

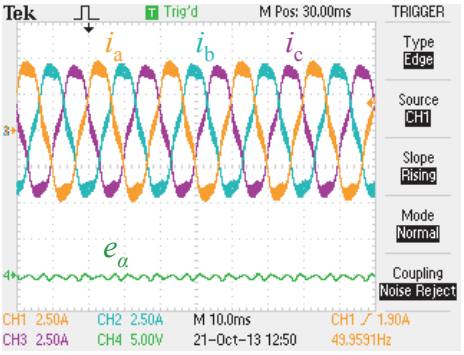

(a) Steady-state captures of i_a, i_b, i_c and e_α without harmonic compensation.

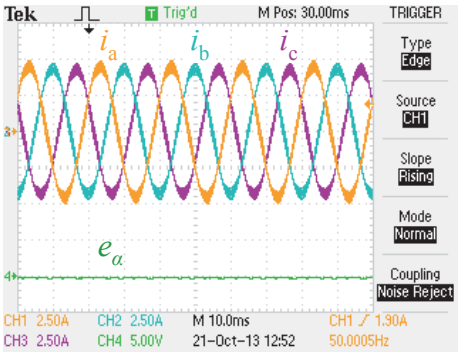

(b) Steady-state captures of i_a, i_b, i_c and e_α with harmonic compensation.

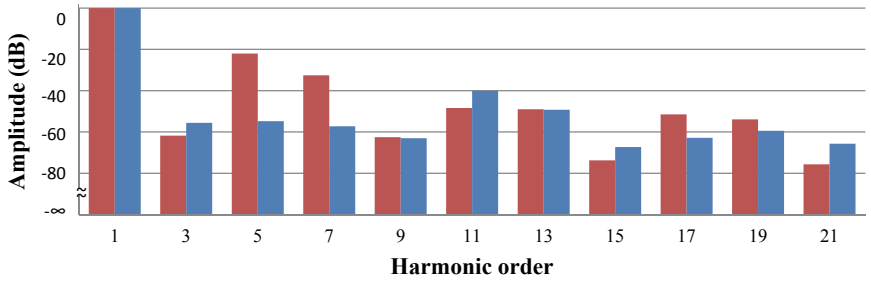

(c) Harmonic spectrum of the current in Figs. 5.10a and 5.10b.

Figure 5.10: THD analysis of VPI controllers at $f_s = 10\,\text{kHz}$. Scales for (a) and (b): i_a, i_b and i_c in $2.5\,\text{A/div}$ and e_α in $5\,\text{A/div}$.

5.4.3 Effect of Sampling Frequency

The same value $K_1 = 669$ as in section §5.3.3 is used in these experimental tests at $f_s = 2.5\,\text{kHz}$. Figs. 5.7e and f show the transient response with the VPI controller caused by a current reference change and the one caused by a disturbance change, respectively. Similar settling times to those with $f_s = 10\,\text{kHz}$ (Figs. 5.7a and b) are achieved in both tests (cf. Table 5.1). It should be noticed that in Figs. 5.7f and 5.8f, the differences between e_α and $\hat{e}_\alpha$ are caused by the current limitation of the Pacific power source during transients, since high current peaks are demanded. Comparing Figs. 5.7e and f to the corresponding ones with the PR controller (Figs. 5.8e and f, with $K_{P_1} = 6.25$ and $K_{I_1} = 5372$), it may be noticed that the PR regulator is still the fastest one at $f_s = 2.5\,\text{kHz}$. Regarding the overshoot, in case of reference change, the VPI controller shows a more damped response, while the contrary happens in case of disturbance change. In any case, the behavior of both controllers (either during transients or in steady state) becomes more similar as f_s decreases (cf. Table 5.1).

5.4.4 THD Analysis

A THD analysis of the current has been carried out for all the different cases considered in sections §5.4.1, §5.4.2 and §5.4.3. Figs. 5.10a-b, 5.11a-b, 5.12a and 5.13a show the grid

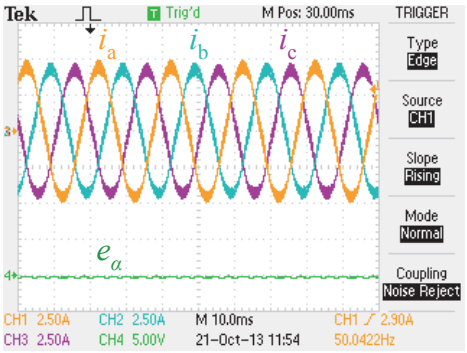

(a) Steady-state captures of i_a, i_b, i_c and e_α without harmonic compensation.

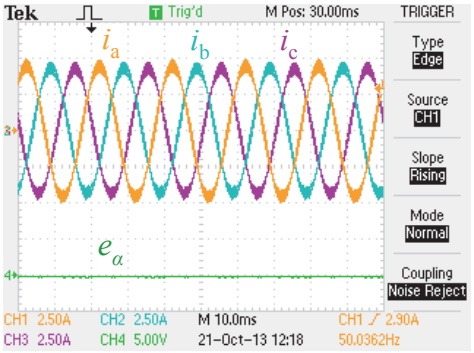

(b) Steady-state captures of i_a, i_b, i_c and e_α with harmonic compensation.

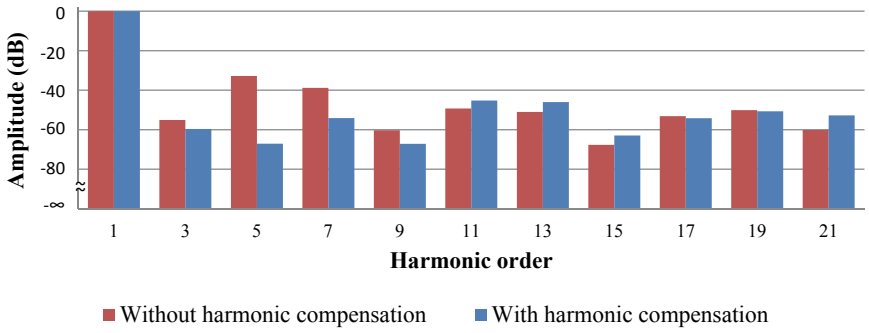

(c) Harmonic spectrum of the current in Figs. 5.11a and 5.11b.

Figure 5.11: THD analysis of PR controllers at $f_s = 10\,\text{kHz}$. Scales for (a) and (b): i_a, i_b and i_c in $2.5\,\text{A/div}$ and e_α in $5\,\text{A/div}$.

currents in the three phases i_a, i_b, i_c and the error signal in the α-axis e_α in steady state. The respective harmonic spectra are displayed in Figs. 5.10c, 5.11c, 5.12b and 5.13b. The corresponding THD values are included in Table 5.1. Even though just the odd harmonics up to the 21st order are displayed in the harmonic spectra, data up to the 39th harmonic has been employed in the THD calculations.

At $f_s = 10\,\text{kHz}$ (note that $f_s = f_{sw}$), when only a resonant controller at the fundamental component is included, a worse harmonic rejection is achieved with the VPI controller: THD $= 8.29\%$ has been obtained, much higher than the 2.65% of the PR controller, as it can be noticed from the red bars in Figs. 5.10c and 5.11c. This fact may also be checked by comparing Figs. 5.7a and b with respectively Figs. 5.8a and b during the first 20 ms (before the corresponding transients): e_α and i_a present larger ripple with the VPI controller than with the PR one. Such difference is caused by the proportional gain of the PR controller, which performs certain compensation at all the frequencies. On the contrary, the VPI controller is more selective, being able to compensate only around its resonant frequency.

When VPI resonant filters tuned at the fifth and seventh harmonics are added to the fundamental one, the THD of the current decreases significantly (from 8.29% to 1.10%, according to Table 5.1). This fact can also be checked from the comparison between the red and the blue bars in Fig. 5.10c.

In a similar way, the spectrum of the current is improved with the PR controller when in-

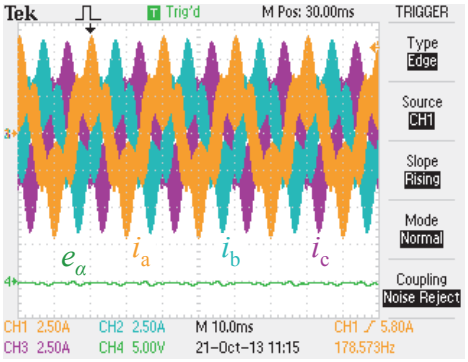

(a) Steady-state captures of i_a, i_b, i_c and e_α without harmonic compensation.

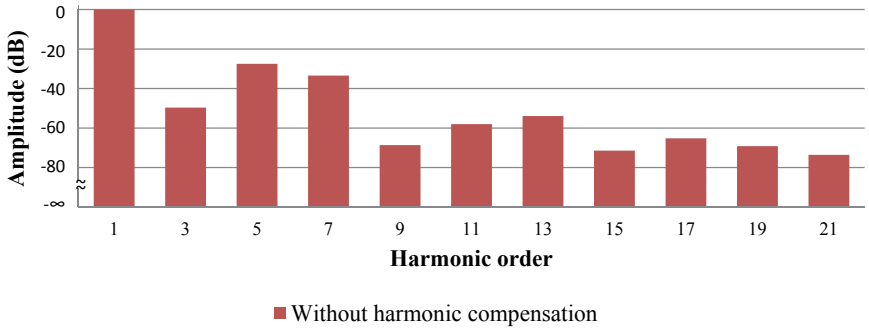

(b) Harmonic spectrum of the current in Fig. 5.12a.

Figure 5.12: THD analysis of VPI controllers at $f_s = 2.5\,\text{kHz}$. Scales for (a): i_a, i_b and i_c in $2.5\,\text{A/div}$ and e_α in $5\,\text{A/div}$.

cluding resonant filters to compensate these harmonics (compare the red and the blue bars in Fig. 5.11c), and hence, the THD is lowered (from 2.65% to 0.92%). However, the improvement is not as important as with the VPI one, since in this case the proportional gain of the PR controller was already offering certain compensation before adding the resonant filters at the harmonic components.

The current harmonic spectrum at $f_s = 2.5\,\text{kHz}$ when a VPI controller tuned to follow the fundamental component is employed is displayed in Fig. 5.12b. The corresponding THD is 4.75%. By comparing these results with those at $f_s = 10\,\text{kHz}$ (see the red bars in Fig. 5.10c), it can be noticed that the distortion has improved at $f_s = 2.5\,\text{kHz}$. The reason is that the amplitude of the voltage harmonics caused by dead times is proportional to the switching frequency [223] (provided that the dead times are maintained for the different f_{sw}).

Finally, Fig. 5.12b illustrates the harmonic spectrum of the current when a PR controller tuned at the fundamental component is implemented at $f_s = 2.5\,\text{kHz}$. The corresponding THD is 4.63%. Comparison of these results with those at $f_s = 10\,\text{kHz}$ (see the red bars in Fig. 5.10c) shows that the harmonic content has increased at this lower f_s. The explanation is that despite having a decrease in the amplitude of the voltage harmonics (caused by dead times), the bandwidth of the PR controller has been considerably reduced (from $K_{P_1} = 25$ at $f_s = 10\,\text{kHz}$ to $K_{P_1} = 6.25$ at $f_s = 2.5\,\text{kHz}$). Therefore, the compensation offered by the proportional gain at all the frequencies is much less significant than at $f_s = 10\,\text{kHz}$. Note that this is not the case of the VPI controller, because its gain K_1 remains practically unchanged. This reasoning also

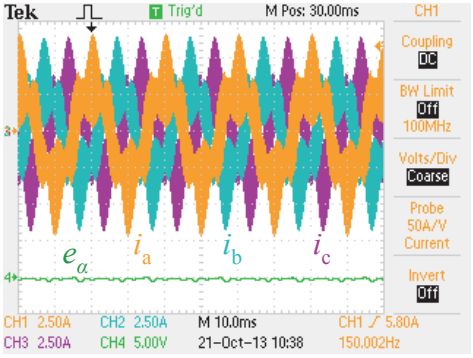

(a) Steady-state captures of i_a, i_b, i_c and e_α without harmonic compensation.

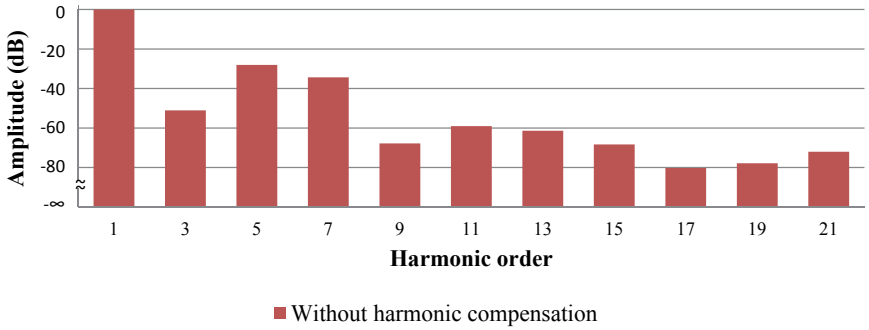

(b) Harmonic spectrum of the current in Fig. 5.13a.

Figure 5.13: THD analysis of PR controllers at $f_s = 2.5\,\text{kHz}$. Scales for (a): i_a, i_b and i_c in $2.5\,\text{A/div}$ and e_α in $5\,\text{A/div}$.

explains why the THD and harmonic spectra obtained at $f_s = 2.5\,\text{kHz}$ with VPI and with PR controllers are quite similar.

5.4.5 Effect of a Feed-Forward Path

This section experimentally evaluates the effect of adding a feedforward of v_{PCC} to the output of the resonant controllers (see the blocks with dashed lines in Fig. 4.1). Only graphics corresponding to test II are depicted since $\widehat{v}_{PCC}$ mainly improves the behavior during grid faults [34]. The error signal components in both α- and β-axes without and with feedforward of v_{PCC} are shown in Figs. 5.14a and b, respectively, at $f_s = 10\,\text{kHz}$, and in Figs. 5.14c and d at $f_s = 2.5\,\text{kHz}$. v_{PCC_a} and i_a waveforms are also displayed. Comparison between these figures permits to observe that the feed-forward path improves the transient response in terms of overshoot and settling time at $f_s = 10\,\text{kHz}$. Nevertheless, at $f_s = 2.5\,\text{kHz}$, it is noticed that, although the amplitude of the oscillations in the error signals is reduced with the feedforward, there is no significant improvement in the settling time. The explanation is that feedforward counteracts the effect of $E_{\Delta v_{PCC}}$ with a delay that depends on f_s [cf. (5.8)]. The lower the f_s, the larger the delay in (5.8), so the feed-forward action $E_{\Delta \widehat{v}_{PCC}}$ is not as fast as in case of higher sampling frequency. In this situation, accurately tuned current controllers are essential to minimize the settling time. Despite having only included results with the VPI controller, analogous graphics and conclusions have been obtained with the PR one.

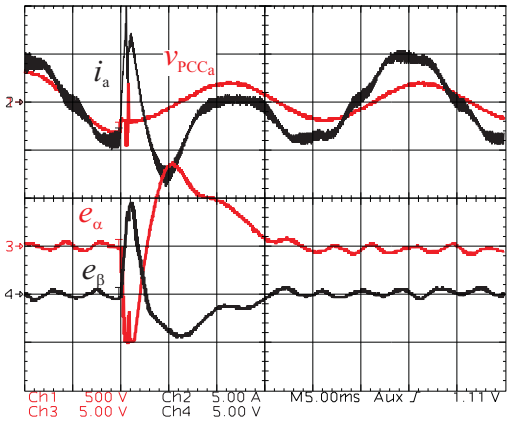

(a) Test II at $f_s = 10\,\text{kHz}$. $K_1 = 629.5$. Without feedforward of v_{PCC}.

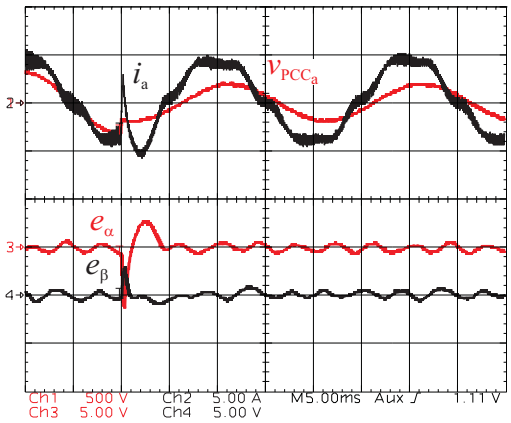

(b) Test II at $f_s = 10\,\text{kHz}$. $K_1 = 629.5$. With feedforward of v_{PCC}.

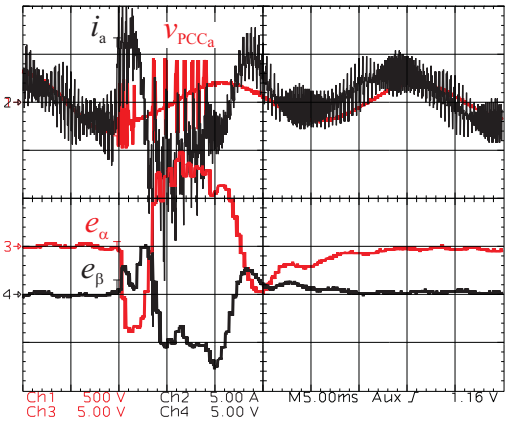

(c) Test II at $f_s = 2.5\,\text{kHz}$. $K_1 = 669$. Without feedforward of v_{PCC}.

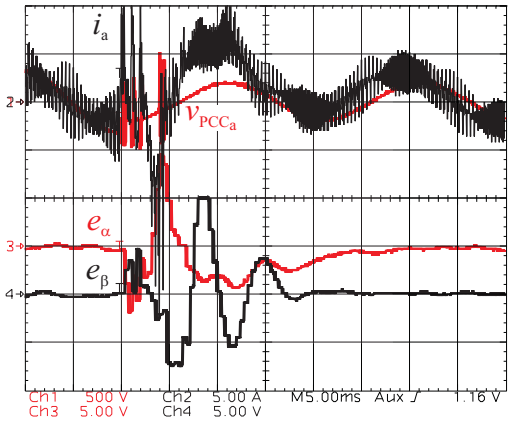

(d) Test II at $f_s = 2.5\,\text{kHz}$. $K_1 = 669$. With feedforward of v_{PCC}.

Figure 5.14: Effect of the feedforward $\widehat{v}_{PCC}$ on the disturbance rejection response with VPI controllers only at the fundamental frequency for different f_s. Scales: v_{PCC_a} in $500\,\text{V/div}$, i_a in $5\,\text{A/div}$, e_α and e_β in $5\,\text{A/div}$, time in $5\,\text{ms/div}$.

5.4.6 Effect of the PLL on the Disturbance Rejection Response

In case of grid faults (test II), the transient in the phase angle estimated by the PLL may have a certain influence on the current error signal. From Fig. 5.6b, θ_1 is only employed to generate (in the outer loop) the current reference $i^*_{\alpha\beta}$ that the current controller will track (in the inner loop). Therefore, the effect of a PLL transient error can be understood as a momentary alteration of the current reference $i^*_{\alpha\beta}$ (not to be mistaken with the case of test I, in which the user deliberately changes i^*_q). In case of being significant, such PLL transient would have two simultaneous consequences: a transitory increase in the current error $e_{\alpha\beta}$ [in addition to the current error directly caused by the grid disturbance in the inner loop, as described by (5.3)] and also a transient v_{dc} error in the outer loop. As the inner loop has much faster dynamics than the outer one, the effect of the outer loop $i^*_{\alpha\beta}$ transient error can be expected to have a reduced impact on the inner loop $e_{\alpha\beta}$.

In order to assess whether such effects are relevant in practice or not, test II experiments have been repeated, this time monitoring extra variables in the control algorithm (cf. Fig. 5.15): the phase error of the PLL e_{PLL} and i^*_d, apart from a-phase v_{PCC} and e_α, which are already present in Figs. 5.7 and 5.8. Results at $f_s = 10\,\text{kHz}$ are shown in Fig. 5.15a and b for the VPI and PR controllers, respectively. Firstly, it can be seen that in both cases e_{PLL} has a maximum of approximately 15° when the sag happens, which is reduced down to 6° in just 5 ms. It may also be observed that when i^*_d starts to change (see the red vertical dashed line), e_{PLL} has already become negligible and e_α has been practically compensated. While the former proves that the effect of the PLL transient on the outer loop behavior is not relevant (the slow increase in i^*_d is caused by a reduction in v_{dc} due to the grid fault), the latter confirms that it is not significant for the inner loop either. For all these reasons, it can be concluded that the influence of the PLL on the disturbance rejection current error is scarce. A similar behavior has been observed at $f_s = 2.5\,\text{kHz}$, either with the VPI controller (Fig. 5.15c) or with the PR one (Fig. 5.15d).

5.5 Conclusions

In this chapter, a study about the convenience of employing VPI controllers in renewable energy grid-connected applications is contributed. Their transient response is assessed by the analysis of the error signal roots. Gain selection is made by choosing the value that makes the dominant poles p_1 and p_2 equal. This criterion aims to minimize the postfault and new reference tracking settling times so that power electronics converters in renewable energy applications can fulfill the most demanding GC requirements (LVRT and grid support), as previously reported for the scheme with PR controllers in chapter §4. Different significant situations considering very demanding scenarios have been analyzed and tested for the VPI controller and compared with those obtained with the PR one. Besides, their ability to reject harmonic distortion is also judged.

At high sampling frequency, VPI controllers lead to transient responses with a longer settling time and a larger overshoot (except for the initial high-frequency oscillations in case of reference change) than PR ones, for both reference and disturbance changes. Moreover, in equivalent steady-state conditions, when VPI controllers are employed, the current waveform presents a higher THD than in the case of PR controllers, so more VPI filters at the observed harmonic frequencies are needed. At $f_s = 2.5\,\text{kHz}$, the behavior of some of the poles as K_1 increases depends on the discretization method applied to the continuous-domain transfer func-

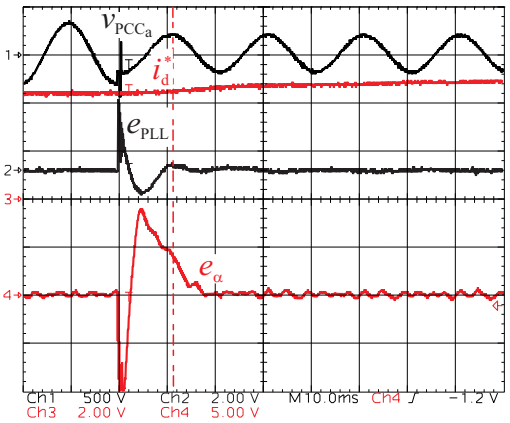

(a) Test II. VPI controller at $f_s = 10\,\text{kHz}$. $K_I = 629.5$

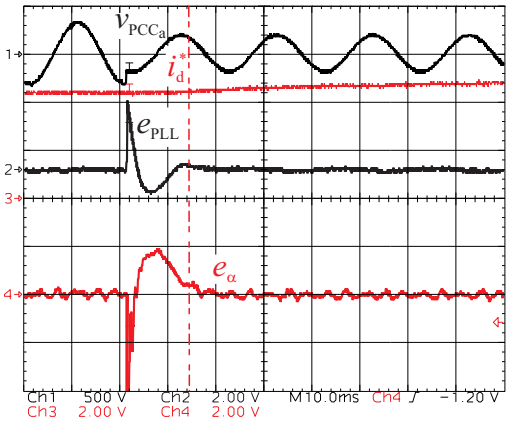

(b) Test II. PR controller at $f_s = 10\,\text{kHz}$. $K_{P_I} = 25$ and $K_{I_I} = 17740$.

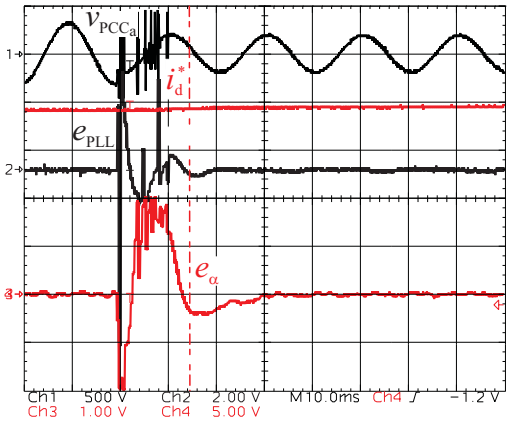

(c) Test II. VPI controller at $f_s = 2.5\,\text{kHz}$. $K_I = 669$.

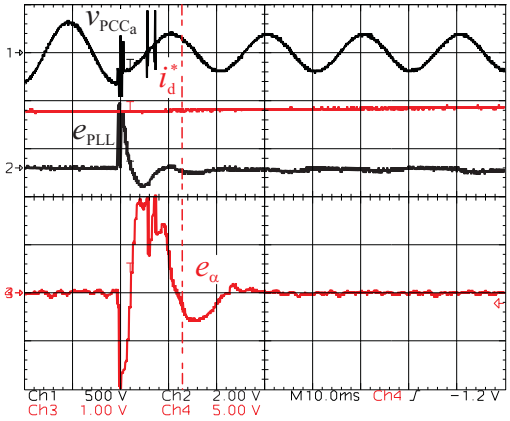

(d) Test II. PR controller at $f_s = 2.5\,\text{kHz}$. $K_{P_I} = 6.25$ and $K_{I_I} = 5372$.

Figure 5.15: Effect of the PLL on the disturbance rejection response when controlling the fundamental component of the current at different sampling frequencies. Scales: v_{PCC_a} in $500\,\text{V/div}$, e_{PLL} in 10°/div, i_d^* in $2\,\text{A/div}$ and e_α in $6\,\text{A/div}$ for (a), (c) and (d) and in $2\,\text{A/div}$ for (b), time in $10\,\text{ms/div}$.

tion of the controller. The best option for VPI controller discretization in terms of transient response has been assessed. At this sampling frequency, the root loci of PR and VPI controllers, and accordingly, their transient responses, present more similarities, although the PR controller is faster. Regarding the THD at $f_s = 2.5\,\text{kHz}$, similar values are obtained with both types of resonant controllers, since PR controllers are usually tuned so that the bandwidth is reduced with the sampling frequency. In addition, the benefits on the disturbance rejection response of adding a feedforward of the PCC-voltage at the two different sampling frequencies are shown. It is also concluded that the effect of the PLL on this kind of transients is scarce.

Contributions of this chapter have been published in the journal IET Power Electronics [8] and presented at an international conference [23].

Chapter 6

Conclusions and Future Research

6.1 Conclusions

This dissertation addresses the transient response analysis and design of current-controlled grid-tied converters. Its main contributions and conclusions are summarized below.

- A method to identify the voltage source converter (VSC) equivalent loss resistance in the plant model of the current loop at specific working conditions is presented, which is particularly oriented to the fulfillment of transient response constraints. The proposed estimation method works in closed loop, and may be implemented either offline, during a precommissioning stage, or online. Moreover, it can be run at any sampling frequency. On the other hand, it is demonstrated that an incorrect estimate of the VSC equivalent loss resistance results in a degraded behavior of the current control loop (e.g., in terms of settling time and overshoot), different from the theoretical one. It is also proved that, although adding a second degree of freedom to the current controller by means of the "active resistance" technique lowers to a certain point the sensitivity to resistance uncertainties, accurate knowledge of the actual resistance value permits to further enhance the transient response. In addition, it is also shown that despite the fact that the overall disturbance rejection improves for greater controller gain values, the ability to reject a particular harmonic does not. Each specific situation should be analyzed to draw conclusions.

- A method to estimate the plant time constant of the current loop in grid-tied VSCs is proposed. Such method permits to identify both the equivalent inductance and resistance in the corresponding plant model, which include the actual interface filter parameters, the effects associated to the converter losses and the impedance seen from the point of common coupling (PCC), all of them at certain working conditions. Furthermore, the method is also valid when LCL filters are employed. The developed algorithm is particularly designed to satisfy time-domain specifications. It works in closed loop, at the same sampling frequency as the rest of the control, and may be implemented either online or offline. The importance of having a precise estimate of the plant parameters to accurately analyze and tune the current loop is also demonstrated. In addition, the validity of modeling an LCL filter as an L one from the point of view of the current loop is analyzed in detail as a function of the controller gain value.

- A methodology to assess and optimize the transient response of proportional-resonant (PR) controllers is proposed, with the purpose of fulfilling the low-voltage ride-through (LVRT) and grid support grid code (GC) requirements. Thus, not only should controller tuning be targeted at minimizing the reference tracking settling time, but also the disturbance rejection one. It is proved that a tradeoff between both goals is needed and that the most critical type of transient, which is the one due to changes in the PCC, should be favored. A criterion for gain selection is developed accordingly. From the experimental results, it is shown that the theoretical expressions accurately estimate the real behavior of the current loop, validating the approach. In addition, it is demonstrated that precisely tuned PR controllers are a suitable option to comply the GC requirements in terms of transient response.

- A comparison between the transient response of the most popular resonant controllers, namely the PR and the vector proportional-integral (VPI) ones, is presented, oriented to evaluate the suitability of implementing the latter in grid-tied applications. Moreover, the ability of these regulators to reject harmonic distortion is also assessed. It is proved that at high sampling frequencies, PR controllers are a better option. VPI regulators lead to longer settling times and larger overshoot for both reference and disturbance changes, as well as to a greater total harmonic distortion (THD). However, as the sampling frequency decreases, the behavior of both controllers becomes more similar. Besides, the importance on the transient response of the discretization method applied to the VPI controller at low sampling frequencies is demonstrated, and the best option is determined. In addition, it is concluded that the effect of the phase-locked loop (PLL) on the disturbance rejection response is scarce and the benefits on it of adding a feedforward of the PCC-voltage at two different sampling frequencies are shown.

6.2 Publications

Research work included in the dissertation has been published in four JCR-indexed journal papers [1, 5, 8, 14] and three conference papers [13, 19, 23]. The contributions of each paper are summarized in the following.

- A method to identify the VSC equivalent loss resistance in grid-tied applications for current control design (chapter §2) has been published in the journal IEEE Transactions on Power Electronics [5]. A preliminary version of this proposal was presented at IEEE Energy Conversion Congress and Exposition (ECCE) 2013 [19].

- The proposal of a method for estimation of the equivalent inductance and resistance in the plant model of current-controlled grid-tied VSCs (chapter §3) has been published in the journal IEEE Transactions on Power Electronics [1]. A preliminary version of this proposal was presented at IEEE Energy Conversion Congress and Exposition (ECCE) 2014 [13].

- A methodology to assess and optimize the transient response of PR current controllers for distributed power generation systems (DPGSs) (chapter §4) has been published in the journal IEEE Transactions on Industrial Electronics [14].

- An evaluation of the transient response of two stationary frame resonant controllers (PR and VPI ones) for grid-connected applications (chapter §5) has been published in the journal IET Power Electronics [8]. A preliminary version of this proposal was presented at IEEE Industrial Electronics Conference (IECON) 2012 [23].

6.3 Future Research

There are several promising topics that may be suggested for further research in digital current control of VSCs for grid-tied applications. The most important ones are listed in the following.

- Study of the VSC equivalent loss resistance at different frequencies, from the control point of view.
- Analysis from the control viewpoint of the correlation between the VSC equivalent loss resistance and the voltage drops caused by dead times, the voltage drops in the transistors, etc.
- Improvement of the parameter estimation technique proposed in chapter §3 in order to also identify capacitive effects on the equivalent impedance of the plant model in current-controlled grid-tied VSCs.
- Obtainment of the overshoot versus settling time trajectories of the current loop step response when resonant regulators are implemented and use of them to define an analytical expression for gain tuning aimed at minimizing both.
- Development of a tuning method to optimize the transient response of the current loop at very low ratios between the sampling and fundamental frequencies.
- Completion of the previous topic with a precise tuning of a resonance damping technique when considering LCL filters.
- Analysis of the different effects (positive and negative) of adding an “active resistance” in order to improve the disturbance rejection capability.
- Study of the interactions between the outer control of the PCC voltage and the inner current one.

Bibliography

[1] A. Vidal, A. G. Yepes, F. D. Freijedo, O. Lopez, F. Malvar, J. Baneira, and J. Doval-Gandoy, "A method for identification of the equivalent inductance and resistance in the plant model of current-controlled grid-tied converters," *IEEE Transactions on Power Electronics*, to be published.

[2] F. D. Freijedo, A. Vidal, A. G. Yepes, J. M. Guerrero, O. Lopez, J. Malvar, and J. Doval-Gandoy, "Tuning of synchronous-frame PI current controllers in grid-connected converters operating at a low sampling rate by MIMO root locus," *IEEE Transactions on Industrial Electronics*, to be published.

[3] A. G. Yepes, J. Malvar, A. Vidal, O. Lopez, and J. Doval-Gandoy, "Current harmonics compensation based on multi-resonant control in synchronous frames for symmetrical n-phase machines," *IEEE Transactions on Industrial Electronics*, to be published.

[4] L. Harnefors, A. G. Yepes, A. Vidal, and J. Doval-Gandoy, "Passivity-based controller design of grid-connected VSCs for prevention of electrical resonance instability," *IEEE Transactions on Industrial Electronics*, vol. 62, no. 2, pp. 702–710, Feb. 2015.

[5] A. Vidal, A. G. Yepes, F. D. Freijedo, J. Malvar, O. Lopez, and J. Doval-Gandoy, "A technique to estimate the equivalent loss resistance of grid-tied converters for current control analysis and design," *IEEE Transactions on Power Electronics*, vol. 30, no. 3, pp. 1747–1761, Mar. 2015.

[6] S. Golestan, F. D. Freijedo, A. Vidal, J. M. Guerrero, and J. Doval-Gandoy, "A quasi-type-1 phase-locked loop structure," *IEEE Transactions on Power Electronics*, vol. 29, no. 12, pp. 6264–6270, Dec. 2014.

[7] L. Harnefors, A. G. Yepes, A. Vidal, and J. Doval-Gandoy, "Passivity-based stabilization of resonant current controllers with consideration of time delay," *IEEE Transactions on Power Electronics*, vol. 29, no. 12, pp. 6260–6263, Dec. 2014.

[8] A. Vidal, F. D. Freijedo, A. G. Yepes, J. Malvar, O. Lopez, and J. Doval-Gandoy, "Transient response evaluation of stationary-frame resonant current controllers for grid-connected applications," *IET Power Electronics*, vol. 7, no. 7, pp. 1714–1724, Jul. 2014.

[9] A. G. Yepes, A. Vidal, O. Lopez, and J. Doval-Gandoy, "Evaluation of techniques for cross-coupling decoupling between orthogonal axes in double synchronous reference frame current control," *IEEE Transactions on Industrial Electronics*, vol. 61, no. 7, pp. 3527–3531, Jul. 2014.

[10] A. G. Yepes, A. Vidal, J. Malvar, O. Lopez, and J. Doval-Gandoy, "Tuning method aimed at optimized settling time and overshoot for synchronous proportional-integral current control in electric machines," *IEEE Transactions on Power Electronics*, vol. 29, no. 6, pp. 3041–3054, Jun. 2014.

[11] J. Malvar, O. Lopez, A. G. Yepes, A. Vidal, F. D. Freijedo, P. Fernandez-Comesana, and J. Doval-Gandoy, "Graphical diagram for subspace and sequence identification of time harmonics in symmetrical multiphase machines," *IEEE Transactions on Industrial Electronics*, vol. 61, no. 1, pp. 29–42, Jan. 2014.

[12] L. Harnefors, A. G. Yepes, A. Vidal, and J. Doval-Gandoy, "Passivity-based stabilization of voltage-source converters equipped with LCL input filters," in *Proceedings of 2014 IEEE Industrial Electronics Society (IECON)*, Nov. 2014.

[13] A. Vidal, A. G. Yepes, F. D. Freijedo, J. Malvar, O. Lopez, and J. Doval-Gandoy, "Estimation of the plant time constant of current-controlled voltage source converters," in *Proceedings of 2014 IEEE Energy Conversion Congress and Exposition (ECCE)*, Sep. 2014, pp. 5008–5015.

[14] A. Vidal, F. D. Freijedo, A. G. Yepes, P. Fernandez-Comesana, J. Malvar, O. Lopez, and J. Doval-Gandoy, "Assessment and optimization of the transient response of proportional-resonant current controllers for distributed power generation systems," *IEEE Transactions on Industrial Electronics*, vol. 60, no. 4, pp. 1367–1383, Apr. 2013.

[15] A. G. Yepes, J. Malvar, A. Vidal, O. Lopez, and J. Doval-Gandoy, "Current harmonic compensation in symmetrical multiphase machines by resonant controllers in synchronous reference frames -Part 1: Extension to any phase number," in *Proceedings of 2013 IEEE Industrial Electronics Society (IECON)*, Nov. 2013, pp. 5155–5160.

[16] ——, "Current harmonic compensation in symmetrical multiphase machines by resonant controllers in synchronous reference frames -Part 2: Computational load," in *Proceedings of 2013 IEEE Industrial Electronics Society (IECON)*, Nov. 2013, pp. 5161–5166.

[17] J. Malvar, O. Lopez, A. G. Yepes, A. Vidal, and J. Doval-Gandoy, "Interactions between time and spatial harmonics in a series-connected five-phase two-motor drive," in *Proceedings of 2013 IEEE Industrial Electronics Society (IECON)*, Nov. 2013, pp. 5197–5202.

[18] F. D. Freijedo, A. Vidal, A. G. Yepes, J. Malvar, O. Lopez, and J. Doval-Gandoy, "Assessment of synchronous-frame PI current control dynamics by means of multivariable analysis with time-delays consideration," in *Energy Conversion Congress and Exposition (ECCE), 2013 IEEE*, Sep. 2013, pp. 4104–4111.

[19] A. Vidal, A. G. Yepes, J. Malvar, O. Lopez, J. Doval-Gandoy, and F. D. Freijedo, "A method to identify the equivalent loss resistance of voltage source converters for current control design," in *Proceedings of 2013 IEEE Energy Conversion Congress and Exposition (ECCE)*, Sep. 2013, pp. 4133–4140.

[20] A. G. Yepes, A. Vidal, F. D. Freijedo, J. Malvar, O. Lopez, and J. Doval-Gandoy, "A simple tuning method aimed at optimal settling time and overshoot for synchronous pi current control in electric machines," in *Proceedings of 2013 IEEE Energy Conversion Congress and Exposition (ECCE)*, Sep. 2013, pp. 1465–1472.

[21] A. G. Yepes, A. Vidal, J. Malvar, O. Lopez, J. Doval-Gandoy, and F. D. Freijedo, "Ineffectiveness of orthogonal axes cross-coupling decoupling technique in dual sequence current control," in *Proceedings of 2013 IEEE Energy Conversion Congress and Exposition (ECCE)*, Sep. 2013, pp. 1047–1053.

[22] A. G. Yepes, J. Malvar, A. Vidal, O. Lopez, and J. Doval-Gandoy, "Optimized harmonic current control strategy for nonlinearities compensation in multiphase ac drives," in *Proceedings of 2013 IEEE Energy Conversion Congress and Exposition (ECCE)*, Sep. 2013, pp. 1458–1464.

[23] A. Vidal, F. D. Freijedo, A. G. Yepes, J. Malvar, O. Lopez, and J. Doval-Gandoy, "Transient response assessment of vector PI current controllers in renewable energy applications," in *Proceedings of 2012 IEEE Industrial Electronics Society (IECON)*, Oct. 2012, pp. 5259–5264.

[24] J. Malvar, A. G. Yepes, A. Vidal, P. Fernandez-Comesana, F. D. Freijedo, O. Lopez, and J. Doval-Gandoy, "Harmonic subspace and sequence mapping in a series-connected six-phase two-motor drive," in *Proceedings of 2012 IEEE Industrial Electronics Society (IECON)*, Oct. 2012, pp. 3622–3627.

[25] O. Lopez, J. Alvarez, J. Malvar, A. G. Yepes, A. Vidal, P. Fernandez-Comesana, F. D. Freijedo, and J. Doval-Gandoy, "Multiphase space vector control modulation technique for voltage source converters," in *Proceedings of 2012 IEEE Industrial Electronics Society (IECON)*, Oct. 2012, pp. 3635–3640.

[26] A. G. Yepes, A. Vidal, F. D. Freijedo, J. Malvar, O. Lopez, and J. Doval-Gandoy, "Transient response evaluation of resonant controllers for AC drives," in *Proceedings of 2012 IEEE Energy Conversion Congress and Exposition (ECCE)*, Sep. 2012, pp. 471–478.

[27] F. D. Freijedo, A. G. Yepes, J. Malvar, O. Lopez, P. Fernandez-Comesana, A. Vidal, and J. Doval-Gandoy, "Frequency tracking of digital resonant filters for control of power converters connected to public distribution systems," *IET Power Electronics*, vol. 4, no. 4, pp. 454–462, Apr. 2011.

[28] F. D. Freijedo, A. G. Yepes, O. Lopez, A. Vidal, and J. Doval-Gandoy, "Three-phase PLLs with fast post-fault re-tracking and steady-state rejection of voltage unbalance and harmonics by means of lead compensation," *IEEE Transactions on Power Electronics*, vol. 26, no. 1, pp. 85–97, Jan. 2011.

[29] A. Vidal, F. D. Freijedo, A. G. Yepes, P. Fernandez-Comesaña, J. Malvar, O. Lopez, and J. Doval-Gandoy, "A fast, accurate and robust algorithm to detect fundamental and harmonic sequences," in *Proceedings of 2010 IEEE Energy Conversion Congress and Exposition (ECCE)*, Sep. 2010, pp. 1047–1052.

[30] F. D. Freijedo, A. Vidal, A. G. Yepes, P. Fernandez-Comesaña, J. Malvar, O. Lopez, A. Nogueiras, and J. Doval-Gandoy, "WLSE for fast, accurate and robust generation of references in power converter applications," in *Proceedings of IEEE International Symposium on Industrial Electronics, ISIE*, Jul. 2010, pp. 2946–2951.

[31] EIA, "Annual Energy Outlook 2014," Apr. 2014. [Online]. Available: http://www.eia.gov/forecasts/aeo/pdf/0383(2014).pdf

[32] REN21, "Renewables 2014 Global Status Report," Jun. 2014. [Online]. Available: http://www.ren21.net

[33] J. M. Carrasco, L. G. Franquelo, J. T. Bialasiewicz, E. Galvan, R. C. P. Guisado, M. A. M. Prats, J. I. Leon, and N. Moreno-Alfonso, "Power-electronic systems for the grid integration of renewable energy sources: A survey," *IEEE Transactions on Industrial Electronics*, vol. 53, no. 4, pp. 1002–1016, Jun. 2006.

[34] A. Timbus, M. Liserre, R. Teodorescu, P. Rodriguez, and F. Blaabjerg, "Evaluation of current controllers for distributed power generation systems," *IEEE Transactions on Power Electronics*, vol. 24, no. 3, pp. 654–664, Mar. 2009.

[35] A. Camacho, M. Castilla, J. Miret, J. Vasquez, and E. Alarcon-Gallo, "Flexible voltage support control for three phase distributed generation inverters under grid fault," *IEEE Transactions on Industrial Electronics*, vol. 60, no. 4, pp. 1429–1441, Apr. 2013.

[36] M. Liserre, F. Blaabjerg, and R. Teodorescu, "Grid impedance estimation via excitation of LCL -filter resonance," *IEEE Transactions on Industry Applications*, vol. 43, no. 5, pp. 1401–1407, Sep. 2007.

[37] BOE, "Requisitos de respuesta frente a huecos de tensión de las instalaciones eólicas, P.O. 12.3," REE, Spain, Oct. 2006.

[38] "Grid code for the local transmission system operator," Walloon Energy Commission, Wallonia, Belgium, May. 2007.

[39] "Grid Code. High and extra high voltage," E. ON Netz GmbH, Germany, 2006.

[40] "Transmission Code 2007. Networks and System Rules of the German Transmission System operators," VDN-e.v. beim VDEW, Germany, 2007.

[41] "Requirements for offshore grid connections in the E.ON Netz Network," E.ON Netz GmbH, Bayreuth, Germany, Apr. 2008.

[42] R. Teodorescu, M. Liserre, and P. Rodriguez, *Grid Converters for Photovoltaic and Wind Power Systems*, ser. Wiley - IEEE. Wiley, 2011.

[43] F. Blaabjerg, Z. Chen, and S. Kjaer, "Power electronics as efficient interface in dispersed power generation systems," *IEEE Transactions on Power Electronics*, vol. 19, no. 5, pp. 1184–1194, Sep. 2004.

[44] F. Blaabjerg and K. Ma, "Future on power electronics for wind turbine systems," *IEEE Journal of Emerging and Selected Topics in Power Electronics*, vol. 1, no. 3, pp. 139–152, Sep. 2013.

[45] Z. Chen, J. Guerrero, and F. Blaabjerg, "A review of the state of the art of power electronics for wind turbines," *IEEE Transactions on Industrial Electronics*, vol. 24, no. 8, pp. 1859–1875, Aug. 2009.

[46] M. Liserre, R. Cardenas, M. Molinas, and J. Rodriguez, "Overview of multi-MW wind turbines and wind parks," *IEEE Transactions on Industrial Electronics*, vol. 58, no. 4, pp. 1081–1095, Apr. 2011.

[47] C. H. Ng, L. Ran, and J. Bumby, "Unbalanced-grid-fault ride-through control for a wind turbine inverter," *IEEE Transactions on Industry Applications*, vol. 44, no. 3, pp. 845 –856, May/Jun. 2008.

[48] S. Alepuz, A. Calle-Prado, S. Busquets-Monge, S. Kouro, and B. Wu, "Use of stored energy in PMSG rotor inertia for low voltage ride-through in back-to-back NPC converter based wind power systems," *IEEE Transactions on Industrial Electronics*, vol. 60, no. 5, pp. 1787–1796, May 2013.

[49] N. A. Orlando, M. Liserre, R. A. Mastromauro, and A. Dell'Aquila, "A survey of control issues in PMSG-based small wind-turbine systems," *IEEE Transactions on Industrial Informatics*, vol. 9, no. 3, pp. 1211–1221, Aug. 2013.

[50] S. B. Kjaer, J. K. Pedersen, and F. Blaabjerg, "A review of single-phase grid-connected inverters for photovoltaic modules," *IEEE Transactions on Industry Applications*, vol. 41, no. 5, pp. 1292–1306, Sep. 2005.

[51] M. Castilla, J. Miret, A. Camacho, J. Matas, and L. de Vicuna, "Reduction of current harmonic distortion in three-phase grid-connected photovoltaic inverters via resonant current control," *IEEE Transactions on Industrial Electronics*, vol. 60, no. 4, pp. 1464–1472, Apr. 2013.

[52] S. Rivera, S. Kouro, B. Wu, S. Alepuz, M. Malinowski, P. Cortes, and J. Rodriguez, "Multilevel direct power control –a generalized approach for grid-tied multilevel converter applications," *IEEE Transactions on Power Electronics*, vol. 29, no. 10, pp. 5592–5604, Oct. 2014.

[53] A. Razali, A. Rahman, G. George, and N. Rahim, "Analysis and design of new switching look-up table for virtual flux direct power control of grid connected three phase PWM AC-DC converter," *IEEE Transactions on Industry Applications*, to be published.

[54] A. Camacho, M. Castilla, J. Miret, A. Borrell, and L. de Vicuna, "Active and reactive power strategies with peak current limitation for distributed generation inverters during unbalanced grid faults," *IEEE Transactions on Industrial Electronics*, to be published.

[55] J. Espi, J. Castello, R. Garcia-Gil, G. Garcera, and E. Figueres, "An adaptive robust predictive current control for three-phase grid-connected inverters," *IEEE Transactions on Industrial Electronics*, vol. 58, no. 8, pp. 3537–3546, Aug. 2011.

[56] M. Prodanovic and T. C. Green, "Control and filter design of three-phase inverters for high power quality grid connection," *IEEE Transactions on Power Electronics*, vol. 18, no. 1, pp. 373–380, Jan. 2003.

[57] J. M. Guerrero, J. C. Vasquez, J. Matas, L. G. de Vicuña, and M. Castilla, "Hierarchical control of droop-controlled AC and DC microgrids-a general approach toward standardization," *IEEE Transactions on Industrial Electronics*, vol. 58, no. 1, pp. 158–172, Jan. 2011.

[58] J. Rocabert, A. Luna, F. Blaabjerg, and P. Rodriguez, "Control of power converters in AC microgrids," *IEEE Transactions on Power Electronics*, vol. 27, no. 11, pp. 4734–4749, Nov. 2012.

[59] K. l. Astrom and T. Hagglund, *PID Controllers: Theory, Design, and Tuning*. Instrument Society of America: Research Triangle Park, 1995.

[60] M. Tsili and S. Papathanassiou, "A review of grid code technical requirements for wind farms," *IET Renewable Power Generation*, vol. 3, no. 3, pp. 308–332, Sep. 2009.

[61] F. Iov, A. Hansen, P. Soerensen, and N. Cutululis, "Mapping of grid faults and grid codes," Risoe National Laboratory, Tech. Rep., 2006.

[62] J. F. Conroy and R. Watson, "Low-voltage ride-through of a full converter wind turbine with permanent magnet generator," *IET Renewable Power Generation*, vol. 1, no. 3, pp. 182–189, Sep. 2007.

[63] S. M. Muyeen, R. Takahashi, T. Murata, and J. Tamura, "A variable speed wind turbine control strategy to meet wind farm grid code requirements," *IEEE Transactions on Power Systems*, vol. 25, no. 1, pp. 331–340, Feb. 2010.

[64] F. Jimenez, E. Gomez-Lazaro, J. A. Fuentes, A. Molina-García, and A. Vigueras-Rodriguez, "Validation of a DFIG wind turbine model submitted to two-phase voltage dips following the Spanish grid code," *Renewable Energy*, vol. 57, pp. 27–34, Sep. 2013.

[65] I. Etxeberria-Otadui, U. Viscarret, M. Caballero, A. Rufer, and S. Bacha, "New optimized PWM VSC control structures and strategies under unbalanced voltage transients," *IEEE Transactions on Industrial Electronics*, vol. 54, no. 5, pp. 2902–2914, Oct. 2007.

[66] P. Rodriguez, A. Timbus, R. Teodorescu, M. Liserre, and F. Blaabjerg, "Flexible active power control of distributed power generation systems during grid faults," *IEEE Transactions on Industrial Electronics*, vol. 54, no. 5, pp. 2583 –2592, Oct. 2007.

[67] ——, "Reactive power control for improving wind turbine system behavior under grid faults," *IEEE Transactions on Power Electronics*, vol. 24, no. 7, pp. 1798 –1801, Jul. 2009.

[68] S. Alepuz, S. Busquets-Monge, J. Bordonau, J. A. Martinez-Velasco, C. A. Silva, J. Pontt, and J. Rodriguez, "Control strategies based on symmetrical components for grid-connected converters under voltage dips," *IEEE Transactions on Industrial Electronics*, vol. 56, no. 6, pp. 2162–2173, Jun. 2009.

[69] F. Wang, J. L. Duarte, and M. A. M. Hendrix, "Pliant active and reactive power control for grid-interactive converters under unbalanced voltage dips," *IEEE Transactions on Power Electronics*, vol. 26, no. 5, pp. 1511–1521, May 2011.

[70] C.-T. Lee, C.-W. Hsu, and P.-T. Cheng, "A low-voltage ride-through technique for grid-connected converters of distributed energy resources," *IEEE Transactions on Industry Applications*, vol. 47, no. 4, pp. 1821–1832, Jul. 2011.

[71] X. Guo, W. Liu, X. Zhang, X. Sun, Z. Lu, and J. M. Guerrero, "Flexible control strategy for grid-connected inverter under unbalanced grid faults without PLL," *IEEE Transactions on Power Electronics*, vol. 30, no. 4, pp. 1773–1778, Apr. 2015.

[72] X. Guo, X. Zhang, B. Wang, W. Wu, and J. M. Guerrero, "Asymmetrical grid fault ride-through strategy of three-phase grid-connected inverter considering network impedance impact in low-voltage grid," *IEEE Transactions on Power Electronics*, vol. 29, no. 3, pp. 1064–1068, Mar. 2014.

[73] A. Junyent-Ferre, O. Gomis-Bellmunt, T. C. Green, and D. E. Soto-Sanchez, "Current control reference calculation issues for the operation of renewable source grid interface VSCs under unbalanced voltage sags," *IEEE Transactions on Power Electronics*, vol. 26, no. 12, pp. 3744–3753, Dec. 2011.

[74] A. Camacho, M. Castilla, J. Miret, R. Guzman, and A. Borrell, "Reactive power control for distributed generation power plants to comply with voltage limits during grid faults," *IEEE Transactions on Power Electronics*, vol. 29, no. 11, pp. 6224–6234, Nov. 2014.

[75] K. Ogata, *Modern Control Engineering*. Prentice Hall, 2009.

[76] D. G. Holmes, T. A. Lipo, B. P. McGrath, and W. Y. Kong, "Optimized design of stationary frame three phase AC current regulators," *IEEE Transactions on Power Electronics*, vol. 24, no. 11, pp. 2417–2426, Nov. 2009.

[77] A. G. Yepes, F. D. Freijedo, J. Doval-Gandoy, and O. Lopez, "Analysis and design of resonant current controllers for voltage source converters by means of Nyquist diagrams and sensitivity function," *IEEE Transactions on Industrial Electronics*, vol. 58, no. 11, pp. 5231–5250, Mar. 2011.

[78] R. Teodorescu and F. Blaabjerg, "Flexible control of small wind turbines with grid failure detection operating in stand-alone and grid-connected mode," *IEEE Transactions on Power Electronics*, vol. 19, no. 5, pp. 1323–1332, Sep. 2004.

[79] A. G. Yepes, F. D. Freijedo, J. Doval-Gandoy, O. Lopez, J. Malvar, and P. Fernandez-Comesana, "Effects of discretization methods on the performance of resonant controllers," *IEEE Transactions on Power Electronics*, vol. 25, no. 7, pp. 1692–1712, Jul. 2010.

[80] S. Buso and P. Mattavelli, *Digital Control in Power Electronics*, J. Hudgins, Ed. Morgan and Claypool Publishers, 2006.

[81] F. Briz, P. Garcia, M. W. Degner, D. Diaz-Reigosa, and J. M. Guerrero, "Dynamic behavior of current controllers for selective harmonic compensation in three-phase active power filters," *IEEE Transactions on Industry Applications*, vol. 49, no. 3, pp. 1411–1420, May/Jun. 2013.

[82] E. Clarke, *Circuit Analysis of AC Power Systems*. Wiley, 1950.

[83] R. Park, "Two reaction theory of synchronous machines," *AIEE Transactions*, vol. 48, pp. 716–730, 1929.

[84] C. Bao, X. Ruan, X. Wang, W. Li, D. Pan, and K. Weng, "Step-by-step controller design for LCL-type grid-connected inverter with capacitor -current-feedback active-damping," *IEEE Transactions on Power Electronics*, vol. 29, no. 3, pp. 1239–1253, Mar. 2014.

[85] A. G. Yepes, "Digital resonant current controllers for voltage source converters," Ph.D. dissertation, Department of Electronics Technology, University of Vigo, 2011.

[86] Y. A.-R. I. Mohamed and E. F. El-Saadany, "Adaptive discrete-time grid-voltage sensorless interfacing scheme for grid-connected DG-inverters based on neural-network identification and deadbeat current regulation," *IEEE Transactions on Power Electronics*, vol. 23, no. 1, pp. 308–321, Jan. 2008.

[87] Y. A.-R. I. Mohamed, E. F. El-Saadany, and M. M. A. Salama, "Adaptive grid-voltage sensorless control scheme for inverter-based distributed generation," *IEEE Transactions on Energy Conversion*, vol. 24, no. 3, pp. 683–694, Sep. 2009.

[88] J. Dannehl, F. W. Fuchs, and P. B. Thogersen, "PI state space current control of grid-connected PWM converters with LCL filters," *IEEE Transactions on Power Electronics*, vol. 25, no. 9, pp. 2320–2330, Sep. 2010.

[89] Y. A.-R. I. Mohamed and E. F. El-Saadany, "Robust high bandwidth discrete-time predictive current control with predictive internal model—A unified approach for voltage-source PWM converters," *IEEE Transactions on Power Electronics*, vol. 23, no. 1, pp. 126–136, Jan. 2008.

[90] N. Hoffmann and F. W. Fuchs, "Minimal invasive equivalent grid impedance estimation in inductive-resistive power networks using extended kalman filter," *IEEE Transactions on Power Electronics*, vol. 29, no. 2, pp. 631–641, Feb. 2014.

[91] S. Cobreces, E. J. Bueno, D. Pizarro, F. J. Rodriguez, and F. Huerta, "Grid impedance monitoring system for distributed power generation electronic interfaces," *IEEE Transactions on Instrumentation and Measurement*, vol. 58, no. 9, pp. 3112–3121, Sep. 2009.

[92] F. Briz, M. W. Degner, and R. D. Lorenz, "Dynamic analysis of current regulators for AC motors using complex vectors," *IEEE Transactions on Industry Applications*, vol. 35, no. 6, pp. 1424–1432, Dec. 1999.

[93] L. Harnefors, A. Antonopoulos, S. Norrga, L. Angquist, and H. Nee, "Dynamic analysis of modular multilevel converters," *IEEE Transactions on Industrial Electronics*, vol. 60, no. 7, pp. 2526–2537, Jul. 2013.

[94] K. Ilves, S. Norrga, L. Harnefors, and H. P. Nee, "On energy storage requirements in modular multilevel converters," *IEEE Transactions on Power Electronics*, vol. 29, no. 1, pp. 77–88, Jan. 2014.

[95] P. W. Lehn and M. R. Iravani, "Discrete time modeling and control of the voltage source converter for improved disturbance rejection," *IEEE Transactions on Power Electronics*, vol. 14, no. 6, pp. 1028–1036, Nov. 1999.

[96] P. Channegowda and V. John, "Filter optimization for grid interactive voltage source inverters," *IEEE Transactions on Industrial Electronics*, vol. 57, no. 12, pp. 4106–4114, Dec. 2010.

[97] I. J. Gabe, V. F. Montagner, and H. Pinheiro, "Design and implementation of a robust current controller for VSI connected to the grid through an LCL filter," *IEEE Transactions on Power Electronics*, vol. 24, no. 6, pp. 1444–1452, Jun. 2009.

[98] M. Wagner, T. Barth, R. Alvarez, C. Ditmanson, and S. Bernet, "Discrete-time active damping of LCL filters by proportional capacitor current feedback," *IEEE Transactions on Industry Applications*, vol. 50, no. 6, pp. 3911–3920, Nov. 2014.

[99] S. G. Parker, B. P. McGrath, and D. G. Holmes, "Regions of active damping control for LCL filters," *IEEE Transactions on Industry Applications*, vol. 50, no. 1, pp. 424–432, Jan. 2014.

[100] J. R. Massing, M. Stefanello, H. A. Grundling, and H. Pinheiro, "Adaptive current control for grid-connected converters with LCL filter," *IEEE Transactions on Industrial Electronics*, vol. 59, no. 12, pp. 4681–4693, Dec. 2012.

[101] J. Xu, S. Xie, and T. Tang, "Evaluations of current control in weak grid case for grid-connected LCL-filtered inverter," *IET Power Electronics*, vol. 6, no. 2, pp. 227–234, Feb. 2013.

[102] M. Liserre, F. Blaabjerg, and S. Hansen, "Design and control of an LCL-filter-based three-phase active rectifier," *IEEE Transactions on Industry Applications*, vol. 41, no. 5, pp. 1281–1291, Sep./Oct. 2005.

[103] Y. A.-R. I. Mohamed, "Mitigation of dynamic, unbalanced, and harmonic voltage disturbances using grid-connected inverters with LCL filter," *IEEE Transactions on Power Electronics*, vol. 58, no. 9, pp. 3914–3924, Sep. 2011.

[104] A. Rockhill, M. Liserre, R. Teodorescu, and P. Rodriguez, "Grid filter design for a multimegawatt medium-voltage voltage source inverter," *IEEE Transactions on Industrial Electronics*, vol. 58, no. 4, pp. 1205–1217, Apr. 2011.

[105] J. Dannehl, M. Liserre, and F. W. Fuchs, "Filter-based active damping of voltage source converters with LCL filter," *IEEE Transactions on Industrial Electronics*, vol. 58, no. 8, pp. 3623 –3633, Aug. 2011.

[106] R. Peña-Alzola, M. Liserre, F. Blaabjerg, R. Sebastian, J. Dannehl, and F. W. Fuchs, "Systematic design of the lead-lag network method for active damping in LCL-filter based three phase converters," *IEEE Transactions on Industrial Informatics*, vol. 10, no. 1, pp. 43–52, Feb. 2014.

[107] J. Xu, S. Xie, and T. Tang, "Improved control strategy with grid-voltage feedforward for LCL-filter-based inverter connected to weak grid," *IET Power Electronics*, vol. 7, no. 10, pp. 2660–2671, Oct. 2014.

[108] M. Liserre, F. Blaabjerg, and A. Dell'Aquila, "Step-by-step design procedure for a grid-connected three-phase PWM voltage source converter," *Int. J. Electron.*, vol. 91, no. 8, pp. 445–460, Aug. 2004.

[109] R. Peña-Alzola, M. Liserre, F. Blaabjerg, M. Ordonez, and Y. Yang, "LCL-filter design for robust active damping in grid-connected converters," *IEEE Transactions on Industrial Informatics*, vol. 10, no. 4, pp. 2192–2203, Nov. 2014.

[110] R. Peña-Alzola, M. Liserre, F. Blaabjerg, M. Ordonez, and T. Kerekes, "A self-commissioning notch filter for active damping in a three-phase LCL -filter-based grid-tie converter," *IEEE Transactions on Power Electronics*, vol. 29, no. 12, pp. 6754–6761, Dec. 2014.

[111] M. Liserre, R. Teodorescu, and F. Blaabjerg, "Stability of photovoltaic and wind turbine grid-connected inverters for a large set of grid impedance values," *IEEE Transactions on Power Electronics*, vol. 21, no. 1, pp. 263–272, Jan. 2006.

[112] M. Sedighy, S. B. Dewan, and F. P. Dawson, "A robust digital current control method for active power filters," *IEEE Transactions on Industry Applications*, vol. 36, no. 4, pp. 1158–1164, Jul./Aug. 2000.

[113] M. Bierhoff and F. Fuchs, "Active damping for three-phase PWM rectifiers with high-order line-side filters," *IEEE Transactions on Industrial Electronics*, vol. 56, no. 2, pp. 371–379, Feb. 2009.

[114] A. G. Yepes, F. D. Freijedo, O. Lopez, and J. Doval-Gandoy, "High-performance digital resonant controllers implemented with two integrators," *IEEE Transactions on Power Electronics*, vol. 26, no. 2, pp. 563–576, Feb. 2011.

[115] T. Roinila, M. Vilkko, and J. Sun, "Online grid impedance measurement using discrete-interval binary sequence injection," *IEEE Journal of Emerging and Selected Topics in Power Electronics*, vol. 2, no. 4, pp. 985–993, Dec. 2014.

[116] M. Cespedes and J. Sun, "Adaptive control of grid-connected inverters based on online grid impedance measurements," *IEEE Trans. Sustainable Energy*, vol. 5, no. 2, pp. 516–523, Apr. 2014.

[117] A. Leon, J. M. Mauricio, J. A. Solsona, and A. Gomez-Exposito, "Adaptive control strategy for VSC-based systems under unbalanced network conditions," *IEEE Trans. Smart Grid*, vol. 1, no. 3, pp. 311–319, Dec. 2010.

[118] L. Asiminoaei, R. Teodorescu, F. Blaabjerg, and U. Borup, "Implementation and test of an online embedded grid impedance estimation technique for PV inverters," *IEEE Transactions on Industrial Electronics*, vol. 52, no. 4, pp. 1136–1144, Aug. 2005.

[119] V. Blasko and V. Kaura, "A new mathematical model and control of a three-phase AC-DC voltage source converter," *IEEE Transactions on Power Electronics*, vol. 12, no. 1, pp. 116–123, Jan. 1997.

[120] K.-J. Lee, B.-G. Park, R. young Kim, and D. seok Hyun, "Robust predictive current controller based on a disturbance estimator in a three-phase grid-connected inverter," *IEEE Transactions on Power Electronics*, vol. 27, no. 1, pp. 276–283, Jan. 2012.

[121] A. Tarkiainen, R. Pollanen, M. Niemela, and J. Pyrhonen, "Identification of grid impedance for purposes of voltage feedback active filtering," *IEEE Power Electron. Lett.*, vol. 2, no. 1, pp. 6–10, Mar. 2004.

[122] M. Singh and A. Chandra, "Real-time implementation of ANFIS control for renewable interfacing inverter in 3P4W distribution network," *IEEE Transactions on Industrial Electronics*, vol. 60, no. 1, pp. 121–128, Jan. 2013.

[123] I. D. Landau, R. Lozano, M. M' Saad, and A. Karimi, *Adaptive Control*, 2nd ed. Springer London, 2011.

[124] H. Kakigano, Y. Miura, and T. Ise, "Distribution voltage control for DC microgrids using fuzzy control and gain-scheduling technique," *IEEE Transactions on Power Electronics*, vol. 28, no. 5, pp. 2246–2258, May 2013.

[125] O. Jimenez, O. Lucia, I. Urriza, L. A. Barragan, P. Mattavelli, and D. Boroyevich, "An FPGA-based gain-scheduled controller for resonant converters applied to induction cooktops," *IEEE Transactions on Power Electronics*, vol. 29, no. 4, pp. 2143–2152, Apr. 2014.

[126] P. Antoniewicz and M. P. Kazmierkowski, "Virtual-flux-based predictive direct power control of AC/DC converters with online inductance estimation," *IEEE Transactions on Industrial Electronics*, vol. 55, no. 12, pp. 4381–4390, Dec. 2008.

[127] X. Sun, J. Chen, J. M. Guerrero, X. Li, and L. Wang, "Fundamental impedance identification method for grid-connected voltage source inverters," *IET Power Electronics*, vol. 7, no. 5, pp. 1099–1105, May 2014.

[128] Y.-R. Mohamed and E. El-Saadany, "An improved deadbeat current control scheme with a novel adaptive self-tuning load model for a three-phase PWM voltage-source inverter," *IEEE Transactions on Industrial Electronics*, vol. 54, no. 2, pp. 747–759, Apr. 2007.

[129] H. P. Whitaker, J. Yamron, and A. Kezer, "Design of a model-reference adaptive control system for aircraft," R-164, MIT, Instrumentation Lab, Cambridge, USA, Tech. Rep., 1958.

[130] L. Zhen and L. Xu, "Sensorless field orientation control of induction machines based on a mutual MRAS scheme," *IEEE Transactions on Industrial Electronics*, vol. 45, no. 5, pp. 824–831, Oct. 1998.

[131] M. Rashed, F. A. Peter, A. MacConnell, A. F. Stronach, and P. Acarnley, "Sensorless indirect-rotor-field-orientation speed control of a permanent-magnet synchronous motor with stator-resistance estimation," *IEEE Transactions on Industrial Electronics*, vol. 54, no. 3, pp. 1664–1675, Jun. 2007.

[132] A. V. Ravi Teja, C. Chakraborty, S. Maiti, and Y. Hori, "A new model reference adaptive controller for four quadrant vector controlled induction motor drives," *IEEE Transactions on Industrial Electronics*, vol. 59, no. 10, pp. 3757–3767, Oct. 2012.

[133] H. M. Kojabadi, L. Chang, and R. Doraiswami, "A MRAS-based adaptive pseudoreduced-order flux observer for sensorless induction motor drives," *IEEE Transactions on Power Electronics*, vol. 20, no. 4, pp. 930–938, Jul. 2005.

[134] T. Boileau, N. Leboeuf, B. Nahid-Mobarakeh, and F. Meibody-Tabar, "Online identification of PMSM parameters: Parameter identifiability and estimator comparative study," *IEEE Transactions on Industry Applications*, vol. 47, no. 4, pp. 1944–1957, Jul./Aug. 2011.

[135] G. Gatto, I. Marongiu, and A. Serpi, "Discrete-time parameter identification of a surface-mounted permanent magnet synchronous machine," *IEEE Transactions on Industrial Electronics*, vol. 60, no. 11, pp. 4869–4880, Feb. 2013.

[136] M. Rashed, P. F. A. MacConnell, and A. F. Stronach, "Nonlinear adaptive state-feedback speed control of a voltage-fed induction motor with varying parameters," *IEEE Transactions on Industry Applications*, vol. 42, no. 3, pp. 723–732, May/Jun. 2006.

[137] P. Mattavelli, "An improved deadbeat control for UPS using disturbance observers," *IEEE Transactions on Industrial Electronics*, vol. 52, no. 1, pp. 206 – 212, Feb. 2005.

[138] C. D. Schauder and R. Caddy, "Current control of voltage-source inverters for fast four-quadrant drive performance," *IEEE Transactions on Industry Applications*, vol. IA-18, no. 2, pp. 163 –171, Mar. 1982.

[139] P. Mattavelli, "Synchronous-frame harmonic control for high-performance AC power supplies," *IEEE Transactions on Industry Applications*, vol. 37, no. 3, pp. 864–872, May 2001.

[140] F. Briz, M. W. Degner, and R. D. Lorenz, "Analysis and design of current regulators using complex vectors," *IEEE Transactions on Industry Applications*, vol. 36, no. 3, pp. 817–825, May 2000.

[141] L. Harnefors and H. P. Nee, "Model-based current control of AC machines using the internal model control method," *IEEE Transactions on Industry Applications*, vol. 34, no. 1, pp. 133–141, Jan./Feb. 1998.

[142] C. Lascu, L. Asiminoaei, I. Boldea, and F. Blaabjerg, "High performance current controller for selective harmonic compensation in active power filters," *IEEE Transactions on Power Electronics*, vol. 22, no. 5, pp. 1826–1835, Sep. 2007.

[143] ——, "Frequency response analysis of current controllers for selective harmonic compensation in active power filters," *IEEE Transactions on Industrial Electronics*, vol. 56, no. 2, pp. 337–347, Feb. 2009.

[144] D. N. Zmood and D. G. Holmes, "Stationary frame current regulation of PWM inverters with zero steady-state error," *IEEE Transactions on Power Electronics*, vol. 18, no. 3, pp. 814–822, May 2003.

[145] S. Fukuda and T. Yoda, "A novel current-tracking method for active filters based on a sinusoidal internal model," *IEEE Transactions on Industry Applications*, vol. 37, no. 3, pp. 888–895, May/Jun. 2001.

[146] X. Yuan, W. Merk, H. Stemmler, and J. Allmeling, "Stationary-frame generalized integrators for current control of active power filters with zero steady-state error for current harmonics of concern under unbalanced and distorted operating conditions," *IEEE Transactions on Industry Applications*, vol. 38, no. 2, pp. 523–532, Mar./Apr. 2002.

[147] R. Bojoi, L. Limongi, F. Profumo, D. Roiu, and A. Tenconi, "Analysis of current controllers for active power filters using selective harmonic compensation schemes," *IEEJ Trans. on Electrical and Electron. Eng.*, vol. 4, no. 2, pp. 139–157, Feb. 2009.

[148] L. Limongi, R. Bojoi, G. Griva, and A. Tenconi, "Digital current-control schemes," *IEEE Industrial Electron. Mag.*, vol. 3, no. 1, pp. 20–31, Mar. 2009.

[149] H. Akagi, E. H. Watanabe, and M. Aredes, *Instantaneous Power Theory and Applications to Power Conditioning*, M. E. El-Hawari, Ed. Wiley-IEEE Press, 2007.

[150] H. Fujita, "A single-phase active filter using an h-bridge PWM converter with a sampling frequency quadruple of the switching frequency," *IEEE Transactions on Power Electronics*, vol. 24, no. 4, pp. 934–941, Apr. 2009.

[151] P. Mattavelli, G. Spiazzi, and P. Tenti, "Predictive digital control of power factor preregulators with input voltage estimation using disturbance observers," *IEEE Transactions on Power Electronics*, vol. 20, no. 1, pp. 140 – 147, jan 2005.

[152] F. D. Freijedo, "Contributions to grid-synchronization techniques for power electronic converters," Ph.D. dissertation, Department of Electronics Technology, University of Vigo, 2009.

[153] J.-S. Yim, S.-K. Sul, B.-H. Bae, N. R. Patel, and S. Hiti, "Modified current control schemes for high-performance permanent-magnet AC drives with low sampling to operating frequency ratio," *IEEE Transactions on Industry Applications*, vol. 45, no. 2, pp. 763–771, Mar./Apr. 2009.

[154] L. Harnefors, L. Zhang, and M. Bongiorno, "Frequency-domain passivity-based current controller design," *IET Power Electronics*, vol. 1, no. 4, pp. 455–465, Dec. 2008.

[155] D. G. Holmes, B. P. McGrath, and S. G. Parker, "Current regulation strategies for vector-controlled induction motor drives," *IEEE Transactions on Industrial Electronics*, vol. 59, no. 10, pp. 3680–3689, Oct. 2012.

[156] M. Rizo, M. Liserre, E. Bueno, F. Rodriguez, and A. Rodriguez, "Distortion-free saturators for power converters under unbalanced conditions," *IEEE Transactions on Power Electronics*, to be published.

[157] Q. Trinh and H. Lee, "An advanced current control strategy for three-phase shunt active power filters," *IEEE Transactions on Industrial Electronics*, vol. 60, no. 12, pp. 5400–5410, Dec. 2013.

[158] J. Miret, M. Castilla, J. Matas, J. Guerrero, and J. Vasquez, "Selective harmonic-compensation control for single-phase active power filter with high harmonic rejection," *IEEE Transactions on Industrial Electronics*, vol. 56, no. 8, pp. 3117–3127, Aug. 2009.

[159] W. Lenwari, M. Sumner, and P. Zanchetta, "The use of genetic algorithms for the design of resonant compensators for active filters," *IEEE Transactions on Industrial Electronics*, vol. 56, no. 8, pp. 2852–2861, Aug. 2009.

[160] R. I. Bojoi, G. Griva, V. Bostan, M. Guerriero, F. Farina, and F. Profumo, "Current control strategy for power conditioners using sinusoidal signal integrators in synchronous reference frame," *IEEE Transactions on Power Electronics*, vol. 20, no. 6, pp. 1402–1412, Nov. 2005.

[161] R. A. Mastromauro, M. Liserre, and A. Dell'Aquila, "Study of the effects of inductor nonlinear behavior on the performance of current controllers for single-phase PV grid converters," *IEEE Transactions on Industrial Electronics*, vol. 55, no. 5, pp. 2043–2052, May 2008.

[162] R. Bojoi, L. R. Limongi, D. Roiu, and A. Tenconi, "Frequency-domain analysis of resonant current controllers for active power conditioners," in *Proceedings of 2008 IEEE Industrial Electronics Society (IECON)*, Nov. 2008, pp. 3141–3148.

[163] F. Blaabjerg, R. Teodorescu, M. Liserre, and A. Timbus, "Overview of control and grid synchronization for distributed power generation systems," *IEEE Transactions on Power Electronics*, vol. 53, no. 5, pp. 1398 –1409, Oct. 2006.

[164] M. Castilla, J. Miret, J. Matas, L. G. de Vicuna, and J. M. Guerrero, "Linear current control scheme with series resonant harmonic compensator for single-phase grid-connected photovoltaic inverters," *IEEE Transactions on Industrial Electronics*, vol. 45, no. 7, pp. 2724–2733, Jul. 2008.

[165] E. Twining and D. Holmes, "Grid current regulation of a three-phase voltage source inverter with an LCL input filter," *IEEE Transactions on Power Electronics*, vol. 18, no. 3, pp. 888–895, May 2003.

[166] L. Asiminoaei, P. Rodriguez, F. Blaabjerg, and M. Malinowski, "Reduction of switching losses in active power filters with a new generalized discontinuous-PWM strategy," *IEEE Transactions on Industrial Electronics*, vol. 55, no. 1, pp. 467–471, Jan. 2008.

[167] G. E. Valderrama, A. M. Stankovic, and P. Mattavelli, "Dissipativity-based adaptive and robust control of UPS in unbalanced operation," *IEEE Transactions on Industrial Electronics*, vol. 18, no. 4, pp. 1056–1062, Jul. 2003.

[168] F. Mwasilu, J. J. Justo, K. S. Ro, and J. W. Jung, "Improvement of dynamic performance of doubly fed induction generator-based wind turbine power system under an unbalanced grid voltage condition," *IET Renewable Power Generation*, vol. 6, no. 6, pp. 424–434, Nov. 2012.

[169] H. Che, E. Levi, M. Jones, H. Ping, and N. Abd Rahim, "Current control methods for an asymmetrical six-phase induction motor drive," *IEEE Transactions on Power Electronics*, vol. 29, no. 1, pp. 407–417, Jan. 2014.

[170] H. Nian and Y. Song, "Direct power control of doubly fed induction generator under distorted grid voltage," *IEEE Transactions on Power Electronics*, vol. 29, no. 2, pp. 894–905, Feb. 2014.

[171] I. Etxeberria-Otadui, A. Lopez De Heredia, H. Gaztanaga, S. Bacha, and M. c. Reyero, "A single synchronous frame hybrid (SSFH) multifrequency controller for power active filters," *IEEE Transactions on Industrial Electronics*, vol. 53, no. 5, pp. 1640–1648, Oct. 2006.

[172] I. Serban and C. Marinescu, "Control strategy of three-phase battery energy storage systems for frequency support in microgrids and with uninterrupted supply of local loads," *IEEE Transactions on Power Electronics*, vol. 29, no. 9, pp. 5010–5020, Sep. 2014.

[173] J. He, Y. W. Li, D. Bosnjak, and B. Harris, "Investigation and active damping of multiple resonances in a parallel-inverter-based microgrid," *IEEE Transactions on Power Electronics*, vol. 28, no. 1, pp. 234–246, Jan. 2013.

[174] X. Wang, F. Blaabjerg, and Z. Chen, "Autonomous control of inverter-interfaced distributed generation units for harmonic current filtering and resonance damping in an islanded microgrid," *IEEE Transactions on Industry Applications*, vol. 50, no. 1, pp. 452–461, Jan./Feb. 2014.

[175] E. Koutroulis and F. Blaabjerg, "Design optimization of transformerless grid-connected PV inverters including reliability," *IEEE Transactions on Power Electronics*, vol. 28, no. 1, pp. 325–335, Jan. 2013.

[176] Y. A.-R. I. Mohamed, M. A-Rahman, and R. Seethapathy, "Robust line-voltage sensorless control and synchronization of LCL -filtered distributed generation inverters for high power quality grid connection," *IEEE Transactions on Power Electronics*, vol. 27, no. 1, pp. 87–98, Jan. 2012.

[177] A. Kulkarni and V. John, "Mitigation of lower order harmonics in a grid-connected single-phase PV inverter," *IEEE Transactions on Power Electronics*, vol. 28, no. 11, pp. 5024–5037, Nov. 2013.

[178] A. de la Villa Jaen, E. Acha, and A. Exposito, "Voltage source converter modeling for power system state estimation: STATCOM and VSC-HVDC," *IEEE Transactions on Power Systems*, vol. 23, no. 4, pp. 1552–1559, Nov. 2008.

[179] Z. Yan, H. Xue-hao, T. Guang-fu, and H. Zhi-yuan, "A study on MMC model and its current control strategies," in *Proceedings of 2010 IEEE International Symposium on Power Electronics for Distributed Generation Systems (PEDG)*, Jun. 2010, pp. 259–264.

[180] D. Soto and R. Pena, "Nonlinear control strategies for cascaded multilevel STATCOMs," *IEEE Transactions on Power Delivery*, vol. 19, no. 4, pp. 1919–1927, Oct. 2004.

[181] B. M. Han, G. G. Karady, J. K. Park, and S. I. Moon, "Interaction analysis model for transmission static compensator with EMTP," *IEEE Transactions on Power Delivery*, vol. 13, no. 4, pp. 1297–1302, Oct. 1998.

[182] E. Acha and B. Kazemtabrizi, "A new STATCOM model for power flows using the newton-raphson method," *IEEE Transactions on Power Systems*, vol. 28, no. 3, pp. 2455–2465, Aug. 2013.

[183] S. Dieckerhoff, S. Bernet, and D. Krug, "Power loss-oriented evaluation of high voltage IGBTs and multilevel converters in transformerless traction applications," *IEEE Transactions on Power Electronics*, vol. 20, no. 6, pp. 1328–1336, Nov. 2005.

[184] M. Schweizer, T. Friedli, and J. W. Kolar, "Comparative evaluation of advanced three-phase three-level inverter/converter topologies against two-level systems," *IEEE Transactions on Industrial Electronics*, vol. 60, no. 12, pp. 5515–5527, Dec. 2013.

[185] M. Singh and A. Chandra, "Application of adaptive network-based fuzzy inference system for sensorless control of PMSG-based wind turbine with nonlinear-load-compensation capabilities," *IEEE Transactions on Power Electronics*, vol. 26, no. 1, pp. 165–175, Jan. 2011.

[186] H. Kim, M. W. Degner, J. M. Guerrero, F. Briz, and R. D. Lorenz, "Discrete-time current regulator design for AC machine drives," *IEEE Transactions on Industry Applications*, vol. 46, no. 4, pp. 1425–1435, Jul./Aug. 2010.

[187] T. E. Marlin, *Process control: designing processes and control systems for dynamic performance*. McGraw-Hill, 2000.

[188] F. Cupertino, G. Pellegrino, P. Giangrande, and L. Salvatore, "Sensorless position control of permanent-magnet motors with pulsating current injection and compensation of motor end effects," *IEEE Transactions on Industry Applications*, vol. 47, no. 3, pp. 1371–1379, May/Jun. 2011.

[189] L. Harnefors, S. E. Saarakkala, and M. Hinkkanen, "Speed control of electrical drives using classical control methods," *IEEE Transactions on Industry Applications*, vol. 49, no. 2, pp. 889–898, Mar./Apr. 2013.

[190] L. Harnefors, K. Pietilainen, and L. Gertmar, "Torque-maximizing field-weakening control: design, analysis, and parameter selection," *IEEE Transactions on Industrial Electronics*, vol. 48, no. 1, pp. 161–168, Feb. 2001.

[191] A. Petersson, L. Harnefors, and T. Thiringer, "Evaluation of current control methods for wind turbines using doubly-fed induction machines," *IEEE Transactions on Power Electronics*, vol. 20, no. 1, pp. 227–235, Jan. 2005.

[192] B. Metidji, N. Taib, L. Baghli, T. Rekioua, and S. Bacha, "Low-cost direct torque control algorithm for induction motor without AC phase current sensors," *IEEE Transactions on Power Electronics*, vol. 27, no. 9, pp. 4132–4139, Sep. 2012.

[193] S.-G. Jeong and M. H. Park, "The analysis and compensation of dead-time effects in PWM inverters," *IEEE Transactions on Industrial Electronics*, vol. 38, no. 2, pp. 108–114, Apr. 1991.

[194] V. Valdivia, A. Lazaro, A. Barrado, P. Zumel, C. Fernandez, and M. Sanz, "Impedance identification procedure of three-phase balanced voltage source inverters based on transient response measurements," *IEEE Transactions on Power Electronics*, vol. 26, no. 12, pp. 381–3816, Dec. 2011.

[195] T.-F. Wu, C.-H. Chang, L.-C. Lin, Y.-C. Chang, and Y.-R. Chang, "Two-phase modulated digital control for three-phase bidirectional inverter with wide inductance variation," *IEEE Transactions on Power Electronics*, vol. 28, no. 4, pp. 1598–1607, Apr. 2013.

[196] T.-F. Wu, K.-H. Sun, C.-L. Kuo, and C.-H. Chang, "Predictive current controlled 5-kW single-phase bidirectional inverter with wide inductance variation for DC-microgrid applications," *IEEE Transactions on Power Electronics*, vol. 25, no. 12, pp. 3076–3084, Dec. 2010.

[197] J. Holtz, J. Quan, J. Pontt, J. Rodriguez, P. Newman, and H. Miranda, "Design of fast and robust current regulators for high-power drives based on complex state variables," *IEEE Transactions on Industry Applications*, vol. 40, no. 5, pp. 1388–1397, Sep./Oct. 2004.

[198] Q. Shafiee, J. M. Guerrero, and J. C. Vasquez, "Distributed secondary control for islanded microgrids–a novel approach," *IEEE Transactions on Power Electronics*, vol. 29, no. 2, pp. 1018–1031, Feb. 2014.

[199] M. Alberdi, M. Amundarain, A. Garrido, I. Garrido, and F. Maseda, "Fault-ride-through capability of oscillating water column-based wave power generation plants equipped with doubly-fed induction generator and air flow control," *IEEE Transactions on Industrial Electronics*, vol. 58, no. 5, pp. 1501–1517, May 2011.

[200] B. Rabelo, W. Hofmann, J. da Silva, R. de Oliveira, and S. Silva, "Reactive power control design in doubly fed induction generators for wind turbines," *IEEE Transactions on Industrial Electronics*, vol. 56, no. 10, pp. 4154–4162, Oct. 2009.

[201] A. Luna, F. de Araujo Lima, D. Santos, P. Rodriguez, E. Watanabe, and S. Arnaltes, "Simplified modeling of a DFIG for transient studies in wind power applications," *IEEE Transactions on Industrial Electronics*, vol. 58, no. 1, pp. 9–20, Jan. 2011.

[202] D. Hung, N. Mithulananthan, and R. Bansal, "Multiple distributed generators placement in primary distribution networks for loss reduction," *IEEE Transactions on Industrial Electronics*, in press.

[203] T. Zhou and B. Francois, "Energy management and power control of a hybrid active wind generator for distributed power generation and grid integration," *IEEE Transactions on Industrial Electronics*, vol. 58, no. 1, pp. 95–104, Jan. 2011.

[204] M. Castilla, J. Miret, A. Camacho, J. Matas, and L. de Vicuna, "Reduction of current harmonic distortion in three-phase grid-connected photovoltaic inverters via resonant current control," *IEEE Transactions on Industrial Electronics*, in press.

[205] M. Rizo, A. Rodriguez, E. Bueno, F. Rodriguez, and C. Giron, "Low voltage ride-through of wind turbine based on interior permanent magnet synchronous generators sensorless vector controlled," in *Proceedings of 2010 IEEE Energy Conversion Congress and Exposition (ECCE)*, Sep. 2010, pp. 2507 –2514.

[206] "IEC 61400-21. Wind turbines - Part 21: Measurement and assessment of power quality characteristics of grid connected wind turbines ," 2008.

[207] J. Niiranen, "About the active and reactive power measurements in unsymmetrical voltage dip ride-through testing," *Wind Energy*, vol. 11, pp. 121–131, Jan./Feb. 2008.

[208] E. Robles, J. Pou, S. Recio, J. Zaragoza, J. Martin, and P. Ibañez, "Frequency adaptive stationary reference frame grid voltage sequence detector for distributed generation systems," *IEEE Transactions on Industrial Electronics*, vol. 58, no. 9, pp. 4275–4287, Sep. 2011.

[209] J. P. da Costa, H. Pinheiro, T. Degner, and G. Arnold, "Robust controller for DFIG of grid connected wind turbines," *IEEE Transactions on Industrial Electronics*, vol. 58, no. 9, pp. 4023–4038, Sep. 2011.

[210] J. Lopez, E. Gubia, E. Olea, J. Ruiz, and L. Marroyo, "Ride through of wind turbines with doubly fed induction generator under symmetrical voltage dips," *IEEE Transactions on Industrial Electronics*, vol. 56, no. 10, pp. 4246–4254, Oct. 2009.

[211] M. Andreica Vallet, S. Bacha, I. Munteanu, I. Bratcu, and D. Roye, "Management and control of operating regimes of cross-flow water turbines," *IEEE Transactions on Industrial Electronics*, vol. 58, no. 5, pp. 1866–1876, May 2011.

[212] Y. A.-R. Ibrahim Mohamed, "Mitigation of dynamic, unbalanced and harmonic voltage disturbances using grid-connected inverters with LCL filter," *IEEE Transactions on Industrial Electronics*, vol. 58, no. 9, pp. 3914–3924, Sep. 2011.

[213] G. Shen, X. Zhu, J. Zhang, and D. Xu, "A new feedback method for PR current control of LCL-filter-based grid-connected inverter," *IEEE Transactions on Industrial Electronics*, vol. 57, no. 6, pp. 2033–2041, Jun. 2010.

[214] J. D. Barros and J. F. Silva, "Multilevel optimal predictive dynamic voltage restorer," *IEEE Transactions on Industrial Electronics*, vol. 57, no. 8, pp. 2747–2760, Aug. 2010.

[215] M. Bollen, "Characterisation of voltage sags experienced by three-phase adjustable-speed drives," *IEEE Transactions on Power Delivery*, vol. 12, no. 4, pp. 1666–1671, Oct. 1997.

[216] F. D. Freijedo, J. Doval-Gandoy, O. Lopez, and E. Acha, "Tuning of phase locked loops for power converters under distorted utility conditions," *IEEE Transactions on Industry Applications*, vol. 45, no. 6, pp. 2039–2047, Nov./Dec. 2009.

[217] A. D. Hansen and G. Michalke, "Multi-pole permanent magnet synchronous generator wind turbines' grid support capability in uninterrupted operation during grid faults," *IET Renewab. Power Gener.*, vol. 3, no. 3, pp. 333–348, Sep. 2009.

[218] M. Rahimi and M. Parniani, "Efficient control scheme of wind turbines with doubly fed induction generators for low-voltage ride-through capability enhancement," *IET Renewab. Power Gener.*, vol. 4, no. 3, pp. 242–252, May 2010.

[219] S. Zhang, K.-J. Tseng, S. S. Choi, T. D. Nguyen, and D. L. Yao, "Advanced control of series voltage compensation to enhance wind turbine ride through," *IEEE Transactions on Power Electronics*, vol. 27, no. 2, pp. 763–772, Feb. 2012.

[220] M. Singh, V. Khadkikar, and A. Chandra, "Grid synchronisation with harmonics and reactive power compensation capability of a permanent magnet synchronous generator-based variable speed wind energy conversion system," *IET Power Electronics*, vol. 4, no. 1, pp. 122–130, Jan. 2011.

[221] M. H. J. Bollen, G. Olguin, and M. Martins, "Voltage dips at the terminals of wind power installations," *Wind Energy*, vol. 8, pp. 307–318, Jul. 2005.

[222] N. Urasaki, T. Senjyu, K. Uezato, and T. Funabashi, "An adaptive dead-time compensation strategy for voltage source inverter fed motor drives," *IEEE Transactions on Power Electronics*, vol. 20, no. 5, pp. 1150–1160, Sep. 2005.

[223] M. Jones, S. N. Vukosavic, D. Dujic, and E. Levi, "A synchronous current control scheme for multiphase induction motor drives," *IEEE Transactions on Energy Conversion*, vol. 24, no. 4, pp. 860–868, Dec. 2009.

[224] X. Yuan, F. Wang, D. Boroyevich, Y. Li, and R. Burgos, "DC-link voltage control of a full power converter for wind generator operating in weak-grid systems," *IEEE Transactions on Power Electronics*, vol. 24, no. 9, pp. 2178–2192, Sep. 2009.

Appendix A

Study of the Disturbance Rejection Capability of the Harmonics Caused by Dead Times in the Experimental Results of Chapter 2

In principle, a greater K value improves the overall disturbance rejection [10]. Nevertheless, this trend is not true for each particular harmonic, as it can be checked from the harmonic content in the current waveforms of Fig. 2.14. In order to demonstrate this assertion, the following study has been conducted. The fifth and seventh harmonics caused by dead times have been considered as a disturbance for the current loop, which is not compensated by the point of common coupling (PCC) voltage feedforward (cf. Fig. 2.2). Thus, those harmonics are included in v_{PCC}. Given the disturbance rejection transfer function

$$G_{\mathrm{DR}}(z) = \left.\frac{i_{\mathrm{dq}}(z)}{v_{\mathrm{PCC_{dq}}}(z)}\right|_{i^*_{\mathrm{dq}}=0} = \frac{-G_{\mathrm{L}}^{\mathrm{Tustin}}(z)}{1+(G_{\mathrm{PI}}(z)-\mathrm{j}\omega_1\widehat{L})G_{\mathrm{PL}}(z)} \tag{A.1}$$

where $G_{\mathrm{L}}^{\mathrm{Tustin}}(z)$ is obtained by applying the Tustin transform to (2.1) [see (26) in [10] with $R^{\mathrm{a}}=0$], the diagrams of the frequency response (in magnitude) of $G_{\mathrm{DR}}(z)$ for the q-axis component have been obtained in different conditions in order to study the following aspects. Note that subscripts $1,2,3$ and/or 4 are employed in this appendix to denote different values of the fundamental gain K and of the estimated resistance $\widehat{R}$, e.g., K_2, $\widehat{R}_1$...

1. The influence on the disturbance rejection of different K values (cf. Fig. A.1): $K_1 = 68.26$ (dark blue curves), the same gain as that in Fig. 2.14a; $K_2 = 421.50$ (green curves), the same gain as that in Fig. 2.14f, $K_3 = K_{\mathrm{opt}}/2 = 1225$ (cyan curves) and $K_4 = K_{\mathrm{opt}} = 2450$ (red curves), where $K_{\mathrm{opt}} = 0.039 \cdot 2\pi f_{\mathrm{s}}$ [10]. For this first test $\widehat{R} = R$ has been considered (note that this is not the case of Figs. 2.14a and f). From Fig. A.1a], it can be checked that the area delimited by the different magnitude curves (and the x axis) becomes smaller as the gain increases, i.e., the global disturbance rejection is enhanced as K grows [10]. However, regarding the capability to reject a specific harmonic, the frequency response has to be analyzed around it. A zoom at the sixth harmonic in the synchronous reference frame (SRF) (cf. Fig. A.1b) permits to observe that the capability to reject the disturbance

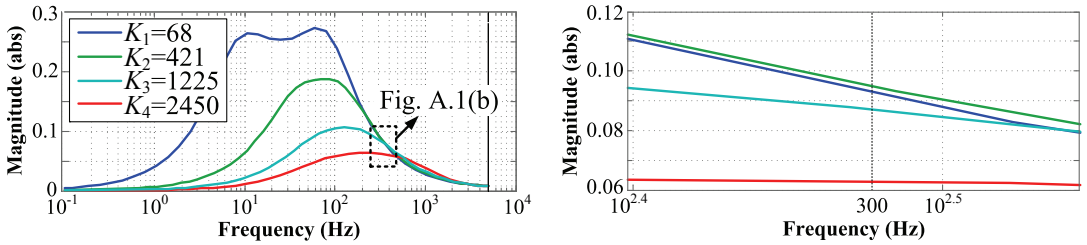

(a) General view. (b) Zoom at 300 Hz.

Figure A.1: Diagrams of magnitude versus frequency of $G_{\mathrm{DR}}(z)$ for different K values: $K_1 = 68.26$ in dark blue, $K_2 = 421.50$ in green, $K_3 = K_{\mathrm{opt}}/2 = 1225$ in cyan and $K_4 = K_{\mathrm{opt}} = 2450$ in red.

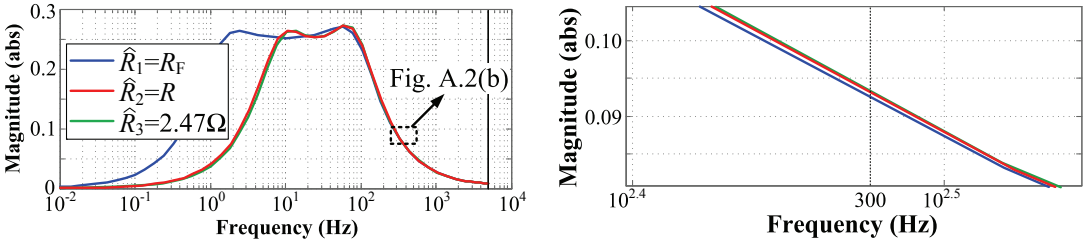

(a) General view. (b) Zoom at 300 Hz.

Figure A.2: Diagrams of magnitude versus frequency of $G_{\mathrm{DR}}(z)$ with $K_1 = 68.26$ for different $\widehat{R}$: $\widehat{R}_1 = R_{\mathrm{F}}$ in dark blue, $\widehat{R}_2 = R$ in red and $\widehat{R}_3 = 2.47\,\Omega$ in green.

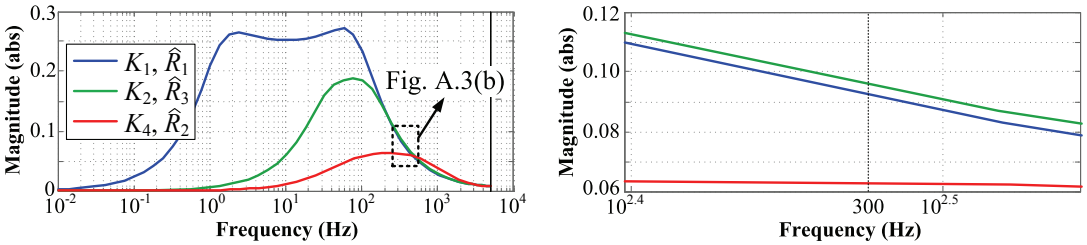

(a) General view. (b) Zoom at 300 Hz.

Figure A.3: Diagrams of magnitude versus frequency of $G_{\mathrm{DR}}(z)$ for the conditions of Fig. 2.14a in dark blue, of Fig. 2.14f in green and optimal conditions for the final implementation in red.

at 300 Hz is better with $K_1 = 68.26$ than with $K_2 = 421.50$ (in Fig. A.1b, the magnitude of the dark blue curve is smaller than that of the green one); the other gains, K_3 and K_4, offer a smaller sensitivity at that specific frequency. This change of tendency at high frequencies, compared to the overall behavior, can also be corroborated from the curve crossings in the right-hand part of Fig. A.1a, which means that the disturbance rejection above a certain frequency worsens for increasing K values.

2. The influence on the disturbance rejection of different R estimates, while its actual value is kept constant at $R = 2.3\,\Omega$ (cf. Fig. A.2): $\widehat{R}_1 = R_\mathrm{F}$ (dark blue curves), $\widehat{R}_2 = R$ (red curves) and $\widehat{R}_3 = 2.47\,\Omega$ (green curves), for $K_1 = 68.26$. From Fig. A.2a, for a very low gain $K_1 = 68.26$, it can be checked that in addition to K, the R estimate influences the overall disturbance rejection capability. The area delimited by the magnitude curves (and the x axis) is larger as $\widehat{R}$ decreases, which means that the global disturbance rejection worsens. Since the R estimate is directly related with the integral gain in chapter §2, i.e., $K_\mathrm{I} = K\widehat{R}$ [10, 141], this fact could be expected. On the other hand, from the zoom at 300 Hz for the three R estimates (cf. Fig. A.2b), it can be observed that the ability to reject the sixth harmonic is better for the lowest $\widehat{R}$ and worse for the largest one. As it happened with K variations, the disturbance rejection above a certain frequency worsens for increasing R estimates (see that the three magnitude curves cross in Fig. A.2a).

   This same study has been repeated for $K_2 = 421.50$ and for $K_4 = K_\mathrm{opt} = 2450$, with equivalent results. It should be highlighted that the differences among the capability to reject the sixth harmonic of the three cases of R estimates become more significant as K grows.

3. Finally, in order to summarize the conclusions, and to link them to the cases in chapter §2, which are more representative, the following frequency responses (in magnitude) are compared in Fig. A.3:

   a) conditions of Fig. 2.14a i.e., $K_1 = 68.26$ and $\widehat{R}_1 = R_\mathrm{F}$ (dark blue curves);

   b) conditions of Fig. 2.14f, i.e., $K_2 = 421.50$ and $\widehat{R}_3 = 2.47\,\Omega$ (green curves);

   c) conditions suggested in section §2.4.4 as appropriate to be implemented during normal operation (after the identification process) when a PI controller with state-feedback cross-coupling decoupling (PICCD) is selected, i.e., $K_4 = K_\mathrm{opt} = 2450$ and $\widehat{R}_2 = R$ (red curves).

   From the comparison between the dark blue and green curves in Fig. A.3, it can be concluded that the former leads to a better disturbance rejection of the sixth harmonic (cf. Fig. A.3b), whereas the latter presents better rejection in most of the rest of the spectrum (cf. Fig. A.3a). Therefore, since the sixth harmonic is usually the most important one in magnitude, once the steady state is reached, it should be expected that the conditions of Fig. 2.14a result in a lower total harmonic distortion (THD) than those of Fig. 2.14f. On the other hand, it should be remarked that the best harmonic rejection is achieved in the conditions suggested to be implemented during normal operation, once R has been identified (see the red curves in Fig. A.3). Not only is the global harmonic rejection better, but also the specific behavior at 300 Hz. Of course, there will be certain harmonic frequencies (higher than these ones) at which the harmonic rejection worsens (see the

crossings in the magnitude curves on the right side of Fig. A.3a). Anyway, selective controllers could be implemented in order to guarantee proper rejection of the harmonic components.

Appendix B

Mathematical Development of the Error Time-Domain Expressions for Chapter 4

This appendix explains how to obtain the error time-domain expression $e_{\Delta i^*}(t)$ from the z-domain one $E_{\Delta i^*}(z)$ in case of reference changes. Regarding disturbance transients, the process to calculate $e_{\Delta v_{\mathrm{PCC}}}(t)$ from $E_{\Delta v_{\mathrm{PCC}}}(z)$ is analogous.

From the factorized expression of $E_{\Delta i^*}(z)$, the corresponding partial-fraction expansion is

$$E_{\Delta i^*}(z) = \sum_{l=1}^{\iota} \frac{r_l z}{z - p_l} \tag{B.1}$$

where ι represents the number of poles ($\iota = 6$ for $E_{\Delta i^*}$ and $\iota = 7$ for $E_{\Delta v_{\mathrm{PCC}}}$). Both real and complex poles without distinction are denoted by $p_l \in \mathbb{C}$, while $r_l \in \mathbb{C}$ are their respective residues. Equation (B.1) can be rewritten as

$$E_{\Delta i^*}(z) = \sum_{i=1}^{\kappa} \underbrace{\frac{r_i z}{z - p_i}}_{\text{real poles}} + \sum_{j=1}^{\chi} \underbrace{\frac{b_j z^2 + c_j z}{(z - p_j)(z - p_j^*)}}_{\text{complex conjugate poles}} \tag{B.2}$$

where $\iota = \kappa + 2\chi$, with being κ the number of real poles p_i and with χ being the number of conjugate pole pairs $p_j - p_j^*$; r_i stands for the residues of the real poles p_i. Concerning the residues of the complex poles r_j, the variables $b_j = 2\mathfrak{Re}(r_j) = r_j + r_j^*$ and $c_j = -(r_j + r_j^*)\mathfrak{Re}(p_j) + (r_j - r_j^*)\mathfrak{Im}(p_j)$ are employed, with $b_j, c_j, r_i \in \mathbb{R}$ and $r_j \in \mathbb{C}$.

From (B.2), the time-domain expression can be obtained from z-inverse transforms:

$$e_{\Delta i^*}(t) = \sum_{i=1}^{\kappa} \underbrace{r_i e^{-p_i' t}}_{\text{real poles}} + \sum_{j=1}^{\chi} \underbrace{\left[d_j' cos(\omega_{\mathrm{d}_j}' t) + f_j' \sin(\omega_{\mathrm{d}_j}' t) \right] e^{-\sigma_j' t}}_{\text{complex conjugate poles}} \tag{B.3}$$

where $p_i' = \ln|p_i|/T_{\mathrm{s}}$, $d_j' = r_j + r_j^*$, $p_j' = \ln|p_j|/T_{\mathrm{s}} = \ln\left|\sigma_j' + j\omega_{\mathrm{d}_j}'\right|/T_{\mathrm{s}}$ and $f_j' = r_j - r_j^*$ with σ_j' and ω_{d_j}' being the real and the imaginary terms of the poles p_j' and p_i'; d_j', σ_j', ω_{d_j}' and $f_j' \in \mathbb{R}$ and $p_j' \in \mathbb{C}$.

Fig. B.1 illustrates an alternative method which permits to obtain the time-domain expressions from the z-domain ones without factorizing and calculating residues. It is based on the impulse response of a discrete filter defined by $E(z)$. This method has been employed to generate the estimated error signals $\hat{e}(t)$ included in the experimental results.

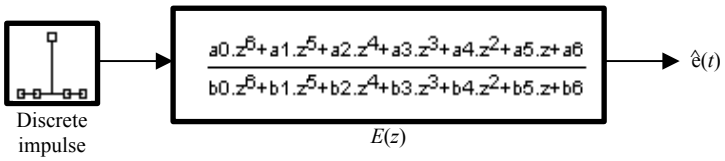

Figure B.1: Block diagram in Simulink that shows how to obtain the error time-domain expression from the z-domain one.